

# UC San Diego

## UC San Diego Electronic Theses and Dissertations

### Title

Biophysical modelling of synaptic plasticity and its function in the dynamics of neuronal networks

### Permalink

<https://escholarship.org/uc/item/3f96d9vc>

### Author

Talathi, Sachin S.

### Publication Date

2006

Peer reviewed|Thesis/dissertation

UNIVERSITY OF CALIFORNIA, SAN DIEGO

**Biophysical modelling of synaptic plasticity and its function in the  
dynamics of neuronal networks**

A dissertation submitted in partial satisfaction of the  
requirements for the degree  
Doctor of Philosophy

in

Physics

by

Sachin S. Talathi

Committee in charge:

Professor Henry D.I. Abarbanel, Chair  
Professor Dan Arovas  
Professor Tim Gentner  
Professor Herbert Levine  
Professor Katja Lindenberg  
Professor Gabriel Silva

2006

Copyright  
Sachin S. Talathi, 2006  
All rights reserved.

The dissertation of Sachin S. Talathi is approved,  
and it is acceptable in quality and form for publi-  
cation on microfilm:

---

---

---

---

---

---

Chair

University of California, San Diego

2006

To My Grandmother

# TABLE OF CONTENTS

|   |   |       |
|---|---|-------|
|   | Signature Page . . . . .  | iii   |
|   | Dedication . . . . .  | iv    |
|   | Table of Contents . . . . .   | v     |
|   | List of Figures . . . . .   | vii   |
|   | List of Tables . . . . .  | xix   |
|   | Acknowledgements . . . . .  | xx    |
|   | Vita, Publications, and Fields of Study . . . . .   | xxii  |
|   | Abstract of the Dissertation . . . . .  | xxiii |
| 1 | Introduction . . . . .  | 1     |
|   | 1.1 Thesis Overview . . . . .   | 2     |
|   | 1.2 Background . . . . .  | 4     |
|   | 1.2.1 Synaptic plasticity . . . . .   | 5     |
|   | 1.2.2 Song System . . . . .   | 6     |
|   | 1.2.3 Neuron model . . . . .  | 8     |
|   | 1.3 Organization . . . . .  | 13    |
| 2 | Biophysical model for synaptic plasticity with discrete state synapses . . . . .                | 16    |
|   | 2.1 Introduction . . . . .  | 16    |
|   | 2.2 Discrete state synapses: General formulation for the transition rate model . . . . .        | 18    |
|   | 2.3 Discrete state synaptic model . . . . .   | 21    |
|   | 2.3.1 Two state model . . . . .   | 21    |
|   | 2.3.2 Three state model . . . . .   | 21    |
|   | 2.3.3 The neuron model for the postsynaptic cell . . . . .                                      | 25    |
|   | 2.4 Results . . . . .   | 33    |
|   | 2.4.1 Determination of the discrete level conductances . . . . .                                | 33    |
|   | 2.4.2 LTP and LTD Induction Protocols . . . . .   | 35    |
|   | 2.4.3 Synchronization of Two Periodic Neural Oscillators with Discrete State Synapses . . . . . | 40    |
|   | 2.5 Discussion . . . . .  | 43    |
| 3 | Dynamics of songbird learning and control . . . . .   | 49    |
|   | 3.1 Introduction . . . . .  | 49    |
|   | 3.2 The RA Nucleus: Structure and Plasticity . . . . .  | 55    |
|   | 3.2.1 RA Structure . . . . .  | 55    |
|   | 3.2.2 RA-PNs . . . . .  | 57    |

|       |  |     |
|-------|--|-----|
| 3.2.3 | RA INs . . . . .   | 61  |
| 3.2.4 | Plasticity in RA . . . . .   | 62  |
| 3.3   | The Anterior forebrain pathway; Structure and its function in producing delay $\Delta T$ . . . . . | 66  |
| 3.3.1 | Area X . . . . .   | 66  |
| 3.3.2 | DLM . . . . .  | 68  |
| 3.3.3 | The IMAN Nucleus . . . . .   | 71  |
| 3.4   | Model Parameters . . . . .   | 72  |
| 3.4.1 | Determining $\Delta T$ . . . . .   | 75  |
| 3.4.2 | The Role of Inhibition from X $\rightarrow$ DLM . . . . .  | 77  |
| 3.5   | Dynamics with Coupling of the RA and the AFP . . . . .   | 79  |
| 3.6   | Summary and Conclusions . . . . .  | 85  |
| 4     | Neural circuitry for recognizing interspike interval sequence . . . . .                            | 89  |
| 4.1   | Introduction . . . . .   | 89  |
| 4.2   | Time Delay Circuits . . . . .  | 93  |
| 4.2.1 | One Neuron Model . . . . .   | 93  |
| 4.2.2 | Two Neuron Model . . . . .   | 95  |
| 4.3   | Three Neuron Model . . . . .   | 98  |
| 4.4   | ISI Reading Unit: IRU . . . . .  | 104 |
| 4.5   | IRU learning . . . . .   | 108 |
| 4.6   | Linear Map for Learning Rule . . . . .   | 117 |
| 4.7   | Discussion . . . . .   | 119 |
| 5     | Implementation of neuronal time delay circuitry in hardware . . . . .                              | 123 |
| 5.1   | Designing Electronic Neuron . . . . .  | 124 |
| 5.2   | Time Delay Circuitry in Electronics . . . . .  | 133 |
| 5.3   | Conclusion . . . . .   | 143 |
|       | Bibliography . . . . .   | 147 |

## LIST OF FIGURES

|     |   |    |
|-----|---|----|
| 1.1 | <p><b>Schematic of the song system in songbirds:</b> The song production motor pathway is shown in brown and blue. The input to HVC is shown in brown from the thalamic nucleus Uva and the neostriatal nucleus Nif. The descending projections from HVC to the nucleus RA in the neostriatum and from RA to vocal nucleus nXIIts, the respiratory nucleus RAm and the laryngeal nucleus Am in the medulla is shown in blue. The song learning anterior fore-brain pathway (AFP) is shown in red. HVC and RA are indirectly linked through the AFP via, Area X, the thalamic DLM nucleus and the lMAN in the neostriatum. lMAN also projects to Area X, closing the loop for the AFP. The auditory region in the neostriatum, Field L, projects to HVC and it is shown in green. The abbreviations for the nuclei mentioned are: Am-nucleus ambiguus; RAm-nucleus retroambiguus; DLM-medial portion of the dorsolateral nucleus of the thalamus; lMAN-lateral portion of magnocellular nucleus of archistriatum; Nif-nucleus interface; RA-robust nucleus of archistriatum; Uva-nucleus uvaformis; nXIIts-tracheosyringeal part of hypoglossal nucleus. (Adapted from Brenowitz et.al., 1997)</p> | 7  |
| 1.2 | <p><b>Dynamics of type I neuron model:</b> (a) Time trace of spiking activity in the model when injected with input current of <math>I_{In} = 3.5\mu A/cm^2</math>. The neuron is firing frequency is approximately 120 Hz. (b) The frequency of firing is plotted as function of input dc current <math>I_{In}</math>. (c) The bifurcation diagram for type I neuron is plotted. In the left column the steady state dynamics of the neuron model is shown when the neuron is in the resting state. We see that as the input current is increased the stable and unstable fixed point approach each other until, the point where they annihilate and the neuron goes into stable spiking mode. In the right column the stable limit cycle behavior is seen. For very large input currents, the limit cycle vanishes through inverse Hopf bifurcation. (d) The phase response curve for the neuron <math>PRC(\theta)</math> is plotted as function of phase <math>\theta</math>, at which infinitesimal perturbation is applied. For type I neuron models, the phase is always advanced in response to perturbations in the membrane potential.</p>   | 10 |



|     |  |    |
|-----|--|----|
| 1.3 | <b>Dynamics of type II neuron model:</b> (a) Time trace of spiking activity in the model when injected with input current of $I_{In} = 3.5\mu A/cm^2$ . The neuron firing frequency is approximately 55 Hz. (b) The frequency current relationship for type II neuron models. For input current $I_{In} > 2.293\mu A/cm^2$ , the neuron starts spiking starting frequency of around 41 Hz. Type II neuron model does not permit wide range of spiking frequencies. (c) The bifurcation diagram for type II neuron model. The mechanism of the neuron to make a transition from the resting state to the spiking state is through Hopf bifurcation, resulting in a regime where the neuron exhibits bistable behavior, of coexisting stable resting and spiking states, separated by an unstable limit cycle. For large input currents, the spiking eventually vanished, through inverse Hopf bifurcation. (d) The phase response curve $PRC(\theta)$ for type II neuron model. The PRC has both positive and negative regions. Thus depending on the phase of input membrane potential perturbation, the neuron spike is either advanced or delayed. . . . . | 12 |
| 2.1 | <b>Three state model of synaptic plasticity.</b> Individual synapses can move among the three states, marked 0 for the “low” state, 1 for the “high” state, and 2 for the “high locked-in” state. The rules for state transition depend on the transition rates, $f(t)$ and $g(t)$ , governed by changes in intracellular calcium concentration. These transition rates are determined by LTP and LTD induction protocols. . . . .   | 23 |
| 2.2 | Steady state values for the transition rates $f$ and $g$ plotted as function of the magnitude of the change in intracellular calcium concentration. $\Delta C$ is in arbitrary units. For small changes in intracellular calcium concentration only $g$ is nonzero, corresponding to LTD induction, and for larger changes in intracellular calcium concentration, both $f$ and $g$ are nonzero with $f$ being greater than $g$ , corresponding to an LTP induction protocol. . . . .  | 24 |
| 2.3 | <b>Schematic of the two compartment postsynaptic neuron model :</b> The diagram shows a somatic compartment comprised of standard HH ionic currents, following type I neuronal dynamics. The soma compartment is electrically coupled to a dendritic compartment consisting of standard HH currents in addition to two potassium currents $I_A$ and $I_M$ and the ligand gated ionic currents of AMPA and NMDA type essential for synaptic plasticity dynamics considered here. There is an additional input through voltage gated calcium currents. In addition the dendritic compartment also involved intracellular calcium dynamics, which governs the synaptic plasticity mechanics. . . . .  | 26 |

2.4 **Frequency-plasticity curve.** The change in normalized AMPA conductance per synapse,  $G_{AMPA}/N_s - 1$ , is plotted as function of the frequency of a periodic burst of 10 presynaptic spikes presented to the presynaptic terminal. The circles represent synaptic plasticity for the full three state model. The upward-pointing triangles represent synaptic plasticity with the term  $g(t)$  set to 0, corresponding to blocking phosphatase activity in the postsynaptic cell. One sees and expects LTP alone. The downward-pointing triangles represent the change in synaptic plasticity with the term  $f(t)$  set to 0, corresponding to blocking kinase activity in the postsynaptic cell. We observe and expect LTD alone in this case. These results are quite similar to the observations of (O'Connor et al., 2005b). . . . 36

2.5 **Spike timing dependent plasticity protocol.** The change in normalized AMPA conductance per synapse,  $G_{AMPA}/N_S - 1$ , plotted as a function of the delay,  $\tau = t_{post} - t_{pre}$  (ms), between presentation of a single presynaptic spike at  $t_{pre}$  and postsynaptic spike induced at  $t_{post}$ . . . . . 37

2.6 (a) Change in normalized synaptic strength as a function of the delay  $\tau = t_{post(2)} - t_{pre}$  when a single presynaptic spike is paired with two postsynaptic spikes 10 ms apart.  $t_{post(2)}$  is the time of the second postsynaptic spike. Model results (*points connected by lines*) are plotted with experimental data of G. M. Wittenberg (*large filled circles with error bars*; Wittenberg, 2003, used with permission). *Normalized synaptic strength*, for the model, is the normalized AMPA conductance per synapse ( $G_{AMPA}/N_S$ ) after the pairing. For the experiments, it is the average peak excitatory postsynaptic current (EPSC) height measured 10-20 minutes after the end of the pairing protocol, normalized by the mean baseline peak EPSC height (*Error bars*: standard error of the mean). In the experiments, pairing was repeated 100 times at 5 Hz. (b) Here we plot change in normalized synaptic strength as a function of the delay  $\tau = t_{post(2)} - t_{pre}$  when a single presynaptic spike is paired with two postsynaptic spikes 15 ms apart. As in case (a), we see a distinct dip in potentiated AMPA conductance is observed for times when presynaptic spike falls in between the two postsynaptic spike presentations. (c) Similar plot of change in normalized synaptic strength as a function of the delay  $\tau = t_{post(2)} - t_{pre}$  when a single presynaptic spike is paired with two postsynaptic spikes 20 ms apart. . . . . 39

|     |  |    |
|-----|--|----|
| 2.7 | (a) $T_1/T_2$ , the ratio of the interspike interval $T_1$ of the presynaptic neuron to the interspike interval $T_2$ of the postsynaptic neuron, is plotted as a function of the presynaptic input frequency, $1000/T_1$ Hz, for a synapse starting at a base AMPA conductance of $g_{AMPA}(t = 0) = 0.1 \text{ mS/cm}^2$ . We see that the one-to-one synchronization window is broadened when the static synapse is replaced by a plastic synapse as determined by the three state model. (b) A similar plot for different value of base AMPA strength, $g_{AMPA}(t = 0) = 0.2 \text{ mS/cm}^2$ . . . . .   | 42 |
| 2.8 | Intracellular calcium concentration, scaled by 15, and the change in normalized synaptic strength, $G_{AMPA}(t)/N_S - 1$ , is plotted as a function of time in the case when a periodically spiking postsynaptic cell is driven by a periodically spiking presynaptic input. . . . .   | 44 |
| 2.9 | $V_{\text{Soma}}(t)$ , $V_{\text{dendrite}}(t)$ and $V_{\text{pre}}(t)$ , plotted as functions of time, when the presynaptic and postsynaptic neurons are synchronized. Note that the presynaptic and postsynaptic neurons are synchronized in-phase with an internal, $V_{\text{Soma}}(t)$ to $V_{\text{spine}}(t)$ , time difference determined by the two compartments of the model neuron. . . . .   | 45 |
| 3.1 | Diagram of the pre-motor pathway, HVC and RA nuclei, and the anterior forebrain pathway, AFP, comprised of Area X, DLM, and lMAN. HVC receives motor instructions which are expressed as sparse bursts to RA and to Area X. The AFP is a control and maintenance pathway. Signals from HVC through the AFP arrive at RA with a time delay $\Delta T \approx 50 \pm 10$ ms. The arrows at the end of lines represent excitatory couplings; the filled circles, inhibitory coupling. The dotted line is a known connection between RA and DLM whose physiological properties are not yet established. . . . .  | 51 |
| 3.2 | <b>The structure of the RA nucleus in our model.</b> RA projection neurons (PN) receive input from both HVC and, through the AFP, from lMAN. RA-PNs are coupled with weak excitation. Populations of RA-PNs project to the syrinx and to the control of the respiratory system. RA interneurons (IN) also receive input from both HVC and lMAN. They receive excitatory signals from the PNs and project back inhibitory couplings. The arborization of the PNs is broad, and it is estimated that the ratio of PNs:INs is about 30:1 (Spiro et al., 1999). Here we represent the RA nucleus with two PNs and one IN. When there is no song input from HVC directly or via the AFP, the PNs are at rest and the INs oscillate at about 15-30 Hz. The output to DLM interneurons is shown in dotted lines. The arrows at the end of lines represent excitatory couplings; the filled circles represent inhibitory coupling. . . . . | 56 |

- 3.3 Membrane voltages of neurons in the model RA nucleus. Before spikes from HVC arrive at the PNs and IN cells, the IN is at rest at -61.4 mV. The PNs are oscillating autonomously at 20 Hz; they are weakly coupled by mutual excitation, but they do not synchronize. When a burst of five spikes from HVC arrives at 475 ms, the PNs are strongly inhibited and the INs begin spiking at higher frequency. As the nucleus recovers from this input, the IN oscillations decrease in frequency. About 250 ms after the arrival of the HVC signal, the nucleus recovers completely and returns to its original state. . . . . 62
- 3.4 Using our biophysical model of synaptic plasticity, we evaluate the change in AMPA conductivity  $\frac{\Delta g_{RA}}{g_0}$  at the HVC  $\rightarrow$  RA connections due to signals arriving from HVC followed by signals arriving from IMAN  $\Delta T$  later. In this figure the HVC signal was a burst of five spikes with Interspike intervals (ISI) of 2 ms. A burst of five spikes with ISI = 2 ms arrives from IMAN  $\Delta T$  later. The zero in  $\frac{\Delta g_{RA}}{g_0}$  near  $\Delta T \approx 50$  ms represents potentially stable plasticity in RA, and thus a potentially stable set of connections in the song pre-motor pathway. Lesions of the AFP would result in  $\Delta T \rightarrow \infty$  which is also a region of  $\frac{\Delta g_{RA}}{g_0} = 0$ . . . . . 65
- 3.5 **The structure of the Area X nucleus in our model.** Spiny neurons (SN) receive input from both HVC and IMAN. In turn the SN inhibits the aspiny, fast firing neurons (AF). The AFs project inhibition to DLM. When there is no song input from HVC, the SNs are at rest and the AFs oscillate at about 15-30 Hz. The arrows at the end of lines represent excitatory couplings; the filled circles, inhibitory coupling. When the AFs are active, they inhibit DLM action. On activation the SNs inhibit the AF neurons, and with the release of AF  $\rightarrow$  DLM, the DLM neurons can rebound and fire. The HVC  $\rightarrow$  AF connection resets the AF oscillations resulting in the SN  $\rightarrow$  AF inhibition release of DLM becoming time coordinated with the arrival of a burst from HVC. . . . . 67
- 3.6 **The structure of the DLM nucleus in our model.** The arrows at the end of lines represent excitatory couplings; the filled circles, inhibitory coupling. The DLM PN receives inhibitory input from the Area X AF neurons. It projects excitatory processes to IMAN. In our model, input from RA excites the DLM INs which project inhibition to the DLM PNs. . . . . 69
- 3.7 The time course of membrane voltages in the AFP neurons after a burst of five spikes with ISI = 2 ms arrives at SN from HVC at time 600 ms. Before the HVC burst arrives at SN, SN is at rest near -66 mV, and AF is oscillating at 20 Hz. AF activity inhibits the DLM projection neuron which shows small variations around rest with the same period as the AF. After the burst from HVC excites SN, it inhibits AF, and then DLM recovers from its inhibition to fire about 67.5 ms later. The action potential in DLM excites IMAN. 76

|      |   |    |
|------|---|----|
| 3.8  | <p><b>UPPER PANEL</b> we show the activity in the DLM PN of the Na activation variable, <math>m_{DLM}(t)</math> and inactivation variable, <math>h_{DLM}(t)</math> following a burst of 5 spikes arriving at SN (in Area X) at time 800 ms. This indicates that the long time delay associated with the AFP is manifested in the slow recovery of the DLM PN from its hyperpolarization due to inhibition from the AF neuron in Area X. When this inhibition is released, the DLM PN responds with a spike as the activation variable slowly rises from 0 in the neuron's hyperpolarized state. <b>LOWER PANEL</b> we have the same time axis and show the membrane voltage in the DLM projection neuron and in the IMAN neuron innervated by the DLM PN firing. The DLM PN fires about 60 ms after the HVC burst arrives at SN, and the IMAN neuron fires about 63 ms after the HVC burst innervates SN. . . . .</p> | 78 |
| 3.9  | <p>The time <math>\Delta T</math> for a signal to traverse the AFP depends on the strength of the AF <math>\rightarrow</math> DLM inhibitory connection. The conductance relative to a baseline value is the ratio <math>R = \frac{g_{AF-DLMPN}}{g_{AF-DLMPN-Baseline}}</math>. Positive slope in <math>\Delta T(R)</math> is associated with stability in RA plasticity by the argument given in the text. . . . .</p>   | 79 |
| 3.10 | <p>The AFP output when the synaptic current between the Area X output neuron, AF, is changed from inhibitory to excitatory by making <math>V_{REVI-DLM} = 0</math> mV instead of -75 mV. There is a burst of spikes from HVC at 980 ms, but the autonomous firing of the SN and other neurons obscures the identification of <math>\Delta T</math>. The RA neuron receives many inputs from the PN in IMAN which are not associated with an HVC burst because of the oscillations of the AFP loop. In this calculation <math>R = 2</math>. . . . .</p>  | 80 |
| 3.11 | <p>With <math>R = 4</math> we start the coupled HVC, RA, AFP dynamical system at <math>g_{RA}(0) = 0.21</math> and then <math>g_{RA}(0) = 0.28</math>. Each initial condition lies within the same basin of attraction of the map <math>g_{RA}(N) \rightarrow g_{RA}(N + 1)</math>, determined by presenting many bursts from HVC separated by 2000 ms. We see <math>g_{RA}(N \rightarrow \infty) \approx 0.095</math> and by examining the stable system we find <math>\Delta T = 51.67</math> ms. If we turn off the RA <math>\rightarrow</math> DLM connection, the map is unstable and <math>g_{RA}(N)</math> grows without bound. . . . .</p>  | 82 |
| 3.12 | <p>With <math>R = 10</math> we start the coupled HVC, RA, AFP dynamical system at <math>g_{RA}(0) = 0.3</math> and then <math>g_{RA}(0) = 0.4</math>. Each initial condition lies within the same basin of attraction of the map <math>g_{RA}(N) \rightarrow g_{RA}(N + 1)</math>, determined by presenting many bursts from HVC separated by 2000 ms. We see <math>g_{RA}(N \rightarrow \infty) \approx 0.038</math> and by examining the stable system we find <math>\Delta T = 51.14</math> ms. If we turn off the RA <math>\rightarrow</math> DLM connection, the map is unstable and <math>g_{RA}(N)</math> grows without bound. . . . .</p>   | 83 |

- 3.13 With  $R = 0.2$  we start the coupled HVC, RA, AFP dynamical system at  $g_{RA}(0) = 0.21$ . In this case the map  $g_{RA}(N) \rightarrow g_{RA}(N + 1)$ , determined by presenting many bursts from HVC separated by 2000 ms drives  $g_{RA}(N)$  to smaller and smaller values. We have had to manually cutoff the decrease of  $g_{RA}(N)$  by imposing a lower bound of 0. This is not built into the model, but could easily be added (Nowotny et.al, 2003). This behavior is seen for all values of  $g_{RA}(0)$  we examined for  $R_{IE} = 0.2$ , and our qualitative arguments in the text suggest this should be so. . . . . 84
- 4.1 (a) **Schematic of the one neuron delay unit model.** The input current is  $I_{IN}(t) = I [\theta(t - t_0) - \theta(V(t) - V_{th})]$  starting at the time  $t_0$  of the input spike and lasting until the first spike from the neuron at time  $t_1$ . The intrinsic dynamics of the neuron to the spiking mode is through a saddle node bifurcation, typical of type I neurons. (b) Output from the delay unit. In this case the neuron produces a delayed spike after about 86 ms. (c) Variation of the delay produced by the neuron as function of the strength of the input step current  $I$ . 94
- 4.2 **Schematic of a two neuron delay unit model.** The input spike arrives at  $t_0$  at neuron B, which is at rest, sending this bistable neuron into a spiking regime and raising the neuron A membrane voltage towards spiking threshold until it eventually spikes at  $t_1$ . The spike from neuron A pushes neuron B back into a stable resting state. (b) The membrane voltages of neurons A and B in response to an input spike at time  $t_0 = 400$  ms. Neuron A fires after a delay of around 42 ms. The delay produced is governed by the strength of the excitatory synaptic connection from neuron B to neuron A. (c) Plot of delay  $\tau(g_E)$  as a function of the strength of the excitatory synaptic input from neuron B to neuron A. Note that  $\frac{d\tau(g_E)}{dg_E} < 0$ . . . 96

- 4.3 **Schematic diagram of the three neuron time-delay unit used in the IRU circuit.** This is abstracted from a time-delay network in the anterior forebrain pathway of the birdsong system as shown in the inset above. The inset shows the AFP loop (Area X, DLM and LMAN) from the birdsong system that suggested our three neuron time-delay unit. Unit A is abstracted from the area X SN neurons, unit B is abstracted from the area X AF neurons, and unit C is abstracted from the thalamic excitatory neurons in DLM. Absent any input spikes neuron A is at rest, neuron B oscillates periodically, and neuron C oscillates around its rest potential driven by periodic inhibitory input from neuron B. When an input spike arrives at neuron A and at neuron B at time  $t_0$ , neuron A fires an action potential and neuron B has the phase of its oscillation reset to be in synchrony with the time of arrival  $t_0$  of the spike. The action potential in neuron A inhibits neuron B, and this releases neuron C to rise to its spiking threshold a time  $\tau(R)$  later.  $R$  is the dimensionless scale of the  $B \rightarrow C$  inhibition. Within a broad range for  $R$ , neuron C will fire a single spike at a time  $t_0 + \tau(R)$ . The value of the conductance for the  $B \rightarrow C$  inhibitory synapse is  $g_I = Rg_{I0}$ , with  $g_{I0}$  a baseline conductance. . . . . 100
- 4.4 (a) For  $R = 0.7$  we show the membrane voltages of neuron A (blue) and neuron C (red) in response to single spike input (black) arriving at neuron A and neuron B at time  $t_0 = 500$  ms. For  $R = 0.7$  we see the output spike from neuron C occurring at  $t = 543.68$  ms, corresponding to  $\tau(R) = 43.6$  ms. (b) For  $R = 0.7$  we again show the membrane voltages of neuron A (blue) and neuron C (red), and in addition now display the membrane voltage of neuron B (green). A single spike input (black) arrives at time  $t = 500$  ms. We see that the periodic action potential generation by neuron B is reset by the incoming signal. (c) The delay  $\tau(R)$  produced by the three neuron time delay unit as a function of  $R$ , the strength of the inhibitory synaptic connection  $B \rightarrow C$ . All other parameters of the time delay circuit are fixed to values given in the text. For  $R < R_L$  the inhibition is too weak to prevent spiking of neuron C. For  $R > R_U$  the inhibitory synapse is so strong that neuron C does not produce any action potential, so effectively the delay is infinity. In Figures 4a and 4b the arrow indicates the time of the spike input to units A and B of our delay unit. . . . . 103

|     |  |     |
|-----|--|-----|
| 4.5 | (a) Schematic of the complete Interspike interval (ISI) reading unit (IRU). The input ISI pattern, enters the IRU at the spike selection unit (SSU) and the IRU responds with a spike output through the detection unit depending on whether it is tuned to the input ISI. (b) Schematic of the spike selection unit (SSU). (c) Schematic of the Time delay unit. Note the excitatory connection C→B. It is required to facilitate spike timing dependent plasticity learning in the delay unit. (d) Schematic of the detection unit. It responds with an output spike only when it receives two input spikes $\delta$ ms, the resolution for ISI recognition by the detection unit. . . . . | 105 |
| 4.6 | (a) Schematic of the detection unit. It receives two input spikes with various time intervals between them. It responds with a spike if the two inputs are within 1 ms of each other. (b) <b>Top panel</b> The scaled response of the detection unit when two input arrive within 2 ms of each other. We see that the integrated input arriving at this delay does not result in neuron spiking. In the <b>bottom panel</b> we show the scaled neuron response to two input spikes arriving within 1 ms of each other. The detection unit produces a spike output, indicating coincidence detection. . . . .   | 107 |
| 4.7 | <b>IRU learning:</b> This is an example showing how the inhibitory synaptic mechanism plays a role in modulating the synaptic strength of the B→C synapse of a given delay unit in the IRU. The insert shows the inhibitory plasticity rule we use in this paper (Haas et al., 2006). . . . .  | 110 |
| 4.8 | Training an IRU to learn an ISI of $T = 55$ ms. The initial values of $g_{BC}(N = 0)$ are set to explore the two scenarios described in the text. $\tau(R)$ (top panel) and $g_{BC}$ (bottom panel) are plotted as function of the number of presentations of the training sequence N. The resolution limit $\delta = 4$ ms is shown in dotted lines for $\tau(R)$ and $T = 55$ ms is shown as a solid line. Parameters for the learning rule are $\alpha = 3$ , $\beta = 0.5$ , for $\Delta t \geq 0$ and $\alpha = 4$ , $\beta = 0.25$ for $\Delta t < 0$ and $g_s = 1.0$ . . . . .  | 112 |
| 4.9 | Raster plot showing the spiking activity in the SSU and the time delay subcircuitry of the IRU when the IRU is being trained to respond to input ISI pattern of 55 ms, as shown in the training example of Figure 7. Tick marks on each panel represent the spike times of that unit. For example, we see that the unit $\alpha_i$ , ( $i=1,2$ ), which are the $\alpha$ neurons of the SSU, receives two input spikes from the training sequence at time 400 ms and 455 ms respectively and each $\alpha$ neuron responds just once, $\alpha_1$ at 400 ms and $\alpha_2$ at 455 ms, as explained in the text. . . . .   | 113 |



|      |   |     |
|------|---|-----|
| 4.10 | Training of IRU on two sets of ISIs.(a) Set one consists of ISI sequence 46, 52 and 60 ms, which falls in the region with the IRU delay parameters set to respond to ISI in the interval of 42 to 65 ms. Parameters for the learning rule used in training this set of ISIs are $\alpha = 3$ , $\beta = .5$ , for $\Delta t \geq 0$ and $\alpha = 4$ , $\beta = 0.25$ for $\Delta t < 0$ and $g_s = 1.0$ . (b) Set two consists of shorter ISI intervals 19, 21, 24 and 27.3 ms. The delay subunit of the IRU has parameters set to produce delays in the range of 15 to 40 ms. Parameters for the learning rule used here are $\alpha = 10$ , $\beta = 1$ , for $\Delta t$ and $g_s = .5$ . For both IRUs the resolution for spike detection is set at 4 ms. In each case in the top panel we plot the delays produced by the IRU as function of training number N and in the bottom panel we plot the evolution of the inhibitory synaptic strength as function of the training number N. . . . . | 114 |
| 4.11 | Training an IRU to learn an ISI of $T = 55$ ms in a noisy environment. The input ISI has a uniform jitter of 2ms. The initial values of $g_{BC}(N = 0)$ are set to explore the two scenarios described in the text. $\tau(R)$ (top panel) and $g_{BC}$ (bottom panel) are plotted as function of the number of presentations of the training sequence N. The resolution limit $\delta = 4$ ms is shown in dotted lines for $\tau(R)$ and $T = 55$ ms is shown as a solid line. Parameters for the learning rule are $\alpha = 3$ , $\beta = .5$ when $\Delta t > 0$ , and $\alpha = 4$ , $\beta = .25$ when $\Delta t \leq 0$ and $g_s = 1.0$ . (a) Multiplicative noise in the inhibitory synaptic plasticity learning rule. (b) Additive noise in the inhibitory synaptic plasticity learning rule. . . . .   | 116 |
| 4.12 | (a) Linear approximation for the delay produced by individual delay unit as function of inhibitory synaptic strength (b) Linear approximation of the learning rule observed for inhibitory synapse in entorhinal cortex. (c) The linear map for evolution of inhibitory synaptic strength is depicted. Sample trajectory for evolution of the inhibitory synaptic strength following the linear learning rule is shown in red. . . . .  | 118 |
| 5.1  | Piece wise linear approximation of $\alpha_m$ . . . . .   | 125 |
| 5.2  | (a) Schematic of the circuit to simulate nonlinear function $\alpha_m(V)$ . (b) Response of the circuit to linear ramp input voltage $v_e$ . The x-axis is $v_e$ and the y-axis represents the output, $\alpha_m(v_e)$ . (c) Schematic of the circuit to simulate nonlinear function $\beta_m(V)$ . (d) Response of the circuit to linear ramp input voltage $v_e$ . The x-axis is $v_e$ and the y-axis represents the output, $\beta_m(v_e)$ . . . . .   | 127 |

|      |  |     |
|------|--|-----|
| 5.3  | (a) Schematic of the circuit to simulate nonlinear function $\alpha_h(V)$ .<br>(b) Response of the circuit to linear ramp input voltage $v_e$ . The x-axis is $v_e$ and the y-axis represents the output, $\alpha_h(v_e)$ . (c) Schematic of the circuit to simulate nonlinear function $\beta_h(V)$ . (d) Response of the circuit to linear ramp input voltage $v_e$ . The x-axis is $v_e$ and the y-axis represents the output, $\beta_h(v_e)$ . . . . . | 128 |
| 5.4  | (a) Schematic of the circuit to simulate nonlinear function $\alpha_n(V)$ .<br>(b) Response of the circuit to linear ramp input voltage $v_e$ . The x-axis is $v_e$ and the y-axis represents the output, $\alpha_n(v_e)$ . (c) Schematic of the circuit to simulate nonlinear function $\beta_n(V)$ . (d) Response of the circuit to linear ramp input voltage $v_e$ . The x-axis is $v_e$ and the y-axis represents the output, $\beta_n(v_e)$ . . . . . | 129 |
| 5.5  | Circuit to simulate the differential equation for $m(t)$ . (a) The schematic circuit implementation for simulating the differential equation for the gating variable $m(t)$ . In inset we show the block diagram of components involved in the circuit implementation. (b) The schematic of circuit elements i) Inverter, ii) Adder and iii) Integrator, used in the differential equation implementation are shown. . . . .                               | 131 |
| 5.6  | Results comparison of simulation v/s Pspice implementation of $m(t)$ , dynamics, for a triangular input pulse . . . . .  | 132 |
| 5.7  | Schematic circuit diagram for solving the first order kinetic equation for gating variable $h(t)$ . . . . .  | 134 |
| 5.8  | Schematic circuit diagram for solving the first order kinetic equation for gating variable $n(t)$ . . . . .  | 135 |
| 5.9  | Results comparison of simulation v/s Pspice implementation of $h(t)$ , dynamics, for a triangular input pulse . . . . .  | 136 |
| 5.10 | Results comparison of simulation v/s Pspice implementation of $n(t)$ , dynamics, for a triangular input pulse . . . . .  | 137 |
| 5.11 | (a)Schematic circuit block diagram to implement the differential equation for the Voltage variable in Equation 5.1. (b) Schematic circuit diagram for the voltage scaling circuitry used in (a) to set the reversal potential of the various currents, in the HH equation. (c) The potentiometer configuration to scale the ionic currents with appropriate conductance values. . . . .  | 138 |
| 5.12 | HH model of type I circuitry implemented on a breadboard. . . . .  | 139 |
| 5.13 | PCB implementation of type II HH neuron model (adapted from Volkovskii) . . . . .  | 140 |
| 5.14 | PCB implementation of the chemical synapse model (adapted from Volkovskii, with permission) . . . . .  | 141 |
| 5.15 | Block diagram for implementing the time delay circuitry in Electronics144  |     |
| 5.16 | The output from the time delay circuitry as seen on the oscilloscope. In pink is the spike output from neuron B, oscillating at 225 Hz. In green is shown the spike output from neuron C after a delay of $\Delta T = 10\text{ms}$ . . . . .   | 145 |

5.17 The output from the time delay circuitry as seen on the oscilloscope.  
In this case the inhibitory synaptic coupling from B→C is increased  
such that the neuron C fires at increased delay of  $\Delta T = 15$  ms. . . . 146

LIST OF TABLES

4.1 . . . . . 115

## ACKNOWLEDGEMENTS

I would like to thank Prof Henry Abarbanel, my advisor, and mentor, for guiding me through all the phases of my career as a graduate student. Henry is an excellent mentor and I learned invaluable skill of asking the right questions and systematic approach to the solution of a given problem. I would like to thank Leif Gibb and Gabriel Mindlin for introducing me to interesting questions in Bird-song research, much of which forms the basis for my thesis work. I would like to acknowledge support from CTBP, for my graduate work.

My stay at INLS was spiced up with excellent intellectual conversations with Thomas Nowotny, with whom I shared office space for the last year and half. Ramon Huerta was always entertaining and it was fun exploring various new ventures with him. I would like to acknowledge guidance by Prof Dan Aravos in my first year as a PhD student at UCSD. Debra was invaluable in getting me through all the finer nuances of student life. Terry and Beryl were of tremendous help, thankyou. Matt Kennel was always around for my computer troubles and I am extremely thankful to him to coming to my rescue with linux. Jonathan was great company during the later part of my stay at INLS. Thanks to Dr Alexander Volkovskii for sharing his knowledge of electronics which was invaluable for me as I explored designs in electronics and building neuron models in hardware. Julie Haas was kind enough to allow me to try my hand at rat invitro electrophysiology. I would also like to thank all the members of INLS, Misha Rabinovich, Lev Tsimring, Shannahoff Khalsa, Rafael Levi and Al Selverston for being part of such an intellectual center as the Institute for Nonlinear Science, and creating a great atmosphere to pursue science.

Thanks to Satya, Ali, Jason, Avinash, Parth and Sushil for being such great friends in good and bad times. My parents deserve special mention for their constant support and encouragement. Finally thanks to Rakhi, my dearest wife for her love, kindness and faith in me.

This thesis is comprised of five chapters including the introduction chapter. The material presented in chapters 2, 3 and 4 is derived from published work by the dissertation author. Most of the material appearing in chapter 2 is published in (Abarbanel H.D.I., Talathi S.S., Gibb L., and Rabinovich M., Physical Review

E, 72, 031914, 2005). Chapter 3 is comprised of material published in (Abarbanel H.D.I., Talathi S.S., Mindlin G., Rabinovich M., and Gibb L., Physical Review E, 70, 051911, 2004). Concise presentation of material appearing in chapter 4 has been published in (Abarbanel H.D.I., and Talathi S.S., Physical Review Letters, 96, 148104, 2006). The dissertation author was the primary researcher in all the published works. The first author supervised the projects and the other collaborators assisted me in my research efforts.

## VITA

|           |   |
|-----------|---|
| April 29  | Born, Pune, India   |
| 2001      | B.S., Engineering Physics<br>Indian Institute of Technology, Bombay, India.               |
| 2003      | M.S., Physics<br>University of California, San Diego.                                     |
| 2001–2002 | Teaching Assistant, Department of Physics<br>University of California, San Diego          |
| 2002–2006 | Graduate Research Assistant, Department of Physics<br>University of California, San Diego |
| 2006      | Ph.D., Physics<br>University of California, San Diego                                     |

## PUBLICATIONS

5. Abarbanel H.D.I., and Talathi S.S., “Neural Circuitry for recognizing interspike interval sequences”, *Phys Rev Lett* **96**: 148104, (2006)
4. Abarbanel H.D.I., Talathi S.S., Gibb L., Rabinovich M.I., “Synaptic plasticity with discrete state synapses”, *Phys Rev E* **72**: 031914, (2005)
3. Abarbanel H.D.I., Talathi S.S., Mindlin G., Rabinovich M.I., Gibb L., “Dynamical model of birdsong maintenance and control”, *Phys Rev E* **70**: 051911, (2004)
2. Abarbanel H.D.I., Gibb L., Mindlin G., Rabinovich M.I., Talathi S.S., “Spike timing and synaptic plasticity in the premotor pathway of birdsong”, *Biol Cybern* **91**: 151-167, (2004)
1. Abarbanel H.D.I., Gibb L., Mindlin G., Talathi S.S., “Mapping neural architecture onto acoustic features of birdsong”, *J Neurophysiol* **92**: 96-110, (2004)

## FIELDS OF STUDY

Major Field: Physics  
Studies in Biological Physics  
Professor H. D. I. Abarbanel

ABSTRACT OF THE DISSERTATION

**Biophysical modelling of synaptic plasticity and its function in the  
dynamics of neuronal networks**

by

Sachin S. Talathi

Doctor of Philosophy in Physics

University of California San Diego, 2006

Professor Henry D.I. Abarbanel, Chair

Plasticity of neuronal circuitry in the brain is a fundamental process thought to underlie behavior, cognition and memory. Recent experimental evidence suggest that plasticity in individual synaptic afferent from CA3 pyramidal cells onto CA1 postsynaptic neurons in the hippocampus involve discrete synaptic states.

In Chapter 2 we develop a theoretical framework to study the biophysical origin of this observed discrete transitions in the synaptic states. The developed biophysical model is tested on various plasticity induction protocols. The key feature of the model is that it provides a natural bound on changes in the synaptic strength.

The later part of the thesis, explores functional significance of synaptic plasticity in neuronal networks. In particular, in Chapter 3 we study the dynamics of song learning in oscine birds. We develop a dynamical model for the song system nuclei and suggest an important dynamical role for synaptic plasticity in the control and maintenance of learned adult birdsong.

In Chapter 4 we study yet another application of synaptic plasticity function in networks. We develop a neuronal network, termed an “Interspike Interval Recognition Unit”, (IRU) that uses synaptic plasticity of inhibitory synapses to train itself onto a given pattern of input spike sequences and is then able to selectively respond to the same input pattern on subsequent presentation.

It is known that neurons communicate through short voltage pulses called ‘spikes’. If all the spikes are similar in shape and structure then, all the information must be encoded in the interspike intervals of these spike sequences. The



IRU thus proposes to provide an answer to an important biological question: What kind of neural circuits in the brain can decode the information in the inter spike interval sequence and what learning mechanism mediates this decoding process?

Finally in Chapter 5, we develop an electronic circuit model for type I neurons and use it to construct a time delay circuit, which is an abstraction from the song system anterior forebrain pathway. The circuit is able to produce precise time delays on the order of 10-100 ms, controlled by strength of intrinsic synaptic strength. We give two examples demonstrating the function of the circuit in producing precise time delays.

# 1

## Introduction

The human brain weighs almost 4 pounds and is comprised of several thousand miles of interconnected nerve cells (about  $10^{12}$  neurons) which control every movement, thought and emotion that make up the human experience. The challenge of understanding such a complex structure is drawing scientists from multiple disciplines together. A number of experimental techniques are being employed to explore the complexity of the brain. Some of the common techniques being employed are: Intracellular multi-unit recordings, optical recordings of columnar organization in the brain with voltage and ion sensitive dyes, large scale measurements of brain activity with positron emission tomography (PET), magnetoencephalogram (MEG) and magnetic resonance imaging (MRI) (Churchland et al., 1993).

On the other hand computational neuroscience is an interdisciplinary field that uses computer simulations and mathematical models to explore the function of the nervous system. The emphasis is on using biological principles to develop new algorithms (Selverston, 1993).

It aims to provide modelling study as an important adjunct to the experimental techniques. The advantages of modelling are varied. (i) A model provides an easy access to experimentation: Experiments that are difficult or even impossible to perform in living tissues, such as selective lesion of particular ion channels, or synapses, can be easily simulated with the use of models. (ii) New ideas can be tested and experiments suggested based on model predictions (iii) Emergent properties through the interaction of multiple brain regions, interacting with each other can be studied. The hope is that through successful integration of all these

techniques it will one day be possible to unravel the mystery of the workings of the brain.

In the present thesis we take the computational approach to explore one important aspect of brain function: “Synaptic plasticity” and its function in collective dynamics of the network of neurons.

## 1.1 Thesis Overview

Synaptic plasticity in the form of long term potentiation (LTP) and long term depression (LTD) and most recently, spike timing dependent plasticity (STDP) are often considered to be the biophysical mechanisms by which memory traces are encoded and stored in the central nervous system (Martin et al., 2000). Some of the biophysics underlying the phenomenon of synaptic plasticity is known. For example it is known that STDP of excitatory synapses depends on the interplay between the dynamics of N-methyl-D-aspartic acid, (NMDA) receptor activation and the timing of action potential back propagating through the dendrites of postsynaptic neurons (Magee and Johnston, 1997; Linden, 1999; Sourdet and Debanne, 1999). A number of biophysical models have been developed to integrate the known biophysical mechanisms underlying the induction of synaptic plasticity, (Abarbanel et al., 2003; Shouval et al., 2002; Castellani et al., 2001; Karmarkar and Buonomano, 2001). The main theme of the existing models was to associate the temporal dynamics of intracellular calcium concentration in the post synaptic neurons to the observed changes in the conductivity of  $\alpha$ -amino-3-hydroxy-5-methyl-4-isoxazole-propionic acid, (AMPA) receptor channels (Sabatini et al., 2001; Yang et al., 1999). The principal weakness of all these models is that there is no intrinsic mechanism in the models to govern a bounded change in the synaptic plasticity strength. Although these models impose mathematical constraints on the level of growth in the synaptic strength.

Recent experimental evidence suggests that changes in the synaptic strengths are associated with discrete levels in the synaptic states (O’Connor et al., 2005b; O’Connor et al., 2005a; Montgomery and Madison, 2004). Minimal stimulation experiments have shown that individual synapses showed “digital” change that occurred only once, at different thresholds, corresponding to the transition in the

synaptic states, during sequences of pairings. The manifestation of the observed graded change in the synaptic strength is then interpreted to be the consequence of the averaged effect over all the large number of synapses in different states contributing in different levels to the observed synaptic strength. It has also been argued that such digital nature of synaptic change has advantages over the conventional analog graded change picture. For example, the digital nature of a synapse provides a better mechanism for coping with noise problems inherent in maintaining a memory over long time despite the turnover of synaptic proteins (Petersen et al., 1998). In this thesis we provide a theoretical framework for the biophysical mechanism underlying this discrete nature of synaptic states. In our model the plasticity induction protocols (see next section) govern the transition rates among the various synaptic states using a phenomenological rule dependent on the temporal dynamics of the intracellular calcium concentration in the post synaptic neuron. The distinct advantage of this approach over earlier efforts is that there exists natural bounds on the levels of growths in the synaptic strengths.

It is known that synaptic plasticity is not a static property of the hippocampal synapse (Bramham and Srebo, 1989) but can be dynamically modulated by learning as well as by an animal’s behaving state. The overt manifestation of memory is not solely due to synaptic properties in their ability to modify or change, but it also depends on the network in which the plasticity is embedded. Networks of neurons and systems determine the manner in which information is encoded and processed in the brain. The question is then to understand the functional significance of the synaptic plasticity mechanism in networks and its ability in structuring network properties. In order to explore the functional significance of the plasticity mechanism in systems level, in this thesis we focus our attention on learning in song birds. Song birds comprise a collection of nuclei, each consisting on the order of 10,000 neurons, called the “Song System”, which is important for birds to sing. The song system also plays an active role in learning of conspecific song by juvenile birds. As discussed in the next section, the song system is known to contain at least two distinct pathways: *Song learning pathway* and the *Song production pathway*. The intrinsic dynamical properties of most of the neurons in each of the nuclei in each of the song system pathways has been studied in details in number of works, (Spiro et al., 1999; Luo and Perkel, 1999b; Luo and Perkel, 1999a; Farries and Perkel, 2000;

Farries and Perkel, 2002; Mooney, 2000). In this thesis, we develop a model for the song system and study the implication of synaptic plasticity mechanism in stabilizing the network in its function to produce precise delays as action potentials propagate through the song learning pathway of the song system. The model predicts a functional role for the known but as yet unexplored synaptic connection between the song production and the song learning pathways.

In another exploration of function of synaptic plasticity in networks, we develop a neural circuitry that uses synaptic plasticity observed in the inhibitory synapses, to provide an answer to a very interesting biological question: How do neural circuits decode information in the sensory world through the sequence of interspike intervals? Our answer is provided in terms of a network, termed “Interspike interval reading unit”, (IRU). The IRU uses a time delay circuitry abstracted from the song system, to produce a replica of the input training sequence and synaptic plasticity mechanism to train itself on to the input training sequence. It is then able to selectively be responsive to the same sequence presented on the subsequent trial. Our network is thus able to be selectively responsive to only particular pattern of input, a task known to be performed by many sensory systems, such as whisker-selective auditory response in the barrel cortex of rats (Welker, 1976; Aarabzadeh et al., 2004), nuclei in the song system that are selectively responsive to birds own song (BOS) playback (Lewicki and Arthur, 1996; Margoliash, 1983; Margoliash, 1986) and motion sensitive cells in the visual cortical areas of primates (Sugase et al., 1999; Buracas et al., 1998).

## 1.2 Background

In this section, I present a short overview on the two primary topics being explored in this thesis: (i) Synaptic plasticity and (ii) The Song system. The mathematical model used as computational tool for the study is then presented. Finally in the last section, I present the organization of the thesis chapters.

### 1.2.1 Synaptic plasticity

In neuroscience, synaptic plasticity, defined as the ability for the connection or the synapse between two neurons, to change in strength, thereby modulating the efficacy of signal transmission, is considered to underlie the basis for learning, memory and neuronal organization during development. The foremost example of plasticity in the vertebrate brain is Long Term Potentiation/Depression (LTP/LTD), the two forms of synaptic plasticity that last much longer than seen in the peripheral synapses. Experimentally, LTP, which results in the strengthening of synapse and LTD, which results in the weakening of synapse can be induced in number of ways. These are outlined below:

**Rate based induction:** A neuron is impaled by an intracellular electrode to record membrane potential while presynaptic fibers are stimulated at varying frequencies by means of second extracellular electrode. Low frequency presynaptic stimulation results in the induction of LTD while high frequency presynaptic stimulation results in the induction of LTP. (Bliss and Collingridge, 1993).

**Pairing induced plasticity:** Voltage clamped postsynaptic neuron presented with burst of presynaptic spike. (Feldman, 2000)

**Spike timing dependent plasticity (STDP):** Plasticity induction depends on the relative timing between presynaptic and postsynaptic stimulation. (Markram et al., 1997; Bi and Poo, 1998)

The exact mechanism underlying synaptic plasticity is yet to emerge. There is general agreement that calcium dynamics in the postsynaptic cell plays an important role in the induction of plasticity. Two lines of evidence suggest that synaptic plasticity is induced by changes in the postsynaptic calcium concentration. It has been shown that high frequency presynaptic stimulation does increase post synaptic calcium concentration and when an increase is prevented by prior injection of calcium buffer, LTP is prevented (Yeckel et al., 1999). Second, postsynaptic calcium elevation by other means and the time course of the elevation in calcium concentration leads to changes in the synaptic efficacy (Malenka et al., 1998; Yang et al., 1999)

### 1.2.2 Song System

Songbirds learn to sing by listening to themselves and to other birds. Song behavior in song birds is coordinated by discrete network of interconnected nuclei that undergo dramatic changes in the anatomical, neurochemical and molecular organization during periods of song learning (Brenowitz et al., 1997; Nordeen and Nordeen, 1997; Clayton, 1997). Two critical pathways in song circuitry are involved in song learning and song production (Margoliash, 1997). In Figure 1.1 we show major elements of this circuitry.

The motor pathway is shown with brown and blue arrows. It controls the production of the song. Some portion of this circuit is also considered to be involved in song learning. This pathway consists of projections from the thalamic nucleus Uva and the neostriatal nucleus NIf to the neostriatal nucleus HVC (High Vocal Center). HVC projects to the robust nucleus of archistriatum (RA). RA then projects to the dorsomedial part of the intercoliculus in the midbrain and to the tracheosyringeal part of hypoglossal motor nucleus in the brain stem (nXIIIts). Output from motor nuclei nXIIIts drive the sound producing organ in songbirds, the syrinx. If any of these nuclei in the song production pathway are inactivated, the bird does not produce song. The RA also projects to nuclei in the medulla, that contain many respiratory related neurons which fire in phase with expiration. The pattern of descending projections from RA are then important for coordination of the syringeal and respiratory muscle activity during song production (Suthers, 1997; Abarbanel et al., 2004c).

The second component, the anterior forebrain pathway (AFP), shown in red in Figure 1.1 is believed to be essential for song learning and recognition (Doupe and Solis, 1997; Margoliash, 1997). It also includes a specialized region of avian basal ganglia (Farries et al., 2005). This pathway consists of projections from HVC, to Area X then to the nucleus DLM in the thalamus, then to the lateral portion of magnocellular nucleus of the neostriatum (lMAN) and finally to RA. The output of AFP, the lMAN, also sends projections back to Area X, thus providing potential for feedback in this pathway. It has been shown recently (Farries et al., 2005) that Area X is a mixture of striatum and globus pallidus and has the same functional organization as circuits in the mammalian basal ganglia. Impairment of Area

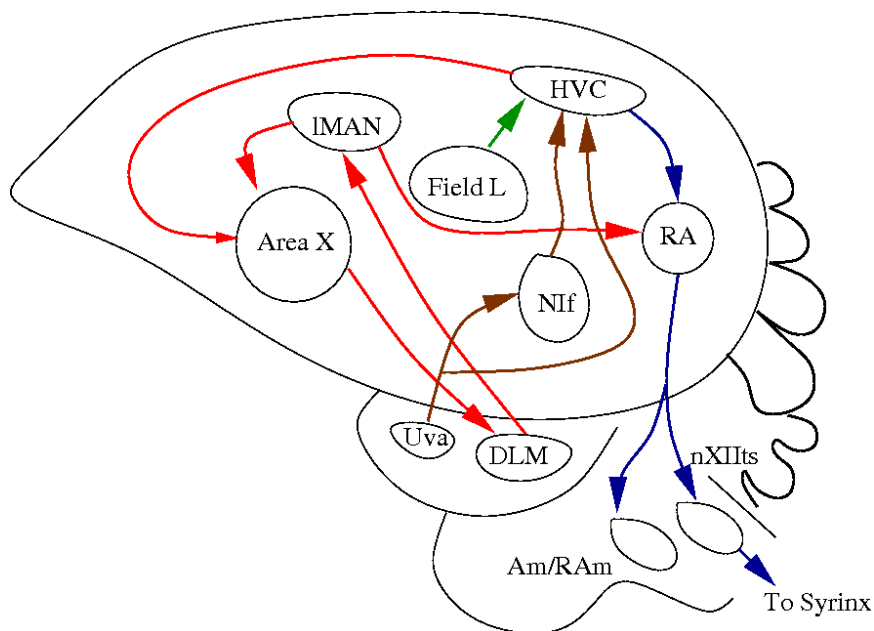


Figure 1.1 **Schematic of the song system in songbirds:** The song production motor pathway is shown in brown and blue. The input to HVC is shown in brown from the thalamic nucleus Uva and the neostriatal nucleus Nif. The descending projections from HVC to the nucleus RA in the neostriatum and from RA to vocal nucleus nXIIIts, the respiratory nucleus RAm and the laryngeal nucleus Am in the medulla is shown in blue. The song learning anterior forebrain pathway (AFP) is shown in red. HVC and RA are indirectly linked through the AFP via, Area X, the thalamic DLM nucleus and the IMAN in the neostriatum. IMAN also projects to Area X, closing the loop for the AFP. The auditory region in the neostriatum, Field L, projects to HVC and it is shown in green. The abbreviations for the nuclei mentioned are: Am-nucleus ambiguus; RAm-nucleus retroambiguus; DLM-medial portion of the dorsolateral nucleus of the thalamus; IMAN-lateral portion of magnocellular nucleus of archistriatum; Nif-nucleus interface; RA-robust nucleus of archistriatum; Uva-nucleus uvaformis; nXIIIts-tracheosyringeal part of hypoglossal nucleus. (Adapted from Brenowitz et.al., 1997)



X, DLM or IMAN apparently does not disrupt the ability of adult birds to sing, whereas the same lesions in juvenile birds disrupts normal song development.

In investigating time differences between signals propagating from HVC to RA through the direct pathway and the same signal propagating to RA through AFP, (Kimpow et al., 2003) have reported a remarkable precision of the time difference between these pathways of  $50 \pm 10$  ms across many songbirds and many trials. In chapter 3 we discuss the mechanism for this precise delay introduced by the AFP and its function in the dynamics of song learning.

### 1.2.3 Neuron model

We use the Hodgkin Huxley (HH) formalism to describe neuronal dynamics. The basic neuron model satisfies the following set of dynamical equations.

$$C_M \frac{dV(t)}{dt} = I_{Na}(t, V(t)) + I_K(t, V(t)) + I_L(V(t)) + I_{In} \quad (1.1)$$

The currents  $I_{Na}$  and  $I_K$  are the HH  $Na^+$  and  $K^+$  currents respectively.  $I_L$  is the leak channel which represents the generalized lossy effects across the membrane.  $I_{In}$  is the external DC current used to set the resting potential of the cell.  $C_M$  is the membrane capacitance.

The current  $I_L$  satisfies the ohmic relationship,

$$I_L(V(t)) = g_L(E_L - V(t)),$$

where  $g_L$  is the conductance of the leak current in  $mS/cm^2$  and  $E_L$  is the reversal potential in  $mV$ . The voltage gated currents  $I_{Na}$  and  $I_K$  are described by

$$I(t, V(t)) = \bar{g}g(t)(E_{eq} - V(t)),$$

where  $E_{eq}$  is the reversal potential in  $mV$  and  $\bar{g}$  is the maximal conductance in  $mS/cm^2$ . The value of  $g(t)$ , the fraction of open channels, on the other hand depends on the membrane potential as function of time.

In the case of channels in which  $g(t)$  changes, the value of  $g(t)$  depends on the

state of ‘gating particles’  $m(t)$  and  $h(t)$ , where  $m(t)$  is the activation gate and  $h(t)$  represents the inactivation gate. If  $N$  is the number of activation gates, and  $M$ , the number of inactivation gates then,

$$g(t) = m(t)^N h(t)^M$$

These gating variables, denoted by  $X(t)$ , are taken to satisfy first order kinetics.

$$\begin{aligned} \frac{dX(t)}{dt} &= \frac{X_0(V(t)) - X(t)}{\tau_X(V(t))} \\ &= \alpha_X(V(t))(1 - X(t)) - \beta_X(V(t))X(t) \end{aligned} \quad (1.2)$$

For the standard HH model, we have the following relations for the conductances of the  $Na^+$  and  $K^+$  currents.

$$\begin{aligned} g_{Na}(t) &= m(t)^3 h(t) \\ g_K(t) &= n(t)^4 \end{aligned}$$

where  $m(t), n(t)$  are activation gating particles and  $h(t)$  represents the inactivation gating particle.

We consider two classes of HH models as described above, Type I neuron model and Type II neuron model.

Type I neuron is a cortical neuron model (Traub and Miles, 1991) with following characteristics.

- The frequency current relationship can be approximated by

$$f = C \sqrt{(I_{In} - I_{cr})}$$

where  $I_{cr}$  is the critical current value above which the neuron starts firing as shown in Figure 1.2b and  $C$  is constant dependent on the parameters of the model.

- It exhibits only one type of dynamical behavior, either a stable resting state or stable limit cycle corresponding to spiking state, for all set of input currents. In Figure 1.2c we show the bifurcation diagram for the neuron. The

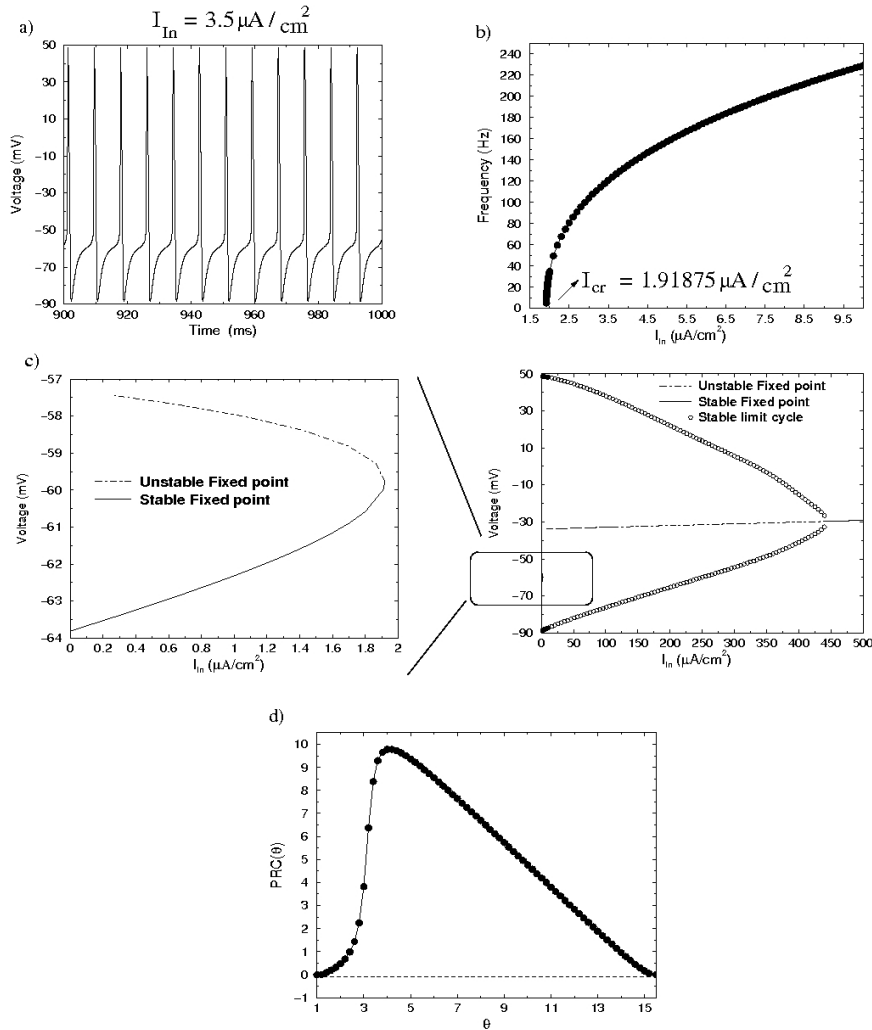


Figure 1.2 **Dynamics of type I neuron model:** (a) Time trace of spiking activity in the model when injected with input current of  $I_{In} = 3.5 \mu\text{A}/\text{cm}^2$ . The neuron firing frequency is approximately 120 Hz. (b) The frequency of firing is plotted as function of input dc current  $I_{In}$ . (c) The bifurcation diagram for type I neuron is plotted. In the left column the steady state dynamics of the neuron model is shown when the neuron is in the resting state. We see that as the input current is increased the stable and unstable fixed point approach each other until, the point where they annihilate and the neuron goes into stable spiking mode. In the right column the stable limit cycle behavior is seen. For very large input currents, the limit cycle vanishes through inverse Hopf bifurcation. (d) The phase response curve for the neuron  $\text{PRC}(\theta)$  is plotted as function of phase  $\theta$ , at which infinitesimal perturbation is applied. For type I neuron models, the phase is always advanced in response to perturbations in the membrane potential.

bifurcation from rest state to spiking regime is through saddle node bifurcation. In Figure 1.2c, left column, we show the bifurcation diagram of the neuron, as function of input current  $I_{In}$  in the region where the neuron is in resting state. As the input current is increased beyond  $I_{cr}$ , the stable resting state vanishes and the neuron is moved into stable spiking state as can be seen from the bifurcation diagram in Figure 1.2c, right column. As the current is increased, the amplitude of the spiking neuron decreases and eventually the limit cycle vanishes through Hopf bifurcation.

- The phase response curve, which quantifies the effect of perturbations on the spiking times of the neuron (Ermentrout, 1996) is non negative for type I neurons as shown in Figure 1.2d. This implies that an infinitesimal perturbation of the membrane potential will never delay the next spike in type I neurons.

The parameter values for type I neuron are,  $C_M = 1\mu F/cm^2$ , and in  $mS/cm^2$   $(g_{Na}, g_K, g_L) = (215, 43, 8.0)$ . The equilibrium reversal potentials in  $mV$ ,

$$(E_{Na}, E_K, E_L) = (50, -95, -64)$$

The following set of activation and inactivation equations are used to describe the type I neuron.

$$\begin{aligned} \alpha_m(V(t)) &= \frac{.32(13-(V(t)-V_{th}))}{e^{\frac{(13-(V(t)-V_{th}))}{4.0}} - 1} & \beta_m(V(t)) &= \frac{0.28((V(t)-V_{th})-40)}{e^{\frac{(V(t)-V_{th})-40}{5}} - 1} \\ \alpha_h(V(t)) &= .128e^{\frac{17-(V(t)-V_{th})}{18}} & \beta_h(V(t)) &= \frac{4}{e^{\frac{40-(V(t)-V_{th})}{5}} + 1} \\ \alpha_n(V(t)) &= \frac{0.032(15-(V(t)-V_{th}))}{e^{\frac{(15-(V(t)-V_{th}))}{5}} - 1} & \beta_n(V(t)) &= \frac{0.5}{e^{\frac{(V(t)-V_{th})-10}{40}}} \end{aligned}$$

where  $V_{th} = -65$  mV.

The type II neuron model is the original HH neuron model, with the following characteristics

- The frequency current relationship is shown in Figure 1.3b. The neuron starts spiking at nonzero frequency of 40.8 Hz, at input current of  $I_{In} = 2.3\mu A/cm^2$

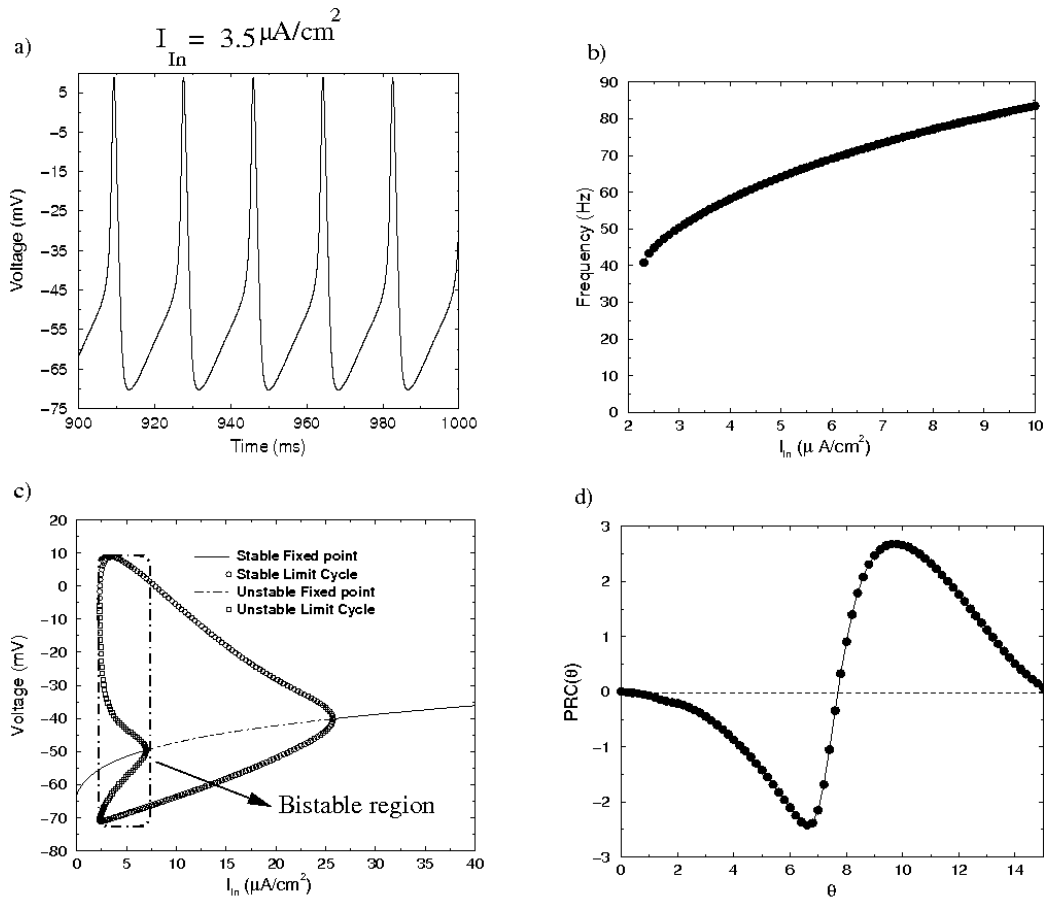


Figure 1.3 **Dynamics of type II neuron model:** (a) Time trace of spiking activity in the model when injected with input current of  $I_{In} = 3.5 \mu A/cm^2$ . The neuron is firing frequency is approximately 55 Hz. (b) The frequency current relationship for type II neuron models. For input current  $I_{In} > 2.293 \mu A/cm^2$ , the neuron starts spiking starting frequency of around 41 Hz. Type II neuron model does not permit wide range of spiking frequencies. (c) The bifurcation diagram for type II neuron model. The mechanism of the neuron to make a transition from the resting state to the spiking state is through Hopf bifurcation, resulting in a regime where the neuron exhibits bistable behavior, of coexisting stable resting and spiking states, separated by an unstable limit cycle. For large input currents, the spiking eventually vanished, through inverse Hopf bifurcation. (d) The phase response curve PRC( $\theta$ ) for type II neuron model. The PRC has both positive and negative regions. Thus depending on the phase of input membrane potential perturbation, the neuron spike is either advanced or delayed.

- For parameter values,  $2.29 < I_{in} < 6.93 \mu A/cm^2$ , the neuron exhibits bistable behavior with co existing resting and spiking states. The bifurcation diagram for the neuron is shown in Figure 1.3c. The transition of neuron from stable resting state to spiking state occurs through Hopf bifurcation of subcritical type (Kuznetsov, 2004). As the input current is increased the amplitude of spiking neuron decreases and eventually the limit cycle vanishes through Hopf bifurcation of supercritical type (Kuznetsov, 2004).
- The phase response curve for neuron has both positive and negative regions as shown in Figure 1.3d. This implies an infinitesimal perturbation in membrane potential can either advance or delay the time of occurrence of next spike depending on the phase at which the pulse is applied.

The parameters of the model are  $C_M = 1\mu F/cm^2$ , in  $mS/cm^2$ ,  $(g_{Na}, g_K, g_L) = (20, 6.2, 0.03)$ , and in  $mV$ ,  $(E_{Na}, E_K, E_L) = (50, -77, -49.4)$ . The activation and inactivation functions are given by

$$\begin{aligned} \alpha_m(V(t)) &= \frac{-0.1(V(t)+35)}{e^{\frac{-(V(t)+35)}{10.0}} - 1} & \beta_m(V(t)) &= 4.0e^{\frac{-(V(t)+60)}{18}} \\ \alpha_h(V(t)) &= 0.07e^{\frac{-(V(t)+60)}{20}} & \beta_h(V(t)) &= \frac{1.0}{e^{\frac{-(V(t)+30)}{10}} + 1} \\ \alpha_n(V(t)) &= \frac{-0.01((V(t)+50))}{e^{\frac{-(V(t)+50)}{10}} - 1} & \beta_n(V(t)) &= .125e^{\frac{-(V(t)+60)}{80}} \end{aligned}$$

### 1.3 Organization

This thesis consists of five chapters including this chapter. In the second chapter, we develop a biophysical model for synaptic plasticity dynamics, in order to provide a theoretical framework for the recently observed phenomenon of discrete states in synapses that contribute to the synaptic plasticity. Using the experimental observation by (O'Connor et al., 2005b; O'Connor et al., 2005a) we develop a three state synaptic model. We determine the normalized conductance values of each of the three discrete synaptic states, with some general arguments based on the measurements by (O'Connor et al., 2005b; O'Connor et al., 2005a). The model so developed is then tested on number of existing induction protocols for synaptic plasticity. In addition we explore the functional significance of our plasticity

model in synchronizing periodically firing pre and post synaptic neurons. An important feature of models built on finite number of discrete synaptic levels is that the synaptic strength always remains bounded above and below. This is in contrast to earlier work on biophysical modelling of synaptic plasticity. The material presented in this chapter has appeared in (Abarbanel H.D.I., Talathi S.S., Gibb L., and Rabinovich M., *Physical Review E*, 72, 031914, 2005). The dissertation author was the primary researcher. The author listed in this work supervised the research and the other collaborators guided the research effort.

In the third chapter, we study the functional significance of synaptic plasticity phenomenon in the song system. We develop a biophysical model for song system network based on electrophysiological measurements in the various nuclei in the song system. As discussed earlier, in the song system, signals generated in nucleus HVC, follow a direct route along premotor pathway to the robust nucleus of archistriatum (RA) as well as an indirect route to RA through the anterior forebrain pathway (AFP). HVC produces very sparse high frequency burst of spikes. The expression of this burst arrives at RA with a time difference of  $\Delta T \approx 50 \pm 10$  ms between the arrival from direct input from HVC and indirect input through the AFP. The observed combination of AMPA and NMDA receptors at the RA projection neurons suggests that LTP and LTD can both be induced by spike timing dependent plasticity through the pairing of the HVC and the AFP signals arriving at RA. We present a dynamical model that stabilizes this synaptic plasticity through a known feedback connection from RA to the AFP. This stabilization occurs dynamically based on the spike timing dependent plasticity rule, and is absent when the RA→AFP connection is removed. The stabilization requires a dynamical selection of  $\Delta T$ . The model does this based on the dynamics of the song system network and the  $\Delta T$  so chosen lies within the observed range. This model represents an illustration of the functional significance of activity dependent synaptic plasticity directly connected with neuroethological observations. Concise presentation of the material appearing in this chapter has been published in (Abarbanel H.D.I., Talathi S.S., Mindlin G., Rabinovich M., and Gibb L., *Physical Review E*, 70, 051911, 2004). The dissertation author was the primary researcher in this project. The cited author supervised the project and the other coauthors guided the research effort.

It is generally accepted that sensory systems pass information about the environment to higher nervous systems through a sequence of action potentials. When these action potentials are identical, all the information is encoded in the interspike intervals (ISIs) of these action potentials. In chapter four, we develop a neural circuit with biologically realistic components termed “Interspike Interval Reading Unit”, (IRU), to decode the information contained in these ISIs. By “decoding” we mean, recognition of specific ISI sequence on which the neural circuitry is trained in preference to any other ISI sequence. The essential ingredients of the IRU are (i) A tunable time delay circuit modelled after one found in the anterior forebrain pathway in the song system (ii) A recently observed rule for inhibitory synaptic plasticity. Our model for the time delay circuitry is tuned to produce delays on the order of 10 ms-100 ms allowing the IRU to learn and recognize ISI sequence within these time intervals. The ideas explored in this chapter has appeared in concise form in (Abarbanel H.D.I., and Talathi S.S., Physical Review Letters, 96, 148104, 2006) . The dissertation author was the primary researcher in the published work. The cited author supervised the research effort.

In the final chapter we develop an electronic neuron model and use it to build a neuronal circuitry for time delays. We give two examples of tuning the circuitry through the inhibitory synaptic connections to produce different delays. We thus provide a working demonstration of the function of time delay circuitry in producing precisely controlled delays on the order of 10 ms-100 ms.



## 2

# Biophysical model for synaptic plasticity with discrete state synapses

## 2.1 Introduction

Experiments on synaptic plasticity at individual synapses in CA3 to CA1 hippocampal pathways reveal an “all-or-none” change in their synaptic strength (Petersen et al., 1998; O’Connor et al., 2005b). Indications of this were seen a decade ago (C. F. Stevens and Y. Wang, personal communication). The recent measurements (O’Connor et al., 2005a) have given substantial standing to the notion that single synapses may operate as a discrete state system in their plastic changes associated with long-term potentiation (LTP) and long-term depression (LTD).

In this chapter we first explore a general formulation of the possibility that individual synapses can express a finite number of discrete levels of conductance rather than the continuous or graded or analog picture often formulated, (Castellani et al., 2001; Karmarkar and Buonomano, 2001; Shouval et al., 2002; Abarbanel et al., 2003). (Petersen et al., 1998) have commented on the positive consequences for reliability of neural memory from discrete state synapses. In addition there is computational evidence for entry of a small number of free  $Ca^{2+}$  ions through voltage gated calcium channels and the NMDA (N-methyl-D-aspartic acid) receptor ligand gated ion channel activated by synaptic stimulation during plasticity induc-

tion protocol (Franks and Sejnowski, 2002). A synapse which must respond to this very small signal might as well select a strategy of an “all-or-none” response in adjusting its strength as a means of achieving a measure of reliability. Discreteness of synaptic states as a useful computational device has been explored in network models, (Del Giudice et al., 2003), though the study did not relate to observations by (Petersen et al., 1998).

After a brief consideration of a general formulation of an  $L$  level synapse, we focus our attention on  $L = 3$ , which is suggested by the recent data of (O’Connor et al., 2005a). With three levels we explore the transitions among the levels using observations of (O’Connor et al., 2005a). With some general arguments based on the measurements, we are able to establish values for the normalized conductances of the individual  $L = 3$  levels, and we suggest an experiment which will determine an interesting ratio among the transition rates.

Montgomery and Madison (Montgomery and Madison, 2004) discuss the possibility of four discrete synaptic states, but it appears that because of the way they identify these states and the stability of one of the state, their identification may be equivalent to that of O’Connor, Wittenberg, and Wang (O’Connor et al., 2005a).

The transition rates themselves depend on a model for how complex chemical pathways lead to the change in AMPA conductance and the number of AMPA receptors at any synapse (Carroll et al., 1999; Lisman et al., 2002; Winder, 2001; Contractor and Heinemann, 2002; Malinow and Malenka, 2002; Sheng and Kim, 2002). We adopt a version of our earlier model, (Abarbanel et al., 2003) of these processes to provide a basis on which to make quantitative predictions of the outcome of various LTP/LTD induction protocols on the changes in AMPA conductance of a postsynaptic cell. We explore spike time dependent protocols as well as presentation of spike bursts of various frequencies to the postsynaptic cell. These compare well with experiments, in particular to results presented in Wittenberg’s dissertation (Wittenberg, 2003), and predictions are made for various spike timing experiments.

We also explore the following setup: a periodically firing conductance based presynaptic neuron provides excitatory synaptic input to a periodically firing conductance based postsynaptic neuron. In certain ranges of frequency and conduc-

tance strength for the excitatory connection these neurons synchronize (Pikovsky et al., 2001). We explore the effect on this synchronization of our discrete synaptic strength model and show that the regime of one-to-one synchronization is significantly enlarged (Zhigulin et al., 2003) for some conductance strengths and that the synchronization is an in-phase firing of the two neurons.

It is an important feature of models built on a finite number of discrete synaptic levels that the synaptic strength (AMPA conductance) is always bounded above and below. This is in contrast to models developed over the years, including ones from our earlier work (Abarbanel et al., 2003; Nowotny et al., 2003), which do not have this property.

## 2.2 Discrete state synapses: General formulation for the transition rate model

The data of (O'Connor et al., 2005a) suggest that three discrete states of AMPA conductance are found at individual synapses. In general if the total number of levels is  $L$  and they are indexed by  $l = 0, 1, 2, \dots, L - 1$ , and there are  $N_S$  synapses indexed by  $n = 1, 2, \dots, N_S$ , then we represent the occupation of synapse  $n$  in state  $l$  at time  $t$  by  $N_l^n(t)$ . These occupation numbers are either zero or unity. They can change in time due to LTP/LTD induction protocols or other biological processes. The average occupation number in state  $l$  is given by

$$p_l(t) = \frac{1}{N_S} \sum_{n=1}^{N_S} N_l^{(n)}(t). \quad (2.1)$$

These  $p_l(t)$  will constitute the main dynamical variables of our model. They are taken to satisfy linear rate equations of the form

$$\frac{dp_l(t)}{dt} = \sum_{k=0}^{L-1} \left\{ W_{(k \rightarrow l)}(t) p_k(t) - W_{(l \rightarrow k)}(t) p_l(t) \right\}. \quad (2.2)$$

The transition rates  $W_{(k \rightarrow l)}(t)$ ,  $W_{(l \rightarrow k)}(t)$  are selected to assure

$$\sum_{k=0}^{L-1} p_k(t) = 1. \quad (2.3)$$

As long as the number of active synapses  $N_S$  is unchanged, this last equation follows from the definition of  $p_k(t)$ . In the limit of  $N_S$  large, we assume that the  $p_l(t)$  remain finite; this is a standard assumption about such a limit for the description of a large number of objects each having a discrete set of states.

A statistical description of  $N_S \gg 1$  independent synapses undergoing time dependent transitions among the allowed  $L$  states yields Equation 2.2 on the average with fluctuations about this mean of order  $\frac{1}{\sqrt{N_S}}$ , as one might expect.

One can collect the average occupation numbers into an  $L$ -dimensional vector  $\mathbf{P}(t) = (p_0(t), p_1(t), \dots, p_{L-1}(t))$  which satisfies

$$\frac{d\mathbf{P}(t)}{dt} = \mathbf{M}(t) \cdot \mathbf{P}(t), \quad (2.4)$$

where  $\mathbf{M}(t)$  is the  $L \times L$  matrix of transition rates. The conservation rule (2.3) means that  $\mathbf{M}(t)$  always has at least one zero eigenvalue (Lawler, 1995; Van Kampen, 1995). The dynamics of  $\mathbf{P}(t)$  takes place in the  $L - 1$  dimensional space orthogonal to the constant  $L$ -dimensional vector  $\mathbf{C} = (1, 1, 1, \dots, 1)$ .

The effect of having this constraint may be seen in the decomposition of  $\mathbf{P}(t) = \mathbf{C} + \mathbf{P}_\perp(t)$  where  $\mathbf{P}_\perp(t) \cdot \mathbf{C} = 0$ . The dynamics of motion for  $\mathbf{P}_\perp(t)$  is

$$\frac{d\mathbf{P}_\perp(t)}{dt} = \mathbf{M}(t) \cdot \mathbf{P}_\perp(t) + \mathbf{M}(t) \cdot \mathbf{C}, \quad (2.5)$$

which is motion of the vector  $\mathbf{P}_\perp(t)$  spanning the  $L - 1$  dimensional space orthogonal to  $\mathbf{C}$  driven by the time dependent forcing  $\mathbf{M}(t) \cdot \mathbf{C}$ .  $\mathbf{P}_\perp(t)$  is defined up to a rotation about  $\mathbf{C}$ . This dynamical description is similar to that of driven precession of a spin in a time dependent magnetic field.

Each discrete level  $l = 0, 1, \dots, L - 1$  has a dimensionless AMPA conductance  $g_l$  normalized to some baseline. The dimensionless AMPA conductance of the neuron

with  $N_S$  synapses is

$$\begin{aligned} G_{AMPA}(t) &= \sum_{n=1}^{N_S} \sum_{l=0}^{L-1} g_l N_l^n(t) \\ &= N_S \sum_{l=0}^{L-1} g_l p_l(t). \end{aligned} \quad (2.6)$$

This means that the quantity

$$\frac{G_{AMPA}(t)}{N_S} = \sum_{l=0}^{L-1} g_l p_l(t), \quad (2.7)$$

the normalized, dimensionless AMPA conductance per synapse, is independent of the number of synapses when  $N_S$  is large, depending only on the average occupation number of the synaptic levels and the conductance associated with each level. By definition of the baseline synaptic state, before any LTP/LTD induction protocols are presented to the postsynaptic neuron, this quantity is equal to one:

$$\frac{G_{AMPA}(t=0)}{N_S} = 1. \quad (2.8)$$

In our work below, we report the quantity  $\frac{G_{AMPA}(t)}{N_S} - 1$  as the output from our simulation of various induction protocols.

To fully specify the model of synaptic plasticity associated with the presence of discrete levels, we must identify the conductances  $g_l$  of each level, and, through some form of dynamics of the postsynaptic neuron, determine the transition rates. In the next section we do this for the suggested three state model of (O'Connor et al., 2005a). However, if observations indicate that there are  $L \neq 3$  levels operating at some synapses, then the general formulation presented here will cover that situation as well.

## 2.3 Discrete state synaptic model

### 2.3.1 Two state model

In (O’Connor et al., 2005b; O’Connor et al., 2005a) there is clear evidence for a discrete two state system at individual synapses and measurements showing that the synapses appears to make sudden jumps between the two states. Yet in (O’Connor et al., 2005b) there is presented evidence that when one presents a saturating LTD protocol followed by saturating LTP protocol, the LTD is fully reversible, while the opposite is not the case. We have chosen to investigate a three state synaptic model in this chapter and include in our model the “locked-in” state called  $H^*$  by O’Connor, Wittenberg, and Wang (O’Connor et al., 2005b). Two state systems have been examined by (Del Giudice et al., 2003), though not using the biophysical model for transitions between or among states developed here.

### 2.3.2 Three state model

If there are three states  $l = 0, 1, 2$  then we need to identify three discrete level conductances  $g_0, g_1, g_2$  and the transition rates among the levels. (O’Connor et al., 2005b) call their three levels “low” (state 0 here), high (state 1 here), and “high locked-in” (state 2 here). They suggest that transitions associated with LTD protocols connect state 1 to state 0, and transitions associated with higher frequency protocols, typically leading to LTP, connect state 0 to state 1 and state 1 to state 2. They also note that when an LTD protocol is applied *following* a saturating LTP protocol to a population of synapses, the synapses cannot be depressed as fully as when the LTD protocol is applied to a naive population of synapses. The amount of depotentiation possible decreases over the 10 minutes following LTP induction. This led them to suggest the presence of a “high locked-in” state, called  $H^*$  by them; we call this state 2. They do not require transitions between state 2 and state 0 to account for their data, and we assume none as well.

Using these observations we associate an “LTD transition rate”  $g(t)$  with the transition between state 1 and state 0. Similarly we associate an “LTP transition rate”  $f(t)$  with transitions between state 0 and state 1. Loosely speaking

we think of  $g(t)$  as an aggregated action of phosphatases leading to the dephosphorylation and/or removal of synaptic AMPA receptors and  $f(t)$  as the aggregated action of kinases operating in the opposite fashion (Lisman et al., 2002; Winder, 2001). In the next section we present the details on the neuron model developed to evaluate the transition rates as function of change in intracellular  $[Ca^{2+}]_i$  concentration. For the moment we note that  $f$  and  $g$  will depend on the elevation of intracellular postsynaptic calcium concentrations  $[Ca^{2+}]_i(t)$  above the equilibrium level  $C_0 \approx 100$  nM. Denoting the time course of postsynaptic intracellular calcium concentration as  $C(t) = [Ca^{2+}]_i(t)$ , we define

$$\Delta C(t) = \frac{C(t) - C_0}{C_0}, \quad (2.9)$$

and the transition rates  $f(t), g(t)$  are determined by  $\Delta C(t)$  in a manner specified in the next section where we present the neuron model dynamics.

The transition between state 1 and the “high locked-in” state called 2 is taken to be proportional to the  $0 \rightarrow 1$  transition rate  $f(t)$ . If one had more detailed information on the biophysical kinase and phosphatase pathways, one could replace this simple assumption by a more complex quantity. We take this transition rate as  $bf(t)$  with  $b$  a constant to be determined.

The picture outlined by (O’Connor et al., 2005b) does not suggest a transition from state 2 to state 1, but we find it is necessary. For the moment we call this transition rate  $h(t)$ , and we will argue that it is proportional to  $f(t)$ .  $h(t)$  cannot be zero, if the transition rate framework is to be consistent with observations associated with a “locked-in” state.

This discussion leads us to the transition rate (or “master”) equations associated with the scheme depicted in Figure 2.1:

$$\begin{aligned} \frac{dp_0(t)}{dt} &= -f(t)p_0(t) + g(t)p_1(t) \\ \frac{dp_1(t)}{dt} &= f(t)p_0(t) + h(t)p_2(t) - g(t)p_1(t) - bf(t)p_1(t) \\ \frac{dp_2(t)}{dt} &= bf(t)p_1(t) - h(t)p_2(t). \end{aligned} \quad (2.10)$$

By construction

$$\frac{d(p_0(t) + p_1(t) + p_2(t))}{dt} = 0. \quad (2.11)$$

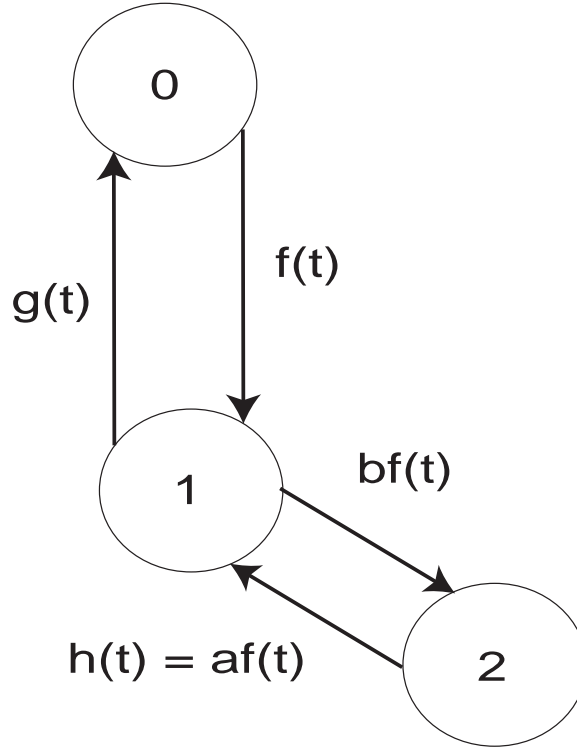


Figure 2.1 **Three state model of synaptic plasticity.** Individual synapses can move among the three states, marked 0 for the “low” state, 1 for the “high” state, and 2 for the “high locked-in” state. The rules for state transition depend on the transition rates,  $f(t)$  and  $g(t)$ , governed by changes in intracellular calcium concentration. These transition rates are determined by LTP and LTD induction protocols.

Under prolonged stimulation the postsynaptic intracellular calcium levels reach approximately constant values, and we can ask what is the behavior of  $\mathbf{P}(t) = [p_0(t), p_1(t), p_2(t)]$  under such circumstances. This means the functions  $f(t)$  and  $g(t)$  are thought of now as constant in time with magnitude determined by the saturated level of  $[\text{Ca}^{2+}]$ . We associate this value of  $\mathbf{P}$ , after long constant  $[\text{Ca}^{2+}]$  elevation, with the fixed point of the equations (2.10) for  $\mathbf{P}(t)$ . The state long after the induction protocol is completed will be the fixed point

$$\mathbf{P}_{\text{fixed point}} = \frac{(gh, fh, bf^2)}{h(f + g) + bf^2}. \quad (2.12)$$



In our models, low values of saturated intracellular calcium elevation  $\Delta C$  are connected with LTD and higher values, with a competition between LTD and LTP (Yang et al., 1999). The specific form of the connection between  $\Delta C$  and  $f$  and  $g$  will be given shortly, but their general dependence is shown in Figure 2 (Bradshaw et al., 2003). In an LTD protocol  $g \neq 0$  but  $f \approx 0$ . In an LTP protocol both  $f$  and  $g$  may be nonzero.

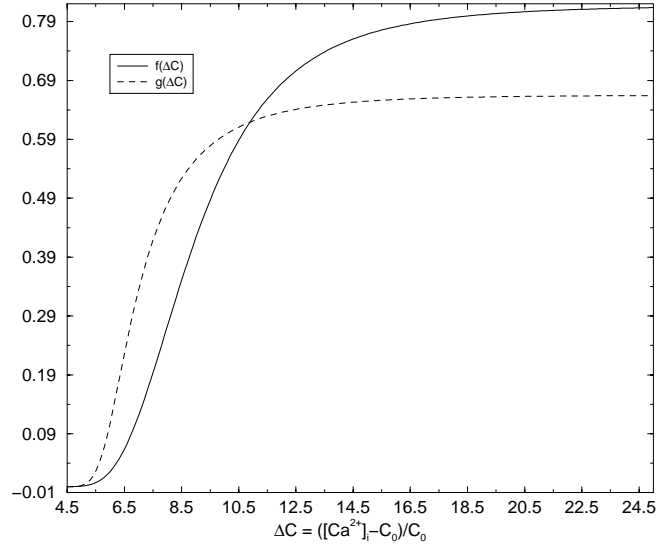


Figure 2.2 Steady state values for the transition rates  $f$  and  $g$  plotted as function of the magnitude of the change in intracellular calcium concentration.  $\Delta C$  is in arbitrary units. For small changes in intracellular calcium concentration only  $g$  is nonzero, corresponding to LTD induction, and for larger changes in intracellular calcium concentration, both  $f$  and  $g$  are nonzero with  $f$  being greater than  $g$ , corresponding to an LTP induction protocol.

If we take  $h = ag$ , then a saturating LTD protocol, with  $g \neq 0, f \approx 0$ , will deplete both states 1 and 2, leading to a final state  $\mathbf{P} = (1, 0, 0)$ .

If, however, we apply a saturating LTP protocol where neither  $f$  nor  $g$  is zero, thus arriving at (2.12), and *then* apply a saturating LTD protocol, the choice  $h = ag$  will lead us back to the state  $\mathbf{P} = (1, 0, 0)$ , which is not what is observed. Indeed, O'Connor et al (O'Connor et al., 2005b) note that the state reached by a

saturating LTP protocol depotentiates to a state intermediate between all synapses in state 0 and the fully saturated state; namely, our fixed point (2.12).

If we choose  $h = af$ , then this saturating LTD protocol following the saturating LTP protocol leads us to

$$\mathbf{P} = \frac{(a(f+g), 0, bf)}{a(f+g) + bf}, \quad (2.13)$$

namely we depopulate state 1 due to the action of  $g$ . This is the kind of depotentiated, but not baseline, state seen by (O'Connor et al., 2005b).

We conclude that the choice  $h = af$  is consistent with the observations, and we cannot have  $a = 0$ . If  $a = 0$ , the high locked state would be totally populated by a strong LTP protocol and the synapse would not leave that state. Indeed, (O'Connor et al., 2005b) indicate that after such a strong LTP protocol (two rounds of theta-burst stimulation), most but not all synapses, about 80%, are in state 2.

This completes the general formulation of the three level transition rate model. We now turn to description of the conductance based neuron model for the postsynaptic cell which permits us to translate electrophysiological activities into transition rates useful in the equations determining  $\mathbf{P}(t)$ . We then go on to determine the AMPA conductance in each level  $l = 0, 1, \dots, L - 1$  from the data presented by (O'Connor et al., 2005b).

### 2.3.3 The neuron model for the postsynaptic cell

Evaluation of the transition rates  $f$  and  $g$  requires a specific model describing how the postsynaptic cell responds to various induction protocols presented either presynaptically or as paired presynaptic and postsynaptic actions. It also requires a model for the dynamics of  $[\text{Ca}^{2+}]$  in the postsynaptic cell. We proceed using the idea that changes in AMPA conductance are induced by the time course of elevation of intracellular  $[\text{Ca}^{2+}]$  (Artola and Singer, 1993; Malenka and Nicoll, 1999; Sabatini et al., 2001; Sjostrom and Nelson, 2002; Soderling and Derkach, 2000). The details of the pathways which follow elevation of  $[\text{Ca}^{2+}]$  are not specified in the phenomenological approach we use. In this regards, we develop a two compartment neuron model, as shown in Figure 2.3. The two compartment model shown separates the cellular dynamics into a somatic compartment where the ac-

tion potentials are generated following the dynamics of type I neuron discussed in chapter 1 and a dendritic compartment where the AMPA and NMDA receptors are located and intracellular calcium dynamics occur.

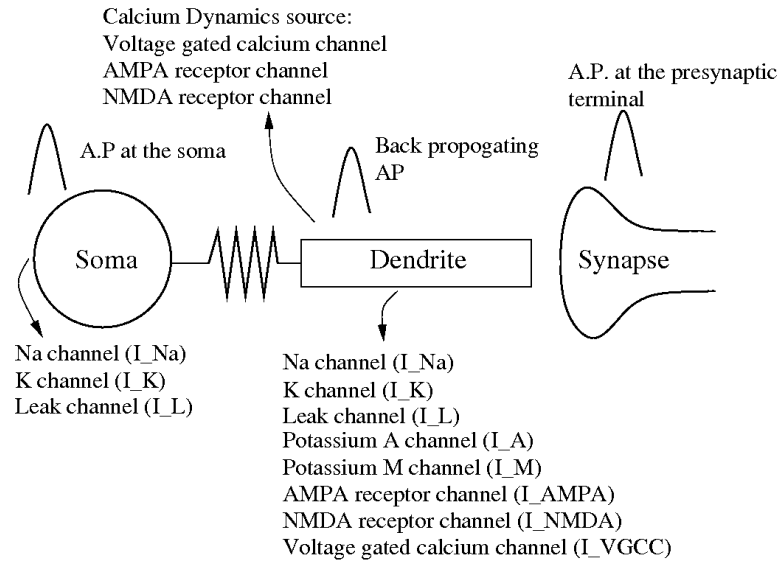


**Figure 2.3 Schematic of the two compartment postsynaptic neuron model** : The diagram shows a somatic compartment comprised of standard HH ionic currents, following type I neuronal dynamics. The soma compartment is electrically coupled to a dendritic compartment consisting of standard HH currents in addition to two potassium currents  $I_A$  and  $I_M$  and the ligand gated ionic currents of AMPA and NMDA type essential for synaptic plasticity dynamics considered here. There is an additional input through voltage gated calcium currents. In addition the dendritic compartment also involved intracellular calcium dynamics, which governs the synaptic plasticity mechanics.

The membrane potential  $V_S(t)$  of the somatic compartment satisfies the following dynamical equation.

$$\begin{aligned} C_M \frac{dV_S(t)}{dt} &= I_{Na}(V_S(t), t) + I_K(V_S(t), t) + I_L(V_S(t)) + I_{Sdc} + I_S(t) \\ &+ G_{S \leftarrow D}(V_D(t) - V_S(t)) \end{aligned} \quad (2.14)$$

$I_{Na}$ ,  $I_K$ , and  $I_L$  are the  $\text{Na}^+$ ,  $\text{K}^+$ , and leak ionic currents similar to that used in the type I neuron model discussed in chapter 1. In addition,  $I_S(t)$  is the externally managed time dependent current injected into the somatic compartment. It allows us to induce an action potential in the soma at a given specific time.  $G_{S \leftarrow D}(V_D(t) - V_S(t))$  is the current flowing into the somatic compartment from the dendritic compartment. It couples the voltages of the somatic and dendritic compartment. The constant DC current injected into the cell,  $I_{Sdc} = -7\mu\text{A}/\text{cm}^2$ , is chosen such that the soma compartment is at resting potential of -75 mV. All the other parameters are similar to that used in the type I neuron model (Chapter 1).

The membrane potential  $V_D(t)$  of the dendritic compartment evolves as follows,

$$\begin{aligned} C_M \frac{dV_D(t)}{dt} &= I_{Na}(V_D(t), t) + I_K(V_D(t), t) + I_L(V_D(t)) \\ &+ I_A(V_D(t), t) + I_M(V_D(t), t) + I_{Ddc} \\ &+ I_{AMPA}(t, V_D(t)) + I_{NMDA}(t, V_D(t)) + I_{VGCC}(t, V_D(t)) \\ &+ G_{D \leftarrow S}(V_S(t) - V_D(t)) \end{aligned} \quad (2.15)$$

$I_{Na}$ ,  $I_K$ , and  $I_L$  are the standard HH currents, of the type I neuron.  $I_{Ddc} = -7\mu\text{A}/\text{cm}^2$  is the constant dc current injected such that the dendritic compartment is also at resting potential of around -75 mV. In addition we have considered two more  $\text{K}^+$  currents  $I_A$  and  $I_M$ .  $I_A$  currents have been reported to modulate the width of action potentials and thereby influencing the dynamics of the intracellular calcium concentration. In our model these two currents attenuate the dendritic action potential induced by back propagating action potential from the soma compartment. The gating equations for  $I_M$  and  $I_A$  are,  $g_M(t) = u^2(t)$  and  $g_A(t) = a(t)b(t)$ , where  $a(t)$ ,  $b(t)$  and  $u(t)$  satisfy the first order kinetic equation of the form given in equation 1.2. The activation and the inactivation functions

$\alpha_X(V)$  and  $\beta_X(V)$  for these gating variables are as given,

$$\begin{aligned}\alpha_u(V) &= \frac{0.016}{e^{-\frac{(V+52.7)}{23}}} & \beta_u(V) &= \frac{0.016}{e^{\frac{(V+52.7)}{18.8}}} \\ \alpha_a(V) &= \frac{-0.05(V+20)}{e^{-\frac{(V+20)}{15}} - 1} & \beta_a(V) &= \frac{0.1(V+10)}{e^{\frac{(V+10)}{8}} - 1} \\ \alpha_b(V) &= \frac{0.00015}{e^{-\frac{(V+18)}{15}}} & \beta_b(V) &= \frac{0.06}{e^{-\frac{(V+73)}{12}} + 1}\end{aligned}$$

$G_{D \leftarrow S}(V_S(t) - V_D(t))$  again represents the coupling current into the dendritic compartment from the soma compartment. In addition to the ionic currents given above we include three other currents essential for synaptic plasticity discussed here. The current associated with the ligand gated NMDA receptor has the form,

$$I_{NMDA}(t, V_D(t)) = g_{NMDA} S_N(t) B(V_D(t)) (V_{NMDA-eq} - V_D(t))$$

where  $g_{NMDA}$  is the maximal conductance associated with the channel.  $S_N(t)$  ranges between zero and unity, representing the percentage of open channels at any time. To achieve the time course of this process in NMDARs, we use a two component form for  $S_N$ ,

$$S_N(t) = w_f S_{N1}(t) + (1 - w_f) S_{N2}(t), \quad (2.16)$$

$0 \leq w_f \leq 1$ , and where  $S_{Nl}(t), l = 1, 2$  satisfies

$$\frac{dS_{Nl}(t)}{dt} = \frac{1}{\tau_{Nl}} \frac{S_0(V_{pre}(t)) - S_{Nl}(t)}{S_{1Nl} - S_0(V_{pre}(t))} \quad (2.17)$$

$V_{pre}$  is scaled to lie between 0 and 1 as it represents the arrival of an action potential at the presynaptic terminal. Its function is in turn to release neurotransmitter.

$S_0(V_{pre}(t))$  is a step function given by,  $S_0(V) = \frac{1}{2}(1 + \tanh(120(V - .1)))$ , which rises sharply from 0 to 1 when neurotransmitter is released as a result of the presynaptic action potential. When this occurs  $S_{Nl}(t)$  rises from zero towards unity with a time constant  $\tau_{Nl}(S_{1Nl} - 1)$ . When the effect of presynaptic action is completed,  $S_{Nl}(t)$  relaxes towards zero with a time constant  $\tau_{Nl}S_{1Nl}$ .  $w_f$  represents the fraction of fast NMDA component contribution to NMDA current. In our model we have chosen  $w_f = .81$ ,  $\tau_{N1} = 67.5$  ms,  $S_{1N1} = 70/67.5$ ,  $\tau_{N2} = 245$  ms,

$S_{1N2} = 250/245$ . In addition the conductance of the NMDA current depends on postsynaptic voltage via the term  $B(V)$  whose form is given as,

$$B(V) = \frac{1}{1 + .288[Mg^{2+}]e^{-.062V}}, \quad (2.18)$$

where the concentration of magnesium is in mM and the voltage is in mV. For simulation purposes we have taken the physiologically reasonable value of  $[Mg^{2+}] = 1$  mM.

This voltage dependent conductance depends on the extracellular magnesium concentration. The voltage dependence of the current is mediated by the magnesium ion which, under normal conditions, blocks the channel. The cell must therefore be sufficiently depolarized to remove the magnesium block. Finally for this excitatory channel  $V_{NMDA-eq} \approx 0$  mV.

$I_{AMPA}$  represents the ligand gated AMPA receptor current. This is taken to be of the form,

$$I_{AMPA}(t, V_D(t)) = g_{AMPA}S_A(t)(V_{AMPA-eq} - V_D(t)) \quad (2.19)$$

where  $g_{AMPA}$  is the maximal conductance for this channel and  $S_A(t)$  is the percentage of open channels, satisfying

$$\frac{dS_A(t)}{dt} = \frac{1}{\tau_A} \frac{S_0(V_{pre}(t)) - S_A(t)}{S_{1A} - S_0(V_{pre}(t))} \quad (2.20)$$

Again the rise time is less than a millisecond. In our formulation this time is  $\tau_A(S_{1A} - 1)$ , which we set to 0.1 ms. AMPA currents decay in approximately 1-3 ms. In our formulation this decay time is  $\tau_A S_{1A}$ , which we set to 1.5 ms. We also take  $V_{AMPA-eq} = 0$  mV.

The final and very important ingredient in inducing synaptic plasticity is the voltage gated calcium channel (VGCC). We have used the low threshold current  $I_T$  for this (McCormick and Huguenard, 1992). The current from this channel takes the form,

$$I_{VGCC}(t, V_D(t)) = g_C G(V(t)) m_c^2(t) h_c(t) \quad (2.21)$$

where  $g_C$  is the maximal conductance of this channel,  $m_c(t)$  is the activation gating variable, and  $h_c(t)$  is the inactivation gating variable, each satisfying equation of form 1.2. The activation and inactivation functions for these gating variables satisfy,

$$m_{co}(V) = \frac{1}{1+e^{-\frac{(52+V)}{6.2}}} \quad \tau_{mc}(V) = .204 + \frac{0.333}{e^{-\frac{(131+V)}{16.7}} + e^{-\frac{(15+V)}{18.2}}}$$

$$h_{co}(V) = \frac{1}{1+e^{-\frac{(72+V)}{4}}} \quad \tau_{hc}(V) = \begin{cases} 0.333e^{\frac{(V+466)}{66.6}} & \text{if } V \leq -81 \text{ mV} \\ 9.32 + 0.333e^{-\frac{(V+21)}{10.5}} & \text{if } V > -81 \text{ mV} \end{cases}$$

$G(V)$  is the Goldman-Hodgkin-Katz function,

$$\begin{aligned} G(V) &= -\frac{V}{C_0} \frac{[Ca^{2+}]_i(t) - [Ca^{2+}]_o e^{-\frac{2VF}{RT}}}{1 - e^{-\frac{2VF}{RT}}} \\ &= -\frac{V}{C_0} \frac{C(t) - [Ca^{2+}]_o e^{-\frac{2VF}{RT}}}{1 - e^{-\frac{2VF}{RT}}} \end{aligned} \quad (2.22)$$

where  $C(t) = [Ca^{2+}]_i(t)$ . The Goldman-Hodgkin-Katz function is used because of the large disparity in the intracellular  $[Ca^{2+}]_i$  and the extracellular  $[Ca^{2+}]_o$  concentrations.  $F$  is Faraday's constant,  $R$  is the gas constant, and  $T$  the absolute temperature. Other factors of the  $G(V)$  equation are absorbed in the conductance  $g_C$ .  $C_0$  is the equilibrium intracellular  $[Ca^{2+}]$  concentration, which is about 100 nM.

The strengths of coupling between the soma and dendritic compartments are determined as follows:

We take the somatic compartment to be a isopotential sphere of  $d_{Soma} = 32.5\mu m$  in diameter and the dendritic compartment to be an isopotential cylinder of diameter  $d_{Dendrite} = 10\mu m$  and length  $l_{Dendrite} = 360\mu m$ . The specific cytoplasmic resistance of the cell is taken to be  $r_i = 200\Omega \text{ cm}$  (Traub and Miles, 1991). Assuming the somatic compartment to be cylindrical of equivalent surface area, the total cytoplasmic resistance of the somatic compartment is given by

$$R_{ISoma} = \frac{r_i l_{Soma}}{X(A_{Soma})} = .007839 \times 10^7 \Omega$$

The cytoplasmic resistance of dendritic compartment is

$$R_{IDendrite} = \frac{r_i l_{Dendrite}}{X(A_{Den})} = 1.713 \times 10^7 \Omega$$

where  $X(A_{Soma}) = \pi d_{Soma}^2/4.0$ , and  $X(A_{Den}) = \pi d_{Dendrite}^2/4.0$ . The average cytoplasmic coupling resistance is then

$$R_I = \frac{R_{ISoma} + R_{IDendrite}}{2} \approx \frac{R_{IDendrite}}{2} = .861 \times 10^7 \Omega$$

The coupling parameters in units of  $mS/cm^2$  are then given by

$$G_{S \leftarrow D} = \frac{1}{A_{Soma} R_I} = 3.5 mS/cm^2 \quad (2.23)$$

and

$$G_{D \leftarrow S} = \frac{1}{A_{Den} R_I} = 1.0 mS/cm^2 \quad (2.24)$$

Finally the dynamics of intracellular calcium  $[Ca^{2+}]_i(t)$  in the dendritic compartment, which affects the efficacy of synaptic strength, is comprised of  $[Ca^{2+}]_i(t)$  decaying to an equilibrium value of  $C_0$ , the basal calcium concentration, normalized to 1 in all the calculations presented here, on a timescale of  $\tau_C \approx 15ms$ , (Sabatini et al., 2001) which we take to be about 30 ms in our model, plus fluxes of  $[Ca^{2+}]_i(t)$  due to the three channels, AMPA, NMDA, and VGCC considered in the dendrite model above. The first order differential equation for  $[Ca^{2+}]_i(t) = C(t)$  then is

$$\begin{aligned} \frac{dC(t)}{dt} &= \frac{1}{\tau_C} (C_0 - C(t)) + C_{NMDA}(t, V_D(t)) + C_{AMPA}(t, V_D(t)) \\ &+ C_{VGCC}(t, V_D(t)) \end{aligned} \quad (2.25)$$

where

$$C_{NMDA}(t, V_D(t)) = g_{NC} S_N(t) B(V_D(t)) (V_{NMDA-eq} - V_D(t))$$

$$C_{AMPA}(t, V_D(t)) = g_{AC} S_A(t) (V_{NMDA-eq} - V_D(t))$$

$$C_{VGCC}(t, V_D(t)) = g_{CC} G(V_D(t)) m_c^2(t) h_c(t)$$

The constants  $g_{NC}$ ,  $g_{AC}$ ,  $g_{CC}$  are not the same, even dimensionally, as the conduc-



tances in the voltage equation. Their values, are  $(g_{NC}, g_{AC}, g_{CC}) = (0.15, 1.5 \times 10^{-5}, 3.5 \times 10^{-5})$  in units of  $\text{mV}^{-1} \text{mS}^{-1}$ , such that the net AMPA current is composed primarily of other ions besides  $[\text{Ca}^{2+}]$  and that NMDA channels are highly permeable to  $[\text{Ca}^{2+}]$  ions. This completes the description of our model.

The output from the biophysical model of neuron described above in form of the intracellular calcium dynamics influence the transition rates  $f(t)$  and  $g(t)$ . The model for the transition rates  $f$  and  $g$  for their dependence on the calcium time course  $C(t) = [\text{Ca}^{2+}]_i(t)$ ,

$$\Delta C(t) = \frac{C(t) - C_0}{C_0}$$

involves two auxiliary variables,  $P(t)$  and  $D(t)$  which satisfy first order kinetics driven by Hill functions dependent on  $\Delta C(t)$ . These variables satisfy

$$\begin{aligned} \frac{dP(t)}{dt} &= F_P(\Delta C(t))(1 - P(t)) - \frac{P(t)}{\tau_P} \\ \frac{dD(t)}{dt} &= F_D(\Delta C(t))(1 - D(t)) - \frac{D(t)}{\tau_D}, \end{aligned} \quad (2.26)$$

with driving terms

$$F_P(x) = \frac{\alpha_P x^L}{\xi_P^L + x^L}; \quad F_D(x) = \frac{\alpha_D x^M}{\xi_D^M + x^M}. \quad (2.27)$$

We used the constants  $\tau_P = 10$  ms,  $\tau_D = 30$  ms,  $\alpha_P = 1.0$ ,  $\alpha_D = 1.25$ ,  $L = 10.5$ ,  $M = 4.75$ ,  $\xi_P = 6.7$ , and  $\xi_D = 13.5$  in our calculations for this work. These equations are discussed in an earlier paper (Abarbanel et al., 2003) by our group.

These kinetic quantities are driven by elevation in  $[\text{Ca}^{2+}]$ ,  $\Delta C a(t) > 0$ , from their resting value of zero. They are taken to be related to the transition rates as

$$\begin{aligned} f(t) &= P(t)D(t)^\eta \\ g(t) &= P(t)^\eta D(t), \end{aligned} \quad (2.28)$$

and  $\eta = 4$  as used in our earlier work (Abarbanel et al., 2003). The quantities  $f(t)$  and  $g(t)$  have dimensions of frequency. Our arguments do not establish their magnitude but only provide a connection to their dependence on elevation of intracellular  $[\text{Ca}^{2+}]$  levels. Multiplying the relations here between  $f(t)$  and  $g(t)$  and

$P(t)$  and  $D(t)$  by a constant rescales the time while not affecting the final states which lead to specific statements of AMPA conductance changes after an induction protocol.

The model for the neuron and the transition rates is now established. To proceed further we specify an electrophysiological protocol. For example we present a burst of spikes to the presynaptic terminal with an average interspike interval (ISI) of our choice. Our presynaptic terminal represents the population of terminals from presynaptic neurons onto a postsynaptic neuron. This induces a voltage and  $[Ca^{2+}]$  response in the postsynaptic cell, and from the time course of  $\Delta C(t)$  we evaluate the transition rates  $f(t)$  and  $g(t)$ . These enter the ‘master’ equation for the average occupations across the population of  $N_S$  synapses. Solving the equations for the  $p_l(t)$  leads to our evaluation of

$$\begin{aligned} \frac{G_{AMPA}(t)}{N_S} &= g_0 p_0(t) + g_1 p_1(t) + g_2 p_2(t). \\ &= 2 - \frac{4p_0(t)}{3}. \end{aligned} \tag{2.29}$$

## 2.4 Results

We first establish, using the measurements in (O’Connor et al., 2005b) the values of the normalized, dimensionless AMPA conductances of the three levels at an individual synapse. Our arguments show that they are determined independently of the specific model for the transition rates. We then use the transition rate model developed above to make predictions about the response of the cell to various LTP and LTD induction protocols.

### 2.4.1 Determination of the discrete level conductances

At  $t = 0$  the average occupation of levels is observed to be  $\mathbf{P}(0) = (\frac{3}{4}, \frac{1}{4}, 0)$ . This means the normalized AMPA conductance is

$$\frac{G_{AMPA}(0)}{N_S} = 1 = \frac{3g_0}{4} + \frac{g_1}{4}. \tag{2.30}$$

If a strong, saturating LTD protocol is applied to this state, we reach  $\mathbf{P} = (1, 0, 0)$ , where the normalized AMPA conductance is  $g_0$ .

It has been observed (O'Connor et al., 2005b) that after the induction  $\frac{G_{AMPA}}{N_S} = 0.65 \pm 0.03$ . We take this to be  $\frac{G_{AMPA}}{N_S} = \frac{2}{3} = g_0$  which implies  $g_1 = 2$ .

Next apply a phosphatase blocker (okadaic acid was used in (O'Connor et al., 2005b)) so  $g = 0$  and, as they did, present a saturating LTP signal to arrive at the state  $\mathbf{P} = \frac{(0, af, bf)}{(a+b)f} = \frac{(0, a, b)}{(a+b)}$ , which is independent of the transition rate  $f$ . This is precisely the fixed point noted above with  $g = 0$  and  $h = af$ . After this protocol, the normalized AMPA conductance is approximately 2, leading to

$$\frac{ag_1 + bg_2}{a + b} = 2, \quad (2.31)$$

and thus  $g_2 = 2$ . Our model corresponds to the set of normalized individual level conductances ( $g_0 = \frac{2}{3}, g_1 = 2, g_2 = 2$ ).

The constants  $a$  and  $b$  are not determined by the observations so far. The normalized conductance values for the three states obtained above are determined independent of specific values for  $a$  and  $b$ . However these constants can be determined by applying various induction protocols once we have a model for the transition rates. The actual time series of

$$\frac{G_{AMPA}(t)}{N_S} = \frac{2}{3}p_0(t) + 2p_1(t) + 2p_2(t) \quad (2.32)$$

will depend on  $a$  and  $b$ .

This ratio  $\frac{a}{b}$  can be determined by another experiment not yet conducted. Start with the naive synapse  $\mathbf{P}(0) = (\frac{3}{4}, \frac{1}{4}, 0)$ , apply okadaic acid, so  $g = 0$ , (as in (O'Connor et al., 2005b)) which blocks phosphatases, and present a saturating LTP protocol. This leads to the state  $\mathbf{P} = \frac{(0, a, b)}{a+b}$ . Now wash out the okadaic acid and apply the kinase blocker k252a, setting  $f = 0$ , and present a saturating LTD protocol. This leads one to the state  $\frac{(a, 0, b)}{a+b}$ . The normalized AMPA conductance in this state is

$$\frac{G_{AMPA}}{N_S} = \frac{ag_0 + bg_2}{a + b} = \frac{\frac{2}{3}\frac{a}{b} + 2}{1 + \frac{a}{b}}. \quad (2.33)$$

Measuring  $\frac{G_{AMPA}}{N_S}$  after this protocol sequence would give us a value for  $\frac{a}{b}$ .

## 2.4.2 LTP and LTD Induction Protocols

### Presynaptic Bursts

The first protocol we used presented a burst of ten spikes to the presynaptic terminal and evaluated  $\frac{G_{AMPA}(t)}{N_S}$  during and at the end of the induction period. The interspike interval (ISI) was constant in the burst, and we show in Figure 2.4 the value of  $\frac{G_{AMPA}(t)}{N_S} - 1$  after the burst as a function of frequency equal to  $\frac{1}{ISI}$ . Three calculations are presented. The first, shown with filled circles, involves the action of both the LTP inducing transition rate  $f(t)$  and the LTD inducing transition rate  $g(t)$ . As in the experimental data there is a region of no change in AMPA conductance per synapse for very low frequencies, then a region of LTD until this crosses into a region of persistent LTP. The second calculation, shown with upright triangles, removes the LTD inducing transition rate, so  $g(t) = 0$ , which is achieved by (O'Connor et al., 2005b) by the use of okadaic acid. In this calculation we see that LTP alone is induced at all frequencies where there is a measurable effect. The maximum AMPA conductance in the present model is  $\frac{G_{AMPA}(t)}{N_S} = 2$  occurring when the lowest state is totally depleted. The value of unity for  $\frac{G_{AMPA}(t)}{N_S} - 1$  is expected when a saturating LTP protocol is applied. Finally, a third result shown in Figure 2.4 is the set of points with inverted triangles which occur when one blocks kinase action, again following the experimental procedures of (O'Connor et al., 2005b), which means  $f(t) = 0$  in our language. Here we see a persistent LTD dropping to  $\frac{G_{AMPA}(t)}{N_S} - 1 \approx -\frac{1}{3}$  above frequencies of 10 Hz. This is the smallest possible value in the present model, as with this induction protocol and  $f(t) = 0$  the lowest state is fully populated, and the AMPA conductance, in dimensionless, normalized units is  $\frac{2}{3}$ .

All of this is consistent with the observations and the expectation of saturating LTP/LTD protocols in the discrete state plasticity model we have developed. It is important to note that the bounded nature of the AMPA conductance is quite important as in many other models, including our own (Karmarkar and Buonomano, 2001; Shouval et al., 2002; Abarbanel et al., 2003), there is no guarantee that  $\frac{G_{AMPA}(t)}{N_S}$  is bounded above or below.

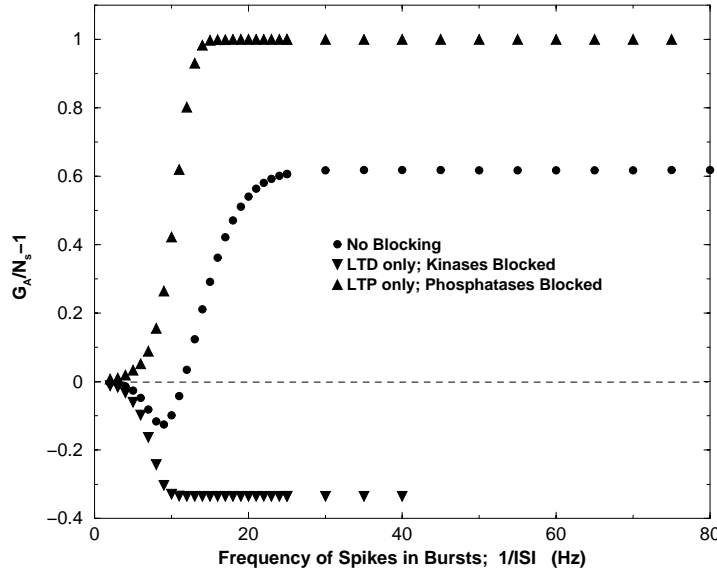


Figure 2.4 **Frequency-plasticity curve.** The change in normalized AMPA conductance per synapse,  $G_{AMPA}/N_s - 1$ , is plotted as function of the frequency of a periodic burst of 10 presynaptic spikes presented to the presynaptic terminal. The circles represent synaptic plasticity for the full three state model. The upward-pointing triangles represent synaptic plasticity with the term  $g(t)$  set to 0, corresponding to blocking phosphatase activity in the postsynaptic cell. One sees and expects LTP alone. The downward-pointing triangles represent the change in synaptic plasticity with the term  $f(t)$  set to 0, corresponding to blocking kinase activity in the postsynaptic cell. We observe and expect LTD alone in this case. These results are quite similar to the observations of (O'Connor et al., 2005b).

### Spike timing plasticity

The exploration of spike timing dependent plasticity at hippocampal synapses has resulted from the investigations of the phenomenon since the work of Debanne and Markram (Debanne et al., 1994; Markram et al., 1997), Poo and his colleagues (Bi and Poo, 2001; Nishiyama et al., 2000; Bi and Poo, 1998), and Feldman (Feldman, 2000) over the past few years. We explored this in the present model by first presenting a spike presynaptically at a time  $t_{pre}$  and evoking a postsynaptic spike at  $t_{post}$ . The change  $\frac{G_{AMPA}(t)}{N_s} - 1$  is a function only of  $\tau = t_{post} - t_{pre}$

and for our model is shown in Figure 2.5. This reproduces the characteristic window of LTP centered near  $\tau = 0$  and of width  $\approx 10$  ms around this point. Also shown in Figure 2.5 are the LTD regions on both sides of this window. The one for  $\tau$  negative is seen in many experiments. The LTD region for  $\tau$  positive has been seen in experiments reported by (Nishiyama et al., 2000), and it is common in models, including ours, which focus on postsynaptic intracellular  $[Ca^{2+}]$  as inducing the chain of events leading to AMPA plasticity.

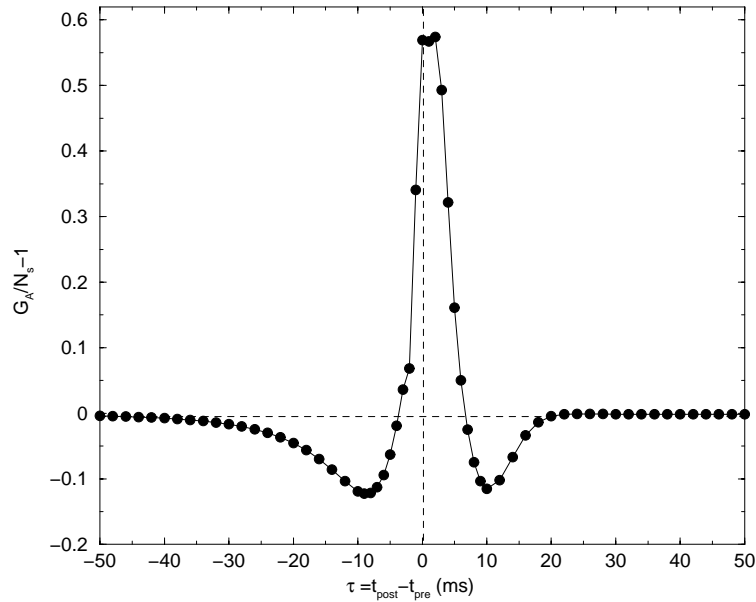


Figure 2.5 **Spike timing dependent plasticity protocol.** The change in normalized AMPA conductance per synapse,  $G_{AMPA}/N_S - 1$ , plotted as a function of the delay,  $\tau = t_{post} - t_{pre}$  (ms), between presentation of a single presynaptic spike at  $t_{pre}$  and postsynaptic spike induced at  $t_{post}$ .

(Nishiyama et al., 2000) used cesium instead of potassium in the intracellular pipette solution, and this has been argued by Wittenberg (Wittenberg, 2003) to depolarize the postsynaptic cell and broaden the action potential artificially. To address this, Wittenberg has performed experiments in which this additional depolarizing effect is mimicked by presenting a spike timing protocol with one

presynaptic spike at time  $t_{pre}$  and *two* postsynaptic spikes with a time difference  $\Delta t$ . She uses  $\Delta t = 10$  ms, and the outcome of this protocol for our model is plotted in Figure 2.6a with the experimental data (Wittenberg, 2003; used with permission). The change in normalized synaptic strength resulting from this protocol ( $G_{AMPA}/N_S - 1$  for the model) is shown as a function of the time of the second postsynaptic spike  $t_{post(2)} - t_{pre}$ . For the experiments, normalized synaptic strength is the average peak excitatory postsynaptic current (EPSC) height measured 10-20 minutes after the end of the pairing protocol, normalized by the mean baseline peak EPSC height. It is clear that the LTP window is substantially larger than when we evoke just one postsynaptic spike and resembles the experimental data. We can regard this as a prediction of our discrete state plasticity model. Further predictions of this protocol are shown in Figures 2.6b and 2.6c where  $\Delta t = 15$  ms and  $\Delta t = 20$  ms respectively. In each case there is a distinct LTD window for positive  $t_{post(2)} - t_{pre}$  and a distinctive dip between the LTP peaks whose separation is dictated by  $\Delta t$ .

Our model exhibits a number of features of LTP and LTD observed experimentally at CA3-CA1 synapses, including trapping of synapses in a high-strength state, separability of potentiation and depression by simulated inhibition of kinase or phosphatase activity, and spike timing-dependent plasticity (O'Connor et al., 2005b; Wittenberg, 2003). However, there are a number of ways in which the model can be developed further. For example, using the protocols of (O'Connor et al., 2005b), population LTP at CA3-CA1 synapses rises gradually to a peak level over a few minutes; LTD takes a few minutes longer than this to develop fully. Our model does not yet include such a long timescale, but could be modified phenomenologically to do so. (O'Connor et al., 2005b) have also found that the high locked-in state in populations of synapses builds up over several minutes. To model this phenomenon, we would again need to include a longer timescale.

While the spike timing-dependent plasticity induced in our model by 1 presynaptic and 2 postsynaptic spikes is similar to that observed by (Wittenberg, 2003), our result for 1 presynaptic and 1 postsynaptic spike appears to differ from experimental observations (G. M. Wittenberg and S. S.-H. Wang, unpublished data quoted with the authors' permission). In particular, they observed little LTP but significant LTD near  $t_{post} - t_{pre} = 0$ . At other values of  $t_{post} - t_{pre}$ , they observed

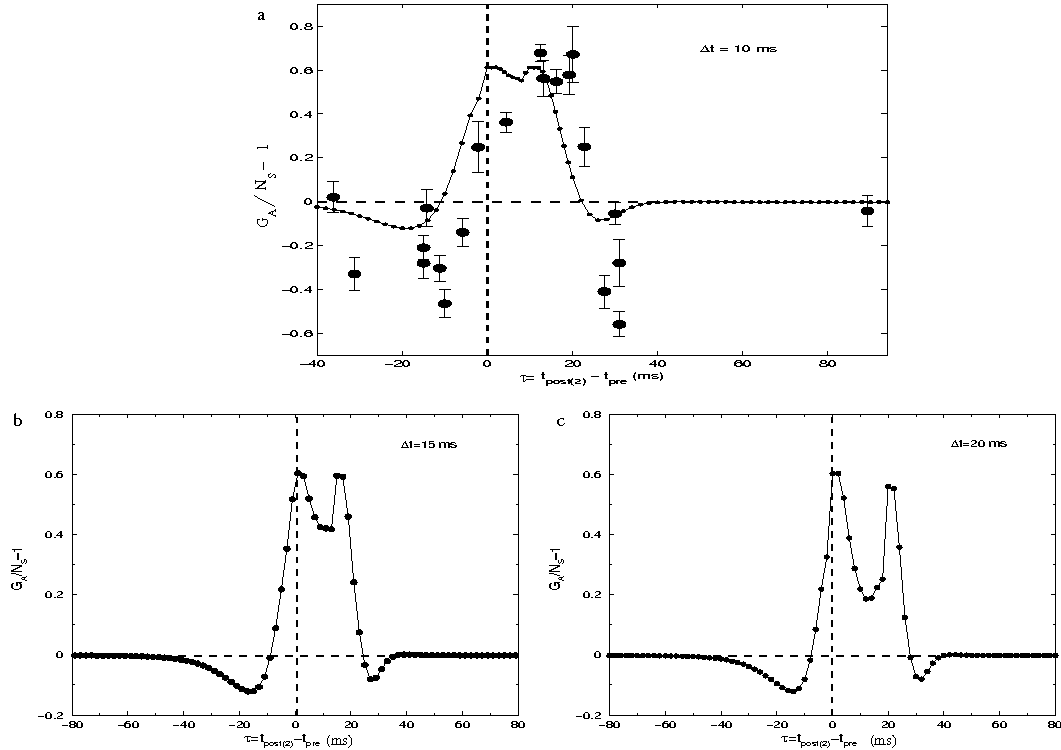


Figure 2.6 (a) Change in normalized synaptic strength as a function of the delay  $\tau = t_{post(2)} - t_{pre}$  when a single presynaptic spike is paired with two postsynaptic spikes 10 ms apart.  $t_{post(2)}$  is the time of the second postsynaptic spike. Model results (*points connected by lines*) are plotted with experimental data of G. M. Wittenberg (*large filled circles with error bars*; Wittenberg, 2003, used with permission). *Normalized synaptic strength*, for the model, is the normalized AMPA conductance per synapse ( $G_{AMPA}/N_S$ ) after the pairing. For the experiments, it is the average peak excitatory postsynaptic current (EPSC) height measured 10-20 minutes after the end of the pairing protocol, normalized by the mean baseline peak EPSC height (*Error bars*: standard error of the mean). In the experiments, pairing was repeated 100 times at 5 Hz. (b) Here we plot change in normalized synaptic strength as a function of the delay  $\tau = t_{post(2)} - t_{pre}$  when a single presynaptic spike is paired with two postsynaptic spikes 15 ms apart. As in case (a), we see a distinct dip in potentiated AMPA conductance is observed for times when presynaptic spike falls in between the two postsynaptic spike presentations. (c) Similar plot of change in normalized synaptic strength as a function of the delay  $\tau = t_{post(2)} - t_{pre}$  when a single presynaptic spike is paired with two postsynaptic spikes 20 ms apart.



only LTD. This suggests that such a protocol provides insufficient postsynaptic  $[Ca^{2+}]$  influx to induce LTP reliably. In contrast, our model shows a narrow but clear window of LTP centered near  $t_{post} - t_{pre} = 0$ . At these values of  $t_{post} - t_{pre}$ , the  $[Ca^{2+}]$  influx in our model is sufficient to give a relatively large value and thus induce LTP. If the data of Wittenberg and Wang are correct, then our model will need to be adjusted so that this  $[Ca^{2+}]$  influx is not sufficient to induce LTP.

In addition, the model can be used to explore the results of various LTP and LTD induction protocols that we have not simulated here but that are used by (O'Connor et al., 2005b) and others in their experiments, such as theta burst stimulation and pairing protocols. In the long term, a model that more accurately describes the postsynaptic signaling pathways will eventually account for all of these various features of the data in a biologically satisfying manner.

### 2.4.3 Synchronization of Two Periodic Neural Oscillators with Discrete State Synapses

The final consequence we have investigated of our discrete state plasticity model is for the synchronization of oscillating neurons. We take as given that synchronization among populations of neurons can play an important role in their performing important functional activity in biological neural networks. We have abstracted the synchronous activity of populations of neurons to the simplest setup: two periodically oscillating Hodgkin-Huxley (HH) neurons coupled by a synaptic current which we explore with and without plastic synapses.

We have selected the postsynaptic neuron to be our two compartment model as described in the chapter and set it into autonomous oscillations with a period  $T_2^0$ . This period is a function of the injected DC current into the somatic compartment. We hold this fixed while we inject a synaptic AMPA current

$$I_{\text{synapse}}(t, V_{\text{post}}(t)) = g_{\text{AMPA}}(t)S_A(t)(E_{\text{rev}} - V_{\text{post}}(t)), \quad (2.34)$$

, where  $E_{\text{rev}} = 0$ , into the postsynaptic soma compartment.  $V_{\text{post}}(t)$  is the membrane voltage of this postsynaptic compartment.  $g_{\text{AMPA}}(t)$  is our time dependent

maximal AMPA conductance, and  $S_A(t)$  satisfies

$$\frac{dS_A(t)}{dt} = \frac{1}{\tau_A} \frac{S_0(V_{pre}(t)) - S_A(t)}{S_{1A} - S_0(V_{pre}(t))} \quad (2.35)$$

as described in earlier.  $V_{pre}(t)$  is the periodic presynaptic voltage which we adjust by selecting the injected DC current into the presynaptic HH neuron. We call the period of this oscillation  $T_1$ .

When  $g_{AMPA} = 0$  the neurons are disconnected and oscillate autonomously. When  $g_{AMPA} \neq 0$  the synaptic current into the postsynaptic neuron changes its period of oscillation from the autonomous  $T_2^0$  to the driven value of  $T_2$ , which we evaluate for various choices of  $T_1$ . We expect from general arguments (Drazin, 1992) that there will be regimes of synchronization where  $\frac{T_1}{T_2}$  equal integers and half-integers over the range of frequencies  $\frac{1}{T_1}$  presented presynaptically. This will be true both for fixed  $g_{AMPA}$  and when  $g_{AMPA}(t)$  varies as determined by our model.

In Figure 2.7a we present  $\frac{T_1}{T_2}$  as function of the frequency  $\frac{1000}{T_1}$  ( $T_1$  is given in milliseconds, so this is in units of Hz) for fixed  $g_{AMPA} = 0.1 \frac{mS}{cm^2}$  and for  $g_{AMPA}(t) = g_{AMPA} \frac{G_{AMPA}(t)}{N_S}$  determined from our model. This value is what we used in our earlier calculations with the two compartment model. It amounts to a choice for the baseline value of the AMPA conductance. The fixed  $g_{AMPA}$  results are in filled upright triangles and, as expected, show a regime of one-to-one synchronization over a range of frequencies. One also sees regions of two-to-one and hints of five-to-two and three-to-one synchronization. These are expected from general arguments on the parametric driving of a nonlinear oscillator by periodic forces.

When we allow  $g_{AMPA}$  to change in time according to the model we have discussed above, we see (unfilled inverted triangles) a substantial increase in the regime of one-to-one synchronization, the appearance of some instances of three-to-two synchronization, and a much smaller regime with two-to-one synchronization. This suggests that the one-to-one synchronization of oscillating neurons, which is what one usually means by neural synchrony, is substantially enhanced when the synaptic coupling between neurons is allowed to vary by the rules we have described.

We show the same results in Figure 2.7b for  $g_{AMPA} = 0.2 \frac{mS}{cm^2}$ . The fixed

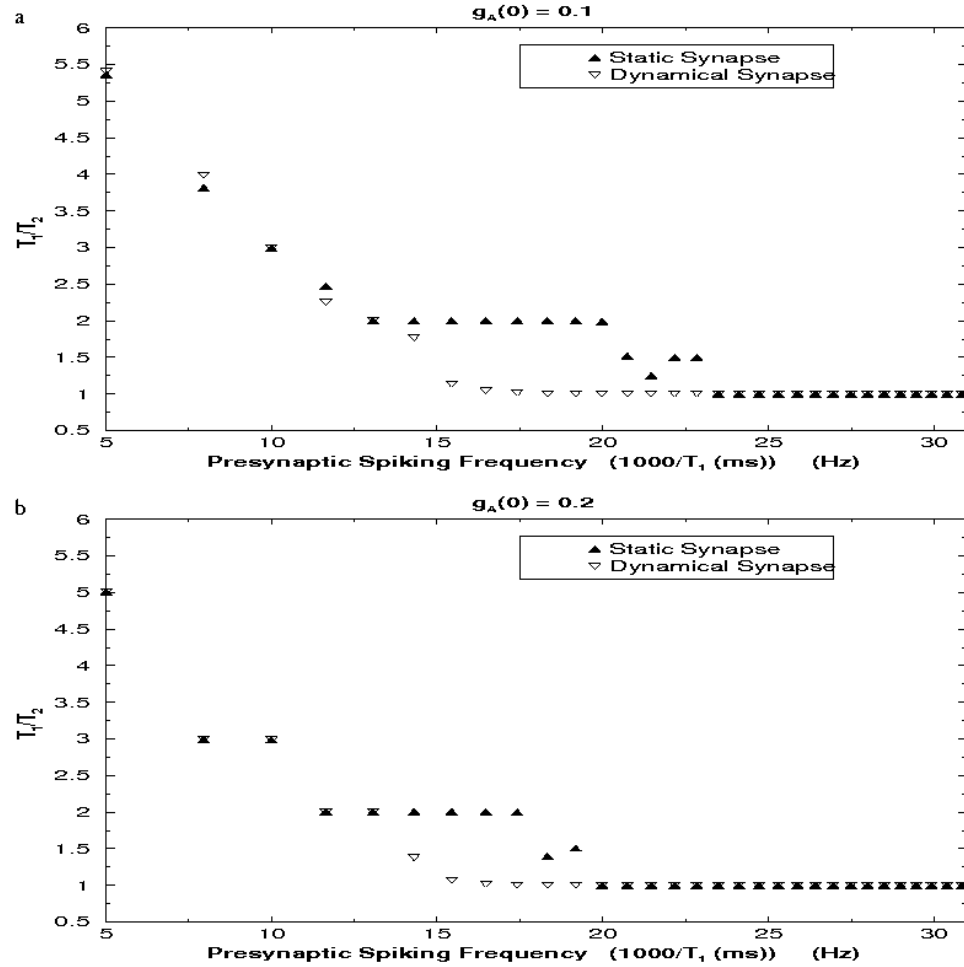


Figure 2.7 (a)  $T_1/T_2$ , the ratio of the interspike interval  $T_1$  of the presynaptic neuron to the interspike interval  $T_2$  of the postsynaptic neuron, is plotted as a function of the presynaptic input frequency,  $1000/T_1$  Hz, for a synapse starting at a base AMPA conductance of  $g_{AMPA}(t=0) = 0.1 \text{ mS/cm}^2$ . We see that the one-to-one synchronization window is broadened when the static synapse is replaced by a plastic synapse as determined by the three state model. (b) A similar plot for different value of base AMPA strength,  $g_{AMPA}(t=0) = 0.2 \text{ mS/cm}^2$

coupling is larger leading to stronger synchronization of the two neurons in a one-to-one manner even for fixed coupling. Here too (inverted, unfilled triangles) we see that allowing  $g_{AMPA}$  to vary in time enlarges the regime of one-to-one synchronization.

In Figures 2.8 and 2.9 we explore aspects of the internal dynamics of plasticity and  $[Ca^{2+}]$  time courses for these results. In Figure 2.8 we show  $C(t) = [Ca^{2+}]_i(t)$  (scaled by a factor of 15 to fit on this graphic) and  $\frac{G_{AMPA}(t)}{N_S} - 1$  in response to a presentation of periodic presynaptic oscillations beginning at a time 300. As noted earlier, the timescales for the intracellular  $[Ca^{2+}]$  processes and the timing in changes in  $G_{AMPA}(t)$  are not determined by our model. An arbitrary constant can multiply the definitions of the transitions rates  $f(t)$  and  $g(t)$ . Both quantities rapidly rise, after a small transient of LTD, to positive but oscillating levels. The maximum  $\frac{G_{AMPA}(t)}{N_S} - 1$  is 1 in our model, and we see that this saturating level is not reached in this protocol.

Finally, in Figure 2.9 we examine how the synchronization manifests itself in the postsynaptic somatic and dendritic compartment membrane potentials. We plot these potentials along with  $V_{pre}(t)$ . It is clear that the one-to-one synchronization occurs with an in-phase oscillation of the presynaptic and postsynaptic cells. The very short time delay between the somatic and dendritic compartments of the postsynaptic neuron is part of the model dynamics and not associated with the presentation of periodic presynaptic spikes to the postsynaptic cell. The in-phase synchronization is not seen in other, less biophysically based, models of plastic synapses and represents a very desirable feature of this model.

## 2.5 Discussion

The observations, recent and over the years, of discrete levels for synaptic strength at individual synapses in the CA3-CA1 hippocampal pathways represents a fundamental property important for the ways we learn and remember. There is a very interesting and important biophysical question about the mechanisms which lead to the expression of a few discrete levels of AMPA conductance at which individual synapses may be found. We do not address this fundamental question in this paper, but we have used the observation to construct a model based on

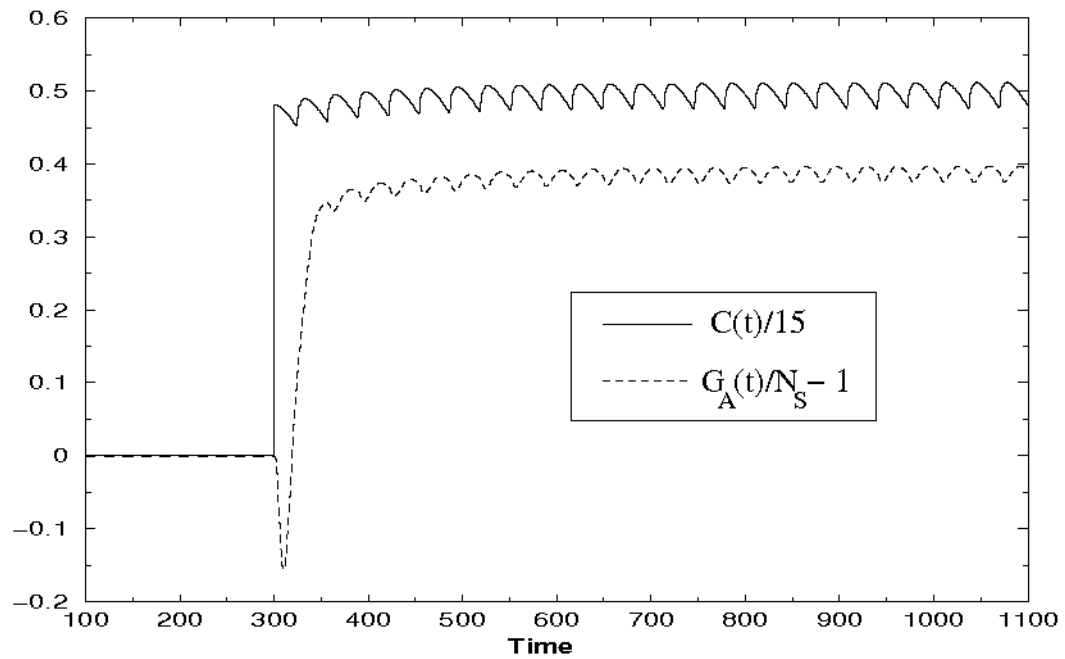


Figure 2.8 Intracellular calcium concentration, scaled by 15, and the change in normalized synaptic strength,  $G_{AMPA}(t)/N_S - 1$ , is plotted as a function of time in the case when a periodically spiking postsynaptic cell is driven by a periodically spiking presynaptic input.

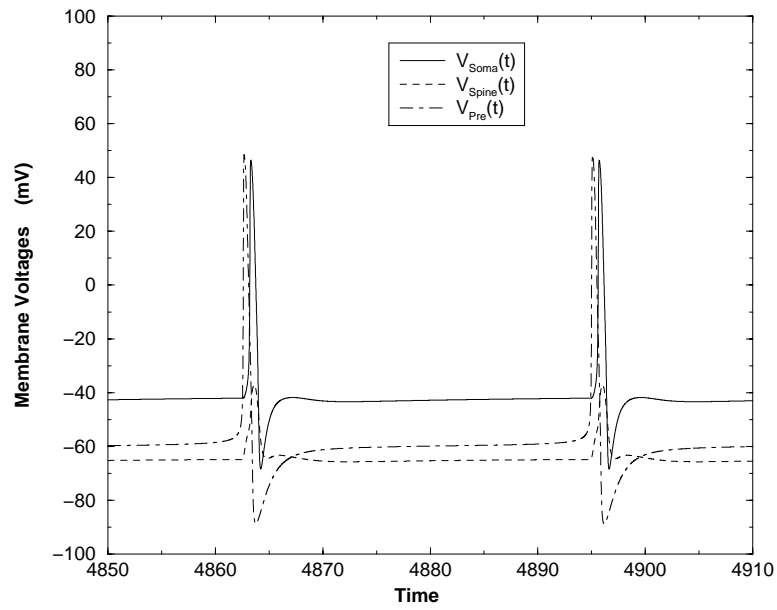


Figure 2.9  $V_{\text{soma}}(t)$ ,  $V_{\text{dendrite}}(t)$  and  $V_{\text{pre}}(t)$ , plotted as functions of time, when the presynaptic and postsynaptic neurons are synchronized. Note that the presynaptic and postsynaptic neurons are synchronized in-phase with an internal,  $V_{\text{soma}}(t)$  to  $V_{\text{spine}}(t)$ , time difference determined by the two compartments of the model neuron.

discrete levels with transition rates among the levels determined by biophysical dynamics.

We have formulated a discrete level synaptic system in a general way with  $L$  levels allowed to the AMPA conductance, and then, following the observations of (O'Connor et al., 2005b) we specialized to  $L = 3$ . The dynamical variables in our model when  $L = 3$  are the average occupation numbers of each level  $\mathbf{P}(t) = [p_0(t), p_1(t), p_2(t)]$ . These are averages over a collection of  $N_S$  synapses which contribute to the overall AMPA determined response of the neuron. While each individual synapse resides in one of three discrete states, so the individual occupation numbers at any given synapse are either zero or one and the average occupation numbers are smoothly varying, subject only to  $p_0(t) + p_1(t) + p_2(t) = 1$ , by definition.

We developed differential equations for  $\mathbf{P}(t)$  which are linear in the  $p_l(t)$ ,  $l = 0, 1, 2$

$$\frac{dp_l(t)}{dt} = \sum_{l'=0}^2 M_{ll'} p_{l'}(t), \quad (2.36)$$

and where the transition rates  $M_{ll'}$  are determined by nonlinear membrane voltage and intracellular  $[\text{Ca}^{2+}]$  dynamics.

From the observations of (O'Connor et al., 2005b) we argued that the transition rates shown in Figure 2.1 sufficed to explain their measurements, and using their reported results we were able to determine that the conductances of the three individual levels in normalized, dimensionless units were  $g_0 = \frac{2}{3}, g_1 = 2, g_2 = 2$ . The time dependence of the normalized, dimensionless AMPA conductance per synapse is then

$$\begin{aligned} \frac{G_{AMPA}(t)}{N_S} &= \sum_{l=0}^2 p_l(t) g_l \\ &= 2 - \frac{4p_0(t)}{3}. \end{aligned} \quad (2.37)$$

Using our values for the  $g_l$  and a dynamical model of the transition rates  $f(t), g(t)$  as shown in Figure 2.1, we reproduced the observed plasticity in response to a burst of presynaptic spikes with interspike intervals (ISIs) over the observed range. Further we made predictions for the response of this model to spike timing

plasticity both for one presynaptic and one postsynaptic spike and for the case of two postsynaptic spikes evoked  $\Delta t$  apart accompanied by one presynaptic spike. We presented our results for  $\Delta t = 10, 15,$  and  $20$  ms.

Finally we examined the dynamical role played by this discrete state plasticity model in the synchronization of two periodically oscillating Hodgkin-Huxley neurons. One such neuron oscillating with period  $T_2^0$  was driven by another such neuron with period  $T_1$ . The final period  $T_2$  of the driven neuron, relative to  $T_1$ , was plotted against  $\frac{1}{T_1}$  and showed familiar regions of synchronization. For fixed AMPA coupling  $g_{AMPA} = \frac{G_{AMPA}}{N_S}$  we found synchronization over some range of  $\frac{1}{T_1}$  and then demonstrated that allowing  $g_{AMPA}$  to vary according to the plasticity model resulted in a much larger regime of one-to-one synchronization with the two neurons oscillating in-phase. The results for synchronization have not been tested experimentally, though some experiments using dynamic clamp based synapses have been performed (Nowotny et al., 2003).

One striking aspect of the discrete state model, certainly not limited to our own work, is that the AMPA conductance has natural upper and lower bounds. Many other models of plasticity, including our own, do not share this important feature.

Some of our results, in particular the strengths of the normalized, dimensionless conductances of the synaptic levels are dependent primarily on the data of (O'Connor et al., 2005b). All of the transition rates are determined by our two compartment model for the neuron, as presented in this chapter.

This model will change over time and be improved by further understanding of the biophysical processes leading to the discrete states and their transitions among themselves. The general framework we have presented describing how the three observed states are connected and several general results about that system will remain as the representation of the transition rates is improved.

While our model is based on the idea of discrete state synapses, by design it describes only populations of such synapses. Future work in this direction should address this discreteness at the level of single synapses and small numbers of synapses. Questions of interest would include: (1) when the number of synapses is small, does the spread in the experimental data from trial to trial on excitation of individual synapses correspond to the fluctuations observed in our



model over many trials; (2) is there evidence for heterosynaptic interaction; our model arises when we take  $N_S \gg 1$  independent synapses undergoing essentially the same transitions and average over the synapses. If there is interaction among synapses, this would need to be modified, and it is likely that in the examination of the dynamics of a few synapses, rather than the many studied here, it will be possible to develop an understanding of interactions among synapses. (Nishiyama et al., 2000) provide evidence for heterosynaptic interactions via calcium dynamics, perhaps mediated by the endoplasmic reticulum; (3) what is the role, when the number of synapses is small, of the probabilistic nature of presynaptic vesicle release? We have passed over these interesting issues in this chapter while focusing on the whole cell behavior.

The dynamics of discrete state synapses is likely to be most interesting when placed in a network context. What new phenomena will arise when the synaptic strengths are bounded below and above while working in a network with learning is yet to be explored. We have made some preliminary calculations with the discrete state model we presented in this chapter, when it is used in our description of the role of plasticity in maintaining adult birdsong (Abarbanel et al., 2004a). The indications are that the important fixed point in that investigation is retained while the runaway behavior seen there is "cured." However, it is clear that there is much yet to explore in this regard.

Most of the material appearing in this chapter has been published in (Abarbanel H.D.I., Talathi S.S., Gibb L., and Rabinovich M., Physical Review E, 72, 031914, 2005). The dissertation author was the primary researcher in this project.

# 3

## Dynamics of songbird learning and control

In the last chapter we developed a biophysical model for synaptic plasticity dynamics, that explains the observed graded synaptic response through the underlying transitions in discrete synaptic states. The model provides a natural bound on the growth and decay in the synaptic strengths. Earlier models for synaptic plasticity developed in our lab failed in their ability to provide these natural limits on the changes in the synaptic strengths. In this chapter we study an important function of the synaptic plasticity dynamics in neuronal networks. In particular we focus on the song system and study the function of the synaptic plasticity model developed in our lab, in modulating the dynamics of the song system.

### 3.1 Introduction

Learning and maintenance of song in songbirds present an interesting questions about the basic biological physics of birdsong. The study of the detailed mechanism and neurophysiology of the collection of neurons, called nuclei, constituting the song system of songbirds might also inform one's interest in the human speech counterpart of song (Doupe and Kuhl, 1999). Each of the song system nucleus consists on the order of 10,000 neurons and is not homogeneous in its neural composition. There exists some data on the the properties of neurons in each nucleus revealed by electrophysiological experiments in the past decade, and we

shall review this information as we develop the model discussed in this chapter. Notwithstanding the inhomogeneity in each nucleus, the birdsong nuclei in the pre-motor pathway and the nuclei of the anterior forebrain pathway (Figure 1.1), which is closely linked with it, appear to act in a cooperative manner with regard to the timing of signals observed during the song production (Kimpö et al., 2003).

As discussed in chapter 1 the production of song directly involves the pre-motor pathway from the nucleus HVC (used as a proper name) to the robust nucleus of the archistriatum (RA) and then from RA by projection through the tracheosyringeal portion of the hypoglossal nucleus to the syrinx muscles controlling tension in the nonlinear song membrane and through the nucleus ambiguus and nucleus retroambiguus to the motor neurons controlling respiratory action in the songbox. The balance between the timing of the tension signals and the respiratory signals is thought to control the quality and details of song production (Laje and Mindlin, 2002; Mindlin et al., 2003). From vocalization in the songbox there is auditory feedback which plays a critical role in maintaining the song, though the neural correlates of this auditory pathway remain poorly understood (Mooney et al., 2002).

In Figure 3.1 we illustrate the main nuclei involved in both the direct pre-motor pathway from HVC to RA and the indirect connection through the anterior forebrain pathway (AFP) composed of the nuclei Area X, which receives input directly from HVC, the medial nucleus of the dorsolateral thalamus (DLM) which acts as an important relay station receiving inhibition from Area X, and the lateral part of the magnocellular nucleus of the anterior neostriatum (lMAN), which receives input from DLM and projects both to Area X and, as the AFP output, to RA. In addition we show in a dashed line the known, but unexplored, connection from RA to DLM which will play a role in our model for the song system.

The AFP is known to be important in the song development during the sensory learning period when the juvenile bird listens to its tutor and is presumed to make a neural template of his tutor's song. It is also important in the sensorimotor learning phase when the bird listens to his own song and perfects it to resemble the tutor's instructions. If the AFP is lesioned during these periods, completion of learning, called crystallization, occurs prematurely with only poor quality song resulting. If the AFP is lesioned in an adult, following crystallization

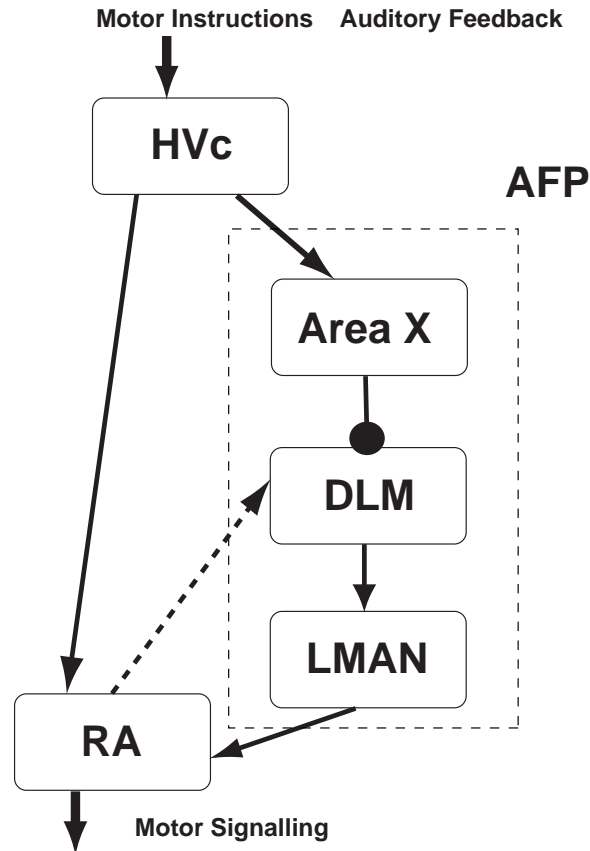


Figure 3.1 Diagram of the pre-motor pathway, HVC and RA nuclei, and the anterior forebrain pathway, AFP, comprised of Area X, DLM, and LMAN. HVC receives motor instructions which are expressed as sparse bursts to RA and to Area X. The AFP is a control and maintenance pathway. Signals from HVC through the AFP arrive at RA with a time delay  $\Delta T \approx 50 \pm 10$  ms. The arrows at the end of lines represent excitatory couplings; the filled circles, inhibitory coupling. The dotted line is a known connection between RA and DLM whose physiological properties are not yet established.

of the song, the song remains relatively stable. If the bird is deafened as an adult, song slowly degenerates, but simultaneous lesioning of LMAN prevents this degeneration (Brainard and Doupe, 2000). This suggests, as noted in (Mooney et al., 2002), that the AFP processes input from HVC to provide a signal to RA which can be variable and sculpting of the song in the juvenile, while retaining a role in maintaining adult song.

Experiments on the action of HVC neurons projecting to RA along the pre-motor pathway show that each HVC neuron fires sparsely, once every motif in

a song or about once every 1000 ms, and during this burst of activity produces  $4.5 \pm 2$  spikes in a time lasting  $6.1 \pm 2$  ms (Hahnloser et al., 2002). HVC also projects processes to Area X, and the evidence is that this signaling is also sparse with, perhaps, three times the frequency of short bursts observed going to RA.

RA acts primarily as a ‘junction box’ processing, in a one-to-many fashion, elementary signals from  $HVC \rightarrow RA$  projection neurons and gathering collections of these signals into population organized instruction signals to the syrinx and to the respiratory system for song production. In this chapter we will suggest another role for RA, namely conveying through a closed feedback loop information about the timing of signals it receives from HVC and the AFP and using this information to direct maintenance of song developed in the sensorimotor phase of learning.

Observations by (Kimpo et al., 2003) have demonstrated that neural activity from the output nucleus of the AFP, the IMAN, and from RA activity has two correlation peaks: one is associated with action in IMAN occurring about 10 ms before it arrives by a known neural pathway to RA, and the other is associated with direct action from HVC arriving at RA followed by a delay of order  $50 \pm 10$  ms associated with the time to traverse the AFP. This result is remarkable as it shows that the coordinated action of the AFP maintains precise timing information about HVC signals even though the signal must pass through several stations of neural action, namely Area X, then DLM, and then IMAN, each of which will involve unreliable synaptic firing.

The measurements of (Kimpo et al., 2003) both suggest that timing is critical in the operation of the song system, shown in Figure 3.1, and that the nuclei in the AFP though composed of numerous, unreliable components might be seen as a coherent, coordinated dynamical system in terms of its role in timing of neural signals reaching RA.

In this chapter we investigate this picture of the song system using the important approximation that cell types in each nucleus, to the extent they are known, can be represented by a small number of excitable nonlinear oscillators represented by conductance based Hodgkin-Huxley (HH) neurons. We will treat HVC as a fundamental signal generator. It will initiate, in a manner not addressed here, sparse bursts of high frequency ( $613 \pm 210$  Hz) spikes projecting to RA and Area X. RA processes these sparse bursts in a fashion that has been explored in (Abarbanel et

al., 2004c), while the AFP relays these sparse bursts to RA producing a time delay  $\Delta T$  whose biophysical origin we will explore.

Using observations on the neural structure of RA (Spiro et al., 1999; Yu and Margoliash, 1996) and the distribution of AMPA and NMDA glutamate receptors at RA (Stark and Perkel, 1999) along with our previously explored biophysical model for synaptic plasticity at AMPA receptors (Abarbanel et al., 2003), we will investigate the change in AMPA channel strength as a function of  $\Delta T$  showing that  $\Delta T \approx 50$  ms is a region where the change in synaptic strength is nearly zero (Abarbanel et al., 2004b).

Then we will examine the biophysical origins of  $\Delta T$  in our model of the AFP and show that such a  $\Delta T$  is attributable to the nature of the inhibition in Area X and in its projections to DLM. Finally, to connect the apparent utility of  $\Delta T \approx 50$  ms at RA neurons in a stabilized song and the dynamically determined  $\Delta T$  in the AFP, we suggest properties for the known RA  $\rightarrow$  DLM connection which would stabilize the complete HVC, RA, AFP system. The connection we propose has not been explored electrophysiologically, and we make suppositions as to its properties. It can be tested in detail experimentally. It provides one way in which the plasticity in RA needed for the development of song instructions in the pre-motor pathway can be informed of the timing in the AFP. We will demonstrate that there are regions of parameters in the AFP network where the full system is stable and could be the source of stable maintenance of the song, and regions where the strength of the HVC $\rightarrow$ RA AMPA connections are systematically, but reversibly weakened permitting the development of other song patterns. Neuromodulators, such as dopamine, may play a role in dictating which regime is selected in various stages of songbird development (Ding and Perkel, 2002; Ding et al., 2003).

Our plasticity model (Abarbanel et al., 2003) was developed in the context of the small observed changes in AMPA conductivity seen in a variety of experiments (Bi and Poo, 1998). There is neither a saturation at high values of the conductivity nor a lower bound at zero conductivity built into the model, as is the case in the synaptic plasticity model proposed in chapter 2. The biological physics of the synaptic strength changes come from the requirement that the conductivity be greater or equal to zero, and that the resources, ‘silent’ AMPA receptors or other biochemical ingredients (Malenka and Nicoll, 1999; Malinow and Malenka,

2002), in the processes leading to conductivity augmentation are bounded.

The synaptic plasticity model we use here does not have these features. Nonetheless, the feedback coupling we identify allowing the AFP to know what  $\Delta T$  is seen by synapses at the RA nucleus leads to finite AMPA conductivity at the HVC  $\rightarrow$  RA synapses. Removing this feedback leads to unbounded growth in the AMPA conductivity in our model. This dynamical stability mechanism may be operating in feedback loops in other neural systems. Since this stability is quite robust to the parameters of the model, in particular to the changes in the excitatory and inhibitory couplings in the network, the principle of stability through feedback in neural networks could have broad application.

The model we develop here for the pre-motor (RA and HVC) nuclei and the AFP (Area X, DLM, and IMAN) nuclei uses conductance based HH models for each node of the network and simplified neurotransmitter dynamics at each connection. We have done our best to reproduce the synaptic and intrinsic currents known from a variety of experimental observations, and this results in a somewhat complex model for the system we study. It is interesting to ask if all this could be simplified. It is likely that we could have used rather simpler spiking neural models in almost all locations in our network as many of the HH neurons need only have the ability to produce action potentials to play their role in the dynamics studied here. However, in at least one instance, namely the detailed dynamics of response in the DLM nucleus, the role of the internal variables of an HH model, namely the activation and inactivation dynamics, performs a key task in determining the timing of signal propagating around the AFP. These internal dynamical variables are absent in most simplified spiking neural models. We have chosen, therefore, to present here a model where the full set of ionic and synaptic currents, as we know them from observations, are represented allowing the internal dynamics to unfold where required and providing a model with a uniform representation of the nuclei in the song system. The details of the currents and the synaptic plasticity model are presented as we develop the dynamics of the system below.

## 3.2 The RA Nucleus: Structure and Plasticity

In this section we first discuss the neural structure of the RA nucleus and our representation of that structure. Then we recall our model of synaptic plasticity (Abarbanel et al., 2003) and apply it to the particular distribution of AMPA and NMDA receptors observed to be present in the adult zebra finch (Stark and Perkel, 1999).

### 3.2.1 RA Structure

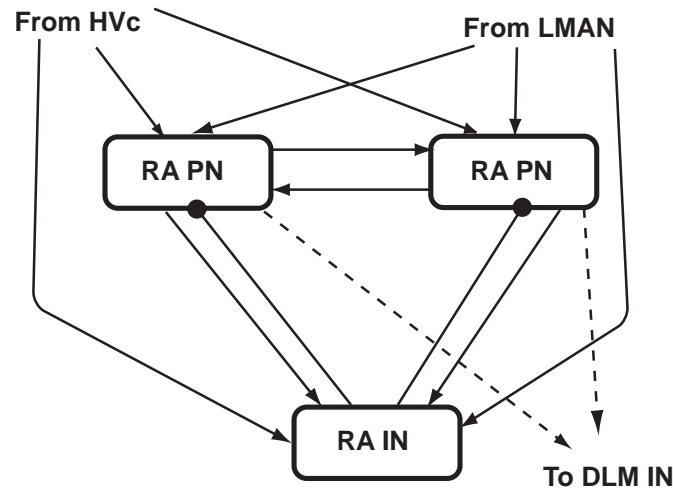
The RA nucleus acts in the main as a ‘junction box’ translating the sparse signals from each RA projecting HVC neuron into instructions to the nonlinear tension of muscles in the syrinx and to the respiratory pressure from the lungs. The correlated application of tension and pressure to the songbox has been shown to be the key driving signals to the songbox in the production of song vocalization (Laje and Mindlin, 2002; Mindlin et al., 2003).

(Spiro et al., 1999) have examined the electrophysiology of neuron types in the RA nucleus. They identified a class of interneurons (INs) which are distinguished morphologically as well as electrophysiologically from RA projection neurons (PNs). The PNs and the INs receive excitatory projections both from HVC along the pre-motor pathway and from lMAN as the output from the AFP. The INs also receive excitatory inputs from the PNs, and the INs, in turn, provide long range GABAergic inhibition to populations of RA-PNs. These populations of PNs project to different sets of motor nuclei which coordinate the respiratory pressure and the nonlinear tension of muscles in the syrinx.

In the absence of input from HVC, and thus from lMAN as its activity is induced by HVC signals into the AFP, the INs are at a resting potential of about  $-66 \pm 3$  mV (Spiro et al., 1999). In the same setting, the PNs are firing nearly periodically at about 15-30 Hz. There is also reported to be a weak mutual excitatory connection among the PNs having their efferents onto the same type of motor nuclei (Private Communication with David Perkel). These connections are weak enough that the PNs appear not to be synchronized. When a burst from HVC arrives at RA, the INs are activated and inhibit the low frequency oscillations of the PNs and allow the PNs to be entrained by the high frequency signal from HVC.



This results in a temporally more precise pattern of PN firing, and this is relayed to vocal and respiratory neural nuclei. The PNs outnumber the INs in RA by an estimated ratio of 30:1.



### Internal Structure of the model RA Nucleus

Figure 3.2 **The structure of the RA nucleus in our model.** RA projection neurons (PN) receive input from both HVC and, through the AFP, from LMAN. RA-PNs are coupled with weak excitation. Populations of RA-PNs project to the syrinx and to the control of the respiratory system. RA interneurons (IN) also receive input from both HVC and LMAN. They receive excitatory signals from the PNs and project back inhibitory couplings. The arborization of the PNs is broad, and it is estimated that the ratio of PNs:INs is about 30:1 (Spiro et al., 1999). Here we represent the RA nucleus with two PNs and one IN. When there is no song input from HVC directly or via the AFP, the PNs are at rest and the INs oscillate at about 15-30 Hz. The output to DLM interneurons is shown in dotted lines. The arrows at the end of lines represent excitatory couplings; the filled circles represent inhibitory coupling.

Our model of the RA nucleus internal structure is shown in Figure 3.2 where we have two PNs and one IN to represent the nucleus. A larger model with order of 100 PNs projecting to muscle control and 100 PNs projecting to respiration control along with 3-5 INs in each population would be required to represent the way the RA nucleus distributes command signals from many HVC to RA projecting neurons and determines the details of syllables in each motif of a song (Abarbanel et al., 2004c). Our focus here is in the mechanisms which control the synaptic plasticity at the HVC  $\rightarrow$  RA junctions, and what we reveal in our calculations will

be operating at each such junction in a larger model. We do not develop a model of song production here, encompassing a discussion of the full matrix of one-to-many HVC  $\rightarrow$  RA connections. Our goal is to understand the dynamics of the synaptic plasticity which can provide stable connections for the fully developed matrix of connections in adult songbirds. Our exploration of the song production through stabilized, and thus fixed over the short term of song production, HVC  $\rightarrow$  RA connections is in (Abarbanel et al., 2004c).

### 3.2.2 RA-PNs

The dynamics of the membrane voltage of the  $j^{\text{th}}$  RA-PN,  $V_{RA-PN_j}(t)$ , is given by ( $j = 1, 2, \dots, N_{RA}; N_{RA} = 2$  here) a standard HH conduction based neuron model along with synaptic currents associated with the other network connections (see Figure 3.2):

$$\begin{aligned}
C_M \frac{dV_{RA-PN_j}(t)}{dt} &= I_{HH}(t, V_{RA-PN_j}(t)) + I_{PN \rightarrow PN_j}(t, V_{RA-PN_j}(t)) \\
&+ I_{HVC-NMDA}(t, V_{RA-PN_j}(t)) + I_{HVC-AMPA}(t, V_{RA-PN_j}(t)) \\
&+ I_{IMAN-NMDA}(t, V_{RA-PN_j}(t)) + I_{IMAN-AMPA}(t, V_{RA-PN_j}(t)) \\
&+ I_{DC-PN_j} + I_{IN \rightarrow PN_j}(t, V_{RA-PN_j}(t))
\end{aligned} \tag{3.1}$$

where  $C_M$  is the membrane capacitance, and the intrinsic HH currents are

$$\begin{aligned}
I_{HH}(t, V(t)) &= g_{Na}m(t)^3h(t)(E_{Na} - V(t)) + g_Kn(t)^4(E_K - V(t)) \\
&+ g_L(E_L - V(t)).
\end{aligned} \tag{3.2}$$

$g_{Na}$ ,  $g_K$  and  $g_L$  are the maximal conductances of the sodium, potassium, and leak channels respectively, and the  $E_{\bullet}$  are reversal potentials. The HH component of above equation is taken to satisfy type I neuron dynamics as presented in chapter 1. The kinetics of the activation and the inactivation variables,  $X(t) = (m(t), h(t), n(t))$ , were modified such that they satisfy the following first order equation,  $\frac{dX(t)}{dt} = \nu[\alpha_X(V)(1 - X(t)) - \beta_X(V)X(t)]$ , with  $\nu = 10$ . The scaling factor of  $\nu$  is used to increase the spiking rate of RA neuron model, as observed in the experimental results (Hahnloser et al., 2002), in response to synaptic input from

HVC.

$I_{DC-PNj}$  is a DC current injected into the RA-PNs. It is set so the autonomous oscillation frequency of the RA-PNs is 15-20 Hz.

The synaptic current due to HVC signals stimulating glutamate to arrive at NMDA receptors is

$$I_{HVC-NMDA}(t, V(t)) = \frac{g_N}{2} S_{N-HVC}(t) B(V(t)) (E_{rev} - V(t)), \quad (3.3)$$

where  $g_N$  is a maximal conductance, and  $B(V)$  is the block of the NMDA receptor (Hille, 2001; Nowak et al., 1984) due to extracellular magnesium ions having concentration  $[Mg^{2+}]$

$$B(V) = \frac{1}{1 + 0.288[Mg^{2+}]e^{-0.062V}}, \quad (3.4)$$

and  $V_{HVC}(t)$  is the voltage of the signal arriving from HVC.

$E_{rev} = 0$  mV is the reversal potential of the excitatory NMDA synapse, and  $S_{N-HVC}(t)$  represents the fraction of open NMDA receptor channels on the post-synaptic RA-PN. To achieve the time course of this process on NMDA receptors we use a two component form for  $S_{N-HVC}(t)$

$$S_{N-HVC}(t) = w_{HVC} S_{N1-HVC}(t) + (1 - w_{HVC}) S_{N2-HVC}(t), \quad (3.5)$$

where the  $S_{Nl-HVC}(t)$   $l = 1, 2$  satisfy

$$\frac{dS_{Nl-HVC}(t)}{dt} = \frac{1}{\tau_{Nl-HVC}} \frac{S_0(V_{HVC}(t)) - S_{Nl-HVC}(t)}{S_{1Nl-HVC} - 1}, \quad (3.6)$$

and  $S_0(V)$  is a ‘step function’ in voltage which rises rapidly from its value of 0, before an action potential appears in  $V$ , to 1 as the action potential arrives, then falls rapidly back to 0. We represent it in our modeling by

$$S_0(V) = 0.5(1 + \tanh(120(V - 0.1))), \quad (3.7)$$

with  $V$  in mV.  $\tau_{Nl-HVC}$  and  $S_{1nl-HVC}$  are two constants determining the docking

and undocking of neurotransmitter represented by  $S_{NI-HVC}(t)$ : neurotransmitter docks with a time constant  $\tau_{NI-HVC}(S_{1nl-HVC} - 1)$  and undocks with a time constant  $\tau_{NI-HVC}S_{1nl-HVC}$ .

This two component model is based on observations by (Stark and Perkel, 1999) who recorded NMDA currents in zebra finches of several different age groups, including adults. They fit these currents with a double exponential decay function and reported fast and slow time constants and the percentage contribution of the slow component. To reflect these measurements we use two processes with different decay time constants. Their measured values for the fast component at HVC-RA synapses were  $20 \pm 7.8$  ms and  $100 \pm 56$  ms for the slow component. The slow component was  $68 \pm 11\%$  of the current. For IMAN-RA NMDA synapses, they observed fast and slow time constants of  $30 \pm 8.6$  ms and  $140 \pm 55$  ms respectively, and  $59 \pm 4.9\%$  slow component.

The synaptic current due to HVC projections to RA associated with AMPA receptors  $I_{HVC-AMPA}(t, V_{RA-PN_j}(t))$  is given by

$$I_{HVC-AMPA}(t, V(t)) = g_{RA}(t)S_{A-HVC}(t)(E_{rev} - V(t)), \quad (3.8)$$

where  $g_{RA}(t)$  is the plastic, time dependent AMPA conductivity determined by our synaptic plasticity dynamics as given below, and  $S_{A-HVC}(t)$  represents the fraction of open AMPA receptors on the postsynaptic RA-PN. It satisfies

$$\frac{dS_{A-HVC}(t)}{dt} = \frac{1}{\tau_A} \frac{S_0(V_{HVC}(t)) - S_{A-HVC}(t)}{S_{1A} - 1}. \quad (3.9)$$

In our model we have taken  $\tau_A = 1.4$  ms and  $S_{1A} = 15/14$  leading to a glutamate docking time constant of 0.1 ms and an undocking time constant of 1.5 ms.

The synaptic current due to IMAN signals at NMDA receptors is

$$I_{IMAN-NMDA}(t, V(t)) = g_N S_{N-IMAN}(t) B(V(t)) \times (E_{rev} - V(t)).$$

$S_{N-IMAN}(t)$  represents the fraction of glutamate docked on the NMDA receptors of the postsynaptic RA-PN. To achieve the time course of this process on NMDA

receptors we use a two component form for  $S_{N-IMAN}(t)$

$$S_{N-IMAN}(t) = (1 - w_{IMAN})S_{N2-IMAN}(t) + w_{IMAN}S_{N1-IMAN}(t), \quad (3.10)$$

where the  $S_{Nl-IMAN}(V(t))$   $l = 1, 2$  satisfy

$$\frac{dS_{Nl-IMAN}(t)}{dt} = \frac{1}{\tau_{Nl-IMAN}} \frac{S_0(V_{IMAN}(t)) - S_{Nl-IMAN}(t)}{S_{1Nl-IMAN} - 1}. \quad (3.11)$$

$\tau_{Nl-IMAN}$  and  $S_{1nl-IMAN}$  are two constants determining the docking and undocking of neurotransmitter represented by  $S_{Nl-IMAN}(t, V(t))$ : neurotransmitter docks with a time constant  $\tau_{Nl-IMAN}(S_{1nl-IMAN} - 1)$  and undocks with a time constant  $\tau_{Nl-IMAN}S_{1nl-IMAN}$ .

In our model we have chosen  $w_{HVC} = 0.21$ ,  $w_{IMAN} = 0.41$ ,  $\tau_{N1-HVC} = 19.75$  ms,  $\tau_{N2-HVC} = 99.75$  ms,  $S_{N1-HVC} = 20/19.75$ ,  $S_{N2-HVC} = 100/99.75$ ,  $\tau_{N1-IMAN} = 29$  ms,  $\tau_{N2-IMAN} = 139$  ms,  $S_{N1-IMAN} = 30/29$ ,  $S_{N2-IMAN} = 140/139$ .

The synaptic current due to IMAN projections to RA associated with AMPA receptors is given by

$$I_{IMAN-AMPA}(t, V(t)) = \frac{g_{RA}(t)}{10} S_{A-IMAN}(t)(E_{rev} - V(t)). \quad (3.12)$$

The relative amounts of NMDA and AMPA receptors at the HVC  $\rightarrow$  RA and IMAN  $\rightarrow$  RA junctions are suggested by the measurements of (Stark and Perkel, 1999).

The current  $I_{IN \rightarrow PN_j}(t, V_{RA-PN_j}(t))$  from the IN to the  $j^{th}$  PN is given as

$$I_{IN \rightarrow PN_j}(t, V_{RA-PN_j}(t)) = g_{RA-IN} S_G(t)(E_{revI} - V_{RA-PN_j}(t)) \quad (3.13)$$

where  $g_{RA-IN}$  is a maximal conductance, and  $E_{revI} = -80$  mV is the inhibitory reversal potential.  $S_G(t)$  represents the percentage of open GABA receptors. It satisfies

$$\frac{dS_G(t)}{dt} = 0.15 \frac{1 - S_G(t)}{1 + e^{-(V_{RA-IN}(t) - 10)/mV}} - 0.2275 S_G(t). \quad (3.14)$$

Finally, the synaptic current to the  $j^{th}$  PN from other PNs is given by

$$I_{PN \rightarrow PN_j}(t, V_{RA-PN_j}(t)) = g_{RA-PN} \sum_{\substack{k=1 \\ k \neq j}}^{N_{RA}} S_{RA-PN_k}(t) \times (E_{rev} - V_{RA-PN_j}(t)), \quad (3.15)$$

with  $g_{RA-PN}$  another maximal conductance and  $S_{RA-PN_j}$  representing the fraction of AMPA receptors docked onto the postsynaptic neuron  $RA - PN_j$ .

### 3.2.3 RA INs

The RA INs are at their resting potential when no song (signal from HVC) is expressed. The membrane voltage of the IN  $V_{RA-IN}(t)$  is determined by

$$\begin{aligned} C_M \frac{dV_{RA-IN}(t)}{dt} = & I_{HH}(t, V_{RA-IN}(t)) + I_{DC-RAIN} + \sum_{j=1}^{N_{RA}} I_{PN_j \rightarrow IN}(t, V_{RA-PN_j}(t)), \\ & + I_{HVC-NMDA}(t, V_{RA-IN}(t)) + I_{HVC-AMPA}(t, V_{RA-IN}(t)) \\ & + I_{IMAN-NMDA}(t, V_{RA-IN}(t)) + I_{IMAN-AMPA}(t, V_{RA-IN}(t)) \end{aligned} \quad (3.16)$$

with the NMDA and AMPA currents as for the RA-PNs (of course, using  $V_{RA-IN}(t)$  in place of  $V_{RA-PN_j}(t)$ ) and

$$I_{PN_j \rightarrow IN}(t, V_{RA-PN_j}(t)) = g_{PN_j-IN} S_{RA-PN_j}(t) (E_{rev} - V_{RA-IN}(t)). \quad (3.17)$$

where  $g_{PN_j-IN}$  is the maximal conductance of the excitatory synaptic current from the RA-PN neurons to the RA-IN, and  $I_{DC-RAIN}$  is a constant DC current injected into the RA-IN neuron.

This completely describes the model RA nucleus used in our work. When there is no signal from HVC or lMAN, the IN is silent at a rest potential of -61.4 mV, and the PN's are oscillating at 20 Hz. This behavior can be seen in Figure 3. When a burst of spikes from HVC arrives (at 475 ms in Figure 3.3), the PNs are strongly inhibited by the INs, while the INs oscillate at a higher frequency in response to the excitation by the burst. As the RA returns to its 'rest' state, the INs slow

down and return to their resting potential.

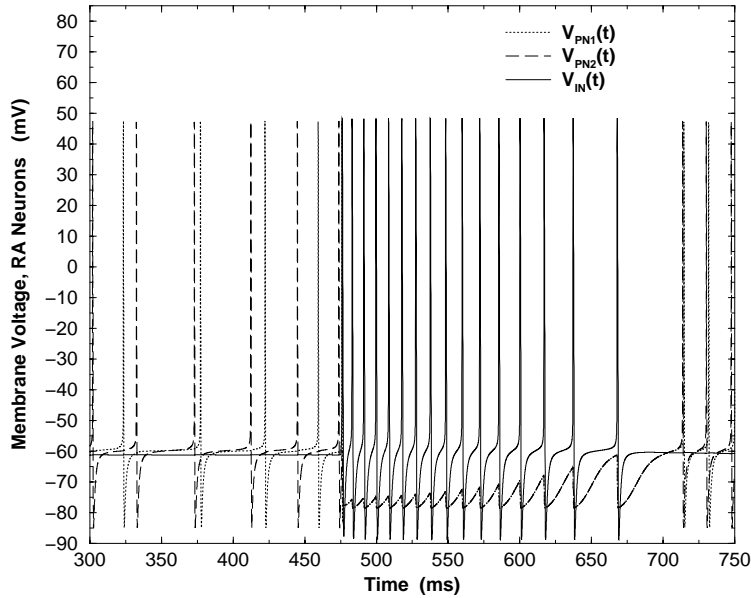


Figure 3.3 Membrane voltages of neurons in the model RA nucleus. Before spikes from HVC arrive at the PNs and IN cells, the IN is at rest at  $-61.4$  mV. The PNs are oscillating autonomously at 20 Hz; they are weakly coupled by mutual excitation, but they do not synchronize. When a burst of five spikes from HVC arrives at 475 ms, the PNs are strongly inhibited and the INs begin spiking at higher frequency. As the nucleus recovers from this input, the IN oscillations decrease in frequency. About 250 ms after the arrival of the HVC signal, the nucleus recovers completely and returns to its original state.

### 3.2.4 Plasticity in RA

The presence of AMPA and NMDA receptors on RA dendrites suggests that they will act to induce long term potentiation or depression, LTP or LTD, through the induction of postsynaptic  $[Ca^{2+}]$  elevation (Yang et al., 1999). In particular, the induction of LTP or LTD through the timing of bursts arriving from HVC and IMAN separated by  $\Delta T$  suggests that mechanisms similar to those operating in

spike timing plasticity (Abarbanel et al., 2003; Bi and Poo, 1998) could be present here. At this time there are no direct measurements of LTP and LTD in the RA cells receiving input from HVC, however, we proceed on the assumption that the dynamics of plasticity seen elsewhere when NMDA and AMPA receptors coexist in a postsynaptic density is appropriate here.

The detailed course of the biochemical pathways induced on elevating intracellular  $[Ca^{2+}]$  in the postsynaptic cells is not settled at this time (Zhabotinsky, 2000). We have introduced a phenomenological model (Abarbanel et al., 2003) which attempts to capture the competition known to exist in these pathways between kinases which augment AMPA conductivity by direct action on AMPA receptors or possibly by causing ‘silent synapses’ from a store in the neuron to be placed into the postsynaptic density and phosphatases which have the opposite effect. Our model posits two intermediate phenomenological variables,  $P(t)$  and  $D(t)$ , which satisfy first order kinetics

$$\begin{aligned}\frac{dP(t)}{dt} &= f_P(Ca(t) - C_0)(1 - P(t)) - \frac{P(t)}{\tau_P} \\ \frac{dD(t)}{dt} &= f_D(Ca(t) - C_0)(1 - D(t)) - \frac{D(t)}{\tau_D},\end{aligned}\quad (3.18)$$

where each variable has a driving function dependent on the departure of the intracellular  $[Ca^{2+}]$  concentration,  $Ca(t)$  from its equilibrium value  $C_0 \approx 100nM$  and taken to be of the form

$$f_k(x) = \frac{x^L}{\xi^L + x^L} \quad k = P, D, \quad (3.19)$$

and  $\tau_P$  and  $\tau_D$  are time constants for the competing processes.

These auxiliary variables are then related to the change in AMPA conductivity at the RA cells via the nonlinear competition

$$\frac{1}{g_0} \frac{dg_{RA}(t)}{dt} = \gamma(P(t)D(t)^\eta - D(t)P(t)^\eta), \quad (3.20)$$

where  $g_0$  is a baseline conductivity and  $\gamma$  and  $\eta$  are dimensionless constants.



The dynamics of the  $[Ca^{2+}]$  time course  $Ca(t)$  is determined by

$$\begin{aligned} \frac{dCa(t)}{dt} &= \frac{C_0 - Ca(t)}{\tau_C} + C_{HVC-NMDA}(t, V(t)) \\ &+ C_{HVC-AMPA}(t, V(t)) + C_{IMAN-NMDA}(t, V(t)) \\ &+ C_{IMAN-AMPA}(t, V(t)), \end{aligned} \quad (3.21)$$

where the first term gives relaxation back to the baseline concentration of  $[Ca^{2+}]$ ,  $C_0$ , with a time constant  $\tau_C = 28$  ms, and the other terms are  $[Ca^{2+}]$  flux terms associated with NMDA and AMPA channels as they receive signals from HVC and IMAN. The voltage  $V(t)$  refers to the membrane potential of the cell where the intracellular  $[Ca^{2+}]$  is located.

These  $[Ca^{2+}]$  fluxes are

$$\begin{aligned} C_{HVC-NMDA}(t, V(t)) &= g_{NC}S_{N-HVC}(t)B(V(t))(E_{rev} - V(t)) \\ C_{HVC-AMPA}(t, V(t)) &= g_{AC}S_{A-HVC}(t)(E_{rev} - V(t)) \\ C_{IMAN-NMDA}(t, V(t)) &= g_{NC}S_{N-IMAN}(t)B(V(t))(E_{rev} - V(t)) \\ C_{IMAN-AMPA}(t, V(t)) &= g_{AC}S_{A-IMAN}(t)(E_{rev} - V(t)) \end{aligned} \quad (3.22)$$

The intracellular voltages and the innervation from HVC and IMAN determine  $Ca(t)$ , and from the phenomenological model of AMPA conductance changes we determine  $g_{RA}(t)$ .

This model has been tested against the observations of LTP and LTD using a variety of induction protocols: spike timing (Bi and Poo, 1998), presentation of high frequency bursts to the presynaptic terminal (Bliss and Collingridge, 1993), and action potentials presented to the presynaptic terminal when the postsynaptic neuron is depolarized at various levels (Malinow and Malenka, 2002). To our knowledge at this time there is no direct observation of synaptic potentiation or depression at the HVC  $\rightarrow$  RA junctions.

When we present a burst of five spikes with ISIs = 2 ms from HVC to this model of the RA nucleus and  $\Delta T$  later present one, three or five spikes with the same ISIs from IMAN, we find, using our plasticity model along with the observed ratios of NMDA and AMPA receptors at the HVC and IMAN terminals (Stark and Perkel, 1999), curves for the  $\Delta g_{RA}$  versus  $\Delta T$  dependence such as that presented

in Figure 3.4. This result has  $N_{HVC} = 5$ ,  $N_{IMAN} = 5$  spikes, but the results are essentially the same for  $N_{HVC} = 5$  and  $N_{IMAN} = 1$  or 3 (Abarbanel et al., 2004b).

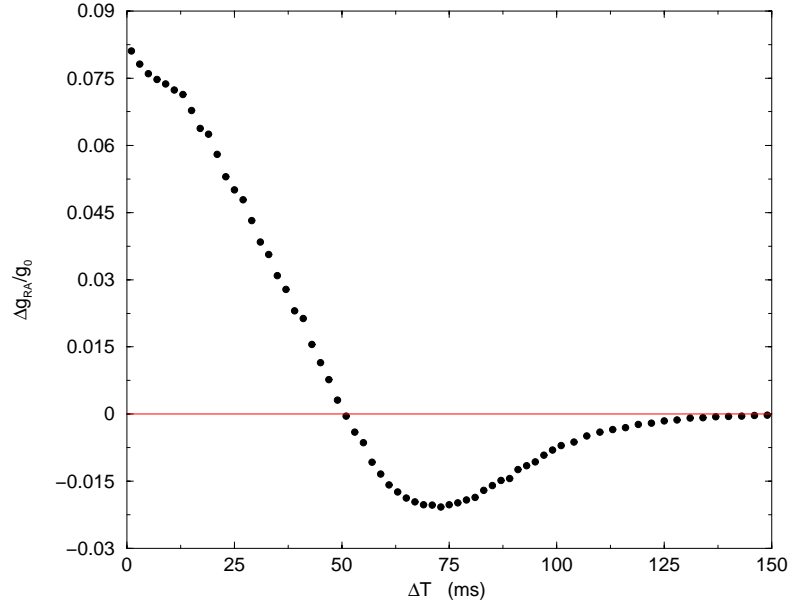


Figure 3.4 Using our biophysical model of synaptic plasticity, we evaluate the change in AMPA conductivity  $\frac{\Delta g_{RA}}{g_0}$  at the HVC  $\rightarrow$  RA connections due to signals arriving from HVC followed by signals arriving from IMAN  $\Delta T$  later. In this figure the HVC signal was a burst of five spikes with Interspike intervals (ISI) of 2 ms. A burst of five spikes with ISI = 2 ms arrives from IMAN  $\Delta T$  later. The zero in  $\frac{\Delta g_{RA}}{g_0}$  near  $\Delta T \approx 50$  ms represents potentially stable plasticity in RA, and thus a potentially stable set of connections in the song pre-motor pathway. Lesions of the AFP would result in  $\Delta T \rightarrow \infty$  which is also a region of  $\frac{\Delta g_{RA}}{g_0} = 0$ .

The most striking feature of this result is the zero in  $\frac{\Delta g_{RA}}{g_0}$  near  $\Delta T = 50$  ms. This is on the order of the observed delay of signals from HVC between their direct path to RA along a pre-motor route and their indirect path to RA through the AFP. The appearance of this zero is very suggestive of a role for the AFP coupled with observed synaptic plasticity dynamics as the determinant of HVC  $\rightarrow$  RA synaptic strengths. When  $\frac{\Delta g_{RA}}{g_0} = 0$ , there is the opportunity for stability in these connections which would be associated with stable song since it is the instructions from HVC through these junctions in RA which determines the population control

of tension in the syrinx and the respiratory pressure. At this stage we have no way to establish the stability of this zero, but in the next sections we will address that.

There is another zero of  $\frac{\Delta g_{RA}}{g_0}$  which is when  $\Delta T \rightarrow \infty$ . If one were to lesion nuclei of the AFP, this would result in this value for  $\Delta T$  as no signals could traverse the AFP from HVC to reach RA. Lesioning AFP nuclei is known to result in little change in adult birdsong, so this zero also has an attractive role in explaining observations in the song system.

### 3.3 The Anterior forebrain pathway; Structure and its function in producing delay $\Delta T$

Our model of the AFP elaborates on structure in the Area X nucleus and the DLM nucleus based on observations about the excitatory and inhibitory connections within them and on electrophysiological measurements of cells in each nucleus (Farries and Perkel, 2000; Farries and Perkel, 2002; Luo and Perkel, 1999b; Luo and Perkel, 1999a; Luo et al., 2001; Luo and Perkel, 2002). Area X will be partly represented by a spiny neuron (SN) which receives the input from HVC signals. Absent these signals it is at rest. The other cell in the Area X representation is an aspiny, fast firing neuron (AF) which oscillates at 15- 30 Hz when there is no input from HVC. The DLM is represented by a projection neuron which receives inhibition from the AF and projects to IMAN. There is also a DLM interneuron which receives input from RA and in turn inhibits the DLM PN.

#### 3.3.1 Area X

Our representation of Area X is shown in Figure 3.5. Two classes of neuron are observed in Area X (Farries and Perkel, 2000; Farries and Perkel, 2002). We discuss them separately now.

##### The SN Neuron

The SN is represented by a standard HH model of type II (Figure 1.3) with Na, K, and leak currents; a DC current is also present in the model. SN receives

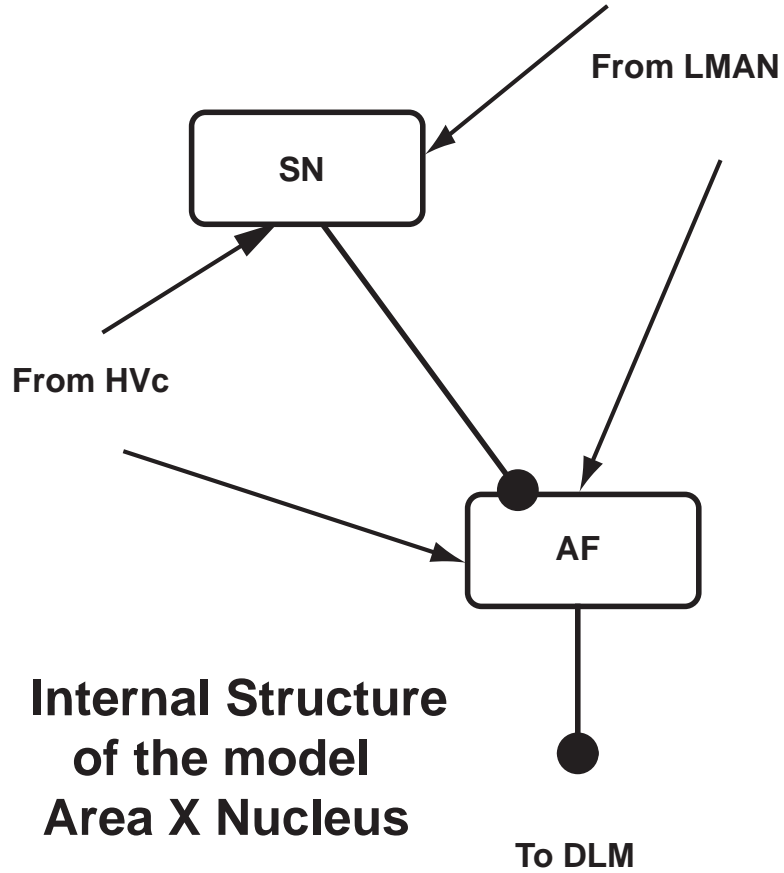


Figure 3.5 **The structure of the Area X nucleus in our model.** Spiny neurons (SN) receive input from both HVC and LMAN. In turn the SN inhibits the aspy, fast firing neurons (AF). The AFs project inhibition to DLM. When there is no song input from HVC, the SNs are at rest and the AFs oscillate at about 15-30 Hz. The arrows at the end of lines represent excitatory couplings; the filled circles, inhibitory coupling. When the AFs are active, they inhibit DLM action. On activation the SNs inhibit the AF neurons, and with the release of AF  $\rightarrow$  DLM, the DLM neurons can rebound and fire. The HVC  $\rightarrow$  AF connection resets the AF oscillations resulting in the SN  $\rightarrow$  AF inhibition release of DLM becoming time coordinated with the arrival of a burst from HVC.

input from HVC and from LMAN. The dynamics of the  $V_{SN}(t)$  follows:

$$\begin{aligned}
 C_M \frac{dV_{SN}(t)}{dt} &= I_{HH-AFP}(t, V_{SN}(t)) + I_{DC-SN}, \\
 &+ [g_{HVC-SN} S_{A-HVC}(t) + g_{LMAN-SN} S_{A-HVC}(t)] \\
 &\times (E_{rev} - V_{SN}(t))
 \end{aligned} \tag{3.23}$$

where

$$\begin{aligned}
I_{HH-AFP}(t, V(t)) &= g_{Na}m_{AFP}(t)^3h_{AFP}(t)(E_{NA} - V(t)) + g_Kn_{AFP}(t)^4(E_K - V(t)) \\
&+ g_L(E_L - V(t)), \tag{3.24}
\end{aligned}$$

is the familiar set of HH currents with type II neuron dynamics as presented in chapter 1.

### The AF Neuron

The membrane voltage  $V_{AF}(t)$  of the AF neuron is determined by the standard HH ion currents plus inhibitory input from the SN and excitation from HVC and from lMAN:

$$\begin{aligned}
C_M \frac{dV_{AF}(t)}{dt} &= I_{HH-AFP}(t, V_{AF}(t)) + g_{SN-AF}S_{A-SN}(t)(E_{revI} - V_{AF}(t)) + I_{DC-AF} \\
&+ [g_{HVC-SN}S_{A-HVC}(t) + g_{lMAN-SN}S_{A-lMAN}(t)] \\
&\times (E_{rev} - V_{AF}(t)), \tag{3.25}
\end{aligned}$$

and  $I_{DC-AF}$  is chosen so that the AF neuron, absent inhibitory input from SN, oscillates at 15-30 Hz.

### 3.3.2 DLM

DLM also exhibits two classes of neuron (Luo and Perkel, 2002). The first, called type I by Luo and Perkel (Luo and Perkel, 1999a; Luo and Perkel, 2002) (not associated with the dynamic type I neuron model discussed in this thesis), is a projection neuron which receives inhibition from the AF in Area X and projects excitation to lMAN. It has characteristics of thalamic neurons (McCormick and Pape, 1990; McCormick and Huguenard, 1992) including indications of the presence of the current  $I_h$ . These type I cells also exhibit a high frequency sequence of action potentials when depolarized by currents of order 100 pA. Luo and Perkel show that it is probably associated with a  $[Ca^{2+}]$  dependent current. They suggest one could expect this from the interaction of the low threshold  $[Ca^{2+}]$  current  $I_T$  with  $I_h$ ; our model for the type I cells has both. In addition to the type I cells,

which we call the DLM PNs, there is a type II cell (not associated with the dynamical type II neuron described in this thesis), which we call the DLM INs. These do not exhibit  $[Ca^{2+}]$  spikes.

Our model of the DLM is illustrated in Figure 3.6. The dashed line shows the RA  $\rightarrow$  DLM projection we address in the next Section.

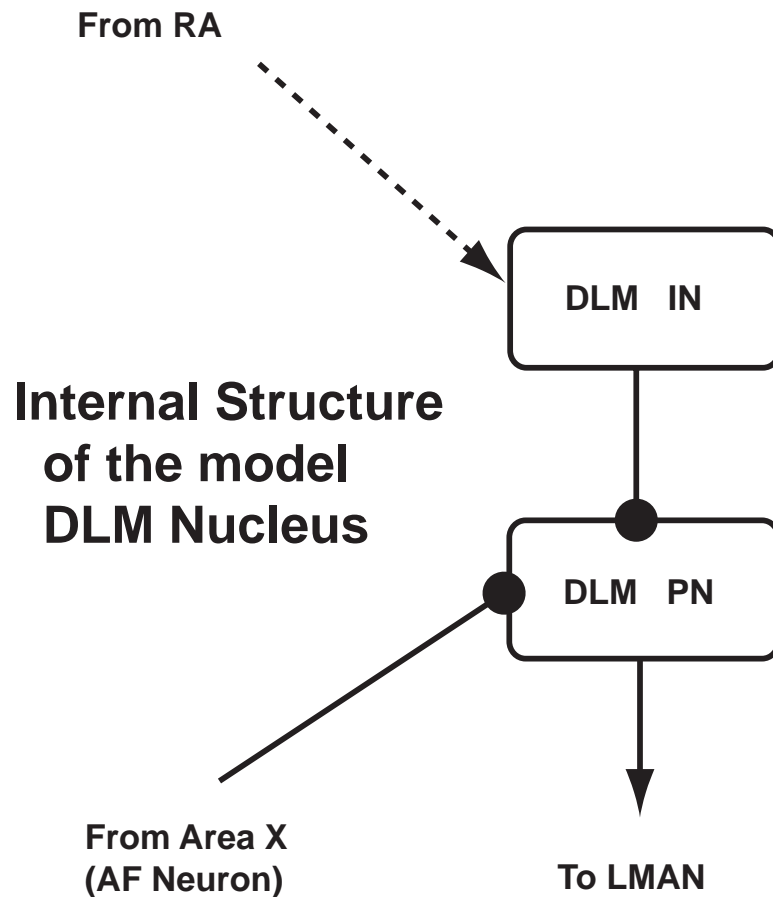


Figure 3.6 **The structure of the DLM nucleus in our model.** The arrows at the end of lines represent excitatory couplings; the filled circles, inhibitory coupling. The DLM PN receives inhibitory input from the Area X AF neurons. It projects excitatory processes to LMAN. In our model, input from RA excites the DLM INs which project inhibition to the DLM PNs.

### The DLM Projection Neuron: DLM-PN

This neuron is taken to satisfy the equation for its membrane voltage  $V_{DLMPN}(t)$

$$\begin{aligned}
C_M \frac{dV_{DLMPN}(t)}{dt} &= I_{HH-AFP}(t, V_{DLMPN}(t)) + I_h(t, V_{DLMPN}(t)) + I_T(t, V_{DLMPN}(t)) \\
&+ I_{AF-DLMPN}(t, V_{DLMPN}(t)) + I_{DLMIN-DLMPN}(t, V_{DLMPN}(t)) \\
&+ I_{DC-DLMPN}
\end{aligned} \tag{3.26}$$

where

$$\begin{aligned}
I_h(t, V_{DLMPN}(t)) &= g_h m_h(t) (E_h - V_{DLMPN}(t)), \\
I_T(t, V_{DLMPN}(t)) &= g_T m_c(t) h_c(t) GHK(V_{DLMPN}(t)), \\
I_{t,AF-DLMPN}(t, V_{DLMPN}(t)) &= g_{AF-DLMPN} S_{A-AF}(t) (E_{revI} - V_{DLMPN}(t)), \\
I_{DLMIN-DLMPN}(t, V_{DLMPN}(t)) &= g_{DLMIN-DLMPN} S_{G-DLMIN}(t) \\
&\times (E_{revI} - V_{DLMPN}(t))
\end{aligned} \tag{3.27}$$

In these expressions we have the Goldman-Hodgkin-Katz expression

$$GHK(V) = -V \frac{1 - \frac{[Ca^{2+}]_o}{[Ca^{2+}]_i} e^{-V/12.9}}{1 - e^{-V/12.9}}, \tag{3.28}$$

where the ratio of extracellular  $[Ca^{2+}]$ ,  $[Ca^{2+}]_o$ , to intracellular  $[Ca^{2+}]$ ,  $[Ca^{2+}]_i$ , appears. This ratio is taken to be 40,000 in our calculations.

The activation and inactivation variables  $U(t) = m_h(t), m_c(t), h_c(t)$  satisfy the first order kinetic equations

$$\frac{dU(t)}{dt} = \frac{m_{U0}(V(t)) - U(t)}{\tau_U(V(t))}, \tag{3.29}$$

where  $V(t)$  is the membrane voltage of the cell, and, with  $\tau_U(V)$  in ms and  $V$  in mV,

$$\begin{aligned}
m_{c0}(V) &= \frac{1}{1+e^{-(V+60)/6.2}} & \tau_{m_c}(V) &= 0.612 + \frac{1}{e^{-(131+V)/16.7} + e^{-(16.8+V)/12.9}} \\
h_{c0}(V) &= \frac{1}{1+e^{(84+V)/4.03}} & \tau_{h_c}(V) &= \begin{cases} e^{(467+V)/66.6} & \text{if } V \leq -80 \text{ mV} \\ 28 + e^{-(28.8+V)/10.2} & \text{if } V > -80 \text{ mV} \end{cases} \\
m_{h0}(V) &= \frac{1}{1+e^{(V+75)/5.5}} & \tau_h(V) &= 0.612 + \frac{1}{e^{-(V+131.6)/16.7} + e^{(V+16.8)/18.2}}
\end{aligned}$$

### The DLM Interneuron: DLM-IN

The membrane potential  $V_{DLMIN}(t)$  is taken to satisfy the ordinary HH model with synaptic currents from RA:

$$\begin{aligned}
C_M \frac{dV_{DLMIN}(t)}{dt} &= I_{HH-AFP}(t, V_{DLMIN}(t)) + I_{DC-DLMIN} \\
&+ I_{RA-DLMIN}(t, V_{DLMIN}(t)),
\end{aligned} \tag{3.30}$$

with

$$I_{RA-DLMIN}(t, V_{DLMIN}(t)) = g_{RA-DLMIN} \sum_{k=1}^{N_{RA}} S_{RA-PNk}(t) (E_{revI} - V_{DLMIN}(t)) \tag{3.31}$$

### 3.3.3 The IMAN Nucleus

The membrane voltage of our IMAN nucleus  $V_{IMAN}(t)$ , see Figure 3.1, is represented by the HH model plus synaptic input from DLM:

$$C_M \frac{dV_{IMAN}(t)}{dt} = I_{HH-AFP}(t, V_{IMAN}(t)) + I_{DC-IMAN} + I_{DLMPN-IMAN}(t, V_{IMAN}(t)), \tag{3.32}$$

with

$$I_{DLMPN-IMAN}(V_{IMAN}(t)) = g_{DLMPN-IMAN} S_{A-DLMPN}(t) (E_{rev} - V_{IMAN}(t)) \tag{3.33}$$



### 3.4 Model Parameters

1. **RA Projection Neurons** As discussed earlier the kinetics of activation and inactivation of sodium and potassium currents in our model of RA neurons were modified from a model of hippocampal pyramidal neurons (Traub and Miles, 1991). We have used faster kinetics to emulate the spiking behavior of RA projection neurons, in response to synaptic input from HVC neurons. The following are the parameters used for the HH type model used for RA projection neurons.  $C_M = 1\mu F/cm^2$ ,  $g_{Na} = 215 \frac{mS}{cm^2}$ ,  $g_K = 43 \frac{mS}{cm^2}$ ,  $g_L = .83 \frac{mS}{cm^2}$ ,  $E_L = -65mV$ ,  $E_{Na} = 50mV$ ,  $E_K = -95mV$ .

NMDA currents of the synapses from HVC and IMAN were two component models which reproduce the observed fast and slow decay times as seen by Stark and Perkel (Stark and Perkel, 1999).  $g_N = .75 \frac{mS}{cm^2}$  represents the strength of NMDA synapse from HVC onto RA which is 10 times the strength of NMDA synapse onto RA from IMAN. The percentage contributions of the fast NMDA component of the synaptic connections from HVC and IMAN were  $w_{HVC} = .21$  and  $w_{IMAN} = .41$ , respectively. The fast and slow NMDA decay time constants of the synaptic connections from HVC were  $\tau_{N1-HVC} = 19.75ms$  and  $\tau_{N2-HVC} = 99.75ms$ , respectively; while that for synaptic connections from IMAN were  $\tau_{N1-IMAN} = 29ms$  and  $\tau_{N2-IMAN} = 139ms$ . The constants characterizing rise times for the two NMDA components for the HVC to RA synapse were  $S_{N1-HVC} = 20/19.75$  and  $S_{N2-HVC} = 100/99.75$ , while for the IMAN to RA synapse were  $S_{N1-IMAN} = 30/29$  and  $S_{N2-IMAN} = 140/139$ . The extracellular magnesium concentration was chosen to be  $[Mg^{2+}] = 1mM$  which is a standard value (Koch, 1999). The maximal conductance and reversal potential of the inhibitory GABAergic synaptic connections from RA interneurons were  $g_{RA-IN} = 15 \frac{mS}{cm^2}$  and  $E_{revI} = -80mV$ . Weak coupling between the RA projection neurons was characterised by  $g_{RA-PN} = .05 \frac{mS}{cm^2}$  representing the fact that spontaneous oscillatory behavior of RA projection neurons are unsynchronized. The DC currents  $I_{DC-PN1} = I_{DC-PN2} = 1.93 \frac{\mu A}{cm^2}$ , were required to obtain the approximately 20 Hz spontaneous spiking behaviour observed in RA projection neurons.

2. **RA Interneurons** The passive and active membrane parameters of the RA interneuron were the same as those of RA projection neurons:  $C_M = 1\mu F/cm^2$ ,  $g_{Na} = 215 \frac{mS}{cm^2}$ ,  $g_K = 43 \frac{mS}{cm^2}$ ,  $g_L = .83 \frac{mS}{cm^2}$ ,  $E_L = -65mV$ ,  $E_{Na} = 50mV$ ,  $E_K = -95mV$ .  $w_{HVC} = .21$ ,  $w_{IMAN} = .41$ ,  $\tau_{N1-HVC} = 19.75ms$ ,  $\tau_{N2-HVC} = 99.75ms$ ,  $\tau_{N1-IMAN} = 29.ms$ ,  $\tau_{N2-IMAN} = 139ms$ ,  $S_{N1-HVC} = 20/19.75$ ,  $S_{N2-HVC} = 100/99.75$ ,  $S_{N1-IMAN} = 30/29$ ,  $S_{N2-IMAN} = 130/129$ , and  $[Mg^{2+}] = 1mM$ . The maximal conductance of the synaptic connections from the RA projection neurons on to the interneurons was  $g_{PNj-IN} = .01 \frac{mS}{cm^2}$ . The injected DC current was  $I_{DC-RAIN} = 1.6 \frac{\mu A}{cm^2}$ ; this is below threshold for spontaneous oscillations of these RA INs.
3. **Area X Spiny Neurons, SN** The kinetics of the activation and inactivation of the sodium and potassium currents in our model of area X spiny neurons and other AFP neurons were those of Hodgkin and Huxley (Koch, 1999). The following parameters were used for HH model used to describe Area X Spiny Neurons.  $C_M = 1\mu F/cm^2$ ,  $g_{Na} = 20 \frac{mS}{cm^2}$ ,  $g_K = 6.2 \frac{mS}{cm^2}$ ,  $g_L = .03 \frac{mS}{cm^2}$ ,  $E_L = -49.4mV$ ,  $E_{Na} = 50mV$ ,  $E_K = -99mV$ . The maximal conductances of the synaptic connection from HVC and IMAN were  $g_{HVC-SN} = g_{IMAN-SN} = .4 \frac{mS}{cm^2}$ . These are adjusted so a spike in HVC/IMAN is propagated to SN with delay of the order of 3-5 ms. The injected DC current was  $I_{DC-SN} = -.55 \frac{\mu A}{cm^2}$ ; this is below threshold for oscillation.
4. **Area X Aspiny Fast Firing Neurons, AF** The passive and active membrane parameters of the HH model representing AF neurons were same as that for SN neurons,  $C_M = 1\mu F/cm^2$ ,  $g_{Na} = 20 \frac{mS}{cm^2}$ ,  $g_K = 6.2 \frac{mS}{cm^2}$ ,  $g_L = .03 \frac{mS}{cm^2}$ ,  $E_L = -49.4mV$ ,  $E_{Na} = 50mV$ ,  $E_K = -99mV$ . The DC current,  $I_{DC-AF} = -.146 \frac{\mu A}{cm^2}$ , was adjusted so the AF neuron spontaneously spikes at about 20 Hz. The maximal conductance of the GABAergic synaptic connection from the SN was  $g_{SN-AF} = g_I \frac{mS}{cm^2}$ , where  $g_I = g_E R_{IE}$ ,  $g_E = .4 \frac{mS}{cm^2}$ , and  $R_{IE}$  varies as indicated in the text.
5. **DLM projection neuron: DLM-PN** The passive parameters and sodium and potassium currents of the type I DLM neuron were the same as those other AFP neurons:  $C_M = 1 \mu F/cm^2$ ,  $g_{Na} = 20 \frac{mS}{cm^2}$ ,  $g_K = 6.2 \frac{mS}{cm^2}$ ,  $g_L = .03$

$\frac{mS}{cm^2}$ ,  $E_L = -49.4mV$ ,  $E_{Na} = 50mV$ , and  $E_K = -99mV$ . In addition, these neurons contain the hyperpolarization-activated current  $I_h$  and the low-threshold  $Ca^{2+}$  current  $I_T$ . The maximal conductance of  $I_h$  and  $I_T$  were chosen as  $g_h = .045 \frac{mS}{cm^2}$ , and  $g_T = 3.775 \times 10^{-5} \frac{mS}{cm^2}$ , respectively. The equilibrium ratio of extracellular to intracellular calcium was taken to be  $\frac{[Ca^{2+}]_o}{[Ca^{2+}]_in} = 40,000$  (Hille, 2001). The maximal conductance of the GABAergic synaptic connection from the DLM-IN neuron was  $g_{DLMIN-DLMPN} = 4.0 \frac{mS}{cm^2}$ , and the maximal conductance of the GABAergic synaptic connection from the AF was  $g_{AF-DLMPN} = g_I mS/cm^2$ , where  $g_I = g_E R_{IE}$ ,  $g_E = .4 \frac{mS}{cm^2}$ , and  $R_{IE}$  varies as indicated in the text.

6. **DLM interneuron: DLM-IN** The passive and active membrane parameters of the DLM-IN neuron were the same as those of spiny, AF, and IMAN neurons:  $C_M = 1 \mu F/cm^2$ ,  $g_{Na} = 20 \frac{mS}{cm^2}$ ,  $g_K = 6.2 \frac{mS}{cm^2}$ ,  $g_L = .03 \frac{mS}{cm^2}$ ,  $E_L = -49.4mV$ ,  $E_{Na} = 50mV$ , and  $E_K = -99mV$ . The injected DC current was  $I_{DC-AF} = -.55 \frac{\mu A}{cm^2}$ . The maximal conductance of the synaptic connections from the RA projection neurons was  $g_{RA-DLMIN} = 4.0 \frac{mS}{cm^2}$ . The value of this coupling term was chosen so activity changes in RA projection neurons are rapidly transmitted to the DLM-IN neuron through the excitatory coupling.
7. **IMAN Neuron** The role for IMAN in this model is just to act as relay neuron transmitting the response of DLM firing timings back to RA as output of AFP loop. The parameters of the HH model for IMAN are the same as that used for other AFP neurons:  $C_M = 1 \mu F/cm^2$ ,  $g_{Na} = 20 \frac{mS}{cm^2}$ ,  $g_K = 6.2 \frac{mS}{cm^2}$ ,  $g_L = .03 \frac{mS}{cm^2}$ ,  $E_L = -49.4mV$ ,  $E_{Na} = 50mV$ , and  $E_K = -99mV$ . The injected DC current was  $I_{DC-IMAN} = -.55 \frac{\mu A}{cm^2}$ , while the maximal conductance of the synaptic connections from the DLM-PN neuron was  $g_{DLMPN-IMAN} = .04 \frac{mS}{cm^2}$ .
8. **Synaptic Plasticity Model** Our model of synaptic plasticity at HVC-RA synapses was the same model we have used previously (Abarbanel et al., 2003). The intracellular  $Ca^{2+}$  concentration was scaled to the equilibrium resting value  $C_0 = 100nM$ , for convenience. The  $Ca^{2+}$  decay time constant was set to  $\tau_C = 28ms$ , rather than 80 ms as in our earlier paper, to better

approximate recent experimental data (Sabatini et al., 2001). The parameters of our plasticity model were taken from our earlier results (Abarbanel et al., 2003): the decay time constants for our phenomenological variables  $P(t)$  and  $D(t)$  were  $\tau_P = 10ms$  and  $\tau_D = 30ms$ , respectively. The constants in the driving functions of  $P(t)$  and  $D(t)$  are  $L = 4$ ,  $M = 8$ , and  $\xi = 6.75$ . The constants in our nonlinear competition between  $P(t)$  and  $D(t)$  were  $\gamma = 1$  and  $\eta = 4$ . The constants controlling the influx of  $Ca^{2+}$  through NMDA and AMPA receptors at the HVC-RA synapses were  $g_{NC} = .057mV^{-1}$  and  $g_{AC} = 10^{-6}mV^{-1}$ , respectively.

This completes the description of the network model for the song system. We now explore the dynamics of the AFP in producing delays  $\Delta T \approx 50 \pm 10$  ms and its function in modulating the synaptic connection from HVC to RA through the synaptic plasticity rule.

### 3.4.1 Determining $\Delta T$

The description of the neurons in our representation of the AFP is now complete. In a realistic model of the song system one would replicate these ingredients many times over to form a larger network which has the possibility of describing the heterogeneity of the nuclei in the RA as well as the richness of RA. Our focus in this chapter is on the dynamics of each of these copies of the RA and AFP circuitry and their role in the timing of signals arriving at RA. It is in the spirit of (Kimpo et al., 2003) where the nuclei of the AFP appear to act in a coherent manner in transmitting timing information about HVC bursts to RA that we argue that our, clearly coarse grained, approximation is appropriate.

We treat the HVC nucleus as a signal generator which produces sparse bursts of spikes. The internal dynamics of the HVC is set aside now. A burst of five spikes from HVC is presented to the SN neuron in Area X, and using our model of the AFP, we evaluate the time  $\Delta T$  it takes for the IMAN nucleus to fire an action potential.  $\Delta T$  depends on the parameters in the model AFP.

An important parameter in determining  $\Delta T$  is the strength of the inhibitory connection between the AF neuron in Area X and the projection neuron DLM nucleus,  $g_{AF-DLMPN}$ . We establish a baseline value for this in building the AFP,

and then explore the ratio of this value to the baseline choice; we call this ratio  $R = \frac{g_{AF-DLMPN}}{g_{AF-DLMPN-Baseline}}$ .  $R$  is critical in our model as it is modified by the input from RA which we introduce shortly. As input from RA to the DLM nucleus comes through exciting the DLM interneuron which inhibits the DLM projection neuron, the strength of the RA signal effectively determines the effective strength of the inhibition of the DLM projection neuron.

By applying GABA antagonists to nucleus DLM, one can directly influence  $R$ . This suggests an experiment directly along the lines of Kimpo, *et al* (Kimpo et al., 2003) which measures  $\Delta T$  as a function of  $R$ .

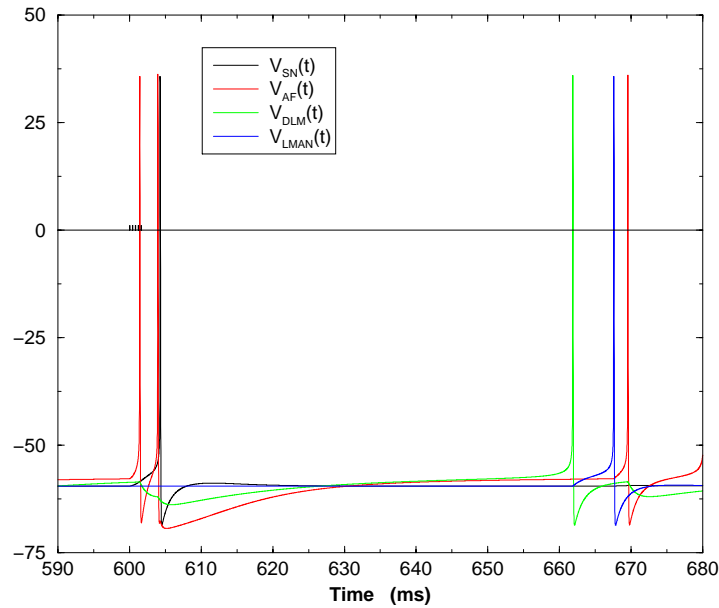


Figure 3.7 The time course of membrane voltages in the AFP neurons after a burst of five spikes with  $ISI = 2$  ms arrives at SN from HVC at time 600 ms. Before the HVC burst arrives at SN, SN is at rest near -66 mV, and AF is oscillating at 20 Hz. AF activity inhibits the DLM projection neuron which shows small variations around rest with the same period as the AF. After the burst from HVC excites SN, it inhibits AF, and then DLM recovers from its inhibition to fire about 67.5 ms later. The action potential in DLM excites IMAN.

In Figure 3.7 we present a typical time course for the response of the AFP

following presentation of five HVC spikes with  $ISI = 2$  ms at time 600 ms. Before these spikes arrive at the SN neuron, the AF is firing periodically at 20 Hz. This “resting” activity of AF inhibits the DLMPN which responds with small variations around its rest potential of  $\approx -65$  mV. The excitation of SN by the arrival of the HVC burst inhibits AF which, in turn, releases the DLMPN. AF is also excited by this HVC burst, and this resets the AF oscillation effectively synchronizing the HVC arrival time and the time of inhibition of AF by SN. The DLMPN then recovers from its hyperpolarized state and fires an action potential about 67 ms after the HVC burst arrives at SN followed shortly thereafter, at about 71 ms by an action potential in lMAN. This last action potential corresponds to the correlation observed by (Kimpo et al., 2003).

Figure 3.8 explores in a bit more detail what is happening to make the response of the DLMPN appear so long after the action potential in SN inhibits AF and releases the DLMPN. Here we see the burst of five HVC spikes with  $ISI = 2$  ms arrive at time 800 ms. In the top panel we show the spikes at 800 ms as well as the activation  $m_{DLM}(t)$  and inactivation  $h_{DLM}(t)$  variables for the Na channel in the DLMPN. Because the DLMPN is hyperpolarized by the inhibitory action of the AF periodic firing, it undergoes a slow recovery before firing an action potential. In the lower panel we show the DLMPN and lMAN action potentials associated with this burst from HVC arriving at SN. The time delay  $\Delta T$  for this event is  $\approx 63$  ms. In Figure 3.9 we plot the variation of  $\Delta T$  as a function of  $R$  in our model AFP. It will turn out to be quite important that both positive and negative slopes appear in this result. The positive slopes of  $\Delta T(R)$  will be associated with stability in the synaptic plasticity dynamics at RA. The value of  $R$  can be affected by introducing antagonists to the GABA (inhibitory) connections within the DLM. In principle, therefore, one can experimentally explore a curve similar to Figure 3.9.

### 3.4.2 The Role of Inhibition from X $\rightarrow$ DLM

The inhibition in projections from Area X to DLM cells is well established, and if one looks at the overall block diagram of the AFP as represented in Figure 3.1, we see it is the only internuclear inhibition in the AFP. It is interesting to ask what would happen if we replaced this inhibitory coupling with an excitatory

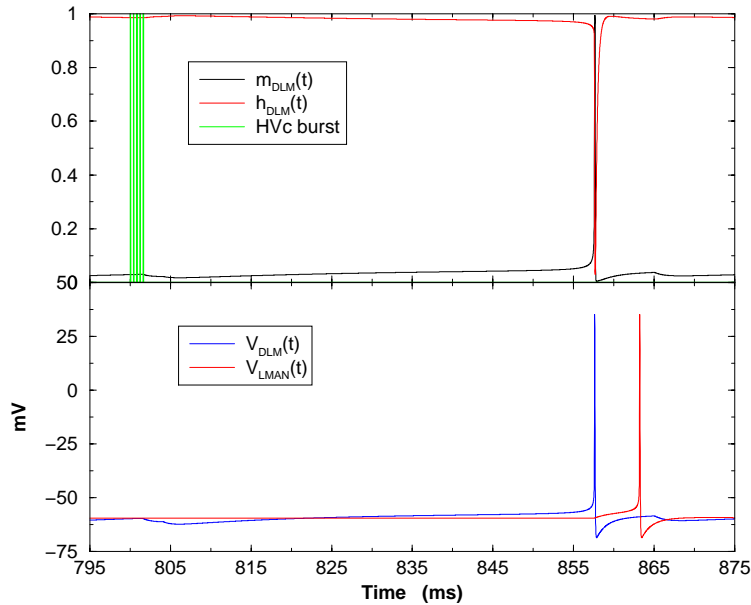


Figure 3.8 **UPPER PANEL** we show the activity in the DLM PN of the Na activation variable,  $m_{DLM}(t)$  and inactivation variable,  $h_{DLM}(t)$  following a burst of 5 spikes arriving at SN (in Area X) at time 800 ms. This indicates that the long time delay associated with the AFP is manifested in the slow recovery of the DLM PN from its hyperpolarization due to inhibition from the AF neuron in Area X. When this inhibition is released, the DLM PN responds with a spike as the activation variable slowly rises from 0 in the neuron's hyperpolarized state. **LOWER PANEL** we have the same time axis and show the membrane voltage in the DLM projection neuron and in the IMAN neuron innervated by the DLM PN firing. The DLM PN fires about 60 ms after the HVC burst arrives at SN, and the IMAN neuron fires about 63 ms after the HVC burst innervates SN.

connection. We did that by changing the reversal potential in the AF  $\rightarrow$  DLM connection from -75 mV to 0 mV, leaving all else in the circuit the same. A typical result of this change is seen in Figure 3.10 where a burst of five spikes from HVC with ISI = 2 ms arrives at Area X at  $t = 980$  ms. The firing of IMAN/PN, and all the other cells actually, is rather independent of the presence of this innervation from HVC. Clearly, SN fires immediately upon this innervation from HVC, but the autonomous oscillations preceding the HVC burst continue. The membrane

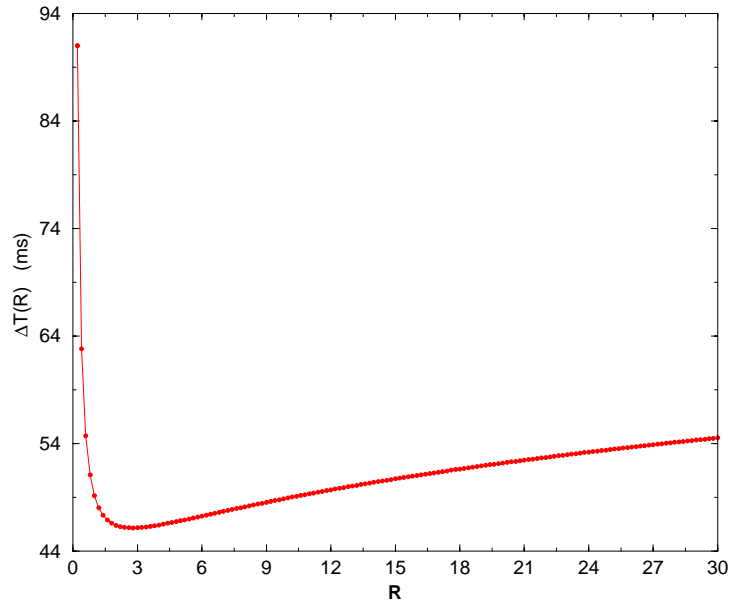


Figure 3.9 The time  $\Delta T$  for a signal to traverse the AFP depends on the strength of the AF  $\rightarrow$  DLM inhibitory connection. The conductance relative to a baseline value is the ratio  $R = \frac{g_{AF-DLMPN}}{g_{AF-DLMPN-Baseline}}$ . Positive slope in  $\Delta T(R)$  is associated with stability in RA plasticity by the argument given in the text.

voltage of the AF neuron is not shown, but it exhibits regular oscillations away from  $t = 980$  ms.

### 3.5 Dynamics with Coupling of the RA and the AFP

We now have two, as yet unconnected, results on the dynamics of the birdsong system:

1. a time delay of  $\Delta T \approx 50$  ms yields a zero in changes in AMPA conductivity at the AMPA receptors on RA neurons using the observed distribution of AMPA and NMDA receptors and a biophysically motivated model of plasticity, and



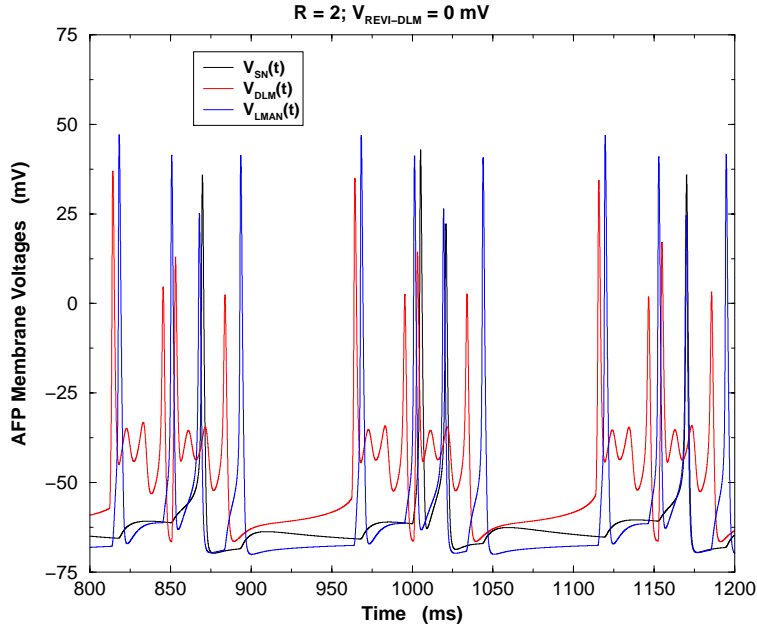


Figure 3.10 The AFP output when the synaptic current between the Area X output neuron, AF, is changed from inhibitory to excitatory by making  $V_{REVI-DLM} = 0$  mV instead of  $-75$  mV. There is a burst of spikes from HVC at 980 ms, but the autonomous firing of the SN and other neurons obscures the identification of  $\Delta T$ . The RA neuron receives many inputs from the PN in IMAN which are not associated with an HVC burst because of the oscillations of the AFP loop. In this calculation  $R = 2$ .

2. a time delay of  $\Delta T \approx 50$  ms arises in a model of the control pathway, the AFP, when various levels of excitation relative to inhibition in the AFP loop are considered.

We now wish to connect these two results. Our proposal for this begins with the question how the RA “knows” that the AFP has selected a relevant time delay  $\Delta T$ , and equivalently how the AFP “knows” the time delay it has selected has resulted in no further change in synaptic plasticity at the HVC  $\rightarrow$  RA junctions, leading to the alteration in the song pre-motor pathway and thus the song.

A natural solution to this would be a neural connection between RA and the AFP which would feedback this information to each. There is a known, but phys-

iologically unexplored, RA  $\rightarrow$  DLM connection (Vates et al., 1997; Wild, 1993). (Dave and Margoliash, 2000) and (Luo and Perkel, 2002) have discussed the role of this RA  $\rightarrow$  DLM connection. Indeed, our attention was drawn to this connection by D. Perkel (private communication). These authors did not develop the conjectures central to our model concerning the detailed RA excitatory connection to the DLM INs and then through them via inhibition to the DLM PNs. Nor did they draw the quantitative conclusions resulting from this connection flowing from our model.

We are not proceeding on solid experimental ground here, but we have explored the possibility that the RA-PNs project excitatory connections to the DLM INs which then project inhibition to the DLM PNs. These connections are indicated by the dashed lines in our graphical representation of the various nuclei and the HVC, RA, AFP system. The equations for these connections have all been given in the previous section.

This connection provides the feedback loop required to make the simultaneous determination of  $g_{RA}(t)$  and  $\Delta T$ . We can argue how, qualitatively, this connection might stabilize the coupled system. Suppose the parameters of the system,  $R$  and others, are such that if we begin at some initial value of  $g_{RA}(t) = g_{RA}(0)$ , one burst of HVC arriving directly at RA and arriving  $\Delta T$  later via the AFP leads to  $\Delta g_{RA} > 0$ . This implies, from Figure 3.4,  $\Delta T < 50$  ms. If this change in  $\Delta g_{RA}$  leads to  $\Delta T > 0$ , namely the slope  $\frac{\partial \Delta T}{\partial g_{RA}} > 0$ , i.e., the positive slope region in Figure 3.9, then  $\Delta T$  approaches the zero around 50 ms from the left. If  $\Delta T > 50$ , then looking at Figure 3.4, we see that this would tend to lead to  $\Delta g_{RA} < 0$ , resulting in  $\Delta T$  approaching the zero at 50 ms from the right and we might achieve stability. If the slope were opposite at the selected parameter values, the opposite effect would occur, and we might anticipate instability in the coupled system.

The argument couched in terms of the slope  $\frac{\partial \Delta T}{\partial R}$  leads to the conclusion that positive values of this slope result in stabilizing changes in  $\Delta g_{RA}$ , while negative slopes lead to instability. Increasing  $g_{RA}$  increases the level of *inhibition* in the AFP because RA connects to the AFP via excitation of a neuron, the DLM IN, which inhibits the DLM PN. Thus  $\Delta g_{RA} > 0$  is approximately equivalent to  $\Delta R > 0$ . The  $\Delta T(R)$  relationship for our model shown in Figure 3.9 allows for both stable and unstable dynamics of the conductance  $g_{RA}$ . If these qualitative arguments

are borne out, then by changing AFP parameters,  $R$  among them, one might be able to stabilize and destabilize the song by using neuromodulators to change such critical ratios.

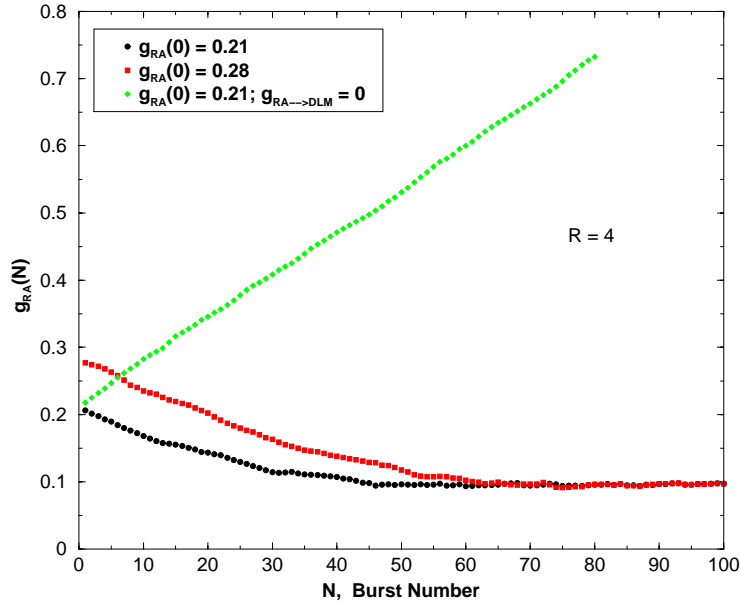


Figure 3.11 With  $R = 4$  we start the coupled HVC, RA, AFP dynamical system at  $g_{RA}(0) = 0.21$  and then  $g_{RA}(0) = 0.28$ . Each initial condition lies within the same basin of attraction of the map  $g_{RA}(N) \rightarrow g_{RA}(N + 1)$ , determined by presenting many bursts from HVC separated by 2000 ms. We see  $g_{RA}(N \rightarrow \infty) \approx 0.095$  and by examining the stable system we find  $\Delta T = 51.67$  ms. If we turn off the RA  $\rightarrow$  DLM connection, the map is unstable and  $g_{RA}(N)$  grows without bound.

Our first example selects  $R = 4$  in the AFP. We then select  $g_{RA}(0)$  and present a sequence of HVC bursts comprised of five spikes with  $ISI = 2$  ms to both RA and to the SN neuron in Area X. Through our synaptic plasticity rule, we evaluate  $\Delta g_{RA}(0)$  and, keeping  $R$  fixed, change  $g_{RA}$  to  $g_{RA}(1) = g_{RA}(0) + \Delta g_{RA}(0)$ . By presenting a sequence of HVC bursts, labeled by  $N = 1, 2, \dots$ , separated by 2000 ms between bursts, we then define a dynamical map  $g_{RA}(N) \rightarrow g_{RA}(N + 1) = g_{RA}(N) + \Delta g_{RA}(N)$ . Such maps are quite familiar from the study of discrete time dynamical systems.

In Figure 3.11 we show the outcome of iterating this map for three cases when  $R = 4$ : (1)  $g_{RA}(0) = 0.21$  with the RA  $\rightarrow$  DLM IN connection on, and (2) with that connection turned off. Then we set  $g_{RA}(0) = 0.28$  and recalculate  $g_{RA}(N)$  with the RA  $\rightarrow$  DLM coupling on. We see that for  $R = 4$  the dynamical map has a wide basin of attraction within which  $g_{RA}(N \rightarrow \infty) \approx 0.095$ . This is a stable fixed point of the map, and the associated  $\Delta T$  as  $N \rightarrow \infty$  is 51.67 ms. If we turn off the RA  $\rightarrow$  DLM connection, these become unstable points for the plasticity dynamics, and from each initial condition,  $g_{RA}(N)$  grows without bound. Only the growth from  $g_{RA}(0) = 0.21$  is shown in the figure.

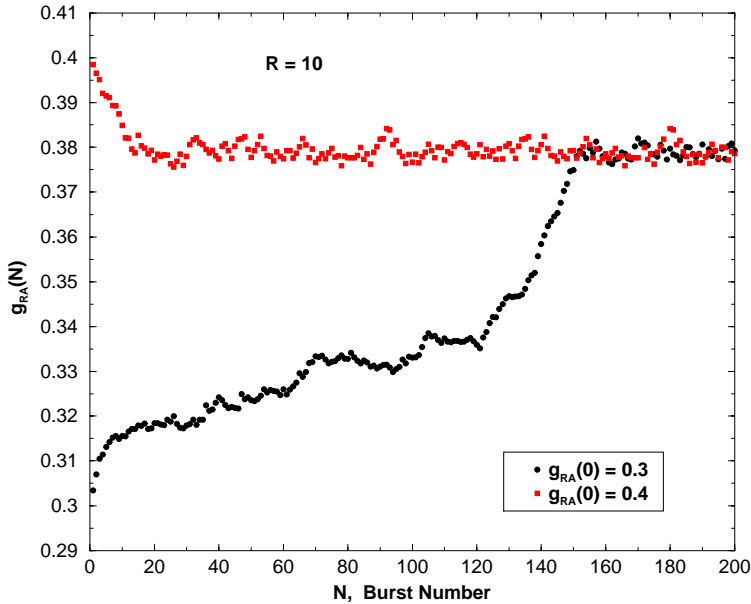


Figure 3.12 With  $R = 10$  we start the coupled HVC, RA, AFP dynamical system at  $g_{RA}(0) = 0.3$  and then  $g_{RA}(0) = 0.4$ . Each initial condition lies within the same basin of attraction of the map  $g_{RA}(N) \rightarrow g_{RA}(N + 1)$ , determined by presenting many bursts from HVC separated by 2000 ms. We see  $g_{RA}(N \rightarrow \infty) \approx 0.038$  and by examining the stable system we find  $\Delta T = 51.14$  ms. If we turn off the RA  $\rightarrow$  DLM connection, the map is unstable and  $g_{RA}(N)$  grows without bound.

Next we selected  $R = 10$  and performed the same set of calculations for  $g_{RA}(0) = 0.3$  and for  $g_{RA}(0) = 0.4$ . This time  $g_{RA}(N \rightarrow \infty) = 0.038$  and the

associated  $\Delta T = 51.14$  ms. Again, removing the RA  $\rightarrow$  DLM connection destabilizes the system. Figure 3.12 shown  $g_{RA}(N)$  when the RA  $\rightarrow$  DLM connection is on.

Finally, selecting  $R = 0.2$ , where we expect instability from our qualitative arguments, we see in Figure 3.13 that  $g_{RA}(N)$ , starting at  $g_{RA}(0) = 0.21$ , systematically decreases. We have manually cut off this decrease at 0 for biophysical reasons. This could be built into the plasticity model (Nowotny et al., 2003). Other initial conditions  $g_{RA}(0)$  over a range of 0.25 to 1.5 behaved the same way at this value of  $R$ .

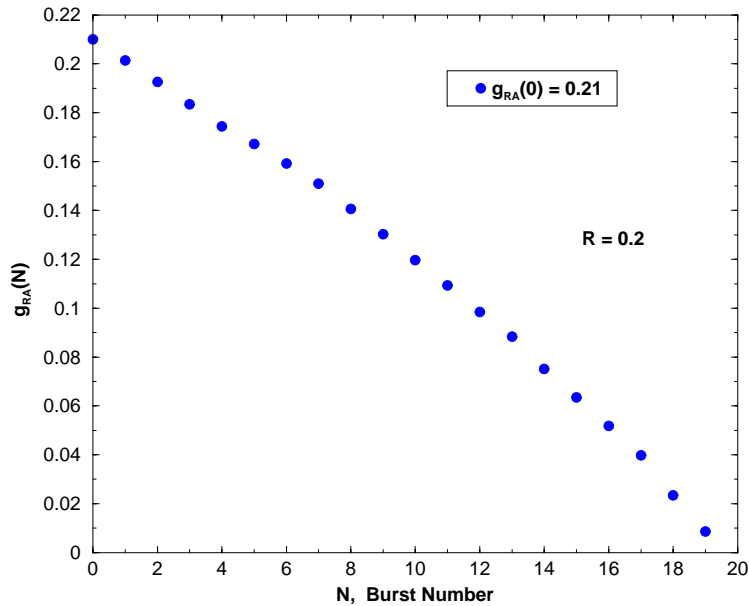


Figure 3.13 With  $R = 0.2$  we start the coupled HVC, RA, AFP dynamical system at  $g_{RA}(0) = 0.21$ . In this case the map  $g_{RA}(N) \rightarrow g_{RA}(N + 1)$ , determined by presenting many bursts from HVC separated by 2000 ms drives  $g_{RA}(N)$  to smaller and smaller values. We have had to manually cutoff the decrease of  $g_{RA}(N)$  by imposing a lower bound of 0. This is not built into the model, but could easily be added (Nowotny et.al, 2003). This behavior is seen for all values of  $g_{RA}(0)$  we examined for  $R_{IE} = 0.2$ , and our qualitative arguments in the text suggest this should be so.

### 3.6 Summary and Conclusions

We have explored the neural dynamics of the song system as shown in Figure 3.1 using anatomical and electrophysiological information about the structure of the neural nuclei in this system and the connections among them. Using observations about the relative amounts of NMDA and AMPA receptors at the RA junctions of HVC and IMAN projections (Stark and Perkel, 1999), we explored the implications of our biophysical model of synaptic plasticity (Abarbanel et al., 2003). This indicated that in response to bursts of spikes from HVC and IMAN separated by  $\Delta T$  the changes in AMPA conductivity  $\Delta g_{RA}$  would be zero around 50-60 ms. This is much larger time delay than a similar structure seen in experiments in mammalian cortex and other preparations (Bi and Poo, 1998; Nishiyama et al., 2000) where about 10 ms is appropriate. We attribute this to the specific distribution of NMDA and AMPA receptors at the RA dendrites.

It was very interesting that this time delay  $\Delta T \approx 50 - 60$  ms is also that seen in experiments on correlation between firing in RA and neural activity in IMAN (Kimpo et al., 2003) where two significant peaks were seen: one peak in correlated activity was observed for RA firing about  $10 \pm 3$  ms after IMAN activity, and a second peak where RA is active about  $50 \pm 10$  ms before IMAN activity. The first peak is associated with the known excitatory connection from IMAN to RA (Okuhata and Saito, 1987; Mooney, 1992; Bottjer et al., 1989), while the second was identified as coming from common input from HVC directly to RA and through the AFP. This interpretation was strengthened by the consistency of correlations between HVC and other nuclei both in (Kimpo et al., 2003; Hahnloser et al., 2002) and elsewhere. The results of (Kimpo et al., 2003) are also a strong indication that the nuclei of the song system act in a coherent fashion suggestive of some intranuclear synchronization among the many neurons in each nucleus as well as act coherently in an internuclear manner to propagate timing information from HVC to RA through two paths.

We then inquired into the operation of the AFP effectively as a time delay transfer function conveying information to RA with a delay  $\Delta T$ . We found that delays of order 50 to 60 ms were produced by treating each nucleus of the AFP as a collection of individual HH model neurons with cell properties known from

experiments and synaptic connections as observed. The time delay depended in an interesting manner on the relative inhibitory connection  $R$  to the DLM projection neuron.

Within the AFP model we addressed an additional question: What happens if the Area X  $\rightarrow$  DLM connection were excitatory instead of inhibitory as observed? This is not testable experimentally, but we saw that an excitatory Area X  $\rightarrow$  DLM connection leads to regular, apparently autonomous firing of the AFP. This is not consistent with the observations (Kimpo et al., 2003) as one might expect.

The plasticity calculations and the AFP time delay calculations, though interesting, and quite suggestive gave no clue as to how the RA and the AFP communicated  $\Delta T$  to each other. To accomplish this we noted the existence of a connection between RA and DLM (Wild, 1993; Vates et al., 1997) whose electrophysiological properties are not explored. Using a conjecture on this connection; namely, that RA projects excitation to the known DLM IN (Luo and Perkel, 2002) and in its turn this inhibits the DLM PN which projects to lMAN while also receiving input from AF in the Area X nucleus.

Because strengthening the HVC  $\rightarrow$  RA excitatory connections,  $g_{RA}$ , enhances inhibition to the AFP through this conjecture, we anticipated that in regions of  $\Delta T(R)$  with positive slope, stability in the plasticity dynamics would be seen. Indeed, we demonstrated this in several examples, and two were presented in Figures 3.11 and 3.12. It is also shown there that removing the RA  $\rightarrow$  DLM connection destabilized the HVC  $\rightarrow$  RA connection as the plasticity rule led to steadily increasing  $g_{RA}$  in time measured by the number of HVC bursts, separated by 2000 ms, presented to RA and to the AFP.

The network structure we have presented is consistent both within itself and with observations (Kimpo et al., 2003; Spiro et al., 1999; Stark and Perkel, 1999; Luo and Perkel, 2002). Because it relies on unmeasured properties of the RA  $\rightarrow$  DLM connection it can be checked in a qualitative manner by electrophysiological and pharmacological measurements at that connection. Additionally we have suggested that  $\Delta T$  in the AFP loop (Kimpo et al., 2003) can be directly affected by neuromodulators which alter  $R$  and that both positive and negative slopes in the function  $\Delta T(R)$  should be present.

This suggests the interesting idea that if the song system uses the connectivity

we suggest here, stabilized adult song could be destabilized by neuromodulators. If  $R$  is changed from a region where  $g_{RA}$  is stable to one where it is unstable, such as we enabled in our model and shown in Figure 3.13, one could significantly reduce the strength of the HVC  $\rightarrow$  RA couplings and thus significantly alter the song produced because the instructions from HVC to RA to the songbox would have altered. This too has not been seen, but is testable.

In our model we bypassed the origin of sparse signaling from HVC to RA (Hahnloser et al., 2002) and let HVC act as a sparse signal generator projecting to both RA and Area X. We also did not address the issue of auditory feedback from the songbox via various pathways back to HVC, and perhaps other song system nuclei. These need to be addressed to achieve a deeper understanding of learning and memory in this neural system, while our results may shed light on how the song is stabilized within this larger picture.

Finally, as noted in our introduction, we have chosen to significantly simplify the birdsong system by representing each nucleus by at most a few HH model neurons for each observed cell type within the nucleus. Even this simplification leads to the moderately complex model discussed in this paper as each ion channel and synaptic connection has dynamics of its own. It is possible that many of the representations of individual neurons could be further simplified, perhaps using FitzHugh-Nagumo two degree of freedom, spiking neurons (Koch, 1999) at many of the nodes of our full network. This could not be done at the DLM projection neuron where the dynamical response of the internal, activation and inactivation, degrees of freedom play an essential role in determining the time delay  $\Delta T$  in the AFP. We have not explored a further simplification of our model in any detail, though replacing the IMAN nucleus, for example, by a simplified spiking neuron would not change our results. We would arrive at a kind of “hybrid” model, however, where a mixture of simplified spiking neurons and biophysically realistic neurons would both play a role. It is not clear yet whether this would provide an interesting representation of the already simplified biological physics of this network. In connecting the dynamics explored here of the coupled pre-motor and AFP pathways with the mechanisms for the generation of song (Abarbanel et al., 2004c) we may need a much larger network for each nucleus, and then the issue of simplification of the nodes may become essential.



Most of the material appearing in this chapter has been published in (Abarbanel H.D.I., Talathi S.S., Mindlin G., Rabinovich M., and Gibb L., Physical Review E, 70, 051911, 2004). The dissertation author was the primary researcher in this effort.

# 4

## Neural circuitry for recognizing interspike interval sequence

In the last chapter we introduced the song system and proposed a model based on spike timing dependent plasticity for the control and maintenance of the learned adult bird song. We discussed the role for the AFP in producing time delays on the order of  $50\pm 10$  ms and its function in modulating the HVC $\rightarrow$ RA synaptic connection. In this chapter we propose a novel neural architecture abstracted from the time delay component of the song system AFP loop to provide an answer to a very interesting biological question, How do neural circuits in the brain decode the temporal information in the sensory input?

### 4.1 Introduction

It is known that sensory systems transform environmental analog signals into a format composed of essentially identical action potentials. These are sent for further processing to other areas of a central nervous system. When these action potentials or spikes are comprised of identical waveforms all information about the environment is contained in the intervals between spike arrival times (Fano, 1961). There are many examples of sensitive stimulus-response properties characterizing how neurons respond to specific stimuli. These include whisker-selective neural response in barrel cortex (Welker, 1976; Aarabzadeh et al., 2004) of rats and motion sensitive cells in the visual cortical areas of primates (Sugase et al., 1999; Buracas

et al., 1998).

One striking example is the selective auditory response of neurons in the song-bird telencephalic nucleus HVC (used as a proper name) (Lewicki and Arthur, 1996; Margoliash, 1983; Margoliash, 1986; Coleman and Mooney, 2004). As we have discussed in the last chapter, the projection neurons in the HVC fire sparse bursts of spikes when presented with auditory playback of the bird’s own song (BOS) and are quite unresponsive to other auditory inputs. Nucleus Nif (interfacial nucleus of nidopallium), through which auditory signals reach HVC (Figure 1.1) (Coleman and Mooney, 2004; Janata and Margoliash, 1999; Carr and Konishi, 1990; Cardin et al., 2005; Rosen and Mooney, 2006), also strongly responds to BOS in addition to responding to a broad range of other auditory stimuli. Nif projects to HVC, and the similarity of Nif responses to the auditory input and the subthreshold activity in HVC neurons suggests that Nif could be acting as a nonlinear filter for BOS, preferentially passing that important signal on to HVC. These examples from the song bird system, lead us to investigate the interspike interval recognition problem considered here.

We develop a neuronal network and demonstrate how biologically realistic neurons and synapses can be used to construct and train such a network to decode the temporal information in the input spike pattern. We call the resulting network an ISI Reading Unit (IRU). By “decoding” we mean recognition of the specific ISI sequence on which the network was trained in preference to other ISI sequences.

Key to the functioning of an IRU are two biological processes:

1. A time delay unit which produces an output spike at time  $t_0 + \tau(R)$  after receiving a spike at time  $t_0$ .  $R$  is a dimensionless parameter characterizing an inhibitory synaptic strength that can be used to tune the time delay  $\tau(R)$ ;
2. A method for tuning the time delays  $\tau(R)$  in the IRU using observed synaptic plasticity of the inhibitory synapses (Haas et al., 2006).

Time delay circuits, thought of primarily as an abstract idea rather than as a particular biological circuit realization, have been considered before, (Buonomano and Karmarkar, 2002; Mauk and Buonomano, 2004; Ivry, 1996). One exception to the descriptive modelling of neural time keeping processes is the work of Buonomano (Buonomano, 2000) which studies a two neuron model which can be tuned

to respond to time delays. Buonomano identifies synaptic changes as the tuning mechanism that might underlie detection of time intervals. His model relies on a balance between excitatory and inhibitory synaptic strengths. We do not explore the scheme proposed by Buonomano here, instead we present an alternative scheme to decode the ISI signal.

As discussed by the authors mentioned above, circuits for telling time more or less divide into three categories:

- Time delays along pieces of axon resulting in delays as short as a few microseconds. These are found in detection circuits for interaural time differences (Carr and Konishi, 1990; Carr and Konishi, 1988; Knudsen and Konishi, 1996; Koppel, 1997);
- Time delays of order hours or days connected with circadian rhythms. A detailed model of the biochemical processes thought to underly the  $\approx 24$  h circadian rhythm is found in recent work by Forger and Peskin (Forger and Peskin, 2003; Forger and Peskin, 2004), where a limit cycle oscillator with a period slightly more than 24 hours is identified and analyzed, and
- Time delays of tens to hundreds of milliseconds associated with cortical and other neural processing.

Our realization of the time delay circuit abstracted from the song system, addresses this third category of time keeping using ideas from an observed neural circuit in the birdsong system.

In investigating time differences between signals propagating from the birdsong nucleus HVC directly to the pre-motor nucleus RA and the same signal propagating to RA around the neural loop known as the anterior forebrain pathway (AFP), (Kimpo et al., 2003) reported a remarkable precision of the time difference between these pathways of  $50 \pm 10$  ms across many songbirds and many trials. We developed a model for song system in the last chapter based on detailed electrophysiological measurements by (Perkel, 2004), in each of the three nuclei of the AFP (Figure 3.1) to explain the observed time delay in the signal propagating through the AFP loop. This circuit demonstrated a tunable time delay adjusted by the strength of inhibition of synapse from the nucleus Area X to the nucleus

DLM. The precise value of the time delay in the birdsong circuit was attributed to a fixed point in the overall dynamics including excitatory synaptic plasticity at the HVC  $\rightarrow$  RA junction. This investigation suggested a general form of time delay circuit that could be tuned by changing the strength of an inhibitory synaptic connection. We develop that idea here.

Using these biologically motivated ingredients, we have built a simplified neural time-delay circuit and show here how it can be tuned to produce time delays over a range of about 20 ms within an overall scale of about 10 ms to 100 ms. We then demonstrate the role of this time delay circuit in neural circuit termed as, “Interspike Interval Recognition Unit”, (IRU), which is trained using a given specific interspike interval (ISI) sequence and then show how the IRU robustly recognizes the desired ISI sequence. Recognition is implemented here using a detection circuit that fires an action potential when two input spikes arrive within a short temporal window of  $\delta$  ms and responds with subthreshold activity otherwise.

The overall IRU circuit, made up of a sub-circuit of time delay unit, a spike selection unit (SSU, described below), and a detection unit (DU), operates by producing a replica of the given ISI sequence. It then uses inhibitory synaptic plasticity to adjust the delay produced by the time-delay sub circuit to match the ISI in the input sequences within a chosen resolution threshold of  $\delta$  ms. Success in this matching is seen in the spiking activity of the detection circuit. The IRU circuit is thus a candidate for how biological networks can accurately select particular environmental signals, potentially usable for further processing for decision making and required functionality, by keying on the representation of environmental signals as a specific spike sequence.

We first discuss the construction of the time delay circuit beginning with the design of a smallest possible biologically feasible neural circuit consisting of two neurons and then explain the mechanism of the three neuron time delay circuit abstracted from the birdsong system. We then proceed to develop our full ISI Reading Unit (IRU) and explain the function of the spike selection unit and the detection unit that together with the time delay subcircuitry makeup the complete IRU.

Next we address the issue of training the IRU using synaptic plasticity of the inhibitory synapses, as observed in the recordings in the entorhinal cortical regions

of rat brain, (Haas et al., 2006) to detect an input ISI sequence. We then show how the IRU can be used to recognize a specific ISI sequence on which it has been trained. We study the robustness of the IRU by training the IRU in noisy environment where in there is random jitter in the input training sequence.

All the neuron models discussed in this chapter follow the HH conductance based formalism as discussed in chapter 1.

In this chapter, it is not our aim to develop exact models for nuclei in the song bird, which was done in the last chapter. The idea for a particular three neuron model for the time delay circuitry we develop here was inspired from our study of the song system, as presented in the last chapter.

## 4.2 Time Delay Circuits

The time delay circuits presented here are constructed using type I HH conductance based neuron model. As discussed in chapter 1, type I neurons can produce spikes at very low frequencies and will therefore allow us long time delays in the circuit we discuss now.

The dynamics of membrane voltage for type I neuron models obey,

$$C_M \frac{dV(t)}{dt} = I_{IN}(t) + g_{Na}m(t)^3h(t)(V_{Na} - V(t)) + g_Kn(t)^4(V_K - V(t)) + g_L(V_L - V(t)) \quad (4.1)$$

where all the model parameters are as described for type I neuron in chapter 1.

For type I neurons we know that (chapter 1) the frequency of spiking as function of constant input current  $I_{In}$  obeys,

$$f = C\sqrt{I_{In} - I_0} \quad (4.2)$$

where  $I_0$  is the spiking threshold and C is function of model parameters.

### 4.2.1 One Neuron Model

Using the above described neuron model, we construct a one neuron time delay circuit as shown in Figure 4.1. The input to the neuron is

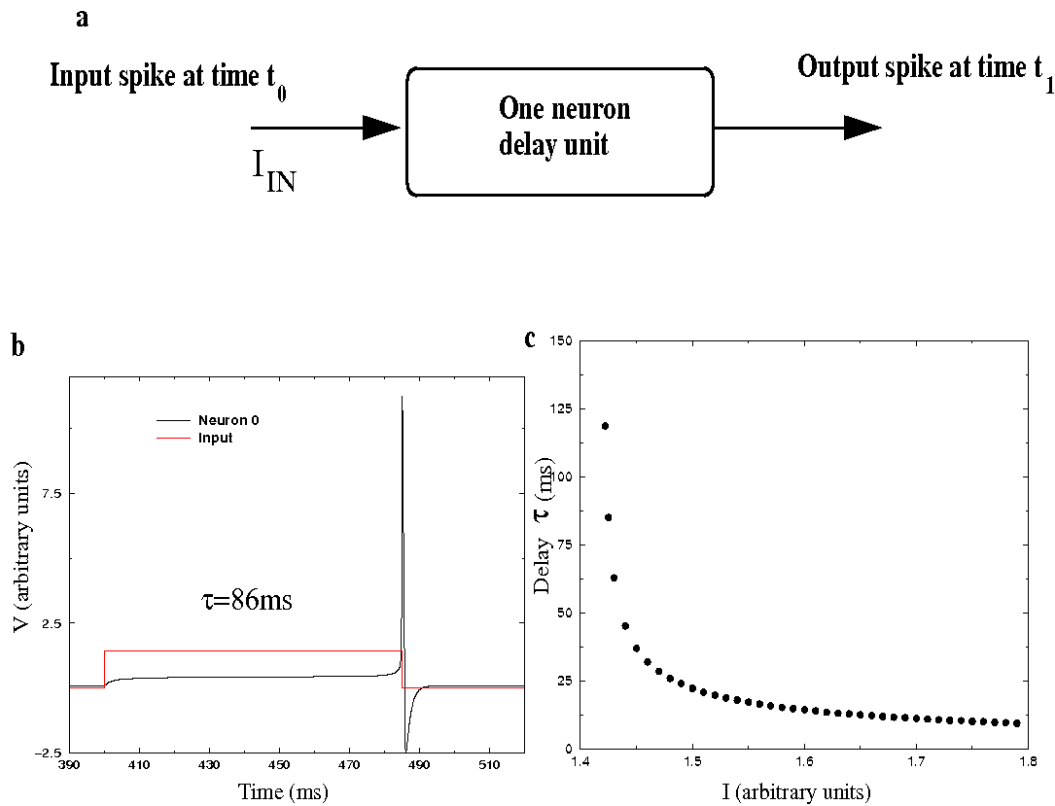


Figure 4.1 (a) **Schematic of the one neuron delay unit model.** The input current is  $I_{IN}(t) = I [\theta(t - t_0) - \theta(V(t) - V_{th})]$  starting at the time  $t_0$  of the input spike and lasting until the first spike from the neuron at time  $t_1$ . The intrinsic dynamics of the neuron to the spiking mode is through a saddle node bifurcation, typical of type I neurons. (b) Output from the delay unit. In this case the neuron produces a delayed spike after about 86 ms. (c) Variation of the delay produced by the neuron as function of the strength of the input step current  $I$ .

$$I_{IN}(t) = I [\Theta(t - t_0) - \Theta(V(t) - V_0)]$$

, where  $\Theta(x) = 0$  when  $x \leq 0$  and  $\Theta(x) = 1$  when  $x > 0$ .  $t_0$  is the time of an input spike to the neuron.  $V_0$  is the threshold for action potential production, and we set that to 0 mV. When  $V(t)$  exceeds this value, the neuron produces a spike. We call this  $t_1$ , and the time delay  $\tau(I) = t_1 - t_0$ . The input current  $I_{IN}(t)$  turns on a constant current  $I$  at time  $t_0$  and the type I neuron equations integrate the HH equations driven by this current until the voltage rises above  $V_0$  and a spike appears at  $t_1$ . At  $t_1$  the current is turned off. The period of spiking,  $T = (1000/f)$  ms for type I neurons obeys  $T = 1000/C\sqrt{I_{IN} - I_0}$ , i.e.,  $T \rightarrow \infty$ , as  $I_{IN} \rightarrow I_0$ , where  $I_0$  is the critical input current at which the type I neuron behavior bifurcates from a fixed point at the neuron rest potential to periodic spiking dynamics.

Using this type I neuron model, with step input current for the duration of first spike, we can construct a time delay unit to obtain various time delays as a function of the strength of  $I_{IN}$ . In Figure 4.1b we show a sample trace of the output from the single neuron delay unit for  $I \approx 1.4$  leading to  $\tau = 86$  ms. In Figure 4.1c we show the delay  $\tau(I) = t_1 - t_0$  from this one neuron model.

The one neuron model does not involve any synapses, so synaptic plasticity cannot be used to train the time delay to a desired value. Further, though the neuron is a biologically realistic HH model neuron, the circuit requires a step current input which is not.

## 4.2.2 Two Neuron Model

A two neuron delay unit model is constructed using an extension of the ideas from our one neuron model; the schematic is shown in Figure 4.2a. Neuron B is bistable. It exhibits a rest state and a spiking state at the same parameter values. This is observed in many neuron models (Guttman et al., 1980). Neuron A is of type I as discussed above.



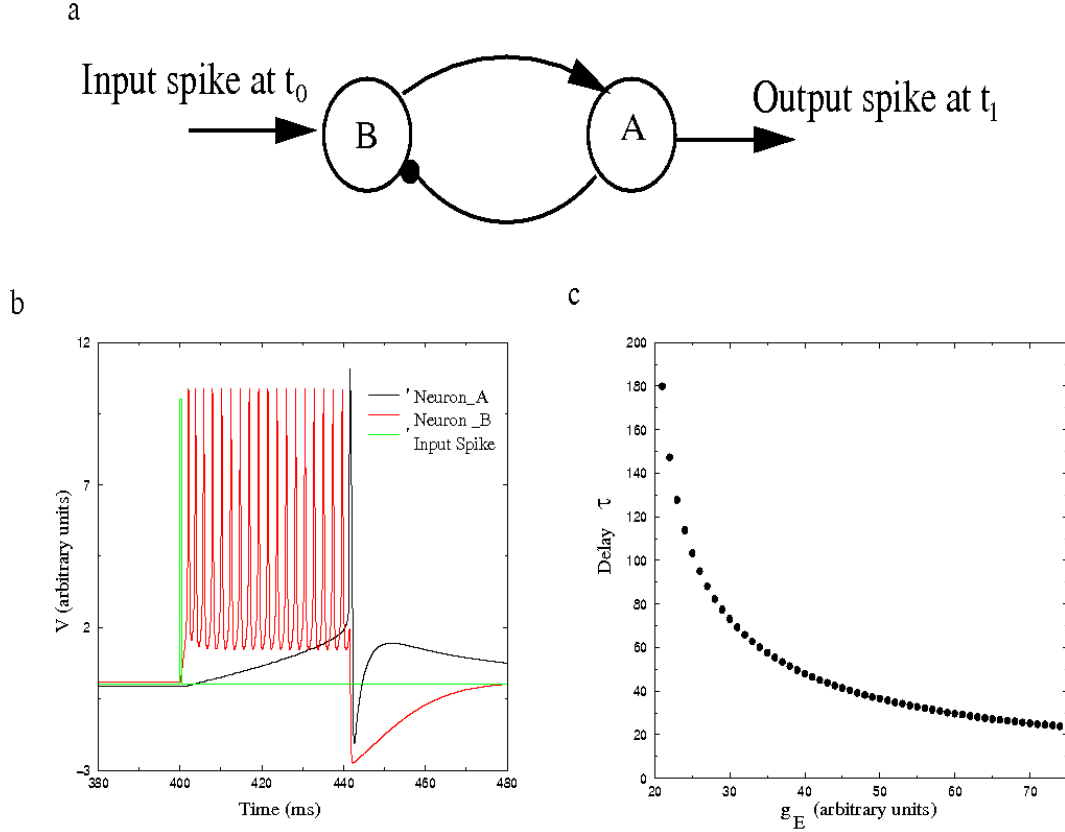


Figure 4.2 **Schematic of a two neuron delay unit model.** The input spike arrives at  $t_0$  at neuron B, which is at rest, sending this bistable neuron into a spiking regime and raising the neuron A membrane voltage towards spiking threshold until it eventually spikes at  $t_1$ . The spike from neuron A pushes neuron B back into a stable resting state. (b) The membrane voltages of neurons A and B in response to an input spike at time  $t_0 = 400$  ms. Neuron A fires after a delay of around 42 ms. The delay produced is governed by the strength of the excitatory synaptic connection from neuron B to neuron A. (c) Plot of delay  $\tau(g_E)$  as a function of the strength of the excitatory synaptic input from neuron B to neuron A. Note that  $\frac{d\tau(g_E)}{dg_E} < 0$ .

The bistable neuron B satisfies

$$\begin{aligned}
 C_M \frac{dV_B(t)}{dt} &= I_{syn}(t, V_B(t)) + I_{DC1} + g_{Na} m_\infty(V(t))(V_{Na} - V_B(t)) \\
 &+ g_K n(t)(V_K - V_B(t)) + g_L(V_L - V_B(t))
 \end{aligned}
 \tag{4.3}$$

where the gating variables  $n(t)$  satisfies the kinetic equation,

$$\frac{dn(t)}{dt} = \frac{n_\infty(V(t)) - n(t)}{\tau_n}, \quad (4.4)$$

and the activation functions  $X_\infty(V) = \{m_\infty(V), n_\infty(V)\}$  depend on voltage  $V$  as

$$X_\infty(V) = 1/(1 + \exp((V_X - V)/k_X)) \quad (4.5)$$

The parameters appearing in the bistable neuron equations are chosen as  $C_M = 1 \frac{\mu F}{cm^2}$ ;  $g_{Na} = 20$ ,  $g_K = 10$ ,  $g_L = 8.0$ , in units of  $mS/cm^2$ ;  $V_{Na} = 60$ ,  $V_K = -90$ , and  $V_L = -80$ ,  $V_m = -20$ , and  $V_n = -25$  in units of mV;  $k_m = 15$  mV,  $k_n = 5$  mV, and  $\tau_n = .16$  ms.

$I_{syn}$  is a inhibitory synaptic current from neuron A to neuron B. It has the form

$$I_{syn}(t, V_B(t)) = g_{I1} S_I(t) (V_{revI} - V_B(t)), \quad (4.6)$$

with  $V_{revI} = -75$  and  $g_I = 1$  mS/cm<sup>2</sup>.

$S_I(t)$  is taken to satisfy the following first order kinetic equation, similar to the synaptic model discussed in the last chapter.

$$\frac{dS_I(t)}{dt} = \frac{S_0(V_A(t)) - S_I(t)}{\tau_I(S_{1I} - S_0(V_A(t)))}, \quad (4.7)$$

which involves two time constants for the docking  $\tau_I(S_{1I} - 1)$  and undocking  $\tau_I S_{1I}$  of the neurotransmitter which induces current flow at the inhibitory postsynaptic receptor. We have chosen  $\tau_I = 1.2$  ms and  $S_{1I} = 4.6$ , giving a docking time of  $\tau_I(S_{1I} - 1) \approx 4.3$  ms and an undocking time of  $\tau_I S_{1I} \approx 5.5$  ms.  $S_0(V)$  is a step function in voltage. In our calculations we use  $S_0(x) = 0.5(1 + \tanh(120(x - 0.1)))$ .

The excitatory synapse from  $B \rightarrow A$  is modelled as an NMDA type excitatory synapse. This is required by the long times needed for neuron B to provide enough excitatory input to neuron A so A spikes. The excitatory synaptic current from  $B \rightarrow A$  enters the type I HH equation for  $V_A(t)$  and is given by

$$I_{B \rightarrow A}(t, V_A(t)) = g_E S_E(t) B(V_A(t)) (V_{revE} - V_A(t)), \quad (4.8)$$

where  $B(V(t)) = 1.0/(1 + 0.288 \exp(-0.062V(t)))$ .  $g_E$  is 0.1 mS/cm<sup>2</sup>.  $V_{revE} = 0$  mV. The function  $S_E(t)$  satisfies

$$\frac{dS_E(t)}{dt} = \frac{S_0(V_B(t)) - S_E(t)}{\tau_E(S_{1E} - S_0(V_B(t)))}, \quad (4.9)$$

and we choose  $\tau_E = 69.5$  ms and  $S_{1E} = 1.027$ , for a docking time of 1.9 ms and an undocking time of 71.5 ms. These times are characteristic of NMDA excitatory synapses.

Initially both neurons are at rest. The input is a spike  $t_0$  arriving at neuron B. The output of the model is a single spike at time  $t_1$  from neuron A;  $\tau = t_1 - t_0$ . This can be changed as a function  $g_E$ . A single input spike into neuron B moves it into its spiking regime, providing enough depolarizing current into neuron A until it fires a spike. In order for the spiking neuron B to provide enough depolarization to neuron A for it to eventually fire, the firing frequency of neuron B should be greater than the inverse decay time of the excitatory synaptic connection from B to A. We achieve this by using a slow NMDA type excitatory synaptic connection from neuron B to A. A spike from neuron A then provides a hyperpolarizing input to neuron B and sets it back into its rest state.

In Figure 4.2b we show a sample trace of the output from the two neuron delay model, the input to the model, and the activity in the bistable neuron as function of time. In this particular example the delay observed is around 42 ms. In Figure 4.2c we show a plot of the time delay of this model  $\tau(g_E)$ .

This dependence of  $\tau(g_E)$  on a synaptic strength is typical for excitatory synapses. As the excitation increases, the time to produce a spike decreases. The opposite, as we shall see below, is the case for inhibition.

### 4.3 Three Neuron Model

The three neuron model for the time delay circuit is abstracted from the AFP loop in the song bird (Figure 4.3 inset). As discussed in chapter 1, the AFP is comprised of three nuclei: area X, DLM and the IMAN, each having a few times 10,000 neurons (Brenowitz et al., 1997; Brainard and Doupe, 2002). The output of the AFP is IMAN nuclei, leaving the AFP to innervate the RA nucleus. Within the

area X, two distinct neuron types, spiny neurons (SN) and aspiny fast firing (AF) neurons, receive direct innervation from HVC (Farries et al., 2005). In the absence of signals from HVC the SNs are at rest while the AF neurons are oscillating at about 20 Hz. The SNs inhibit the AF neurons, and these, in turn, inhibit neurons in DLM, a thalamic nucleus in the AFP (Farries and Perkel, 2002). The DLM neurons receiving this input from Area X are below threshold for action potential production and do not produce action potentials while the AF neuron oscillates. When the AF  $\rightarrow$  DLM inhibition is released, the DLM neurons rebound and fire periodic action potentials. These propagate to LMAN and are then transmitted to RA. These propagate to LMAN and are then transmitted to RA. The time around this path differs from the direct HVC  $\rightarrow$  RA innervation by  $50 \pm 10$  ms (Kimpso et al., 2003).

In our modelling effort presented in the last chapter, treating each nuclei as a coherent action potential generating device, we found that LMAN played an unessential role in determining the time delay around the AFP while the strength of the AF  $\rightarrow$  DLM inhibition could tune the time delay over a few tens of milliseconds.

From these observations we have constructed a biologically feasible time delay circuit comprised of three neural units and two inhibitory synapses with a tunable synaptic strength. The time delay circuit is displayed in Figure 4.3. Neuron A (similar to the SN in Area X) receives an excitatory input signal from some source. It is at rest when the source is quiet, and when activated it inhibits neuron B (similar to the AF neuron in Area X). Neuron B receives an excitatory input from the same source. It oscillates periodically when there is no input from the source. Neuron B inhibits neuron C (similar to a DLM neuron). Neuron C produces periodic spiking in the absence of inhibition from neuron B. The tunable synaptic strength is that connecting neuron B to neuron C.

Each of the A, B and C neuron are modelled as type I neuron with the same set of model parameters as presented in chapter 1. A more detailed neuron model for neuron C could include hyperpolarization activated  $I_h$  channels and low threshold calcium  $I_T$  channels, which facilitate post inhibitory rebound spikes, as presented in the last chapter for DLM neuron dynamics. Indeed in the DLM neurons of the birdsong AFP this mechanism leads to calcium spikes as the output of “neuron C”.

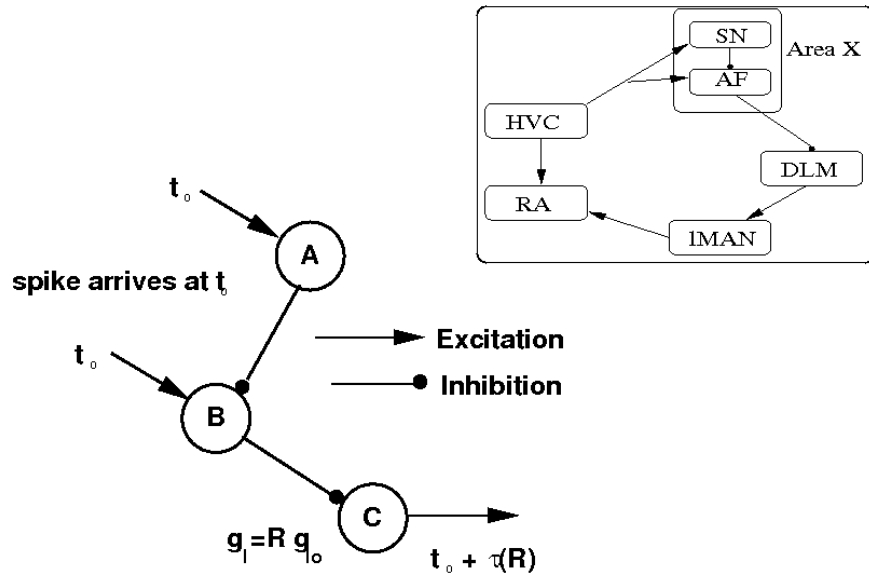


Figure 4.3 **Schematic diagram of the three neuron time-delay unit used in the IRU circuit.** This is abstracted from a time-delay network in the anterior forebrain pathway of the birdsong system as shown in the inset above. The inset shows the AFP loop (Area X, DLM and LMAN) from the birdsong system that suggested our three neuron time-delay unit. Unit A is abstracted from the area X SN neurons, unit B is abstracted from the area X AF neurons, and unit C is abstracted from the thalamic excitatory neurons in DLM. Absent any input spikes neuron A is at rest, neuron B oscillates periodically, and neuron C oscillates around its rest potential driven by periodic inhibitory input from neuron B. When an input spike arrives at neuron A and at neuron B at time  $t_0$ , neuron A fires an action potential and neuron B has the phase of its oscillation reset to be in synchrony with the time of arrival  $t_0$  of the spike. The action potential in neuron A inhibits neuron B, and this releases neuron C to rise to its spiking threshold a time  $\tau(R)$  later.  $R$  is the dimensionless scale of the  $B \rightarrow C$  inhibition. Within a broad range for  $R$ , neuron C will fire a single spike at a time  $t_0 + \tau(R)$ . The value of the conductance for the  $B \rightarrow C$  inhibitory synapse is  $g_I = Rg_{I0}$ , with  $g_{I0}$  a baseline conductance.

When the inhibition from neuron B to neuron C is released by the inhibitory signal from neuron A to neuron B, neuron C rebounds and produces an action potential some time later. This is due to the intrinsic stable spiking of neuron C in the absence of any inhibition from neuron B.

This time delay is dependent on the strength of the B→C inhibition, as the stronger that is set the further below threshold neuron C is driven and the further it must rise in membrane voltage to reach the action potential threshold. This means the larger the B→C inhibition, the longer the time delay produced by the circuit. Other parameters in the circuit, such as the membrane time constants, set the scale of the overall time delay.

The direct excitation of neuron B by the signal source is critical. It serves to reset the phase of the neuron B oscillation, as a result of which the spike from neuron C is measured with respect to the input signal and thus makes the timing of the circuit precise relative to the arrival of the initiating spike. Without this excitation to neuron B, the phase of its oscillation is uncorrelated with the arrival time of a signal from the source, and the time delay of the circuit varies over the period of oscillation of neuron B. This is not a desirable outcome, nor is it the way the AFP circuit appears to work.

The dynamical equation for the three HH neurons shown in Figure 4.3 are:

$$\begin{aligned}
C_M \frac{dV_i(t)}{dt} &= g_{Na} m(t, V_i(t))^3 h(t, V_i(t)) (V_{Na} - V_i(t)) \\
&+ g_K n(t, V_i(t))^4 (V_K - V_i(t)) + g_L (V_L - V_i(t)) \\
&+ g_{ij}^I S_I(t) (V_{revI} - V_i(t)) + I_i^{syn}(t, V_i(t)) + I_i^{DC}, \quad (4.10)
\end{aligned}$$

where (i,j)=[A, B, C]. All the model parameters are the same as that described for type I neurons in the overview chapter.  $I_i^{DC}$  is the DC current into the A, B or C neuron. These are selected such that neuron A is resting at -63.74 mV in the absence of any synaptic input, neuron B is spiking at around 20 Hz, and neuron C would also spiking at around 20 Hz in the absence of any synaptic inputs. In addition,  $I_i^{syn} = g_i^E S_E(t) (V_{revE} - V_i(t))$  is the synaptic input to the delay circuit at neuron A and B. It is innervated by a spike from the signal source at time  $t_0$ ;  $g_i^E = (g_A, g_B, 0)$ . The nonzero inhibitory synaptic strengths  $g_{ij}^I$  in the delay circuit are  $g_{BA} = R^0 g_I$  and  $g_{CB} = R g_I$ . The dimensionless factors, R and  $R^0$ , set the

strength of  $B \rightarrow C$  and  $A \rightarrow B$  inhibitory connections respectively, relative to baseline strength  $g_I$ , which is set to 1 in all the calculations presented here.

$g_A = g_B = 0.5 \text{ mS/cm}^2$ .  $g_I = 1 \text{ mS/cm}^2$ ,  $R^0 = 50.0$ , and  $R$  varies as given in text.  $V_{revE} = 0 \text{ mV}$ , and  $V_{revI} = -80 \text{ mV}$ .  $\tau_E = 1.0 \text{ ms}$ ,  $S_{1E} = 1.5$ ,  $\tau_I = 1.2 \text{ ms}$ ,  $S_{1I} = 4.6$ . The DC currents in the neurons are taken as  $I_A^{DC} = 0.0 \mu\text{A/cm}^2$ ,  $I_B^{DC} = 1.97 \mu\text{A/cm}^2$  and  $I_C^{DC} = 1.96 \mu\text{A/cm}^2$ .

$S_E(t)$  represents the fraction of excitatory neurotransmitter docked on the postsynaptic cell receptors as a function of time. It varies between 0 and 1 and is associated with two time constants, one for the docking of the neurotransmitter and the other for undocking of the neurotransmitter. It satisfies,

$$\frac{dS_E(t)}{dt} = \frac{S_0(V_{pre}(t)) - S_E(t)}{\tau_E(S_{1E} - S_0(V_{pre}(t)))}$$

With  $\tau_E = 1 \text{ ms}$  and  $S_{1E} = 1.5$ , the docking time constant for the neurotransmitter is  $\tau_E(S_{1E} - 1) = 0.5 \text{ ms}$ , and the undocking time constant  $\tau_E S_{1E} = 1.5 \text{ ms}$ . These times are characteristics of AMPA synapses.

Similarly  $S_I(t)$  represents the percentage of inhibitory neurotransmitter docked on the postsynaptic cell as function of time. It satisfies the following equation

$$\frac{dS_I(t)}{dt} = \frac{S_0(V_{pre}(t)) - S_I(t)}{\tau_I(S_{1I} - S_0(V_{pre}(t)))}$$

where we select  $\tau_I = 1.2 \text{ ms}$  and  $S_{1I} = 4.6$  for docking time of 4.32 ms and undocking time of 5.52 ms. The range of time delays produced by the three neuron delay circuit depends on the docking and undocking times of this synapse.

For the values above, we find  $\tau(R)$  as shown in Figure 4.4c. For  $R$  too small,  $R < R_L$  in Figure 4.4, the inhibition from  $B \rightarrow C$  does not prevent production of action potentials. For  $R$  too large,  $R > R_U$  in Figure 4.4, the  $C$  neuron is inhibited so strongly it never spikes. Over the range of  $R_L \leq R \leq R_U$  we typically find  $\tau(R)$  ranges over about 20 ms within an overall scale of about 10 ms to 100 ms. In Figures 4.4a and 4.4b we present examples of the response of the time delay circuit just described. In Figure 4.4a a single spike is presented to neurons  $A$  and  $B$  at  $t_0 = 500.0 \text{ ms}$ .  $R = 0.7$  and  $\tau(R) = 43.68 \text{ ms}$ . In 4.4a we show the membrane voltage of neurons  $A$  and  $C$ . To expose the dynamical processes taking

[ht!]

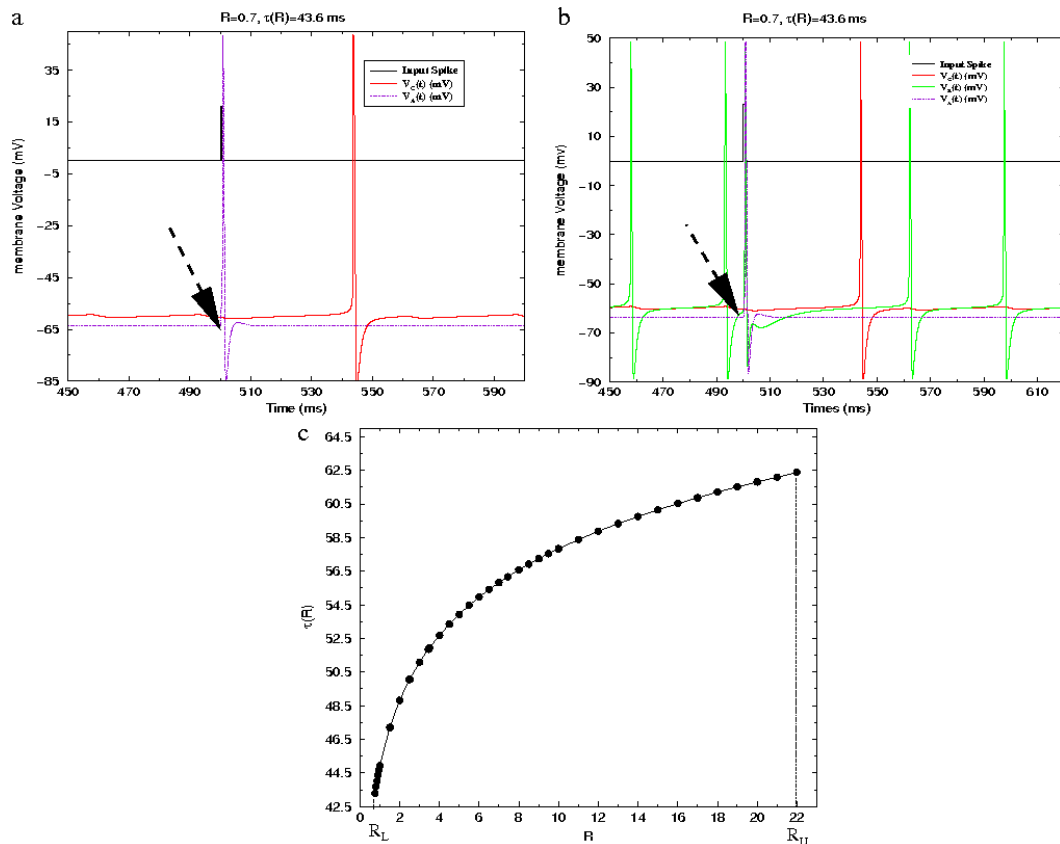


Figure 4.4 (a) For  $R = 0.7$  we show the membrane voltages of neuron A (blue) and neuron C (red) in response to single spike input (black) arriving at neuron A and neuron B at time  $t_0 = 500$  ms. For  $R = 0.7$  we see the output spike from neuron C occurring at  $t = 543.68$  ms, corresponding to  $\tau(R) = 43.6$  ms. (b) For  $R = 0.7$  we again show the membrane voltages of neuron A (blue) and neuron C (red), and in addition now display the membrane voltage of neuron B (green). A single spike input (black) arrives at time  $t = 500$  ms. We see that the periodic action potential generation by neuron B is reset by the incoming signal. (c) The delay  $\tau(R)$  produced by the three neuron time delay unit as a function of  $R$ , the strength of the inhibitory synaptic connection  $B \rightarrow C$ . All other parameters of the time delay circuit are fixed to values given in the text. For  $R < R_L$  the inhibition is too weak to prevent spiking of neuron C. For  $R > R_U$  the inhibitory synapse is so strong that neuron C does not produce any action potential, so effectively the delay is infinity. In Figures 4a and 4b the arrow indicates the time of the spike input to units A and B of our delay unit.



place in the time delay unit after the spike at  $t_0$  arrives. In Figure 4.4b we also show the membrane voltage of neuron B. It is clear in Figure 4.4b that the oscillations of neuron B are reset by the incoming signal, and the action potential generated at neuron C is a result of its internal dynamics, not of the period of oscillation of neuron B. The variation of the time delay with the strength of the B→C inhibitory strength  $R$  is shown in Figure 4.4c for the particular set of parameters listed above. It is important that  $\frac{d\tau(R)}{dR} > 0$ . As noted, one can, by changing the membrane capacitance and the strengths of the various maximal conductances and time course of inhibitory synaptic connections, place the variation of  $\tau(R)$  near 10 ms or near 100 ms. In one of the calculations for training the IRU (Figure 4.10), we set the parameters of the delay circuitry such that delays in the range of 15 to 40 ms are obtained.

## 4.4 ISI Reading Unit: IRU

Using the three neuron time delay circuit we now construct a circuit that can be trained to be selective for a chosen ISI by repeated presentation of that ISI input. The main idea is that an ISI comprising a spike pair at time  $t_0$  and  $t_0 + T$  induces a replica of itself using the time delay unit with time delay  $\tau(R)$ . This replica sequence is compared to the original input and, if  $|T - \tau(R)| > \delta$  ms, where  $\delta$  is the resolution of spike detection, then an inhibitory synaptic plasticity rule, discussed in the following section, modulates the delay unit, so that this difference  $|T - \tau(R)|$  is reduced towards the tolerance limit of  $\delta$  ms. When  $|T - \tau(R)| \leq \delta$  ms for the input ISI in the training sequence, the IRU is considered trained. We choose the parameters of the detection unit such that  $\delta \approx 4$  ms, which is around twice the width of biological action potentials. Mathematically we could choose any  $\delta > 0$  as our convergence criterion (section 4.6). Training of the delay units in IRU is clearly a function of the learning rule implemented to adjust the  $\tau(R)$ .

The schematic diagram of the IRU is shown in Figure 4.5a. The input ISI sequence enters the “spike selection unit” (SSU) part of the IRU, which selectively distributes the individual input spikes to the neurons in the time delay subcircuitry. The purpose of this is to facilitate spike timing dependent plasticity learning, as explained in the next section. The detection unit is comprised of a neuron (or small

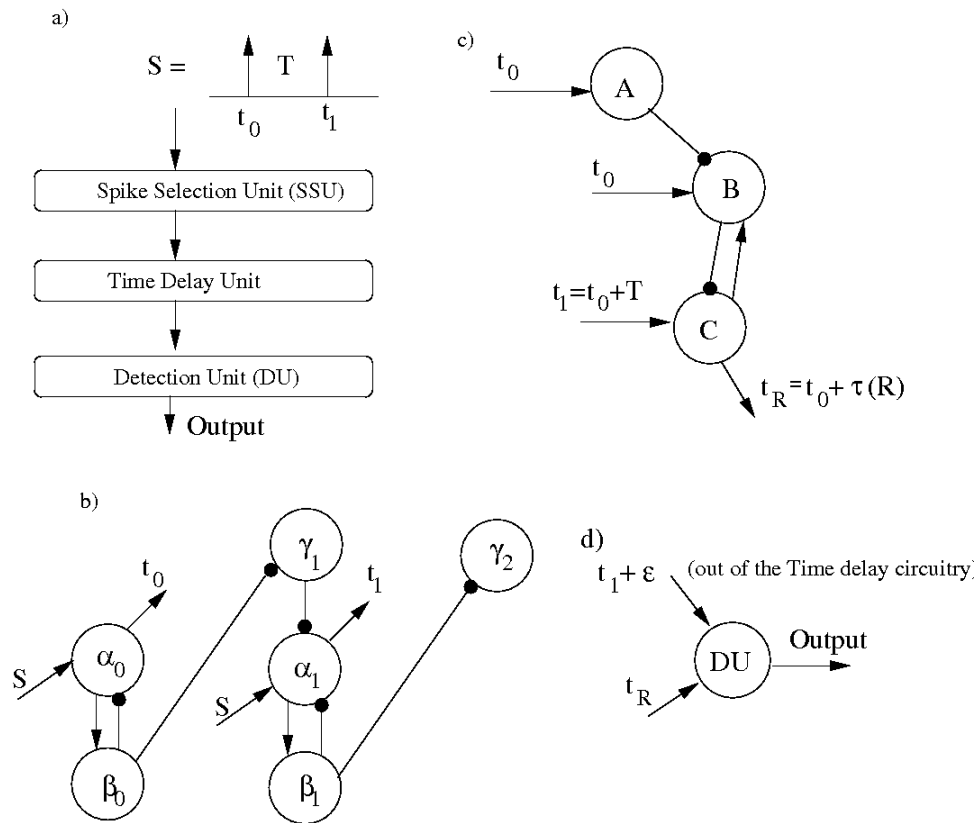


Figure 4.5 (a) Schematic of the complete Interspike interval (ISI) reading unit (IRU). The input ISI pattern, enters the IRU at the spike selection unit (SSU) and the IRU responds with a spike output through the detection unit depending on whether it is tuned to the input ISI. (b) Schematic of the spike selection unit (SSU). (c) Schematic of the Time delay unit. Note the excitatory connection  $C \rightarrow B$ . It is required to facilitate spike timing dependent plasticity learning in the delay unit. (d) Schematic of the detection unit. It responds with an output spike only when it receives two input spikes  $\delta$  ms, the resolution for ISI recognition by the detection unit.

circuits of neurons) that fires when two spikes arrive within  $\delta$  ms of each other. It remains below its action potential threshold otherwise. There are many ways to accomplish this. The detection unit circuitry we implement in our construction of the IRU is shown in Figure 4.6

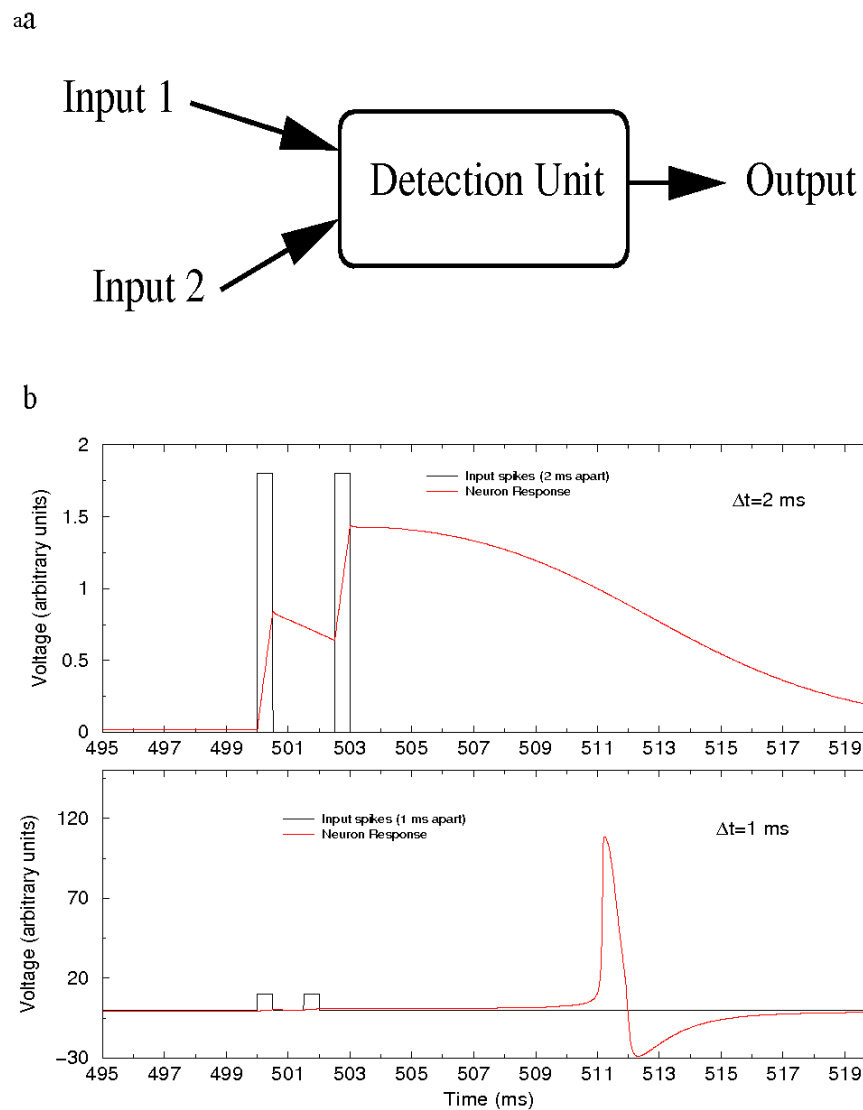
It is modelled as a single neuron (Figure 4.6a) following type I dynamics. It is tuned to respond to two input spikes arriving within  $\delta$  ms of each other. In Figure 4.6b, top panel, we show the response of the detection unit when it receives two input spikes, 2 ms apart. In this calculation we set  $\delta = 1$  ms, so that when two input spikes are 2 ms apart, the detection unit responds with a corresponding subthreshold EPSP. However, when the two inputs arrive sufficiently close to each other, i.e., within  $\delta = 1$  ms, as shown in Figure 4.6b bottom panel, the total integrated input is sufficient to push the neuron above its spiking threshold. Now it responds with a spike after a delay of around 10 ms. This is governed by the integration time constant of the neuron dynamics.

The SSU is required to allow us to send only pairs of spikes at time  $t_n$  and  $t_{n+1}$   $n = 0, 1, ..$  to the time delay unit which is to be trained to adjust its time delay  $\tau(R)$  to  $T_n = t_{n+1} - t_n$ . If we try to send the whole spike train to a time delay unit, it does not respond properly to produce a single spike from its “neuron C.”

The SSU is shown in Figure 4.5b. Neural units  $\beta_n$  and  $\gamma_n$  are bistable neurons, similar to the one we discussed in the two neuron model for time delay circuitry (Equations 4.3, 4.4 and 4.5). The model parameters are the same as used to describe the two neuron model. In addition, the constant DC current in the  $\gamma_n$  neurons is set to  $6 \mu A/cm^2$  so that it is in the stable oscillating state. The neurons  $\beta_n$  are in stable resting state.  $\alpha_n$  neuron follows type I dynamics as discussed earlier.

The excitatory and inhibitory synapse follow the same first order kinetics as in equations 4.7 and 4.9. The excitatory synaptic strength is  $g_{\alpha\beta} = 1 \frac{mS}{cm^2}$  and the inhibitory synaptic strength  $g_{\beta\alpha} = 70 \frac{mS}{cm^2}$  and  $g_{\beta\gamma} = 7 \frac{mS}{cm^2}$  respectively. An SSU can select spikes from a sequences od spike time  $\{t_0, t_1, ...t_N\}$ . Here we present results on N=2 to illustrate the operation of the SSU.

The input to the SSU in Figure 4.5b is the input ISI sequence  $S$  comprising of two spikes at times  $S = \{t_0, t_1 = t_0 + T\}$ , where T is the ISI upon which the IRU



is trained. When the spike at  $t_0$  arrives at neuron  $\alpha_0$ , that neuron is excited into its spiking state. It then excites neuron  $\beta_0$ , and it produces an output spike at  $t_0$ . When excited, neuron  $\beta_0$  begins oscillating and inhibiting neuron  $\alpha_0$ ; no further spikes from  $S$  excite  $\alpha_0$ .  $\beta_0$  also inhibits neuron  $\gamma_1$  moving it from oscillation to rest. The quieting of  $\gamma_1$  allows neuron  $\alpha_1$  to respond to the spike in  $S$  at  $t_1$  producing an output spike at  $t_1$ . Neuron  $\beta_1$  now is excited to oscillation and inhibits  $\alpha_1$  and  $\gamma_2$ .  $\alpha_1$  does not respond to any other spikes in the sequence  $S$ .

Not shown in this schematic is the final step whereby all neurons  $\beta_n$  are returned to rest, and all neurons  $\gamma_n$  are returned to their oscillating state. This is accomplished by global inhibition of the  $\beta_n$  and excitation of the  $\gamma_n$  after  $S$  has stimulated output spikes from all neurons  $\alpha_n$ , which can be done through a signal sent back to the SSU after the detection unit has triggered a spike.

At present there is no electrophysiological or anatomical data for the presence of SSU and the detection unit in the bird brain or that of any other animal.

Finally for the IRU to be able to be selectively tuned to detect an input ISI, we need a mechanism to train the time delay unit to adjust  $|T - \tau(R)| \leq \delta$  ms. This is done by invoking the spiking timing dependent plasticity rule for inhibitory synapses (Haas et al., 2006). The C unit of the time delay circuitry fires a rebound action potential at time  $t_0 + \tau(R)$  which results in spike response in the presynaptic neuron B. Neuron C also receives an input from the SSU at time  $t_0 + T$  (Figure 4.5c). If these are more than  $\delta$  ms apart, the inhibitory spike timing dependent plasticity rule will adjust it to be less than or equal to  $\delta$  ms as discussed in the next section. There we discuss the experimentally observed spike timing dependent plasticity rule for an inhibitory synapse and explain how it plays a role in training the IRU to accurately detect the input ISI sequence.

## 4.5 IRU learning

A spike timing dependent plasticity rule for inhibitory synapses has recently been observed in layer II of entorhinal cortex by Haas, (Haas et al., 2006). It gives the change in the inhibitory synaptic conductance associated with the arrival of a spike at  $t_{pre}$  at the presynaptic terminal and spiking of a postsynaptic neuron at  $t_{post}$ . As a function of  $\Delta t = t_{post} - t_{pre}$  the change in synaptic conductance  $\Delta g_I(\Delta t)$

normalized by the baseline synaptic conductance  $g_{I0}$  is given by

$$\frac{\Delta g_I(\Delta t)}{g_{I0}} = \alpha^\beta \Delta t |\Delta t|^{\beta-1} \exp(-\alpha |\Delta t|). \quad (4.11)$$

An empirical fit to the data gives  $\beta\alpha \approx 5$  to  $10 \text{ ms}^{-1}$ . The parameters  $\beta$  and  $\alpha$  chosen for the computations presented here are given in the caption of the appropriate figures. This empirical learning rule (see graphic inset Figure 4.7) allows tuning of the inhibitory synapse from B  $\rightarrow$  C in the delay unit of the IRU. In order to implement the rule in the IRU, we identify  $t_{pre}$  with the spike times in the neuron B and  $t_{post}$  with action potential generated in the postsynaptic neuron C. The STDP rule discussed above is obtained for a single pre-post spike pair and the interesting feature of the rule is the zero around  $\Delta t = 0$  ms. This rule provides a biophysical mechanism to tune the delay  $\tau(R)$  in the time delay unit to the interspike interval T thereby facilitating learning by the IRU.

In order to facilitate correct interpretation of the STDP rule for inhibitory synaptic plasticity, we introduce the excitatory AMPA connection, with same first order kinetics as discussed earlier for excitatory synapse, from neural unit C to B in the time delay subcircuitry as shown in Figure 4.5c. Values of the excitatory synaptic conductance used for IRU training are given in table 4.1.

In order to understand the training in IRU, consider the situation shown in Figure 4.7, i.e.,  $T < \tau(R)$  such that  $|T - \tau(R)| > \delta$ . In this situation neuron C fires a spike at time  $t_0 + T$ , which is earlier than the rebound spike for C. Due to the presence of the excitatory connection C  $\rightarrow$  B, firing of C at  $t_0 + T$  excites neuron B, which in turn inhibits neuron C, and as a result neuron C is prevented from producing any more spikes. The detection unit thus receives just one spike input and does not fire.

As a result in this case the most effective presynaptic spike contribution to the STDP learning rule is the next presynaptic spike produced by B as it resumes its oscillations. This occurs at time  $t_0 + T + t_B$  with  $t_B > 0$ . This is greater than  $t_0 + \tau(R)$  when neuron C would have fired had there not been a input spike at  $t_0 + T < t_0 + \tau(R)$ . The STDP rule thus sees  $\Delta t = (t_0 + T) - (t_0 + T + t_B) < 0$ . This leads to decrease in R and as shown in Figure 4.7, a decrease in  $\tau(R)$ . The decrease in  $\tau(R)$  continues until  $\tau(R) \approx T$ , when the time delay unit has completed

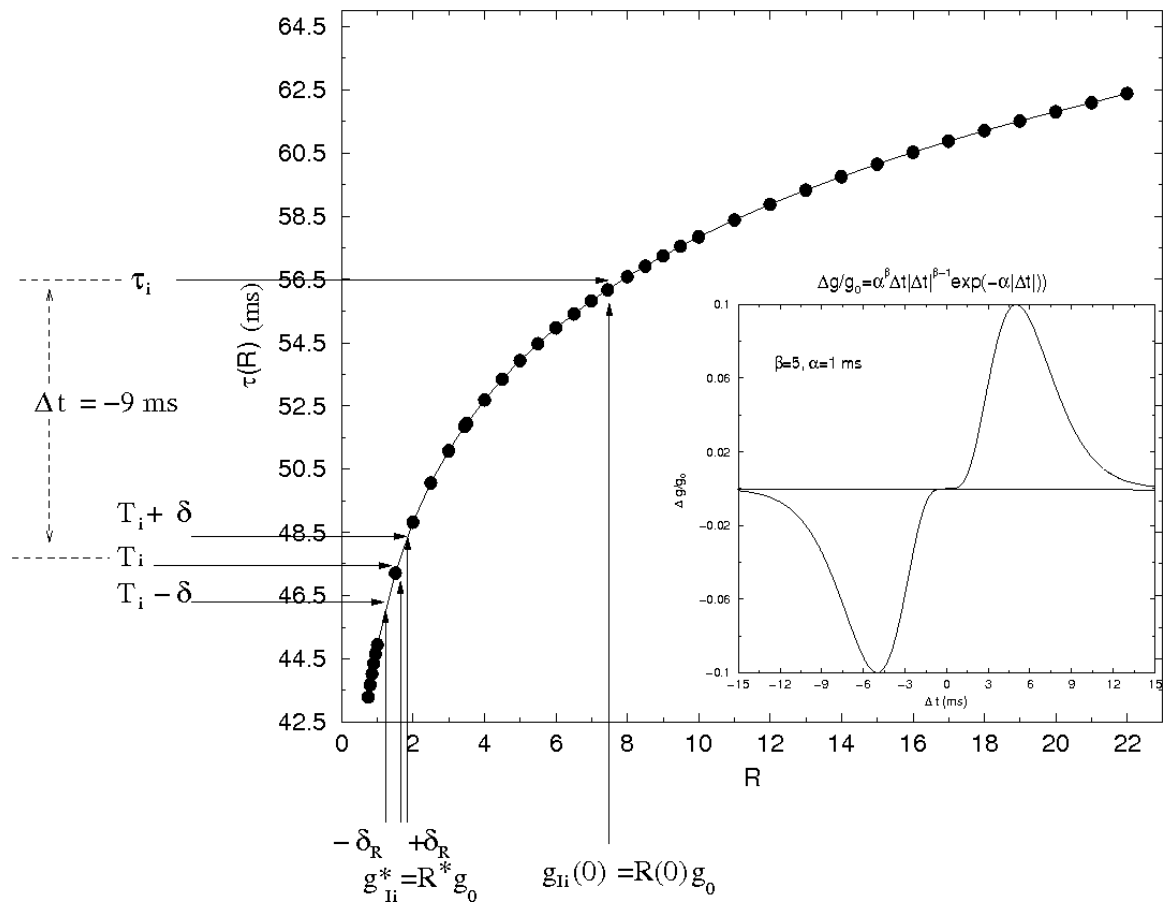


Figure 4.7 **IRU learning**: This is an example showing how the inhibitory synaptic mechanism plays a role in modulating the synaptic strength of the B→C synapse of a given delay unit in the IRU. The insert shows the inhibitory plasticity rule we use in this paper (Haas et al., 2006).

its learning.  $\tau(R)$  does not decrease beyond  $T$  for then we would have the situation where  $T > \tau(R)$ , and as we will see below, the STDP operates to send  $\tau(R) \rightarrow T$  in that case. Of course, when  $|\tau(R) - T| < \delta$ , the detection unit fires, and learning is completed. Note the importance here of  $\frac{d\tau(R)}{dR}$  for our time delay unit model.

In the opposite situation, when  $T > \tau(R)$  and  $|T - \tau(R)| > \delta$ , the learning rule must be invoked to increase  $\tau(R)$ . Neuron C produces a spike at time  $t_0 + \tau(R)$  resulting in a spike response in neuron B at time  $t_0 + \tau(R) + \epsilon$  where  $\epsilon$  corresponds to the synaptic delay, which is due to the excitatory feedback from neuron C onto neuron B. This excitation of neuron B is presynaptic to the  $B \rightarrow C$  inhibitory coupling and is identified with  $t_{pre}$  in the STDP rule. Neuron C again receives excitatory input at time  $t_0 + T$ . This is postsynaptic to the  $B \rightarrow C$  inhibitory coupling and we set  $t_{post} = t_0 + T$  so that  $\Delta t = T - \tau(R)$ .

This combination of spiking activity in neurons B and C results in an increase in the  $B \rightarrow C$  inhibitory synaptic connection. Since  $\frac{d\tau(R)}{dR} > 0$ ,  $\tau(R)$  increases, approaching  $T$  from below. This learning process continues until  $|T - \tau(R)| < \delta$  when the detection unit fires.

We present the spike sequence many times  $N = 0, 1, 2, \dots$  to the IRU to train the time delays to accurately reflect the individual ISIs in the sequence. In Figure 4.8 we show results from training two IRU units tuned to detect an ISI of  $T = 55$  ms. The first IRU has  $g_{BC}(N = 0) = 2$ , corresponding to  $\tau(R) \approx 43$  ms, so  $T > \tau(R)$ . The second has  $g_{BC}(N = 0) = 30$  leading to  $\tau(R) \approx 60$  ms, so  $T < \tau(R)$ . Each IRU trains itself on the given ISI input presented  $N = 1, 2, \dots$  times. In the detection unit we set  $\delta = 4$  ms. This is a resolution which approximates the refractory period of a typical neuron.

The training is completed when the detection unit responds with a spike output. The contribution of multiple spike pairs in the STDP learning is considered additively (Froemke and Dan, 2002). Additive rules for multiple spike pairs have also been considered in earlier works, (Kempster et al., 1999; Roberts, 1999). IRUs are trained by invoking the inhibitory STDP rule as

$$\Delta g_{BC} = \frac{g_s}{g_{norm}} \sum_j \alpha^\beta \Delta t_j |\Delta t_j|^{\beta-1} \exp(-\alpha |\Delta t_j|)$$

, with  $g_s = 1$  and  $g_{norm} = \beta^\beta e^{-\beta}$ , where  $\Delta t_j = T_C - T_{B_j}$  and when we have



one postsynaptic spike in neuron C at time  $T_C$  and  $T_{B_j}$  represents the presynaptic spike times of neuron B. In the situation when there are two postsynaptic spikes in neuron C at times  $T_{C_1}$  and  $T_{C_2}$ , such that  $T_{C_1} < T_{C_2}$  as in the case when  $T > \tau(R)$ , we compute  $\Delta t_j$  as

$$\begin{aligned}\Delta t_j &= T_{C_1} - T_{B_j}, & T_{B_j} \leq T_{C_1} \\ &= T_{C_2} - T_{B_j}, & T_{B_j} > T_{C_2} \\ &= (T_{C_1} - T_{B_j}) + (T_{C_2} - T_{B_j}), & T_{C_1} < T_{B_j} \leq T_{C_2}.\end{aligned}$$

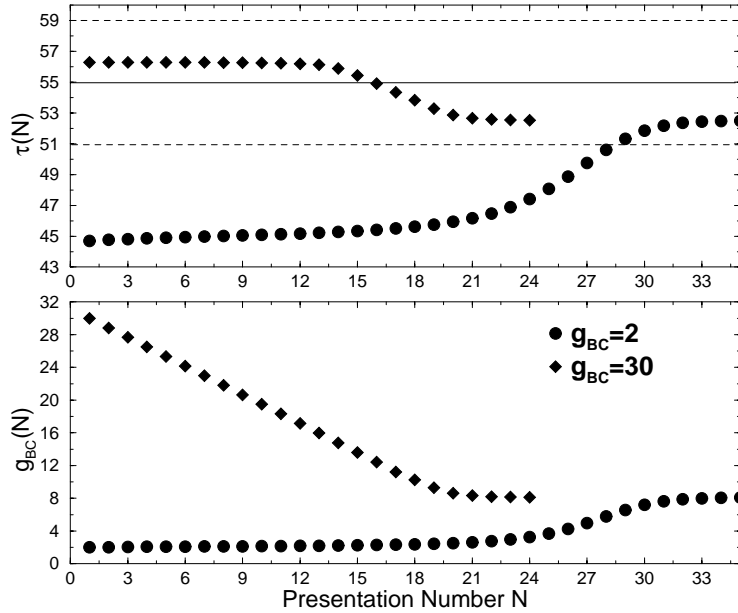


Figure 4.8 Training an IRU to learn an ISI of  $T = 55$  ms. The initial values of  $g_{BC}(N = 0)$  are set to explore the two scenarios described in the text.  $\tau(R)$  (top panel) and  $g_{BC}$  (bottom panel) are plotted as function of the number of presentations of the training sequence  $N$ . The resolution limit  $\delta = 4$  ms is shown in dotted lines for  $\tau(R)$  and  $T = 55$  ms is shown as a solid line. Parameters for the learning rule are  $\alpha = 3$ ,  $\beta = 0.5$ , for  $\Delta t \geq 0$  and  $\alpha = 4$ ,  $\beta = 0.25$  for  $\Delta t < 0$  and  $g_s = 1.0$

The parameters for the empirical learning rule were taken as  $\alpha = 0.5$ ,  $\beta = 3$  for  $\Delta t \geq 0$  and  $\alpha = .25$ ,  $\beta = 5$  for  $\Delta t < 0$ . In Figure 4.8, top panel, we show  $\tau(R)$

as function of presentation number  $N$ , and in Figure 4.8, bottom panel,  $g_{BC}(R)$  as a function of  $N$ . We see that in each case both IRUs train themselves to the same values of  $\tau(R)$  and  $g_{BC}$ . The former is within the resolution  $\delta = 4$  ms.

In Figure 4.9 we show the raster plot of activity in all the neural units in the IRU, after the training has been completed, and the IRU has learned to respond to the correct ISI input.

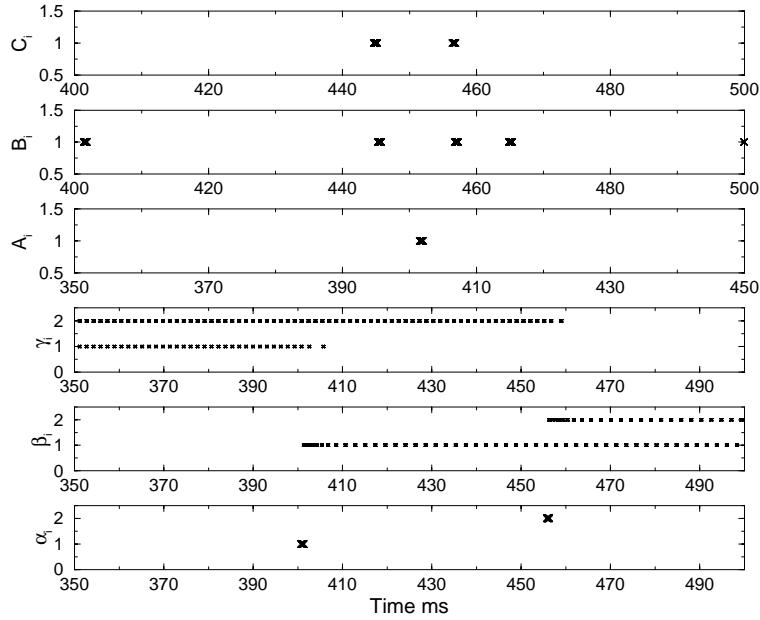


Figure 4.9 Raster plot showing the spiking activity in the SSU and the time delay subcircuitry of the IRU when the IRU is being trained to respond to input ISI pattern of 55 ms, as shown in the training example of Figure 7. Tick marks on each panel represent the spike times of that unit. For example, we see that the unit  $\alpha_i$ , ( $i=1,2$ ), which are the  $\alpha$  neurons of the SSU, receives two input spikes from the training sequence at time 400 ms and 455 ms respectively and each  $\alpha$  neuron responds just once,  $\alpha_1$  at 400 ms and  $\alpha_2$  at 455 ms, as explained in the text.

In Figure 4.10 we show an example of training the IRU on two different sets of ISI intervals. In table 4.1 below we give the details on the parameters used here. The training example shown in Figure 4.10a corresponds to the values used in Figure 4.8. The ISI sequence on which the IRUs are trained is 46 ms, 52 ms and 60 ms. The range of delay values on which this IRU can train itself is from 42

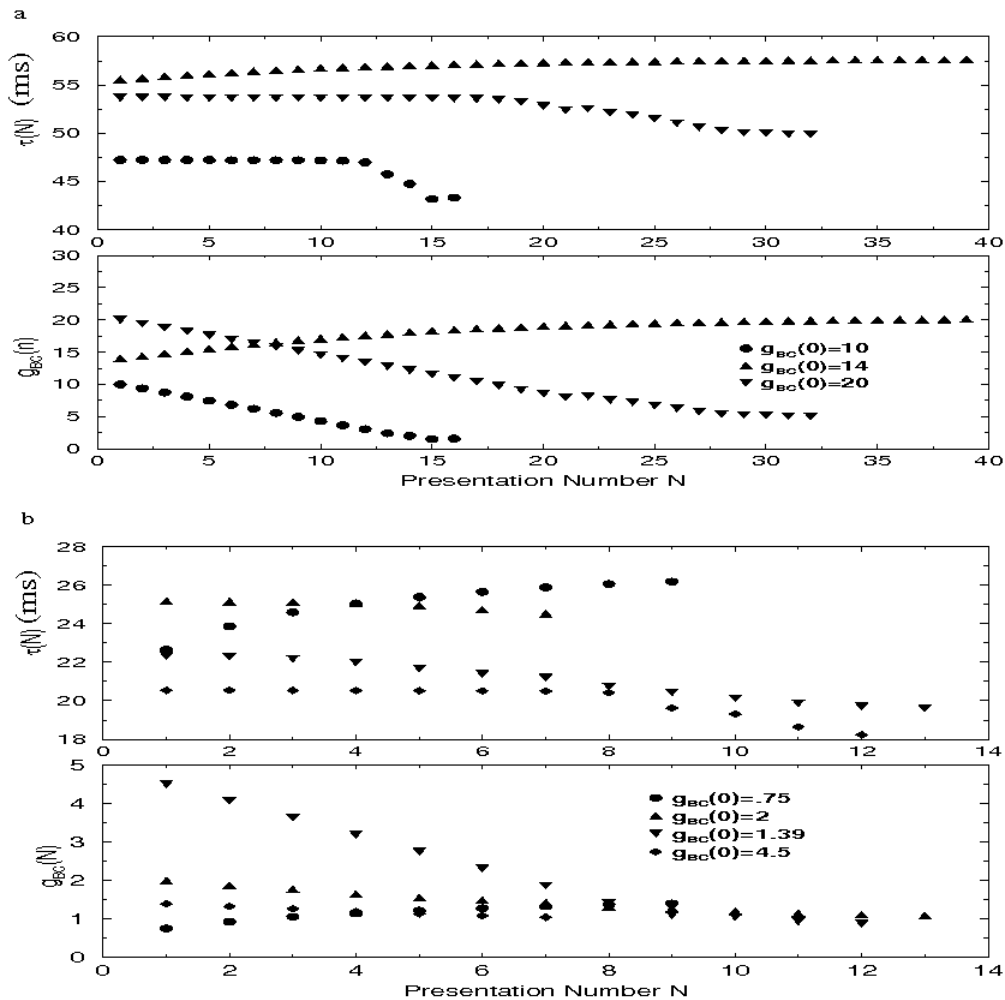


Figure 4.10 Training of IRU on two sets of ISIs. (a) Set one consists of ISI sequence 46, 52 and 60 ms, which falls in the region with the IRU delay parameters set to respond to ISI in the interval of 42 to 65 ms. Parameters for the learning rule used in training this set of ISIs are  $\alpha = 3$ ,  $\beta = .5$ , for  $\Delta t \geq 0$  and  $\alpha = 4$ ,  $\beta = 0.25$  for  $\Delta t < 0$  and  $g_s = 1.0$ . (b) Set two consists of shorter ISI intervals 19, 21, 24 and 27.3 ms. The delay subunit of the IRU has parameters set to produce delays in the range of 15 to 40 ms. Parameters for the learning rule used here are  $\alpha = 10$ ,  $\beta = 1$ , for  $\Delta t$  and  $g_s = .5$ . For both IRUs the resolution for spike detection is set at 4 ms. In each case in the top panel we plot the delays produced by the IRU as function of training number  $N$  and in the bottom panel we plot the evolution of the inhibitory synaptic strength as function of the training number  $N$ .

Table 4.1:

|                    |        | $C_M$ | $s$               | $g_A$   | $g_B$          | $g_C$   | $g_{CB}$ |
|--------------------|--------|-------|-------------------|---------|----------------|---------|----------|
| Time Delay Circuit | Fig 9a | 1     | 1                 | 0.5     | 0.5            | 0.5     | 0.5      |
|                    | Fig 9b | 0.38  | 3.5               | 0.25    | 0.25           | 0.1     | .25      |
|                    |        |       | $\alpha$          | $\beta$ | $\alpha$       | $\beta$ | $g_s$    |
|                    |        |       | $\Delta t \geq 0$ |         | $\Delta t < 0$ |         |          |
| Learning Rule      | Fig 9a |       | 3                 | 0.5     | 4              | 0.25    | 1.0      |
|                    | Fig 9b |       | 10                | 1       | 10             | 1       | 0.5      |

ms-65 ms. In Figure 4.10b, we give an example of training an IRU for shorter ISI intervals, with the time delay subcircuitry set such that it produces delays in the range, 15 ms to 40 ms. The ISI sequence shown in Figure 4.10b is 19 ms, 21 ms, 24 ms and 27.3 ms.

Finally in Figure 4.11 we test the robustness of this IRU by testing its training by an ISI sequence that has a uniform jitter of  $\pm 2$  ms for the same set of parameters as in Figure 4.8 with two types of noise source in the inhibitory synaptic plasticity rule. In Figure 4.11a we show the training of the IRU when the noise appears in the learning rule in multiplicative form as:

$$\Delta g_{BC} = \frac{g_s}{g_{norm}} (1 + \eta) \sum_j \alpha^\beta \Delta t_j |\Delta t_j|^{\beta-1} \exp(-\alpha |\Delta t_j|)$$

where  $\eta$  is uniformly distributed over  $[-1:1]$ . In Figure 4.11b we show the training of the IRU when the noise in the learning rule appears in additive form:

$$\Delta g_{BC} = \eta + \frac{g_s}{g_{norm}} \sum_j \alpha^\beta \Delta t_j |\Delta t_j|^{\beta-1} \exp(-\alpha |\Delta t_j|)$$

. where  $\eta$  is uniformly distributed over  $[-0.1:0.1]$ .

For these levels of noise, the IRU training successfully converges within the tolerance limit of  $\delta = 4$  ms. We have also tried IRU training by increasing the noise level to  $\pm 4$  ms jitter. However if the spike detection resolution window is also 4 ms, the IRUs either terminated their training prematurely by detecting spurious spikes, or the system failed to converge by presentation 200.

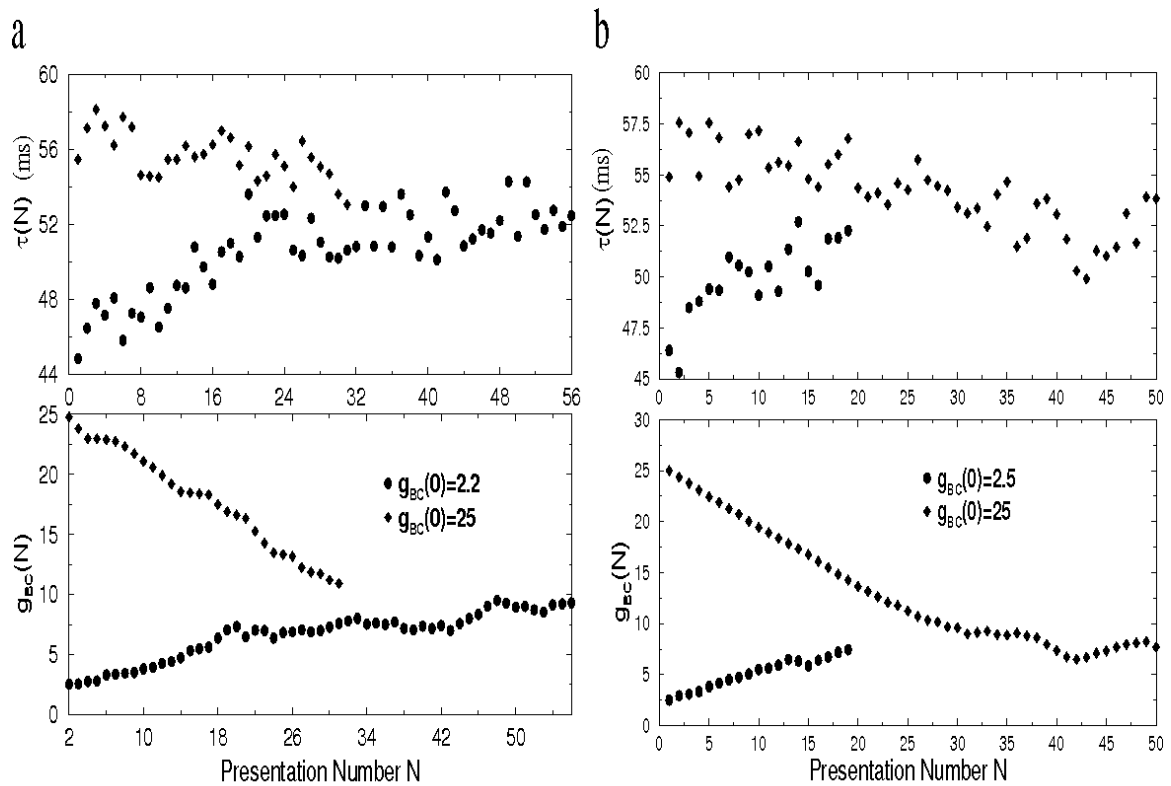


Figure 4.11 Training an IRU to learn an ISI of  $T = 55$  ms in a noisy environment. The input ISI has a uniform jitter of 2ms. The initial values of  $g_{BC}(N = 0)$  are set to explore the two scenarios described in the text.  $\tau(R)$  (top panel) and  $g_{BC}$  (bottom panel) are plotted as function of the number of presentations of the training sequence  $N$ . The resolution limit  $\delta = 4$  ms is shown in dotted lines for  $\tau(R)$  and  $T = 55$  ms is shown as a solid line. Parameters for the learning rule are  $\alpha = 3$ ,  $\beta = .5$  when  $\Delta t > 0$ , and  $\alpha = 4$ ,  $\beta = .25$  when  $\Delta t \leq 0$  and  $g_s = 1.0$ . (a) Multiplicative noise in the inhibitory synaptic plasticity learning rule. (b) Additive noise in the inhibitory synaptic plasticity learning rule.

## 4.6 Linear Map for Learning Rule

In order to analyse the dynamics of learning in the time delay circuitry of the IRU, we consider an approximation of the learning rule for evolution of the inhibitory synapse, and the delay produced by each delay unit as function of the strength of inhibitory connection from  $B \rightarrow C$ , as shown in Figure 4.12a and 4.12b. We compute an analytical expression for number of training sequence steps required for a delay unit to detect a spike within  $\delta$  ms resolution of an ISI. The approximation shown in Figure 4.12a and 4.12b results in the following,

$$\begin{aligned}
 \frac{\Delta g_I}{g_{I_0}} &= b\Delta t, \quad (|\Delta t| \leq A) \\
 &= -b\Delta t + 2Ab, \quad (A < |\Delta t| \leq 2A) \\
 &= 0, \quad (|\Delta t| > 2A)
 \end{aligned} \tag{4.12}$$

with,  $\tau = ag_I + c$  ( $g_L \leq g_I \leq g_U$ ) and  $\tau = 0$  ( $g_I < g_L$ ) and  $\tau = \tau(g_U)$  ( $g_I > g_U$ ). The fact that  $\Delta g = 0$  for  $|\Delta t| > 2A$  implies that, learning will occur only for  $\Delta t$  in the range of  $\pm 2A$  ms, or in the map  $f(g_I(N))$  the allowed variation in  $g_I(N)$  is from  $(T-c-2A)/a$  to  $(T-c+2A)/a$ . Depending on the initial inhibitory synaptic strength of  $g_I(0) = g_0$ , with above linear learning rule, the number of steps for the delay unit to set its delay output within  $\delta$  ms of actual ISI time that it needs to detect,  $N(\delta)$ , can be obtained as follows,

The trivial case of initial condition being within the  $\delta$  window of actual ISI, results in  $N(\delta) = 0$ . In the situation when  $|\Delta t| \leq A$ , the number of training iterations required for learning, is given by  $N(\delta) = 1 + n_1$ , where  $n_1$ , can be computed as follows. We begin in the region  $\Delta t = T - \tau_0 \leq A$ , which corresponds to initial inhibitory synaptic strength lying in the interval,  $(T - c - A)/a \leq g_I(0) \leq (T - c - \delta)/a$ . At each iteration step  $i$ , as shown in the example path in Figure 4.12c,  $g(i)$ , increments by amount,  $\Delta g_I(i)/(1 - ab')$ , where  $b' = bg_{I_0}$ . The total number of integer steps required for  $g_I(0) = g_0$ , to evolve to within  $\delta$  ms window

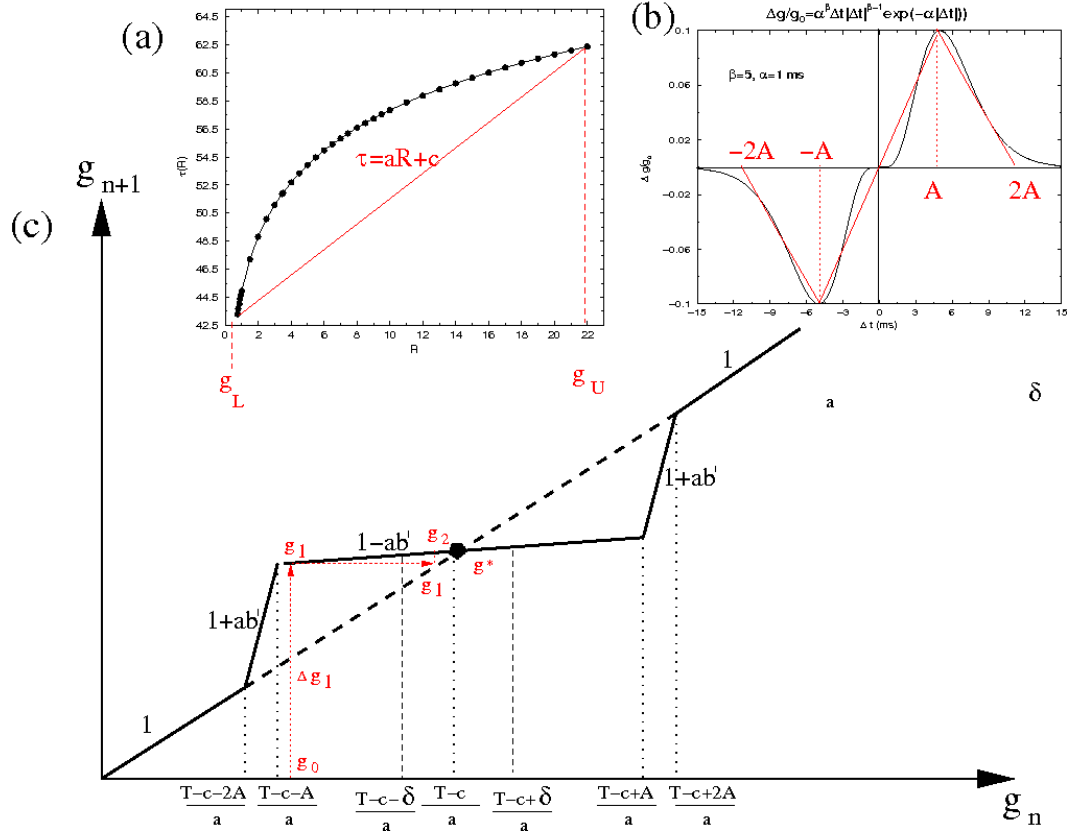


Figure 4.12 (a) Linear approximation for the delay produced by individual delay unit as function of inhibitory synaptic strength (b) Linear approximation of the learning rule observed for inhibitory synapse in entorhinal cortex. (c) The linear map for evolution of inhibitory synaptic strength is depicted. Sample trajectory for evolution of the inhibitory synaptic strength following the linear learning rule is shown in red.

of  $T$ , is then given by

$$n_1 = \left\lceil \frac{\log\left(\frac{\delta}{(|T-\tau_0|)}\right)}{\log(1-ab')} \right\rceil \quad (4.13)$$

where  $\tau_0 = ag_0 + c$  and  $[x]$ , is the largest integer less than or equal to  $x$ .

It is important to note the factor of  $b'$  appearing in the denominator of above equation. In the scheme of learning rule we have used in the main calculations, as  $\Delta t \rightarrow 0$ ,  $b'$ , which represents the slope of the learning curve approaches 0, and as we can see from above, theoretically the exact convergence of learning, i.e.,  $\Delta t = 0$

requires an infinity of training steps.

In the situation when the initial condition is such that  $A < |\Delta t| < 2A$ , the number of training iterations required is given by  $N(\delta) = 2 + n_1 + n_2$ , where

$$n_1 = \left\lceil \frac{\log\left(\frac{A}{|2A+\tau_0-T|}\right)}{\log(1+ab')} \right\rceil \quad (4.14)$$

$$n_2 = \left\lceil \frac{\log\left(\frac{\delta}{|(T-c)-a\tilde{g}|}\right)}{\log(1-ab')} \right\rceil \quad (4.15)$$

$$\tilde{g} = g_0(1+ab')^{n_1+1} + \frac{((1+ab')^{n_1+1} - 1)(2A - (T - c))}{a} \quad (4.16)$$

Linear fit to the learning rule used in the main text, which is abstracted from empirical fit to entorhinal cortex data, gives,  $A = 5\text{ms}$ ,  $b' = 0.02\text{ms}^{-1}$  and linear  $\tau(g)$  curve implies,  $a = 0.9$  ms  $c = 42.58$  ms,  $g_L = .75$  and  $g_U = 22.0$ . In this approximation the maximum number of steps will correspond to beginning with  $\Delta t$  error of  $\pm 2A = 10\text{ms}$ . For a particular case of  $T=60$  ms, and beginning with  $\tau_0 = 51\text{ms}$ , giving  $\Delta t = 9\text{ms}$ , and taking  $\delta = 1\text{ms}$ , solving the above equation gives,  $N=179$ , as total number of training cycles for the delay unit to learn.

## 4.7 Discussion

We have discussed a circuit composed of biologically motivated neurons and biologically motivated synaptic connections designed to respond selectively to a particular ISI sequence. We begin with the possibility of constructing a time delay circuit with the fewest neurons, two in this case. Then we described a three neuron time delay circuit model, abstracted from the birdsong system. The untrained IRU network has a set of time delay units constructed from three neurons, each of which has an adjustable time delay set by the strength of an inhibitory synapse. These time delays are themselves set by a synaptic plasticity rule which compares the ISIs in the ISI sequence of interest to the time delays in the time delay units and adjusts the latter until they match the presented ISIs within a certain error, taken here to be 4 ms.

The construction of the overall IRU circuit to read ISIs in the chosen sequence



is quite general and is not solely connected with the observations which motivated its construction. It could be, though we do not have anatomical or electrophysiological evidence for this at this time, that such circuitry could be used generally to recognize the specific ISI sequences produced by sensory systems in response to environmental stimuli.

It seems clear that some circuit of this kind, whether or not it is the one we construct here, may well be utilized by animals for recognition of important sensory inputs. Those inputs are transformed by the sensory system into spike sequences, and in situation when all the spikes produced are identical, all the information is represented in the spike sequence. Reading those sequences in pre-motor or decision processing is required for various functional activities.

Our time delay circuit is constructed by analogy with one found in the AFP of the song system of songbirds. It is slightly simplified by the elimination of an output nucleus (IMAN) that is used for detailed tuning of the pre-motor responses in RA (Kao et al., 2005), and it is represented by a three neuron circuit. Its instantiation in a biological system could, of course, use many more neurons as in the case of birdsong. In an ongoing work we are exploring the network dynamics of the AFP loop in order to understand the key properties of the network that play role in propagation of correlated activity over distant nuclei. In particular we are focussing on the role of inhibitory neurons and the intrinsic dynamics of individual neurons in each of the nuclei in the AFP loop in maintenance of long range correlations in firing activity. The detection of such long range correlations in a large network, as has been shown experimentally (Kimpo et al., 2003), will provide a strong motivation for the possibility of detecting structures like the IRU, in anatomical and electrophysiological studies.

The time delay of this three neuron circuit is set in overall scale by the membrane capacitance of the neurons, and it is tuned in detail by the strength of one of the internal inhibitory connections. This inhibitory synaptic strength is modulated by inhibitory synaptic plasticity using rules recently observed by (Haas et al., 2006). The regime of operation of the IRU utilizing such time delay circuits, is governed by  $\tau(R)$ , and the IRU can train itself on ISIs in the interval  $[\tau(R_L), \tau(R_U)]$

We gave examples of the training of IRU network using an inhibitory synaptic plasticity rule. The raster plot of spike outputs of the fully trained network are

shown in Figures 4.9.

Finally in section 4.6, we derived an analytic expression for the number of steps required for convergence in learning rule, by considering a linear approximation to the actual learning curve preserving the essential features of the rule.

Our analysis of the IRU presented in this chapter does not address the response of an IRU to a desired ISI sequence when it is embedded in an environments with many extraneous spikes, and it does not address the reliability of the synaptic connections as a potential source of error in reading ISI sequences. For example, suppose the second spike in a sequence is missing because of failure of a synapse to fire when expected. How does the IRU performance degrade under such circumstances. It may be that the actual biological environments in which IRUs operate, assuming them to be present, require a statistical measure of detection efficacy. This would need to be carefully connected with the dramatic response of HVC neurons projecting to RA when stimulated by BOS as seen in the work of Coleman and Mooney (Coleman and Mooney, 2004). In connecting the ideas here about reading ISI sequences with models of the NIf and HVC nuclei in the avian birdsong system one will be able to address this and other issues in a quantitative fashion.

While we have not focused here on applying the construction of an interspike interval recognition unit (IRU) to the birdsong system which provided one of the motivating biological examples for it, we will make some speculations in terms of its possible role in birdsong learning as we end the discussion. First, we wish to repeat that to our knowledge there is no anatomical evidence at this time of the neural circuitry we have developed in the birdsong system nuclei or in other biological contexts.

The possible presence of an IRU in the birdsong system would provide an explanation of the idea of a “template” of the bird’s tutor’s song thought to be implanted in juvenile male birds during the early, so-called sensory period, of their lives. Subsequent to the template’s development, a second period of song learning, called the sensory-motor period, consists of the bird signing to itself and “comparing” its own vocalization to that in the template until the tutor’s song is reproduced in the young adult bird. These patterns of learning are widely discussed in the literature, and we have merely summarized them (Brainard and

Doupe, 2002).

Our construction might fit these observations as follows: in the sensory period the juvenile bird has time delay units with time delays approximately tuned by genetic instructions to the expected tutor song's ISIs. These approximate delays, our  $\tau(R)$ 's, are then more finely tuned by the inhibitory plasticity rule as we have discussed.

At the end of the sensory period, the IRU, which we would further conjecture to lie within the nucleus NIf would provides the final auditory input to HVC, itself lying at the sensory-motor junction in the song system. Once tuned to the ISIs representing the coding of the tutor song as it arrives at the central nervous system nucleus NIf, the IRU (or the many IRUs representing the segmented tutor song) functions as a nonlinear filter for auditory signals passing from NIf to HVC and thus into the pre-motor pathway (Brainard and Doupe, 2002).

Once the nonlinear filter is established, the bird can move into the sensory-motor phase of its learning wherein it sings to itself and tunes the junctions between nucleus HVC and nucleus RA through changing excitatory connections via excitatory synaptic plasticity (Abarbanel et al., 2004a). When the bird's own song as produced by instructions from RA to the bird's songbox has been tuned to the tutor song, it will effectively pass through the nonlinear filter in NIf, conjectured to be comprised of IRUs, and that will signal the end of the learning period.

It hardly need be emphasized that while the construction here might suggest all this, it certainly does not demonstrate it in any detail. There is substantial work to be done, both in the understanding of the pre-motor pathway and the exploration of the details of the auditory feedback.

Concise presentation of the results appearing in this chapter are published in (Abarbanel H.D.I., and Talathi S.S., Physical Review Letters, 96, 148104, 2006). The dissertation author was the primary researcher in this project.

# 5

## Implementation of neuronal time delay circuitry in hardware

In the last chapter we abstracted a time delay circuitry (TDC) from the avian song system and studied its function in producing precise time delays on the order of 10 ms to 100 ms, tunable through the intrinsic inhibitory synaptic coupling strength. In this chapter, we implement the same circuitry in hardware by designing an electronic version of a type I neuron model. The circuitry for type I neuron model is designed using Pspice software and the results of the circuit are compared with numerical simulations. We then implement the Pspice design on a breadboard. This hardware neuron model is then coupled to neuron models of type II, developed by (Volkovskii, 2003) in our lab, through circuits of chemical synapse models to implement the TDC. As discussed in the last chapter, the mechanism of time delay is dependent on the strength of inhibitory coupling from neuron B to neuron C and the rebound spiking property of the neuron C. The time delay mechanism of the TDC is independent of the bifurcation dynamics of the underlying neuron model. We therefore couple our implementation of type I neuron dynamics with the neuron models of type II designed by (Volkovskii, 2003) to demonstrate the principle of the working model of the TDC in hardware. Our implementation of the TDC with different underlying neural units also provides an evidence for the robustness of the time delay scheme that is implemented. This circuit implementation of the TDC which is based on biophysical principles, is the first step in the direction of neuromorphic modelling, an emerging branch of science, which aims to

implement neurophysiological phenomenon in silicon to increase our understanding of nervous system and its ability to perform computations.

## 5.1 Designing Electronic Neuron

The model of type I HH neuron which we implement in electronics is given by the following set of four coupled ordinary differential equations,

$$\begin{aligned}
C_M \frac{dV(t)}{dt} &= I_{In} + g_{Na}m(t)^3h(t)(V_{Na} - V(t)) \\
&\quad + g_Kn(t)^4(V_K - V(t)) + g_L(V_L - V(t)) \\
\frac{dm(t)}{dt} &= \alpha_m(1 - m(t)) - \beta_m m(t) \\
\frac{dh(t)}{dt} &= \alpha_h(1 - h(t)) - \beta_h h(t) \\
\frac{dn(t)}{dt} &= \alpha_n(1 - n(t)) - \beta_n n(t)
\end{aligned} \tag{5.1}$$

The nonlinear functions,  $X = \{\alpha_m, \beta_m, \alpha_h, \beta_h, \alpha_n, \beta_n\}$  are given by,

$$\alpha_m(V(t)) = \frac{.32(13-(V(t)-V_{th}))}{e^{\frac{(13-(V(t)-V_{th}))}{4.0}} - 1} \quad \beta_m(V(t)) = \frac{0.28((V(t)-V_{th})-40)}{e^{\frac{((V(t)-V_{th})-40)}{5}} - 1}$$

$$\alpha_h(V(t)) = .128e^{\frac{17-(V(t)-V_{th})}{18}} \quad \beta_h(V(t)) = \frac{4}{e^{\frac{40-(V(t)-V_{th})}{5}} + 1}$$

$$\alpha_n(V(t)) = \frac{0.032(15-(V(t)-V_{th}))}{e^{\frac{(15-(V(t)-V_{th}))}{5}} - 1} \quad \beta_n(V(t)) = \frac{0.5}{e^{\frac{(V(t)-V_{th})-10}{40}}}$$

with  $V_{th} = -65\text{mV}$ .

In order to implement the dynamics, in electronics, we first scale the voltage to lie between, 0 and 6 volts, as  $v_e(t) = .043V(t) + 3.86$ , where  $v_e(t)$ , is the voltage variable for the dynamics to be implemented in electronics and  $V(t)$  is the actual voltage variable as given by above set of differential equations (Equation 5.1). The scaling is required by the saturation constraint on the electronics used to design the neuron model.

The task of implementing the HH model in electronics, begins with circuit design to simulate the nonlinear functions,  $X = \{\alpha_m, \beta_m, \alpha_h, \beta_h, \alpha_n, \beta_n\}$ .

In Figure 5.1a we show a simple inverting op-amp configuration circuit design for piecewise continuous function generation, (Horowitz and Hill, 1989). The

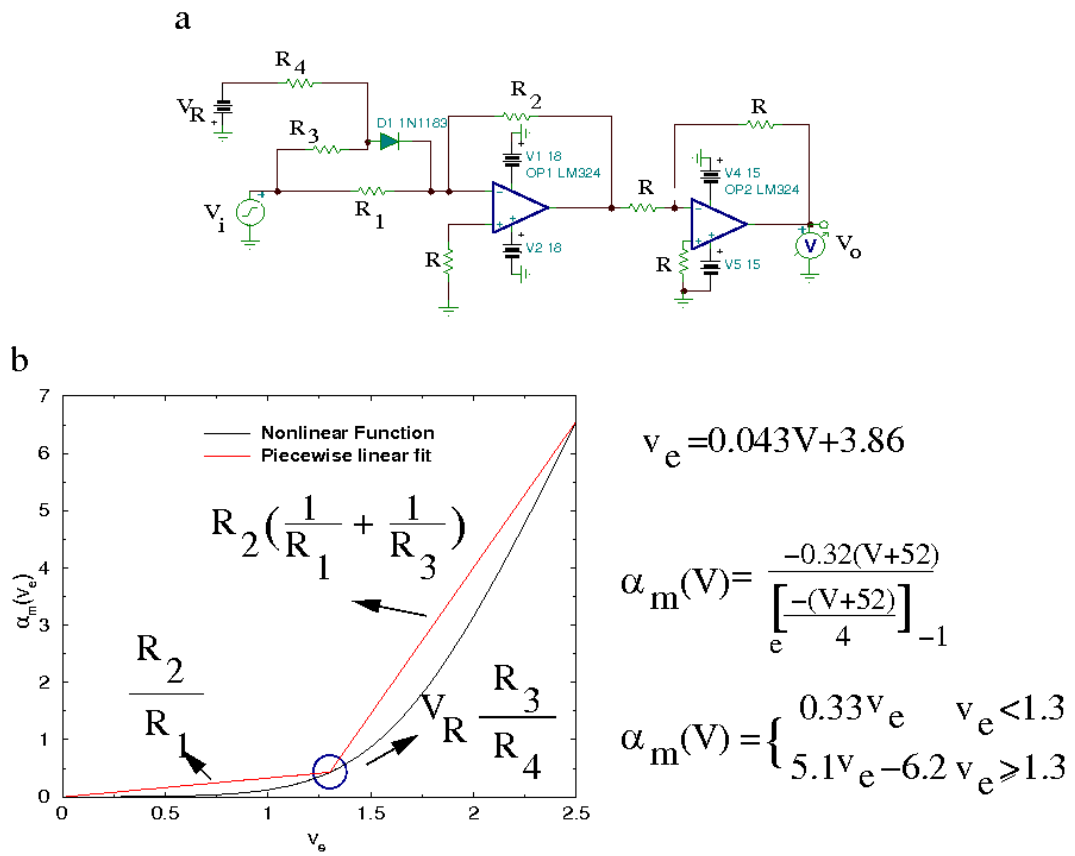


Figure 5.1 Piece wise linear approximation of  $\alpha_m$ .

output of the first opamp is fed to another inverting opamp configuration, such that we get the response function for the circuit as shown in the Figure 5.1b. For input voltage  $v_e < V_R \frac{R_3}{R_4}$ , the diode is off and the gain function of the opamp is  $G = \frac{V_o}{V_i} = \frac{R_2}{R_1}$ . For  $v_e \geq V_R \frac{R_3}{R_4}$ , the diode shorts the resistor  $R_3$  to the virtual ground of the opamp and as a result the gain function of the opamp modifies to  $G = R_2(\frac{1}{R_1} + \frac{1}{R_3})$ . As shown in Figure 5.1b, the circuit parameters are chosen to provide a piecewise continuous approximation to the nonlinear function  $\alpha_m(V)$ .

In Figure 5.2, we implement the circuitry for nonlinear functions  $\alpha_m(V)$  and  $\beta_m(V)$  entering the differential equation for gating variable  $m(t)$  in equation 5.1. The circuitry is implemented by approximating the nonlinear functions by piecewise approximation as explained above. The circuit parameters are chosen to fit the nonlinear functions. In Figure 5.2b the Pspice simulation result of the circuitry implemented to fit  $\alpha_m(V)$  is shown (in brown) along with the actual nonlinear function  $\alpha_m(V)$  (in lime), as function of ramping input voltage  $v_e$ . The intrinsic nonlinearity in the diode, smoothes out the discontinuity in the piecewise approximation and we get a very good fit of the circuit with the actual function. Similarly in Figure 5.2c, we give the schematic of circuit implementation for nonlinear function  $\beta_m(V)$ . The key difference in the implementation of circuit for  $\beta_m$  is that the nonlinear function  $\beta_m$  is a monotonic decreasing function of input voltage  $v_e$ . It is reflected in the orientation of the diode in the circuit shown in Figure 5.2c. In Figure 5.2d, the Pspice implementation of the circuit (in brown) is compared with actual nonlinear function (in lime) for ramping input voltage  $v_e$ .

In simulating the nonlinear functions  $\alpha_m$  and  $\beta_m$  above, the functions in the circuits were scaled by a factor of 0.5, due to the saturation constraints of the opamps used. The scaling back to the original form is done when these circuits enter the larger circuit for simulation of the differential equation for gating variable  $m(t)$  in Figure 5.5.

In Figures 5.3 and 5.4 the circuit implementations for the nonlinear functions  $\alpha_X$  and  $\beta_X$ , ( $X=h,n$ ), are given. We implement these circuits along the similar lines as explained above. Note the response function of nonlinear function  $\beta_h$  in Figure 5.3d, to a ramping input voltage  $v_e$ . The sigmoidal response is obtained with the circuit design shown in 5.3c, with an additional diode placed between the inverting terminal and the output terminal of the first opamp which modulates

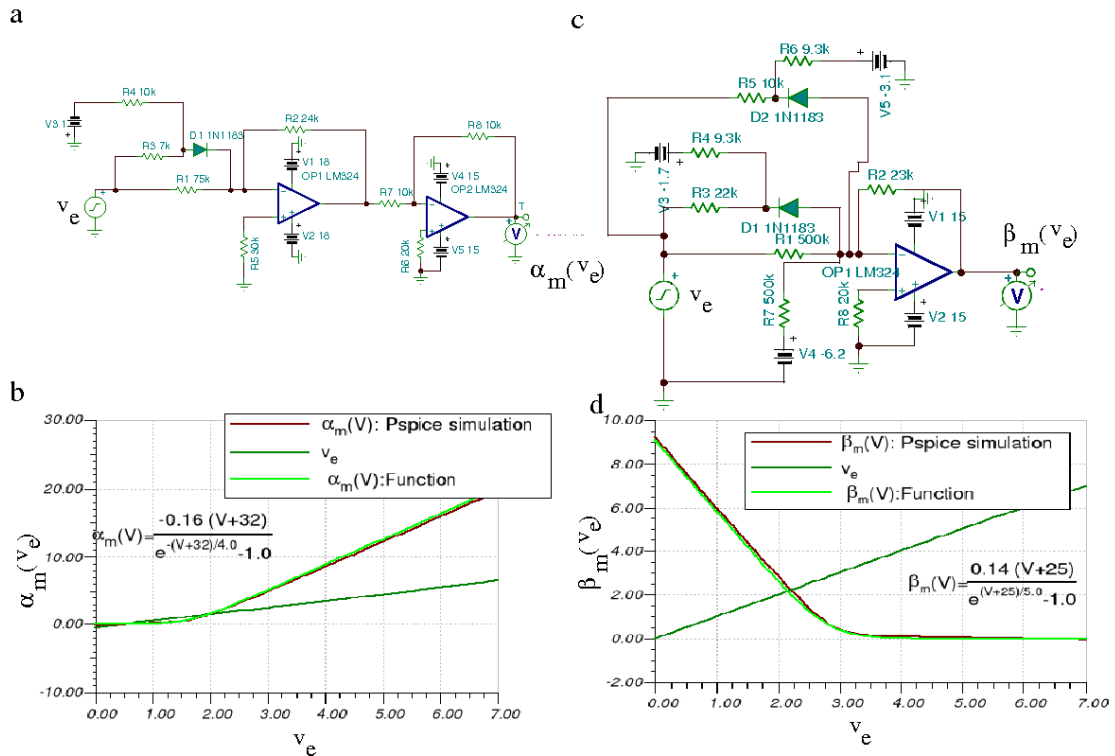


Figure 5.2 (a) Schematic of the circuit to simulate nonlinear function  $\alpha_m(V)$ . (b) Response of the circuit to linear ramp input voltage  $v_e$ . The x-axis is  $v_e$  and the y-axis represents the output,  $\alpha_m(v_e)$ . (c) Schematic of the circuit to simulate nonlinear function  $\beta_m(V)$ . (d) Response of the circuit to linear ramp input voltage  $v_e$ . The x-axis is  $v_e$  and the y-axis represents the output,  $\beta_m(v_e)$ .



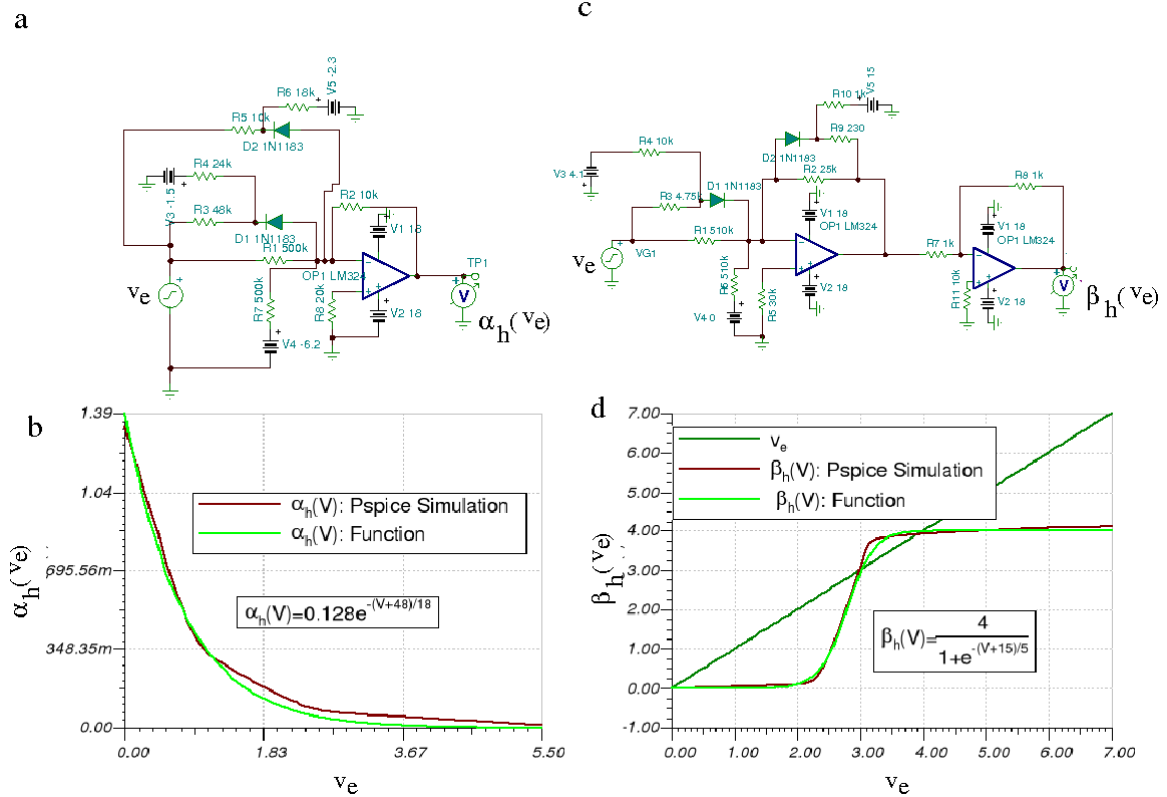


Figure 5.3 (a) Schematic of the circuit to simulate nonlinear function  $\alpha_h(V)$ . (b) Response of the circuit to linear ramp input voltage  $v_e$ . The x-axis is  $v_e$  and the y-axis represents the output,  $\alpha_h(v_e)$ . (c) Schematic of the circuit to simulate nonlinear function  $\beta_h(V)$ . (d) Response of the circuit to linear ramp input voltage  $v_e$ . The x-axis is  $v_e$  and the y-axis represents the output,  $\beta_h(v_e)$ .

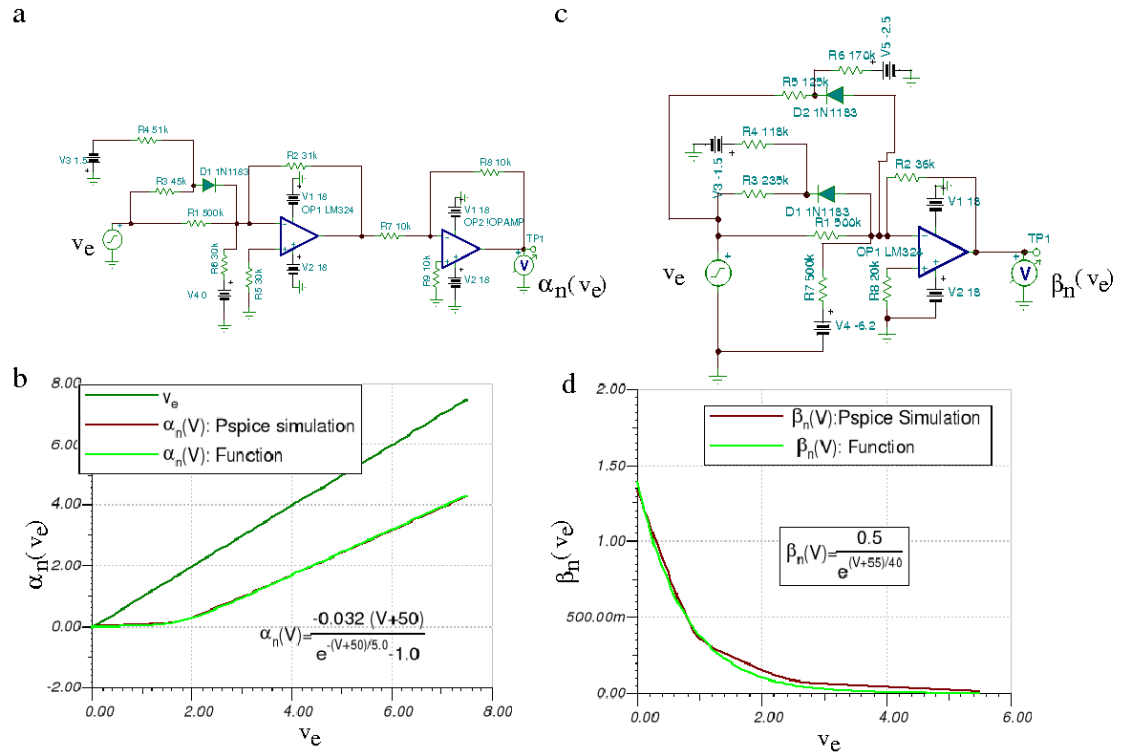


Figure 5.4 (a) Schematic of the circuit to simulate nonlinear function  $\alpha_n(V)$ . (b) Response of the circuit to linear ramp input voltage  $v_e$ . The x-axis is  $v_e$  and the y-axis represents the output,  $\alpha_n(v_e)$ . (c) Schematic of the circuit to simulate nonlinear function  $\beta_n(V)$ . (d) Response of the circuit to linear ramp input voltage  $v_e$ . The x-axis is  $v_e$  and the y-axis represents the output,  $\beta_n(v_e)$ .

the gain of the circuit to produce the required sigmoidal response. As shown in the Figures 5.3 and 5.4, we also present the Pspice simulation results of the circuit implementations along with the response of the actual nonlinear functions,  $\alpha_h$ ,  $\beta_h$ ,  $\alpha_n$  and  $\beta_n$  to monotonically linearly increasing input voltage  $v_e$ .

We now have the circuit elements required to solve the differential equation for the gating variables  $m(t)$ ,  $h(t)$  and  $n(t)$ , which control the spiking dynamics of the membrane voltage,  $V(t)$  in the HH model.

After the design for all nonlinear functions, the next step is to implement the differential equations for the gating variables,  $m(t), n(t)$  and  $h(t)$ . In Figure 5.5 inset, we show the block diagram of circuit implementation for solving the first order kinetic equation for gating variable  $m(t)$ ,  $\frac{dm(t)}{dt} = \alpha_m(1 - m(t)) - \beta_m m(t)$ . The input voltage  $V$ , drives the circuit elements for nonlinear function  $\alpha_m(V)$  and  $\beta_m(V)$ , which are scaled by a factor of 2 to compensate for the scaling of 0.5 in the design of the nonlinear functions above. The output from the  $\alpha_m$  circuit is fed into Adder<sub>1</sub> and the same output also enters the inverter block. The second input into the Adder<sub>1</sub> is from the  $\beta_m$  circuit. The output of Adder<sub>1</sub>, which is  $\alpha_m(V) + \beta_m(V)$  is then fed into multiplier chip AD633, which also receives feedback input from the output of the integrator, the gating variable  $m(t)$ . The input to the integrator is through Adder<sub>2</sub>, which produces at its output the function  $-\alpha_m(V) + m(t)(\alpha_m(V) + \beta_m(V))$ . Finally the integrator circuit perform the integration operation on the input it receives from Adder<sub>2</sub> and we get the implementation of the differential equation for gating variable  $m(t)$ . The value of the capacitor in the integrator component is chosen such that we get integration on the time scale of msec, as is the case in the actual differential equation. The circuit block diagram for the adder, inverter and the integrator components of the circuit for solving the differential equation for the gating variable  $m(t)$  are shown in Figure 5.5b. The entire circuit implementation is given in Figure 5.5a.

We next test the circuit for gating variable  $m(t)$ , as designed above in Pspice for a triangular voltage input. The results of Pspice implementation of the circuit and the corresponding numerical simulation results are compared in Figure 5.6. As can be seen from the Figure, the output of the circuit matches very well with actual numerical simulation results.

In the same spirit we implement the circuits for solving the differential equations

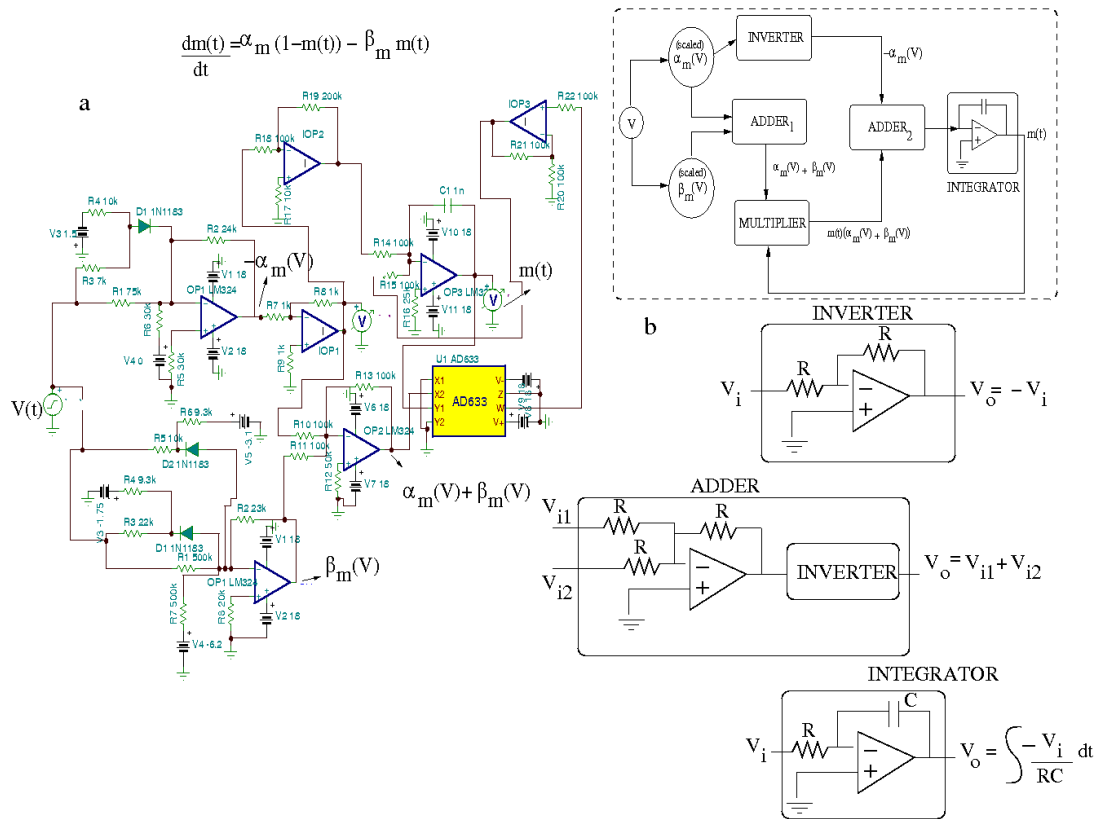


Figure 5.5 Circuit to simulate the differential equation for  $m(t)$ . (a) The schematic circuit implementation for simulating the differential equation for the gating variable  $m(t)$ . In inset we show the block diagram of components involved in the circuit implementation. (b) The schematic of circuit elements i) Inverter, ii) Adder and iii) Integrator, used in the differential equation implementation are shown.

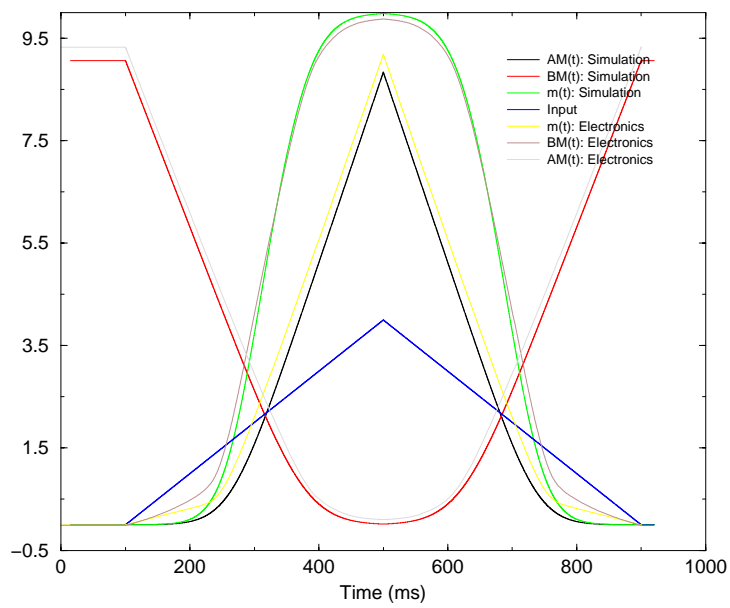


Figure 5.6 Results comparison of simulation v/s Pspice implementation of  $m(t)$ , dynamics, for a triangular input pulse

for the gating variables  $h(t)$  and  $n(t)$ . The schematic circuit diagrams for the implementation of both these circuits are shown in Figures 5.7 and 5.8.

The results of implementing above circuits in Pspice for a triangular voltage input are shown in Figures 5.9 and 5.10. These results match very well, the actual output generated by solving the differential equations numerically.

After the implementation of circuits for solving the differential equations for the gating variables,  $m(t)$ ,  $h(t)$  and  $n(t)$ , the next step is to integrate all these circuit elements into the circuit designed to solve the differential equation for the membrane voltage  $V(t)$ , as given by HH dynamics in equation 5.1. In Figure 5.11a, we show the schematic block diagram of the circuit design to solve for  $V(t)$ . As can be seen from the block diagram, the implementation of voltage dynamics  $V(t)$ , requires input from the gating variables,  $m(t)$ ,  $h(t)$  and  $n(t)$ . After appropriate multiplication using the multiplier chip AD633, and scaling of the voltages through the voltage scaling circuit and the potentiometer as shown in Figures 5.11b and 5.11c respectively, the integrator receives inputs through the Adder element and we have the integration for  $V(t)$  through the integrator.

In Figure 5.12, we implement the above circuit for type I HH neuron in bread-board.

## 5.2 Time Delay Circuitry in Electronics

With the design of type I neuron model, we are in a position now to implement the TDC explored in the last chapter in electronics. (Volkovskii, 2003), in our group developed an electronic models for implementing type II neuronal dynamics in hardware. He also designed an electronic circuitry to implement the chemical synapses. The circuit for the chemical synapse simulates the following synaptic current equations,

$$I_{syn}(t, V) = g_{syn}S(t)(E_{syn} - V) \quad (5.2)$$

. where  $g_{syn}$  is the synaptic conductance in  $\text{mS}/\text{cm}^2$ ,  $E_{syn}$ , is the reversal potential for the synapse in mV. For inhibitory synapse we set it to -82 mV, which is scaled to lie between 0 and 6 V, for implementation in the circuit.  $S(t)$  is the gating

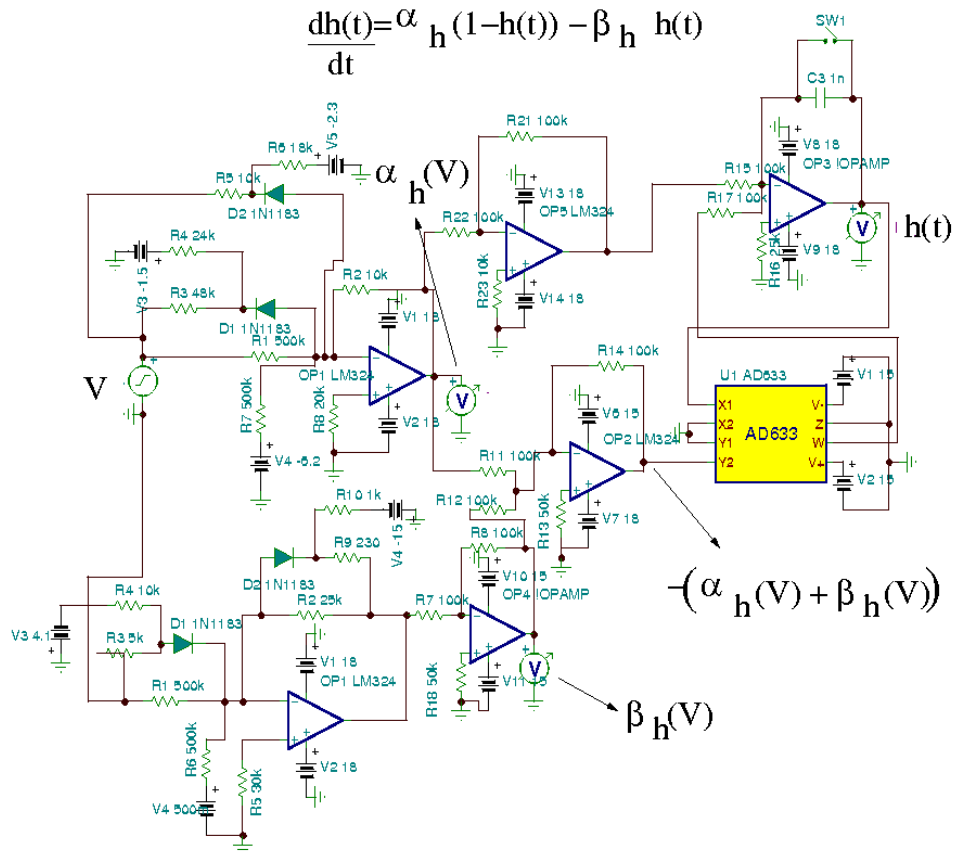


Figure 5.7 Schematic circuit diagram for solving the first order kinetic equation for gating variable  $h(t)$ .

$$\frac{dn(t)}{dt} = \alpha_n (1 - n(t)) - \beta_n n(t)$$

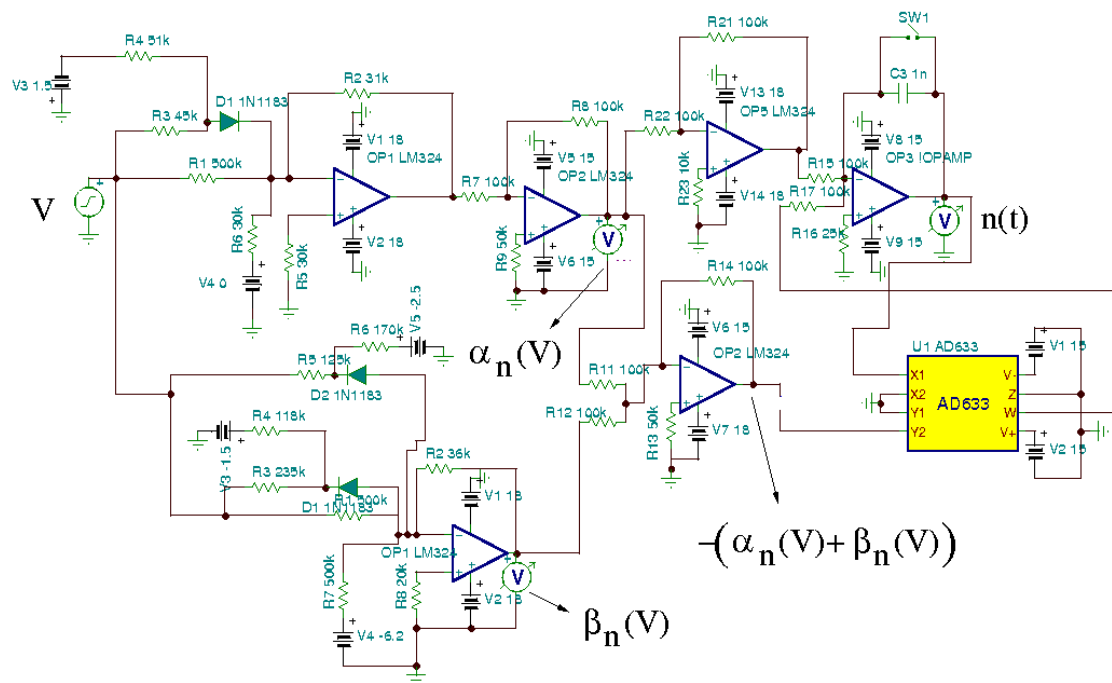


Figure 5.8 Schematic circuit diagram for solving the first order kinetic equation for gating variable  $n(t)$ .



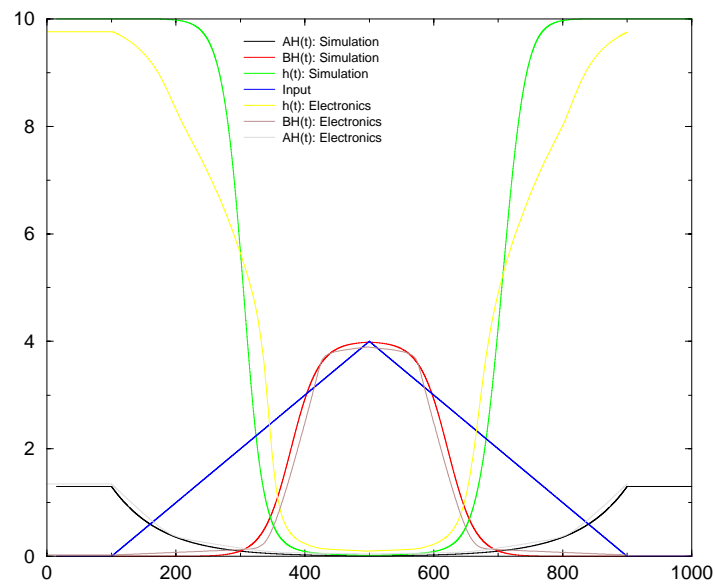


Figure 5.9 Results comparison of simulation v/s Pspice implementation of  $h(t)$ , dynamics, for a triangular input pulse

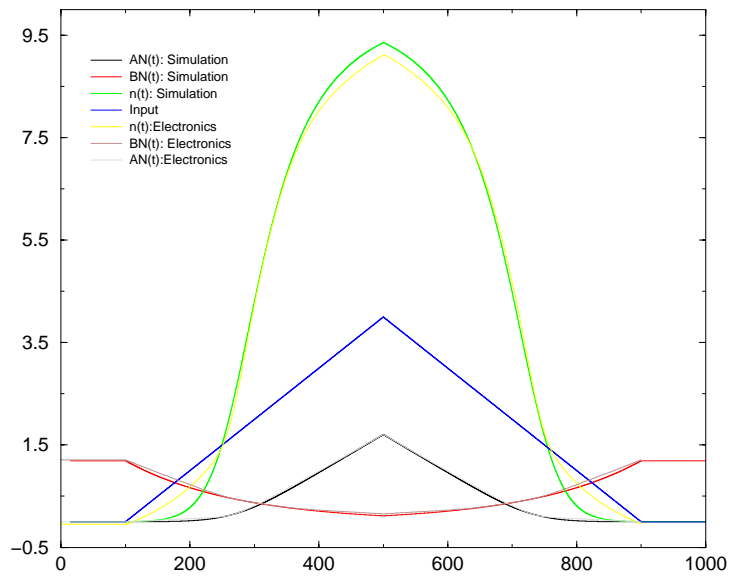


Figure 5.10 Results comparison of simulation v/s Pspice implementation of  $n(t)$ , dynamics, for a triangular input pulse

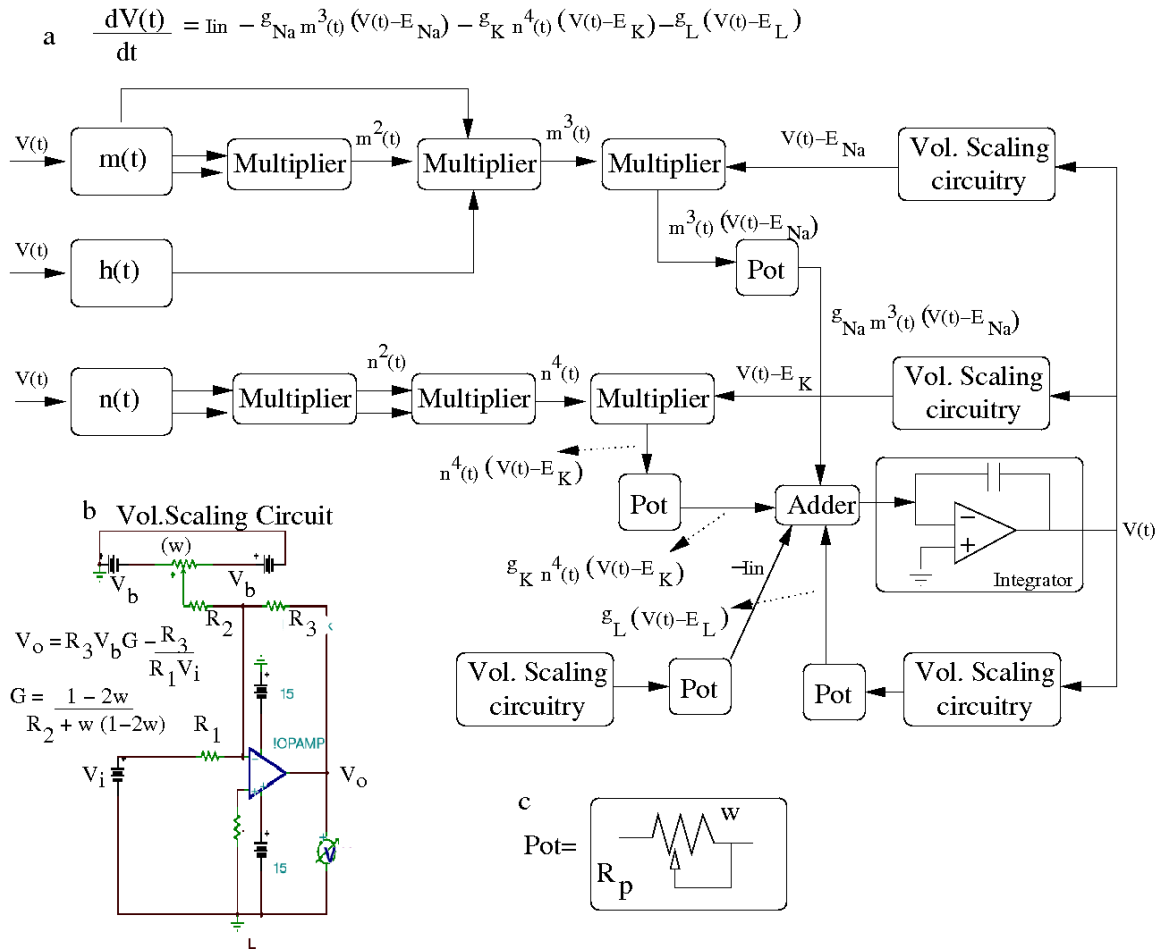


Figure 5.11 (a) Schematic circuit block diagram to implement the differential equation for the Voltage variable in Equation 5.1. (b) Schematic circuit diagram for the voltage scaling circuitry used in (a) to set the reversal potential of the various currents, in the HH equation. (c) The potentiometer configuration to scale the ionic currents with appropriate conductance values.

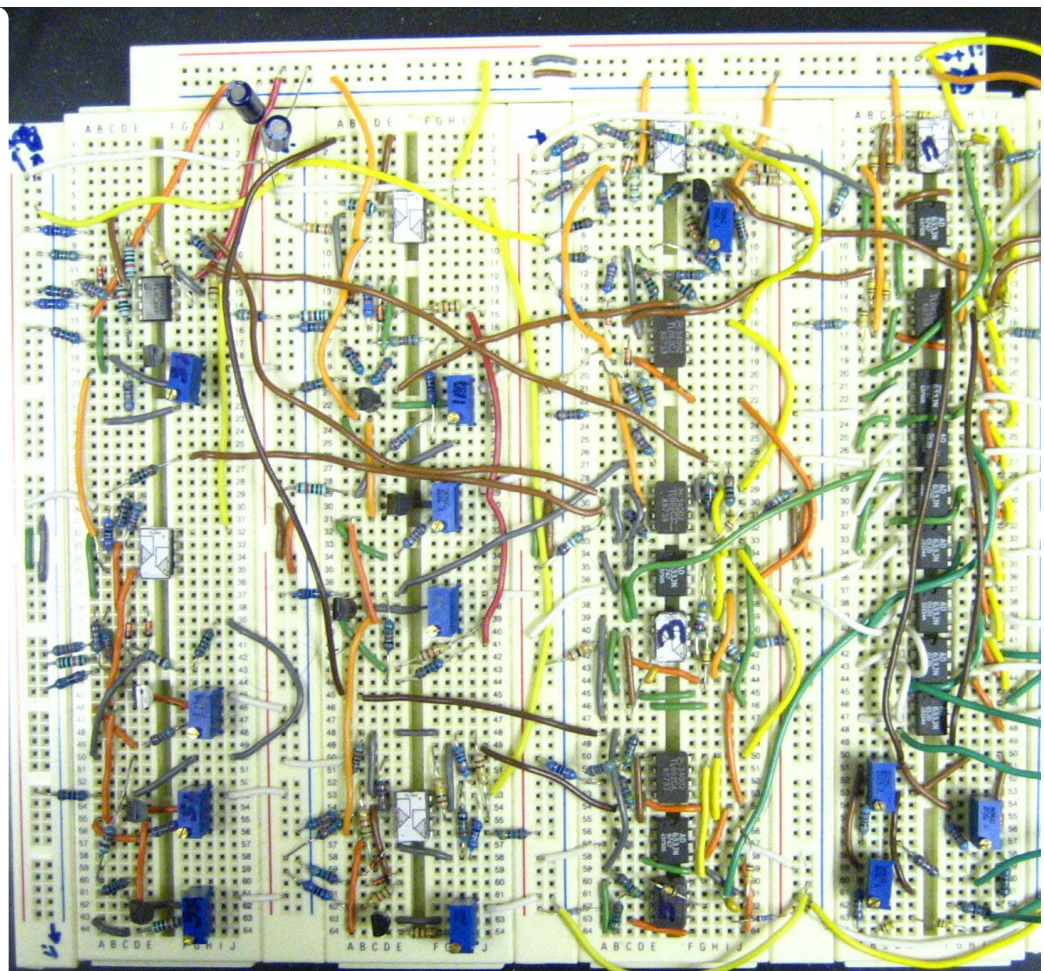


Figure 5.12 HH model of type I circuitry implemented on a breadboard.

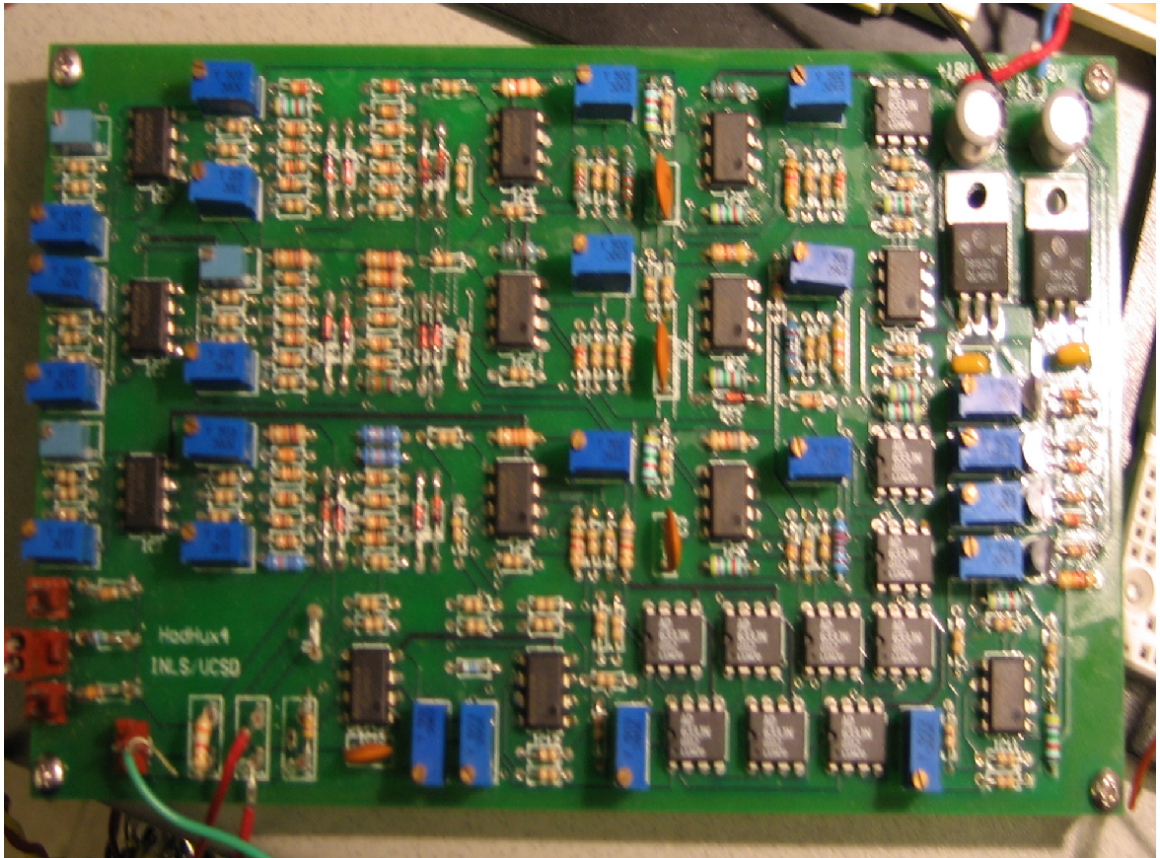


Figure 5.13 PCB implementation of type II HH neuron model (adapted from Volkovskii)

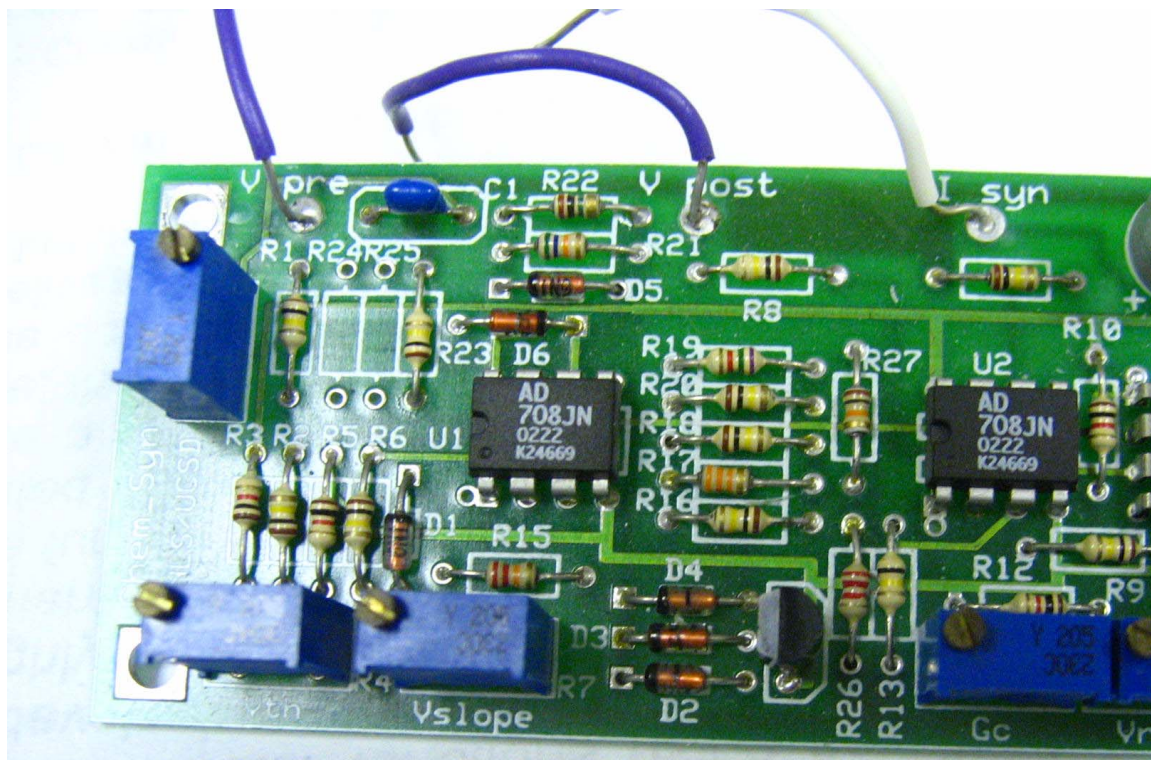


Figure 5.14 PCB implementation of the chemical synapse model (adapted from Volkovskii, with permission)

variable that satisfies the following first order kinetic equations,

$$\frac{dS}{dt} = \frac{S_0(V_{pre}) - S(t)}{\tau_{syn}(S_1 - S_0(V_{pre}))} \quad (5.3)$$

When  $V_{pre}$  is above threshold for spiking,  $S_0(V_{pre})$  is set to 1 and is 0 otherwise. The rise time for the synapse is  $\tau_{syn}(S_1 - 1)$  and the fall time for the synapse is  $\tau_{syn}S_1$ .

In Figure 5.13, we show a picture of PCB implementation of type II neuron model by (Volkovskii, 2003). In Figure 5.14, the PCB implementation of chemical synapse by (Volkovskii, 2003) is shown (Adapted with permission from (Volkovskii, 2003)). We couple the neuron model of type I implemented in this chapter as discussed in the previous section to the type II neuron models of (Volkovskii, 2003) as shown in the schematic block diagram in 5.15. Power supply source of 15 V is used to drive the circuit elements. A signal generator produces an input spike at time  $t_0$ , which feeds into neuron A and neuron B simultaneously as shown in Figure 5.15. Neuron B is the type I neuron designed in this chapter. The constant DC current  $I_{In}$  in the neuron is set such that it is in tonic spiking regime.

As discussed in the last chapter, depending on the strength of inhibition from neuron B onto neuron C, through the inhibitory chemical synapse, neuron C produces a rebound spike  $t_0 + \Delta T$  ms, later. The output from each neuron is recorded on the oscilloscope. In Figure 5.16, we show the output of the TDC in operation. In pink is the spike output from Neuron B, which is tonically spiking at approximately 225 Hz. The voltage output from neuron C which is being constantly inhibited by neuron B is shown in cyan. Neuron A is shown in yellow. It receives an input spike at time  $t_0$ . Neuron B also receives the same input resetting its time for spiking. The spike from neuron A, then inhibits neuron B, and as seen in the oscilloscope output, it produces a strong hyperpolarization in the voltage response of neuron B. During this period the inhibition on neuron C is removed and it produces a rebound spike a time  $t_0 + \Delta T$  ms later. For the particular choice of circuit parameters in this examples  $\Delta T \approx 10$ ms. In Figure 5.17 we give another example demonstrating the working principle of the time delay circuitry in electronics. In this case, we increase the strength of the inhibitory coupling from neuron B to neuron C and as a result the delay produced by the system is  $\Delta T \approx 15$ ms. The

operation of the time delay circuitry can be slowed by tuning the capacitor in the neuron models to obtained time delays on the order of few tens of milliseconds.

### 5.3 Conclusion

In this chapter we develop an electronic circuitry to implement type I neuronal dynamics, as given in Equation 5.1. It is a first step in the direction of neuromorphic computing, where in the endeavor is to develop artificial engineering systems that employ physical properties of the biological nervous system to perform certain task. We then couple the neuron circuitry to circuit implementation of type II neuron model through a chemical synapse model and provide a working demonstration of an electronic time delay circuitry which can be tuned precisely in real time to obtain delays on the order of 10-100 ms. As the results from the implementation of the circuitry show, the operation of the time delay circuitry is independent of the bifurcation mechanism to spiking of the neuron models involved. The system is able to robustly perform in the presence of heterogeneity of the neuronal dynamics and in the presence of 60 Hz, electrical noise. No attempts were made to shield this electrical noise. The key property of the type I neurons is their ability to spike at very low frequencies. Due to the presence of intrinsic 60 Hz electrical noise, the circuit model for the type I neuron failed to spike below 60 Hz. The operation of the system was therefore limited to frequency regions above the 60 Hz value, implying that the maximum delay obtainable through the electronic implementation of the time delay circuitry was around  $2 * 1000/60 \approx 33$  ms. The performance of the circuit can be improved by enclosing the entire circuit in a Faraday cage to eliminate to 60 Hz noise problem.

This working model of the time delay circuitry also motivates implementation of the circuitry in VLSI thereby having a workable chip of time delay circuitry usable in real life operations. For example we could have an IRU implementation in hardware.



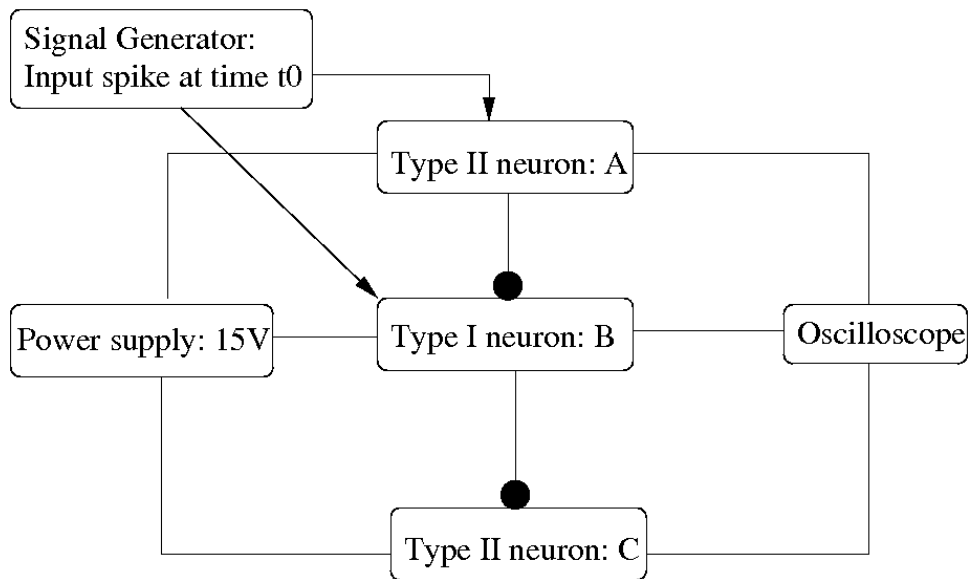


Figure 5.15 Block diagram for implementing the time delay circuitry in Electronics

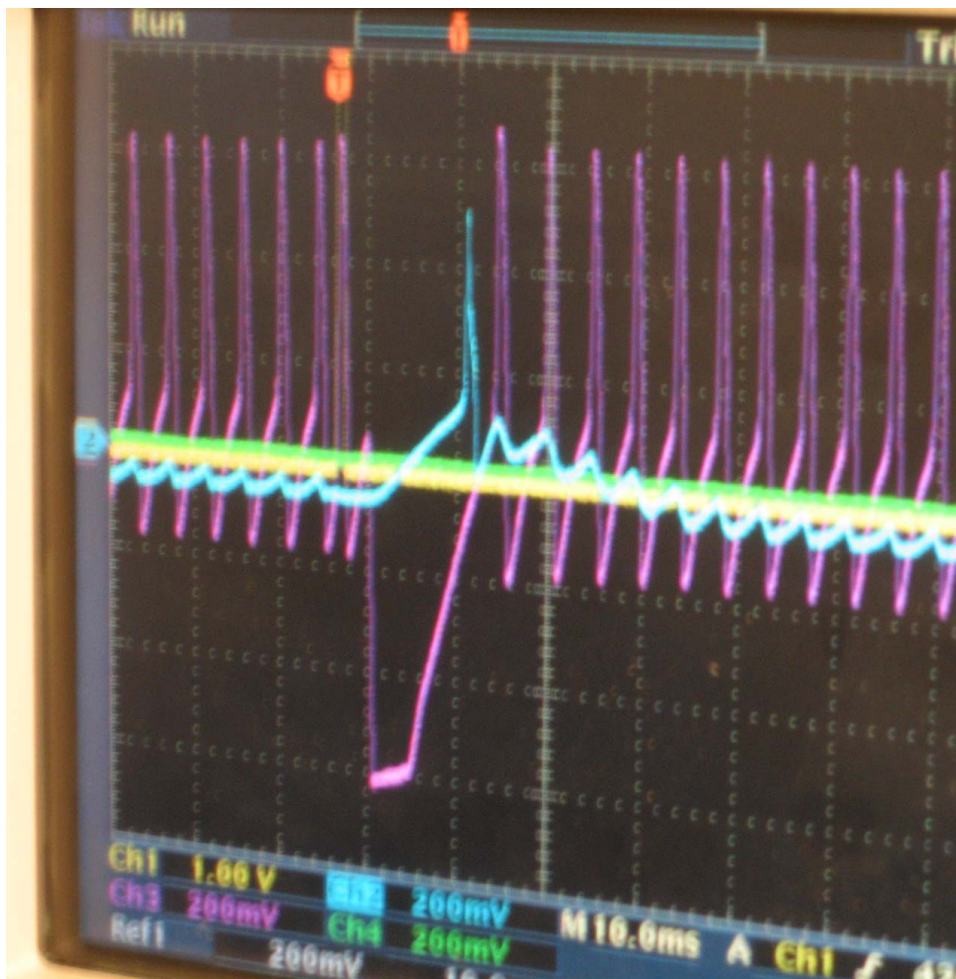


Figure 5.16 The output from the time delay circuitry as seen on the oscilloscope. In pink is the spike output from neuron B, oscillating at 225 Hz. In green is shown the spike output from neuron C after a delay of  $\Delta T = 10\text{ms}$ .

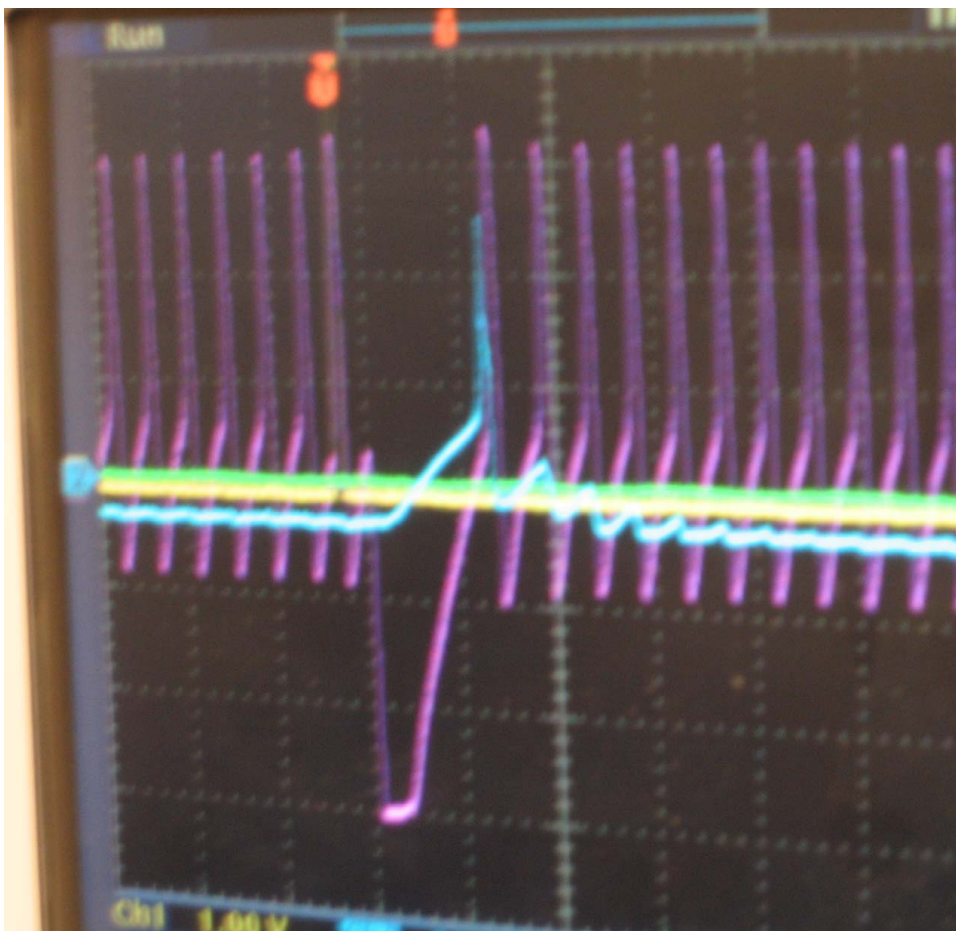


Figure 5.17 The output from the time delay circuitry as seen on the oscilloscope. In this case the inhibitory synaptic coupling from  $B \rightarrow C$  is increased such that the neuron  $C$  fires at increased delay of  $\Delta T = 15$  ms.

# Bibliography

- Aarabzadeh E, Panzeri S, Diamond M (2004) Whisker vibration information carried by rat barrel cortex neurons. *J Neurosci* 24:6011–6020.
- Abarbanel HDI, Gibb L, Huerta R, Rabinovich M (2003) Biophysical model of synaptic plasticity dynamics. *Biol Cybern* 89:214–226.
- Abarbanel HDI, Talathi S, Mindlin G, Gibb L, Rabinovich M (2004a) Dynamical model for birdsong maintenance and control. *Phys Rev E* 70:051911.
- Abarbanel H, Gibb L, Mindlin G, Rabinovich M, Talathi SS (2004b) Spike timing and synaptic plasticity in the premotor pathway of birdsong. *Biological Cybernetics* 91:159–167.
- Abarbanel H, Gibb L, Mindlin G, Talathi S (2004c) Mapping neural architecture onto acoustic features of birdsong. *J Neurophysiol* 92:96–100.
- Abarbanel H, Talathi S (2006) Neural circuitry for recognizing interspike interval sequences. *Phys Rev Lett* 96:148104.
- Abarbanel H, Talathi S, Gibb L, Rabinovich M (2005) Synaptic plasticity with discrete state synapses. *Phys Rev E* 72:031914.
- Artola A, Singer W (1993) Long-term depression of excitatory synaptic transmission and its relationship to long-term potentiation. *Trends Neurosci* 16:480–487.
- Bi G, Poo M (1998) Synaptic modifications in cultured hippocampal neurons: Dependence on spike timing, synaptic strength, and postsynaptic cell type. *J Neurosci* 18:10464–10472.
- Bi G, Poo M (2001) Synaptic modification by correlated activity: Hebb’s postulate revisited. *Ann Rev Neurosci* 24:139–166.
- Bliss T, Collingridge GL (1993) A synaptic model of memory: long-term potentiation in the hippocampus. *Nature* 361:31–39.
- Bottjer SW, Halsema K, Brown S, Miesner E (1989) Axonal connections of a forebrain nucleus involved with vocal learning in zebra finches. *J Comp Neurol* 279:312–326.

- Bradshaw JM, Kubota Y, Meyer T, , Schulman H (2003) An ultrasensitive  $ca^{2+}$ /calmodulin-dependent protein kinase ii -protein phosphatase 1 switch facilitates specificity in postsynaptic calcium signaling. *Proc Natl Acad Sci, USA* 100:10512–10517.
- Brainard MS, Doupe AJ (2000) Interruption of a basal ganglia-forebrain circuit prevents plasticity of learned vocalizations. *Nature* 404:762–766.
- Brainard MS, Doupe A (2002) What songbirds teach us about learning. *Nature* 417:351–358.
- Bramham C, Srebo B (1989) Synaptic plasticity in the hippocampus is modulated by behavioral state. *Brain Res* 493:74–86.
- Brenowitz EA, Margoliash D, Nordeen K (1997) An introduction to birdsong and the avian song system. *J Neurobiol* 33:495–500.
- Buonomano DV (2000) Decoding temporal information: A model based on short-term synaptic plasticity. *J Neurosci* 20:1129–1141.
- Buonomano D, Karmarkar U (2002) How do we tell time? *Neuroscientist* 8:42–51.
- Buracas G, Zador AM, DeWeese M, Albright T (1998) ‘efficient discrimination of temporal patterns by motion sensitive neurons in primate visual cortex. *Neuron* 9:59–69.
- Cardin JA, Raskin JN, Schmidt MF (2005) Sensorimotor nucleus nif is necessary for auditory processing but not vocal motor output in the avian song system. *J Neurophysiol* 93:2157–66.
- Carr CE, Konishi M (1988) Axonal delay lines for time measurement in the owl’s brainstem. *Proc Nat Acad Sci, USA* 85:8311–8315.
- Carr CE, Konishi M (1990) A circuit for detection of interaural time differences in the brain stem of the barn owl. *J Neurosci* 10:3227–46.
- Carroll RC, Lissin D, Zastrow M, Nicoll R, Malenka R (1999) Rapid redistribution of glutamate receptors contributes to long term depression in hippocampal cultures. *Nature Neurosci* 2:454–460.
- Castellani GC, Quinlan E, Cooper L, Shouval H (2001) A biophysical model of bidirectional synaptic plasticity: Dependence on ampa and nmda receptors. *Proc Nat Acad Sci, USA* 98:12772–12777.
- Churchland P, Koch C, Sejnowski T (1993) *Computational Neuroscience* MIT Press, Cambridge, MA.
- Clayton D (1997) Role of gene regulation in song circuit development and song learning. *J Neurobiol* 33:549–571.

- Coleman M, Mooney R (2004) Synaptic transformations underlying highly selective auditory representations of learned birdsong. *J Neurosci* 24:7251–7265.
- Contractor A, Heinemann S (2002) Glutamate receptor trafficking in synaptic plasticity. *Sci STKE* 156:RE14.
- Crawford JD (1991) Introduction to bifurcation theory. *Rev Mod Phys* 63:991–1037.
- Dave AS, Margoliash D (2000) Song replay during sleep and computational rules for sensorimotor vocal learning. *Science* 290:812–816.
- Debanne D, Gahwiler B, Thompson S (1994) Asynchronous pre- and postsynaptic activity induces associative long-term depression in area cal of the rat hippocampus in vitro. *Proc Natl Acad Sci, USA* 91:1148–1152.
- Del Giudice P, Fusi S, Mattila M (2003) Modelling the formation of working memory with networks of integrate-and-fire neurons connected by plastic synapses. *J Physiol. (Paris)* 97:65–681.
- Ding L, Perkel D (2002) Dopamine modulates excitability of spiny neurons in the avian basal ganglia. *J Neurosci* 22:5210–5218.
- Ding L, Perkel D J, M.A. F (2003) Presynaptic depression of glutamatergic synaptic transmission by d1-like dopamine receptor activation in the avian basal ganglia. *J Neurosci* 23:6086–6095.
- Doupe AJ, Kuhl P (1999) Birdsong and human speech: common themes and mechanisms. *Annual Review of Neuroscience* 22:567–631.
- Doupe A, Solis M (1997) Song and order selective neurons develop in the song bird anterior forebrain during vocal learning. *J Neurobiol* 33:694–709.
- Drazin P (1992) *Nonlinear Systems* Cambridge University Press, Cambridge, MA.
- Dutar P, Vu H, Perkel DJ (1998) Multiple cell types distinguished by physiological, pharmacological, and anatomic properties of nucleus hvc of the adult zebra finch,. *J Neurophysiol* 80:1828–1838.
- Ermentrout B (1996) Type i membranes, phase resetting curves and synchrony. *Neural Compute* 8:979–1001.
- Fano R (1961) *Transmission of information; a statistical theory of communications* M.I.T Press, New York, NY.
- Farries M, Ding L, Perkel D (2005) Evidence for “direct” and “indirect” pathways through the song system basal ganglia. *J Comp Neurol* 484:93–104.

- Farries M, Perkel D (2000) Electrophysiological properties of avian basal ganglia neurons recorded in vitro. *J Neurophysiol* 84:2502–2513.
- Farries M, Perkel D (2002) A telencephalic nucleus essential for song learning contains neurons with physiological characteristics of both striatum and globus pallidus. *J Neurosci* 22:3776–3787.
- Feldman D (2000) Timing-based ltp and ltd at vertical inputs to layer ii/iii pyramidal cells in rat barrel cortex. *Neuron* 27:45–56.
- Forger DB, Peskin CS (2003) ‘a detailed predictive model of the mammalian circadian clock. *Proc Nat Acad Sci, USA* 100:14806–11.
- Forger DB, Peskin CS (2004) Model based conjectures on mammalian clock controversies. *J Theor Biol* 230:533–539.
- Franks KM, Sejnowski T (2002) Complexity of calcium signaling in synaptic spines. *Bioessays* 97:659–681.
- Froemke R, Dan Y (2002) Spike-timing-dependent synaptic modification induced by natural spike trains. *Nature* 416:433–438.
- Guttman R, Lewis S, Rinzel J (1980) Control of repetitive firing in squid axon membrane as a model for a neuroneoscillator. *J Physiol* 305:377–395.
- Haas J, Nowotny T, Abarbanel H (2006) Spike-timing-dependent plasticity of inhibitory synapses in the entorhinal cortex. *J Neurophysiol, In review* .
- Hahnloser RHR, Kozhevnikov A, M.S. F (2002) An ultra-sparse code underlies the generation of neural sequences in songbird. *Nature* 419:65–70.
- Hille B (2001) *Ion Channels of excitable membranes, 3rd Ed* Sinauer Associates, Sunderland, MA.
- Horowitz P, Hill W (1989) *The art of Electronics* Cambridge University Press, Cambridge, MA.
- Ivry RB (1996) The representation of temporal information in perception and motor control. *Curr Opin Neurobiol* 6:851–857.
- Janata P, Margoliash D (1999) Gradual emergence of song selectivity in sensorimotor structures of the male zebra finch song system. *J Neurosci* 19:5108–5118.
- Kao MH, Doupe A, Brainard MS (2005) Contributions of an avian basal ganglia-forebrain circuit to real-time modulation of song. *Nature* 433:638–643.
- Karmarkar UR, Buonomano U (2001) A model of spike-timing dependent plasticity: one or two coincidence detectors ? *J Neurophysiol* 88:507–513.

- Kempler R, Gerstner W, van Hemmen J (1999) Hebbian learning and spiking neurons. *Phys Rev E* 59:4498–4514.
- Kimpo R, Theunissen F, A.J. D (2003) Propagation of correlated activity through multiple stages of a neural circuit. *J Neurosci* 23:5750–5761.
- Knudsen E, Konishi M (1996) Space and frequency are represented separately in auditory midbrain of the owl. *J Neurophysiol* 41:870–884.
- Koch C (1999) *Biophysics of computation: information processing in single neurons* Oxford University Press, New York, NY.
- Koppel C (1997) Phase locking to high frequencies in the auditory nerve and cochlear nucleus magnocellularis of the barn owl. *J Neurosci* 17:3312–21.
- Kuznetsov Y (2004) *Elements of applied bifurcation theory- 3rd ed* Springer-Verlag, New York, NY.
- Laje R, Mindlin G (2002) Diversity within a birdsong. *Phys Rev Lett* 89:288102.
- Lawler G (1995) *Introduction to stochastic processes* Chapman and Hall, Boca Raton, FL.
- Lewicki M, Arthur B (1996) Hierarchical organization of auditory context sensitivity. *J Neurosci* 3:1039–57.
- Linden D (1999) The return of the spike, post synaptic action potentials and the induction of ltp and ltd. *Neuron* 4:661–666.
- Lisman J, Schulman H, Cline H (2002) The molecular basis of camkii function in synaptic and behavioural memory. *Nature Rev Neurosci* 3:175–189.
- Luo M, Ding L, Perkel D (2001) An avian basal ganglia pathway essential for vocal learning forms a closed topographic loop. *J Neurosci* 21:6836–6845.
- Luo M, Perkel DJ (2002) Intrinsic and synaptic properties of neurons in an avian thalamic nucleus during song learning. *J Neurophysiol* 88:1903–1914.
- Luo M, Perkel D (1999a) A gabaergic, strongly inhibitory projection to a thalamic nucleus in the zebra finch song system. *J Neurosci* 19:6700–6711.
- Luo M, Perkel D (1999b) Long-range gabaergic projection in a circuit essential for vocal learning. *J Comp Neurol* 403:68–84.
- Magee J, Johnston D (1997) A synaptically controlled associative signal for hebbian plasticity in hippocampal neurons. *Science* 275:209–213.
- Malenka RC, Kauer JA, Zuker RS, Nicoll RA (1998) Postsynaptic calcium is sufficient for potentiation of hippocampal synaptic transmission. *Science* 242:81–84.



- Malenka R, Nicoll R (1999) Long-term potentiation—a decade of progress. *Science* 285:1870–1874.
- Malinow R, Malenka R (2002) Ampa receptor trafficking and synaptic plasticity. *Ann Rev Neurosci* 25:103–126.
- Malinow R, Miller J (1986) Postsynaptic hyperpolarization during conditioning reversibly blocks induction of long-term potentiation. *Nature* 320:529–530.
- Margoliash D (1983) ‘acoustic parameters underlying the responses of song-specific neurons in the white-crowned sparrow. *J Neurosci* 3:1039–57.
- Margoliash D (1986) Preference for autogenous song by auditory neurons in a song system nucleus of the white-crowned sparrow. *J Neurosci* 6:1643–61.
- Margoliash D (1997) Functional organization of forebrain pathways for song production and perception. *J Neurobiol* 33:671–693.
- Margoliash D (2002) Evaluating theories of bird song learning: implications for future directions. *J Comp Physiol A* 188:851–866.
- Markram H, Lubke J, Frotscher M, Sakmann B (1997) Timing-based ltp and ltd at vertical inputs to layer ii/iii pyramidal cells in rat barrel cortex. *Science* 275:213–215.
- Martin S, Grimwood P, Morris R (2000) Synaptic plasticity and memory: An evaluation of hypothesis. *Annu Rev Neurosci* 23:649–711.
- Mauk MD, Buonomano D (2004) The neural basis of temporal processing. *Ann Rev Neurosci* 27:307–340.
- McCormick DA, Huguenard J (1992) A model of the electrophysiological properties of thalamocortical relay neurons. *J Neurophysiol* 68:1384–1400.
- McCormick DA, Pape H (1990) Properties of a hyperpolarization-activated cation current and its role in rhythmic oscillation in thalamic relay neurons. *J Physiol (Lond)* 431:291–318.
- Mindlin GB, Gardner T, Goller F, Suthers R (2003) Experimental support for a model of birdsong production. *Phys Rev E* 68:041908.
- Montgomery JM, Madison D (2004) Discrete synaptic states define a major mechanism of synapse plasticity. *Trends Neurosci* 27:744–750.
- Mooney R (1992) Synaptic basis for developmental plasticity in a birdsong nucleus. *J Neurosci* 12:2464.
- Mooney R (2000) Different subthreshold mechanisms underlie song selectivity in identified hvc neurons of the zebra finch. *J Neurosci* 20:5420–5436.

- Mooney R, J. RM, Sturdy C (2002) A bird's eye view: top down intracellular analyses of auditory selectivity for learned vocalizations. *J Comp Physiol A* 188:879–895.
- Nishiyama MH K, Mikoshiba K, Poo MM, Kato K (2000) Calcium stores regulate the polarity and input specificity of synaptic modification. *Nature* 408:584–588.
- Nordeen KW, Nordeen E (1997) Anatomical and synaptic substrate for avian song ;learning. *J Neurobiol* 33:532–548.
- Nowak L, Bregestovski P, Ascher P, Hebet A, Prochiantz A (1984) Magnesium gates glutamate-activated channels in mouse central neurones. *Nature* 307:462–465.
- Nowotny T, Rabinovich MI, Abarbanel H (2003) Spatial representation of temporal information through spike-timing-dependent plasticity. *Phys Rev E* 68:011908.
- Nowotny T, Zhigulin V, Selverston A, Abarbanel H, M.I R (2003) Enhancement of synchronization in a hybrid neural circuit by spike-timing dependent plasticity. *J Neurosci* 23:9776–9785.
- O'Connor DH, Wittenberg G, S.S-H W (2005a) Dissection of bidirectional synaptic plasticity into saturable unidirectional process. *J Neurophysiol* 94:1565–1573.
- O'Connor D, Wittenberg G, S.S-H. W (2005b) Graded bidirectional synaptic plasticity is composed of switchlike unitary events. *Proc Natl Acad Sci, USA* 102:9679–9684.
- Okuhata S, Saito N (1987) Synaptic connections of thalamo-cerebral vocal control nuclei of the canary. *Brain Res Bull* 18:35–44.
- Perkel DJ (2004) Origin of the anterior forebrain pathway. *Ann N Y Acad Sci, USA* 1016:736–48.
- Petersen C, Malenka R, Nicoll R, Hopfield J (1998) All-or-none potentiation at ca3-ca1 synapses. *Proc Natl Acad Sci, USA* 95:4732–4737.
- Pikovsky A, Rosenblum M, Kurths J (2001) *Synchronization, a universal concept in nonlinear sciences* Cambridge University Press, Cambridge, MA.
- R. M, Victor J, Purpura K, Shapley R (1998) Robust temporal coding of contrast by v1 neurons for transient but not for steady-state stimuli. *J Neurosci* 18:6583–98.
- Roberts P (1999) Computational consequences of temporally asymmetric learning rules: I. differential hebbian learning. *J Comp Neurosci* 7:235–246.
- Rosen MJ, Mooney R (2006) Synaptic interactions underlying song-selectivity in the avian nucleus hvc revealed by dual intracellular recordings. *J Neurophysiol* 95:1158–1175.

- Rubin JE, Gerkin R, Bi GQ, Chow C (2005) Calcium time course as a signal for spike-timing dependent plasticity. *J. Neurophysiol* 93:2600–2613.
- Sabatini BL, Maravall M, Svoboda K (2001)  $[Ca^{2+}]$  signaling in dendritic spines. *Curr Opin Neurobiol* 11:349–356.
- Sabatini BL, Oertner T, Svoboda K (2002) The life cycle of  $Ca^{2+}$  ions in dendritic spines. *Neuron* 33:439–452.
- Selverston A (1993) Modeling of neural circuit: What have we learned? *Ann Rev Neurosci* 16:531–546.
- Sheng M, Kim M (2002) Postsynaptic signaling and plasticity mechanisms. *Science* 298:776–780.
- Shouval HZ, Bear MF, , Cooper LN (2002) A unified model of nmda receptor-dependent bidirectional synaptic plasticity. *Proc Nat Acad Sci, USA* 99:10831–10836.
- Sjostrom PJ, Nelson S (2002) Spike timing, calcium signals and synaptic plasticity. *Curr Opin Neurobiol* 12:305–314.
- Soderling T, Derkach V (2000) Postsynaptic protein phosphorylation and ltp. *Trends Neurosci* 23:75–80.
- Sourdet V, Debanne D (1999) The role of dendritic filtering in associative long term synaptic plasticity. *Learn. Mem* 6:422–447.
- Spiro J, Dalva M, Mooney R (1999) Long-range inhibition within the zebra finch song nucleus ra can coordinate the firing of multiple projection neurons. *J Neurophysiol* 81:3007–3020.
- Stark LL, Perkel D (1999) Two-stage, input-specific synaptic maturation in a nucleus essential for vocal production in the zebra finch. *J Neurosci* 19:9107–9116.
- Sugase Y, Yamane S, Ueno S, Kawano K (1999) Global and fine information coded by single neurons in the temporal visual cortex. *Nature* 400:869–873.
- Suthers R (1997) Peripheral control and laterization of birdsong. *J Neurobiol* 33:632–652.
- Traub R, Miles R (1991) *Neuronal networks of the hippocampus* Cambridge University Press, Cambridge, MA.
- Traub R, Wong R, Miles R, Michelson H (1991) A model of a ca3 hippocampal pyramidal neuron incorporating voltage clamp data on intrinsic conductances. *J Neurophysiol* 66:635–650.
- Van Kampen N (1995) *Stochastic processes in physics and chemistry* Elsevier Science Publishers, Amsterdam, The Netherlands.

- Vates GE, Vicario D, Nottebaum F (1997) Reafferent thalamo-“cortical” loops in the song system of oscine songbirds. *J Comp Neurol* 380:275–290.
- Volkovskii A Electronic circuit implementation of hodgkin huxley neuron model. *Unpublished Results* .
- Welker C (1976) Receptive fields of barrels in the somatosensory neocortex of the rat. *J Comp Neurol* 166:173–189.
- Wild J (1993) Descending projections of the songbird nucleus robustus archistriatalis. *J Comp Neurol* 338:225–241.
- Winder DGS D (2001) Roles of serine/threonine phosphatases in hippocampal synaptic plasticity. *Nature Rev Neurosci* 2:461–473.
- Wittenberg G (2003) *Learning and memory in the hippocampus: events on millisecond to week time scales* PhD, Dissertation, Princeton University, NJ.
- Yang SN, Tang Y, R.S Z (1999) Selective induction of ltp and ltd by postsynaptic [ca2+] elevation. *J Neurophysiol* 81:781–787.
- Yeckel MF, Kapur A, Johnston D (1999) Multiple forms of ltp in ca3 neurons use a common postsynaptic mechanism. *Nature Neurosci* 2:625–633.
- Yu AC, Margoliash D (1996) Temporal hierarchical control of singing in birds. *Science* 273:1871–1875.
- Zhabotinsky AM (2000) Bistability in the [Ca<sup>2+</sup>]/calmodulin-dependent protein kinase-phosphatase system. *Biophys J* 79:2211–2221.
- Zhigulin VP, Rabinovich M, Huerta R, Abarbanel H (2003) Robustness and enhancement of neural synchronization by activity-dependent coupling,. *Phys Rev E* 67:021901.